RICE UNIVERSITY

Bicrystals and Bowties: Photothermoelectric and plasmonic effects of gold nanoscale structures

by

Charlotte I. Evans

A Thesis Submitted
in Partial Fulfillment of the
Requirements for the Degree

Doctor of Philosophy

Approved, Thesis Committee:

Douglas Natelson, Chair
Professor of Physics & Astronomy,
Electrical & Computer Engineering, and
Materials Science & Nanoengineering

Jason Hafner
Professor of Physics & Astronomy and
Chemistry

Bharadwaj

Palash Bharadwaj
Texas Instruments Assistant Professor of
Electrical & Computer Engineering

Houston, Texas

December, 2019

ABSTRACT

Bicrystals and Bowties: Photothermoelectric and plasmonic effects of gold nanoscale structures

by

Charlotte I. Evans

The interaction of light with gold dramatically changes when the size of the gold devices is reduced to the nanoscale. The free electron gas in the metal can collectively oscillate with the electric field of the incident laser in an excitation called plasmons which can result in dramatic enhancements of the local electric field. Electronic transport and open circuit voltage (photothermoelectric) measurements can be powerful tools to characterize a gold nanoscale device heated by an incident laser. This laser can be raster-scanned to probe the response of the device as a function of laser position. The thermoelectric effect has been well-studied since its discovery by Seebeck in the 1820s. A resurgence of thermoelectric studies have been published recently manipulating the thermoelectric properties of thin metal film devices via nanostructuring. Substantial variation of the local Seebeck coefficient has recently been observed in polycrystalline nanowires of uniform thickness and width, a regime where the Seebeck coefficient is generally regarded as a constant value. A study of the photothermoelectric voltage signal of single crystalline wires and bicrystal devices, two single crystals in contact at an individual grain boundary, provides evidence that grain structure does not substantially contribute to the local Seebeck coefficient. Instead, the photovoltages of these single and bicrystal devices are well-correlated with

local variations in strain as detected by electron back-scatter diffraction measurements and with variations in platinum impurity concentration. Therefore, the photovoltage measurements are demonstrated to have sensitivity to intrinsic variations in nanoscale devices that are otherwise difficult to detect using traditional electronic transport and imaging techniques.

In nanoscale molecular junctions, the large enhancements of the local electric field due to local surface plasmon resonances allows for single-molecule Raman measurements, which probe the inelastic energy exchanges between incident photons and the vibrational modes of the molecule. These optical measurements can be combined with electronic transport measurements to detect the energy exchanges between the vibrational and electronic energy states in the molecule. However, the plasmonic resonances that allow for the single-molecule sensitivity also result in high local heating making these energy exchanges difficult to detect. We will discuss one potential way to mitigate the local heating: remote excitation of the nanojunction using propagating surface plasmon polaritons. Electronic transport measurements estimate the local temperature rise of the device due to direct and remote excitation. Large enhancements of the open circuit photovoltages in nanogaps due to hot electron photocurrents from non-radiative plasmon decay are observed. The open circuit photovoltages are then used to probe the interactions of the propagating surface plasmon polaritons with the local modes in the nanogap, demonstrating that the open circuit photovoltages and electronic transport methods are powerful tools to not only characterize nanoscale devices but also to probe the plasmonic properties of the devices.

Acknowledgements

This work is dedicated to my father Keven Rogers and my grandfather Harry Treder.

First and foremost, I would like to thank Dr. Douglas Natelson for taking me on as a student. I couldn't have asked for a better mentor. There's absolutely nothing like listening to him give a short, yet insightful, lesson in physics on the fly that suddenly brings clarity to a topic you couldn't understand just five minutes earlier. I would also like to thank my thesis committee members, Drs. Jason Hafner and Palash Bharadwaj, and my masters committee members, Drs. Huey Huang and Stephen Bradshaw. Thank you for all the mentorship, guidance, and advice you have given me over the years. Thank you to Drs. Stan Dodds, Emilia Morosan, and Kevin Kelly for all the extensive conversations during this journey.

Thank you to the Natelson lab members, especially the optics group: Kenny, Yajing, Xifan, Mahdiyeh, Mathieu, LongJi, and Yunxuan. Thank you to Loah for always being a friend. Thank you to the Dr. Peter Nordlander group, especially Alessandro Alabastri and Jian Yang for theoretical collaboration. Thank you to the Dr. Jon Fan group, especially Lucia, Rui, and Rachel, for the collaboration on one of the most rewarding projects I've ever worked on. Thank you to Pavlo Zolotavin for being my mentor.

Thank you to the National Science Foundation for the Graduate Research Fellowship Program and other grants, the Welch Foundation, and the Army Research Office for funding my research.

Thank you to the professors and instructors who influenced me to study physics: Mr. Tim Cox, Drs. Mary Williams-Norton and Sarah Desotell at Ripon College, Drs. Earl Blodgett and Lowell McCann and the rest of the physics department at University of Wisconsin-River Falls, Dr. Steve List in UWRF math department, and Dr. Tom Furtak at Colorado School of Mines.

Thank you to my family for always supporting me in everything that I do. Thank

you Dad for helping me build projectile launchers for science projects. Thank you Mom for driving for hours to pick me up from the airport on limited sleep. Thank you Angie for sending me funny pictures every day. Thank you Vincent for always being up to play a game with me. Thanks Ben and Cam for spending the holidays with us. Thank you Ice for being a loyal and goofy dog. Grandmie, thank you for your letters that all too often went unreturned.

Thank you to all my friends and loved ones near and far who supported me through grad school, especially Yaqui, Shannon, Justin, Arielle, Minsheng, Ana, Dan P., Sarah F., Sarah G., Sagnak, Eduardo, MacKenzie, Em, Haley, Jane, Brad, Katsuya, Crystal, Will, Brodie, Dan N., George, Leah, Amanda, Shawn, Michele, Chris, Amy, Arriety, Priscilla, and Candace. Thank you to Sarah, Kati, Cat, Libby, and Kaleigh for supporting me through every challenge. Thank you to Drs. Paul Paily, Michael Greaser, Christopher Collaco, Julia Pryzant, and Paul Treder for your excellent care. Thank you to the 72nd IBCT for your encouragement and support. Thank you to Grant for being one of the most selfless people I've ever met. Whether you're helping me finish a beam alignment late at night, helping me recover from an ankle surgery even though we hardly knew each other, or encouraging me to ambitiously follow my professional goals, your unwavering support made every challenge seem possible. Thank you Thea, never in any lifetime would I deserve such a wonderful companion as you.

Contents

List of Figures

List of Equations

List of abbreviations

AFM - atomic force microscopy

α - polarizability

BSF - OptiGrate BragGrate Spatial Filters

E - electric field

e - electron charge

ϵ - dielectric function

γ - plasmon damping constant

G - electrical conductance

G_o - conductasnce quantum

HOMO - highest occupied molecular orbital

I - current

IETS - inelastic electron tunneling spectroscopy

IPA - isopropyl alcohol

IR - infrared

J - current desnity

k_x - wavevector along the x-axis

κ - thermal conductivity

λ - laser wavelength or electron mean free path

LUMO - lowest unoccupied molecular orbital

LSP - local surface plasmon

LSPR - local surface plasmon resonance

m_e - effective mass of electron

MIBK - methyl isobutyl ketone

n_e - electron number density

NIR - near infrared

OCV - open circuit voltage

OCPV - open circuit photovoltage

ω_p - plasma frequency

p - dipole moment

PMMA - polymethyl methacrylate

PTE - photothermoelectric effect

Q-factor - plasmon figure-of-merit

S - Seebeck coefficient

SERS - surface-enhanced Raman spectroscopy

σ - electrical conductivity

σ_{ext} - extinction cross-section

SPP - surface plasmon polariton

STM - scanning tunneling microscopy

T - temperature

TERS - tip enhanced Raman spectroscopy

V - voltage

ZT - thermoelectric figure-of-merit

Chapter 1

Introduction

The interaction of light with gold changes dramatically at the nanoscale. The free electron gas in the metal can collectively oscillate with the incident electric field resulting in large enhancements of the local electric field behaving as a quasiparticle called plasmons. The work in this thesis considers the effects of gold plasmonically active nanostructures under focused laser illumination. First, the photothermoelectric effect is used to probe intrinsic variation in gold "bowtie" devices consisting of a plasmonically-active nanowire between two electrodes. The variation in the detected photovoltages are suggestive of local changes in the Seebeck coefficient in the polycrystalline films. To determine the cause of these local variations, the devices are simplified to single crystalline gold wires and bicrystal devices with a single grain boundary. Comprehensive studies of each demonstrate that these photovoltages are sensitive to small variations in local strain and platinum impurities. Simultaneous optical and electronic transport measurements in molecular junctions can allow for the detection of energy exchanges between the electronic and vibrational states of an individual molecule. The plasmonic resonances in the gold bowtie devices allows for single molecule detection in optical measurements, but also result in sufficiently high local heating that these energy exchanges cannot be well-resolved. A potential way to mitigate this heating, via remote excitation of the nanowire via propagating surface plasmon polaritons, provides a promising path forward for these measurements. The local heating of the nanowire due to remote excitation is estimated via electronic transport measurements while the coupling of the propagating plasmons to the local modes in the nanowire are probed using photovoltages. This work highlights the wealth of information that can be provided via simple electronic transport and open circuit voltage measurements in device characterization.

1.1 Overview and organization of this thesis

The first three chapters will discuss the introductory background information necessary to understand the experimental results. First, Chapter 2 will discuss the advances of the thermoelectric effect in the nanoscale regime, particularly single metal thermocouples. Chapter 3 details how conductance measurements can probe the energy exchanges between tunneling electrons and molecular vibrational modes in molecular junctions. Chapter 4 discusses how the free electrons in gold can couple with incident laser illumination, oscillating in unison as quasiparticles called plasmons, which amplify the local electric field in nanostructures. The local enhancement of the electric field allows for single molecule sensitivity of Raman spectroscopy which probes the vibrational energy exchanges within a molecule through inelastic light scattering. Finally Chapter 5 provides details about the nanoscale device that is primarily discussed in this work: the gold "bowtie" consisting of a plasmonically resonant nanowire constriction between two fan out electrodes. Previous results will be briefly summarized before the experimental methods used throughout this work are discussed.

The results discussed in this work can be broken down into two parts. First, the sensitivity of the photothermoelectric effect to detect small changes in nanoscale devices is discussed. Chapter 6 looks at results of photothermoelectric measurements of intact gold "bowtie" devices and discusses that while nanostructuring devices can result in single metal thermocouples, the photothermoelectric effect shows surprising sensitivity to the crystalline structure of thin polycrystalline gold films with spatial scales smaller than the laser spot size. Chapter 7 looks at the importance of crystalline structure in the photothermoelectric effect of single crystalline gold devices and gold “bicrystal” devices, devices consisting of a single grain boundary. The photothermoelectric voltages are compared to electron back-scatter diffraction measurements which provide insight on the local details of the elastic strain. The correlation between these measurements indicate that the photothermoelectric effect is sensitive to local changes in strain and that the photothermoelectric effect is sensitive to details that would be challenging to detect through traditional electronic transport measurements. Chapter 8 extends this study of the single and bicrystal gold devices to devices with trace platinum impurities which demonstrate that the photothermoelectric voltages are sensitive to the metal purity down to levels that are difficult to measure even in state-of-the-art equipment.

Next, the plasmonic nature of gold “bowtie” devices is discussed. Chapter 9 looks at how plasmonic resonances in nanowires can result in high local heating and how electronic transport measurements can be used to determine the local temperature rise of the nanowire, both from direct illumination and remote excitation from surface plasmon polaritons that propagate from a grating in the electrode design to the nanowire. Then, Chapter 10 discusses how huge enhancements of photovoltages are seen in plasmonically resonant nanowires with electromigrated nanogaps, and that these large signals can be attributed to hot electrons tunneling across the gap and extends the work using photovoltages to detect how surface plasmon polaritons can remotely excite hot electrons which then tunnel across the nanogap.

Finally, Chapter 11 provides a summary of the work discussed throughout this document before discussing potential future directions for the continuation of these findings.

Chapter 2

The Thermoelectric Effect

Imagine you have a bar of some material and you heat one end, such as Fig. 2.1. Electrons tend to diffuse from the hot side to the cold side until thermal equilibrium is established. Now, imagine that you keep one side hot and one side cold - forever. Although electrons will still diffuse from the hot side to the cold side, thermal equilibrium can never be established because you are forcing there to be a permanent temperature gradient (∇T). Net charges will build up on each end - positive charges on the hot side, negative charges on the cold side - to counteract the thermal diffusion of electrons which results in no net charge. If you were to probe the voltage difference between both ends, the charge distribution built up to counteract the thermal diffusion of electrons would result in an open circuit voltage (OCV) proportional to the temperature difference between both ends times some constant, called the Seebeck coefficient (S), that is a material property that describes the propensity of the material to build up charge to counteract a temperature gradient. Briefly put, this describes the thermoelectric effect: an effect that relates the conversion of temperature differences to an electric voltage or vice versa in a material. The name is a bit of a misnomer because the thermoelectric effect actually is comprised of three different, independently found effects: the Seebeck effect, Peltier effect, and Thomson effect. In this chapter, we will briefly discuss the latter two and will discuss in detail the Seebeck effect. After this chapter, mention of the thermoelectric effect will primarily focus on Seebeck effect unless otherwise specified. We will then move on to discuss the Seebeck coefficient and thermocouples. The work described in this thesis is going to touch only on metals, and in particular, gold. While some discussion will touch on more traditional aspects of the thermoelectric effect, the intent of this chapter is to frame the discussion more on what is necessary to understand the thermoelectric effect in terms of nanoscale manipulation of single metal, thin film gold nanoscale thermocouples.

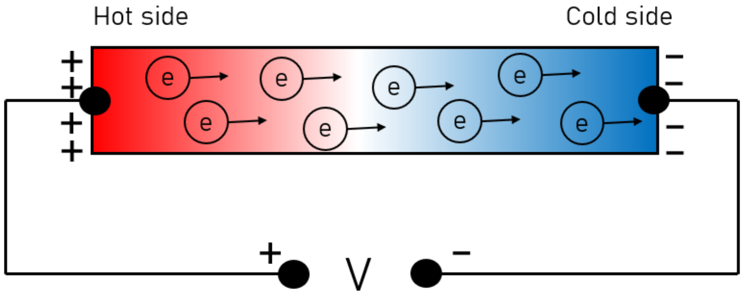

Figure 2.1 : Schematic of the thermoelectric effect: a bar of a single material is placed under a constant, steady state thermal gradient. Electrons will thermally diffuse from the hot side to the cold side. To counteract the thermal diffusion, net charges, positive on the hot side and negative on the cold side, will build up resulting in no net current. Probing both ends would result in an OCV proportional to the applied temperature gradient times the Seebeck coefficient of the material.

2.1 A Brief Introduction to the Thermoelectric Effect

As mentioned in the introduction of this chapter, the thermoelectric effect is actually comprised of three different effects: the Seebeck effect, Peltier effect, and Thomson effect. This section will give a brief introduction to each ot these. The Seebeck effect will be described in greater detail throughout the rest of this chapter.

2.1.1 The Seebeck Effect: Converting a temperature gradient to voltage

Before we can describe the Seebeck effect and the other effects thereafter, we should first briefly define two important concepts: the Seebeck coefficient and thermocouples. The specifics of these terms will be discussed in Sec. 2.2 but a conceptual overview of them will make the thermoelectric effect easier to understand.

For now, consider the Seebeck coefficient as an intrinsic material property that describes the propensity of the material to build up charge to counteract a temperature gradient. The larger S is, the larger the charge build up due to the same temperature gradient. Consider a thermocouple as an electrical device consisting of two (or more) materials with different Seebeck coefficients in contact with each other. This time, imagine you have two bars of differing materials with different S in contact with each other, as in Fig. 2.2. Instead of heating one end vs. the other, heating the interface of the two different materials while keeping both ends constant gives a difference in voltage (ΔV) that is still proportional to the applied ∇T, but the multiplicative factor is the *difference* of the two values of S.

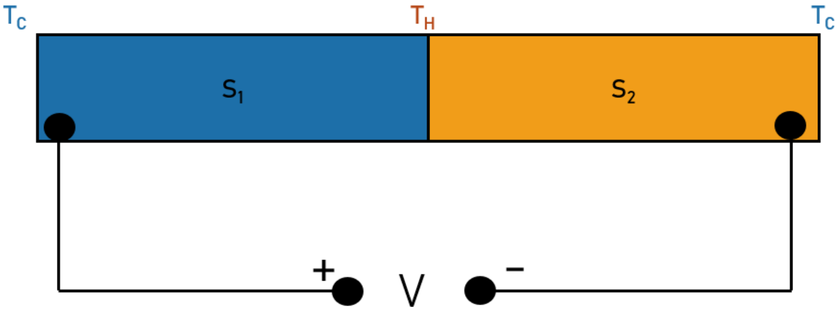

Figure 2.2 : Schematic of a thermocouple: two bars of different materials with unique Seebeck coefficients (S_1 and S_2) in contact with each other. The junction of the two different materials is heated to temperature T_H with ends kept at constant, cold temperature, T_C. This time, a voltage proportional to the applied temperature gradient and the *difference* in Seebeck coefficients can be probed between both ends.

In the steady state, this leads to the equation known as the Seebeck effect[1]:

$$\boxed{\Delta V = -S\Delta \mathrm{T}} \tag{2.1}$$

steady state Seebeck effect

While there is some debate about who discovered the Seebeck effect first*, the honor is typically given to Estonian-German Thomas Seebeck in 1821 who found that heating a junction of a thermocouple would deflect the needle of a magnetic compass.[2]

Equation 2.1 assumes that the system has reached the steady state, that is the net local current density ($\boldsymbol{J}$) is 0. The generalized form of the Seebeck effect is defined by:

$$\boxed{\boldsymbol{J} = \sigma(-\nabla V + E_{emf}) = \sigma(-\nabla V - S\nabla T)} \tag{2.2}$$

general form of the Seebeck effect

which relates the local current density to the local electrical conductivity (σ), the local voltage, ∇V, and the electromotive field, E_{emf}, which is defined as $-S\nabla T$. Setting $\boldsymbol{J}$ to 0 yields 2.1 which appears to be independent of σ. As we will see in Sec. 2.2.1, this isn't completely true, at least with regards to the electronic component of the Seebeck coefficient at the nanoscale.

---

[*] Christophe Goupil *et al.* in the Wiley textbook *Continuum Theory and Modeling of Thermoelectric Elements* first published December 14, 2015 does a beautiful job in the first chapter describing the history and some of the debate between Volta vs. Seebeck being the first to discover the effect and is well worth the read

2.1.2 The Peltier Effect: Converting a voltage to heating or cooling

The Peltier effect is sometimes combined with the Seebeck effect as it's really the same physical process, just with different manifestations. This time, instead of a temperature gradient resulting in a OCV, applying an electrical current across a thermocouple results in generated or removed heat at the interface of the two differing materials. Depending on the direction of the current flow, the junction can either heat up or cool down, as seen in Fig. 2.3. The Peltier effect is best known by the equation:

$$\boxed{\frac{\mathrm{d}Q}{\mathrm{d}t} = (\Pi_A - \Pi_B)I} \tag{2.3}$$

Peltier effect

where $\frac{\mathrm{d}Q}{\mathrm{d}t}$ is the heat generated at the junction per unit time, Peltier coefficient (Π) of the two materials marked A and B, and I is the electric current.[1] Π relates to S by the equation:

$$\boxed{\Pi = TS} \tag{2.4}$$

Relationship between the Peltier and Seebeck coefficients

Because the hot junction depicted in Fig. 2.3 can be placed on a heat sink outside of an insulated area, the Peltier effect can be used for cooling. The Peltier effect is used a lot in electronics, particularly in computer CPUs, because the circuitry can cool without any moving pieces. It is important to remember that Joule heating plays a large role in the total heat generation that isn't included in Equation 2.3. The power of heat generation depends on the product of the total resistance and the square

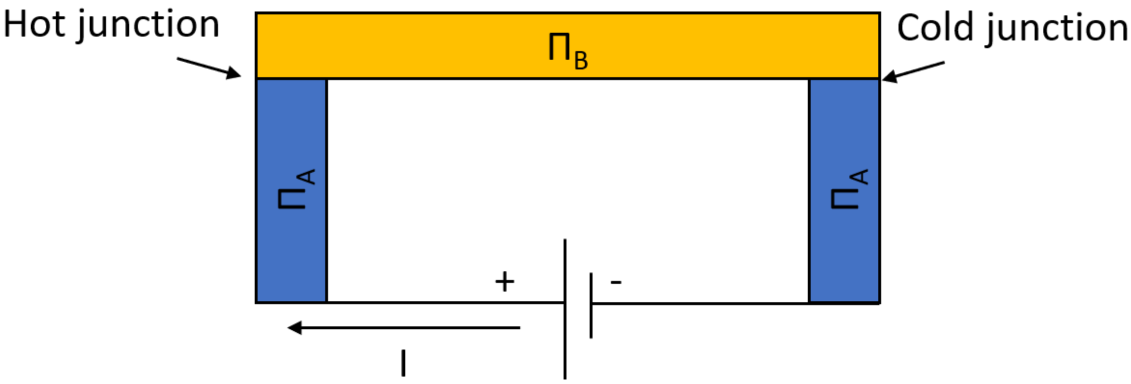

Figure 2.3 : Schematic of the Peltier effect: A circuit consisting of two materials with differing Π in contact with each other have an applied current. One of the junctions of the two materials is heated while the other is cooled, depending on the directionality of the applied current.

of the applied current. While the Peltier effect is present in any thermocouple, the effect may be challenging to detect due to Joule heating unless the thermocouples are specifically designed for thermoelectric cooling, with vastly differing Π values and low resistances to increase the effects described in Equation 2.3.[2]

2.1.3 The Thomson Effect: The continuous Peltier Effect

As seen in Equation 2.4, the Peltier effect and Seebeck effect are closely related, simply multiplying S by the absolute temperature will yield a material's Π. Let's imagine some material with a S that has some temperature dependence, $S(T)$, which we will subject to some $\nabla T(x)$. The material now has a spatial $\nabla S(x)$. Now, applying $\boldsymbol{J}$ through this material will result in a continuous form of the Peltier effect, which is better known as the Thomson effect. The Thomson effect equation describes the heat generated per volume:

$$\boxed{\dot{q} = -K\boldsymbol{J} \cdot \nabla T} \tag{2.5}$$

Thomson effect

Thomson coefficient (K) relates to S and Π using the Thomson relations:[3]

$$\boxed{K = T\frac{\mathrm{d}S}{\mathrm{d}T} = \frac{\mathrm{d}\Pi}{\mathrm{d}T} - S} \tag{2.6}$$

Thomson relations

2.2 The Seebeck Coefficient and Thermocouples

Throughout the entirety of Sec. 2.1, the Seebeck coefficient was extensively mentioned but not discussed in detail. Up until this point, we only considered it as an intrinsic property of a material. In this section, the Seebeck coefficient and its role in thermocouples will be discussed in more detail, particularly in the context of metals.

2.2.1 The Seebeck Coefficient

The Seebeck coefficient, also known as the thermopower, is material property that describes the propensity of the material to build up charge to counteract a temperature gradient with SI units V/K. In the steady state, the Seebeck coefficient can be described by re-arranging Equation 2.1:

$$\boxed{S = -\frac{\Delta V}{\Delta T}} \tag{2.7}$$

Steady-state Seebeck coefficient

As mentioned in the previous section, the Seebeck effect results in an open circuit voltage to counteract thermal diffusion of charge carriers due to a temperature gradient. S of a material cannot be measured directly, as the voltage probe will include an additional voltage contribution due to the thermoelectric effect in the leads due to the applied temperature gradient (this is called "parasitic leads")! For this reason, a measurement of S will not consist of a single material under a temperature gradient to Fig. 2.1. Instead will consist of a thermocouple similar to that seen in Fig. 2.2, so that the probe ends will be the same temperature and the *relative* S between the two different materials will be read. Using a standard, like platinum, can allow for the S to be experimentally measured.

S consists of two different parts: the electronic component and the phonon drag component. The electronic component of S dominates the system at high temperatures and describes the deviation of the electronic system from equilibrium due to an applied ∇T. Likewise, the phonon drag component describes the deviation of the phonons from equilibrium due to an applied ∇T. It additionally describes the electron-phonon interaction. This component is negligible at high temperatures, but plays a major role in temperatures lower than the Debye temperature[4]. For now, we will begin discussion of S considering only the electronic component as this is a valid approximation of S at room temperature. Later on in this section, we will discuss the phonon contribution which plays a much larger role at low temperatures.

The value of S for a specific material highly depends on the density of states of those charge carriers near the Fermi surface. The sign of the charge carriers plays a role in determining the value of S, where materials dominated with holes typically have positive S whereas materials dominated with electrons have negative S. The Seebeck effect can be used to determine which charge carriers are conducting in a system.

The Seebeck coefficient for a metal, considering only the electronic contribution, can be described using the Mott-Jones equation[5]:

$$\boxed{S = -\frac{\pi^2 k_B^2 T}{3e}\left(\frac{\mathrm{d}\ln\sigma}{\mathrm{d}E}\right)\Big|_{E=E_F}} \tag{2.8}$$

Mott-Jones equation for metals

with Boltzmann constant (k_B), temperature (T), electron charge (e), electrical conductivity (σ), Fermi energy (E_F), and electron energy (E). The biggest takeaway from this equation is that S depends strongly on the energy dependent σ of the material. Later, in Sec. 2.2.2, we will discuss how we can manipulate this at the nanoscale for single-metal thermocouples. Note that Equation 2.8 has the log derivative of σ; multiplicative factors in σ or in the density of states do *not* change S!

For bulk materials, assuming Fermi-Dirac statistics, S can be related to carrier concentration (n) by:

$$\boxed{|S| = \frac{8\pi^2 k_B^2}{3eh^2} m^* T (\frac{\pi}{3n})^{2/3}} \tag{2.9}$$

bulk material Seebeck coefficient

with h as Plank's constant, m^* as effective mass and σ=$ne\mu$ where μ is the carrier mobility[6]. Because of their high carrier concentration density, metals in general have low S values, which make them unusual candidates for most thermoelectric effect applications, demonstrated in Fig. 2.4. Semiconductors are much more common in thermoelectric effect devices because they tend to have higher S. One way to determine how effective a thermoelectric effect device can be is through the thermoelectric figure of merit (ZT): a dimensionless value to predict the maximum efficiency of a thermoelectric device detailed here:

$$\boxed{ZT = \frac{\sigma S^2 T}{\kappa}} \tag{2.10}$$

thermoelectric figure of merit

with thermal conductivity (κ). Because ZT depends on the square of S, it's no surprise that metals are not good candidates for industrial energy-harvesting thermoelectric devices.[7]

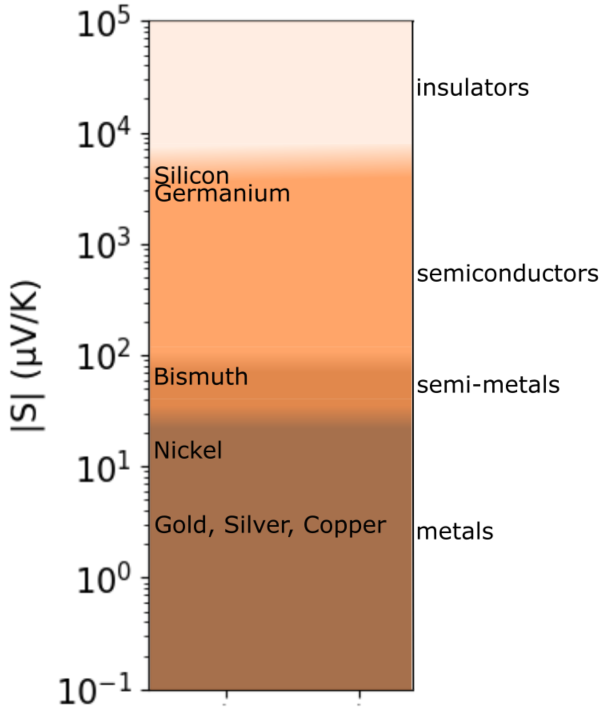

Figure 2.4 : Magnitude of Seebeck coefficients (relative to platinum) of common materials at room temperature. Metals have the lowest Seebeck coefficients of the different solids. Values from the tables in Ref. [8].

From Equations 2.8, 2.9, and 2.10, we can see that the efficiency of thermoelectric effect devices depend on κ, the energy dependence of σ, and the value of S. Achieving a higher ZT for a particular device can be challenging because increasing S for simple materials *decreases* σ, yet increasing σ typically results in an increase of κ because of the Wiedemann-Franz law:

$$\boxed{\frac{\kappa}{\sigma} = LT} \tag{2.11}$$

Wiedemann-Franz law

where L is the proportionality constant called the Lorenz number.[9, 10] A common way to try to increase ZT in silicon nanowire devices is by increasing phonon boundary scattering to decrease lattice κ, without causing much change to σ.[11–16]

Because S originates from the energy dependence of conduction electron properties, such as μ and n, thermoelectric effect measurements can give additional, complementary information on scattering mechanisms and electronic properties in a material compared to other traditional electronic transport measurements. In particular, σ and κ only give you information regarding the average magnitude of those same conduction electron properties. As mentioned in Sec. 2.1.3, the Seebeck coefficient changes with temperature. Fig. 2.5 shows the temperature dependence of platinum's S. From Equation 2.9, S increases linearly with temperature with a slope proportional to m^*. This is true at high temperatures, where the dominant scattering mechanism is electron-phonon scattering. However, metals can have complex electronic structures, scattering mechanisms, and magnetic properties which can deviate the linear relationship between the temperature and S.[17] The linear relationship of S is seen in Fig. 2.5, but at lower temperatures the temperature relationship of S deviates significantly from this theory. At temperatures below the Debye temperature, the scattering mechanisms change as phonon modes begin to freeze out. Now, we can no longer only consider the electronic portion of the Seebeck coefficient and instead must consider the contributions of phonons, and specifically phonon drag, to thermopower.[18]

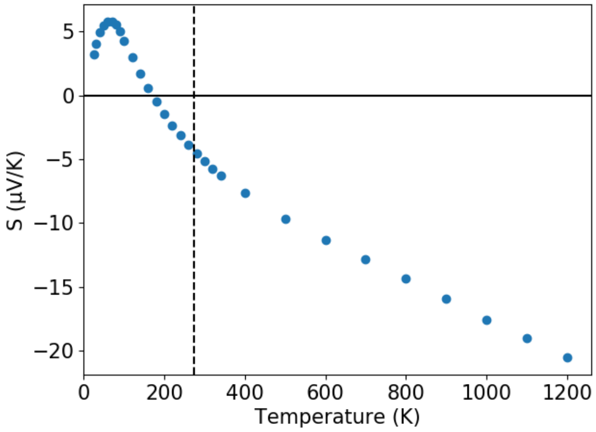

Figure 2.5 : Temperature dependence of platinum's absolute Seebeck coefficient: Data plotted from the tabulated values in Table IV in [18]. The horizontal line at the zero crossing and the vertical dashed line at room temperature are marked as a reference.

When a temperature gradient is applied to a material, the lattice vibrations are not isotropic. Instead, the phonons travel away from the hot end toward the cold end of the material. The directionality of the charge carriers scattering off the phonons is not random, instead the scattering events push the carriers toward the cold end, enhancing S.[19] The OCV that must build up to counteract not only the thermal diffusion of the charge carriers but also the effect of the phonon drag. In general, this phonon drag effect is more prevalent at low temperatures. At very low temperatures, there are not enough phonon modes to contribute to the phonon drag effect, which causes a decrease in S.[20] As more phonon modes populate as the temperature rises, the phonon drag effect will cause an increase in S, until phonon-phonon scattering processes tend to reduce the effect, resulting in a phonon drag "peak".[21] When choosing to reduce κ via impurities to increase ZT, careful consideration must be made to prevent the impurities increasing phonon-phonon scattering negating the phonon drag component of S at low temperature thereby further reducing ZT.[22] The phonon drag contribution is described by Equation 2.12:

$$\boxed{S_p = AT^3 \int_0^{\theta_D/T} \alpha(z) \frac{z^4 e^z}{(e^z - 1)^2} dz} \tag{2.12}$$

phonon drag component of the Seebeck coefficient

where A is a constant, T is the temperature, θ_D is the Debye temperature, e is the charge of the electron, $z = \frac{\hbar\omega}{k_B T}$, ω is the phonon frequency, $\hbar$ is reduced Plank's constant, and $\alpha(z)$ is some function that describes the probability that the phonon with frequency ω interacts with an electron[4].

Fig. 2.6 shows the temperature dependence of S of the noble metals, copper, gold, and silver. While this data, taken from tabulated values in Reference [23], does not include temperatures low enough to see the effects of phonon drag, whose contribution is also positive [24, 25] at temperatures above 1.4 K, the linear relation between the temperature and S of these metals is seen at moderate temperatures and have approximately identical values. At very high temperatures, however, the values of gold and silver's S deviate. Silver tends to rise faster than linear, whereas gold tends to saturate at very high temperatures.[17]

Earlier, it was mentioned that S depends on the energy dependence of σ. Normally the sign of S is the same sign as the charge carriers in the system. The free electron model for gold and the other noble metals predicts a negative S and the Hall coefficient of noble metals is negative, yet Fig. 2.6 shows positive S at all temperatures! σ can be defined as:

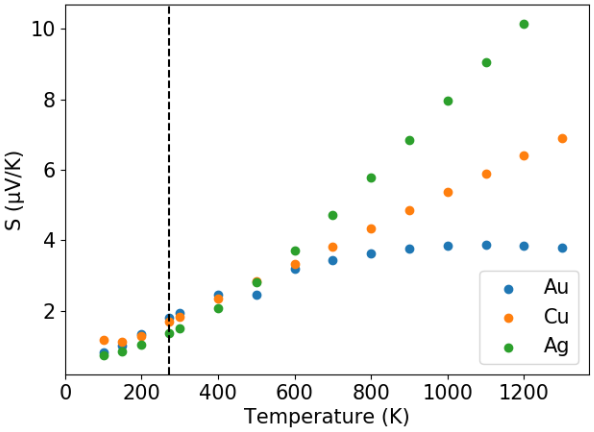

Figure 2.6 : Temperature dependence of gold, copper, and silver's Seebeck coefficient: Data plotted from the tabulated values on page 900 in [23]. The horizontal line at the zero crossing and the vertical dashed line at room temperature are marked as a reference.

$$\boxed{\sigma = \frac{e^2\lambda A}{6\pi^2 h}} \tag{2.13}$$

Definition of electrical conductivity

with Fermi surface area (A) and electron mean free path (λ).[26] S depends on the particulars of the Fermi surface of the material, which is pretty complicated for the noble metals. Fig. 2.7 shows the Fermi surface of gold which contacts the Brillouin zone boundaries. Initially, it was believed that the anisotropy of the Fermi surface could explain why S was positive.[27] However, a Fermi surface that would yield a positive S would also yield a positive Hall coefficient, indicating a hole-like character of the charge carriers. This is not the case in the noble metals, so the Fermi surface cannot be the main reason S is positive. Further supporting the case, even at temperatures above the noble metals' melting points where the Fermi surface is not preserved, S remains positive. Because of this issue, the positive S of noble metals is thought to come primarily from the energy dependence of λ.[28] While the theory is pretty complicated, Ref. [29] discusses how λ can decrease with increasing energy considering a model of electron-phonon scattering resulting in a negative $\left(\frac{\mathrm{d}\ln\sigma}{\mathrm{d}E}\right)\Big|_{E=E_F}$ and therefore positive S for noble metals.

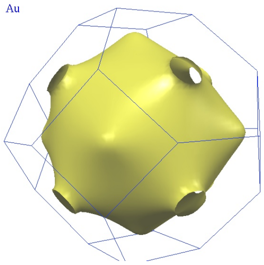

Figure 2.7 : Fermi surface of gold. Reprinted with permission from [30] and [31].

As discussed earlier, in silicon nanowires, the ZT score is increased by increasing phonon boundary scattering. This approach doesn't work as well for thin metal films because surface scattering also decreases electric conductivity, and therefore the electronic mean free path, lowering the electronic contribution to S, as well as the phonon drag component important at low temperatures.[32–37] Changing the thickness of thin metal films can then tune the electronic component of the Seebeck coefficient. The Seebeck coefficient of a thin metal film, S_f, of thickness t can be estimated from the bulk S by

$$\boxed{\frac{S_f}{S} = 1 + \frac{3}{8}(1-p)\frac{\lambda}{t}\frac{U}{1+U}} \tag{2.14}$$

Seebeck coefficient of thin metal film compared to bulk

where $U = \left(\frac{\mathrm{d}\ln\lambda}{\mathrm{d}E}\right)\Big|_{E=E_F}$, p is a specular scattering coefficient discussed in more detail in Ref. [38]. This change in thin film Seebeck coefficient was seen in Au[32], Ag[39], Cu[40], Cr[41], Al[37], Bi[42], Fe[43], Pd and Pd/Au alloys[44], and transition metals[45].

Because the conditions that allow for the positive S in the noble metals are pretty sensitive, slightly alloying gold with other metals can cause large changes in S. Refs. [46] and [47] both conducted similar experiments where the S of gold with varying levels of impurities were measured as as a function of temperature. As seen in Fig. 2.8, alloying gold with increasing the platinum concentration from 0% to 5% can have a drastic effect on the sign and magnitude of S. Adding just 1% platinum to otherwise pure gold changed S from positive to negative. Refs. [48] and [49] discuss similar measurements at lower temperatures and with different transition metals, respectively. Adding almost *any* element to the noble metals even in trace amounts results in an alloy with a lower Seebeck coefficient than the pure metal.[50].

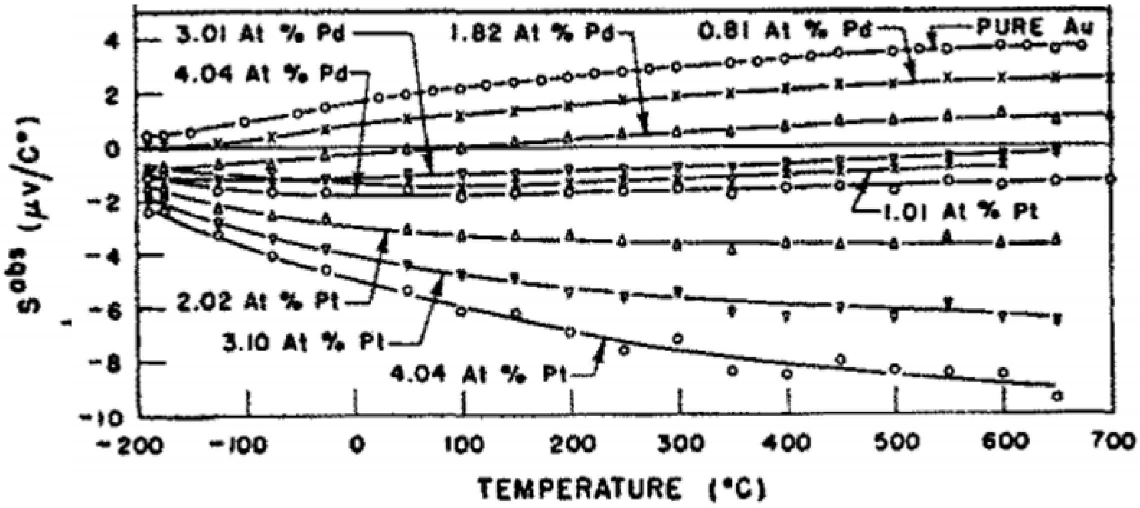

Figure 2.8 : Absolute thermopower of Au-Pd and Au-Pt alloys. As the concentration of platinum impurity increases from 1% to 4%, the Seebeck coefficient of the gold-platinum alloy becomes increasingly negative. Figure reprinted with permission from Ref. [46]. ©1956, American Institute of Physics.

Adding impurities to an otherwise pure metal can cause changes to both the electronic and phonon components of S. In general, the electronic component cares only about the changes to the band structure and electron scattering while the contribution due to phonons will decrease with impurity concentration because phonon-impurity scattering reduces the phonon drag effect. At low temperatures, the contribution of phonon drag to S of dilute AuPt alloys actually becomes negative[47]. Particularly at low temperatures, the phonon drag component of S in a dilute AuPt alloy can be explained by the anisotropy of electron scattering relaxation times [51–53]. The electronic portion of the Seebeck coefficient, described by Equation 2.8, is affected by the alloying as the foreign atoms increase the scattering cross-section which have their own energy dependence.[46, 50]

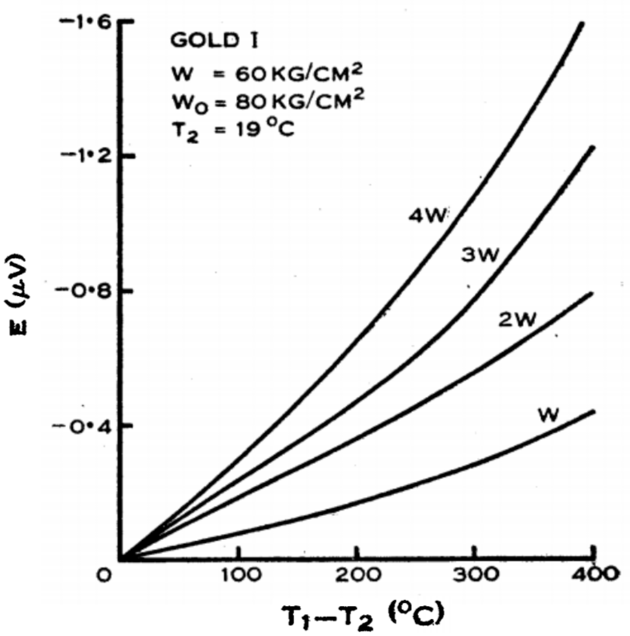

Figure 2.9 : Temperature dependence of the open circuit voltage of a gold wire under various strain intensities, W. Reproduced from Reference [54] ©1953 with permission from CSIRO Publishing.

Impurities and defects can also deform the Fermi surface, further affecting the Seebeck coefficient.[55] Another way to deform the Fermi surface is through tension.[56–59] The Seebeck coefficient of a metal wire has been shown to be sensitive to elastic strain[54, 60–62], as seen in Fig. 2.9, likely due to the deformation of the Fermi surface. Strain engineering[63–65] may be a way to tune the thermoelectric response of a material. Additionally, residual strain due to fabrication processes[66, 67] or annealing may modify the thermoelectric response of the devices.

2.2.2 Thermocouples

Typically, when someone refers to thermocouples, they mean something similar to Fig. 2.2, an electronic device consisting of two dissimilar materials with differing Seebeck coefficients. Applying a temperature gradient to the device while heating the interface of the two materials generates an open circuit voltage. Thermocouples are commonly used as a temperature sensor; if the Seebeck coefficients of the two materials is known, the measured voltage can be converted to a temperature. This temperature detection technique is particularly popular because these inexpensive devices can measure a wide temperature range and do not require any external power supply.[68, 69] The excellent energy conversion capabilities of thermocouples are exploited for on-chip temperature sensing[70, 71], energy harvesting[72], photochemistry[73], and IR detection[74, 75]. Recently, there has been a resurgence in thermoelectric studies. This time, however, the studies focus on thermocouples in the nanoscale. In the nanoscale, the Seebeck coefficient can be tuned to allow for single metal thermocouples, as discussed below. The small size of these nanoscale devices allows for high spatial resolution[76–80] and detection of temperature gradients in sub-microsecond timescales due to the fast thermalization.[81] The rest of this section focuses on nanoscale, single metal thermocouples.

Single metal thermocouples

From Equations 2.8 and 2.13, the Seebeck coefficient can be tuned by changing the electron mean free path. The electron mean free path can be changed via nanostructuring, changing the width or thickness of a device. If there is an abrupt change in geometry in a nanoscale device, thermocouples can be created out of a single material.[82–90] From Equation 2.14, a single metal thermocouple can be created due to an abrupt change in the thickness of a thin film (e.g. bonding pads) which can result in large thermoelectric voltages. Devices of uniform thickness can also be effective thermocouples through abrupt changes in geometry. Fig. 2.10a shows one such example from Ref. [87]. Heating in the interface of the geometric change results in measurable open circuit voltages.

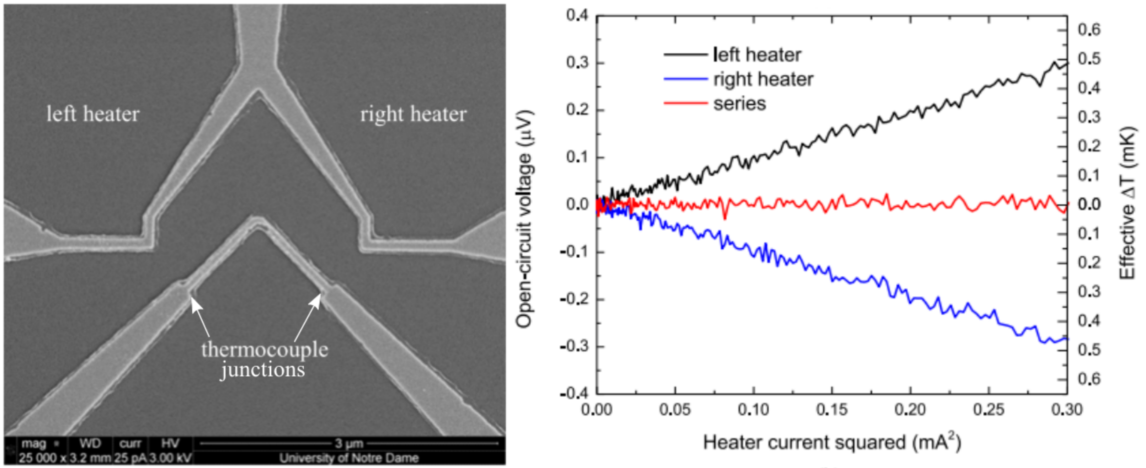

(a)

(b)

Figure 2.10 : Example of single metal thermocouple via nanostructuring. *a*: A thin Ni film abruptly changes geometry, changing the local conductivity. A resisitive heater can locally heat either side of the thermocouple. *b*: Open circuit voltage measurements as a function of heater power. Heating only one side of the device results in a linear increase in open circuit voltage magnitude, with each side having opposite sign polarity. Heating both thermocouple junctions simultaneously results in no detectable voltage signal. Adapted with permission from [87]. ©2015 IEEE.

These devices are commonly heated via a nearby lithographically-defined resistive heater, running current through a conductor results in Joule heating with power proportional to the square of the current. One such example is shown in Fig. 2.10a, where resistive heaters are placed close to the geometric discontinuities on either side. Current can be ran through one side, the other side, or both sides to locally heat the junctions. If only one side is heated, the magnitude of the open circuit voltage increases linearly with the power, Fig. 2.10b. Heating the opposite junction results in the opposite thermovoltage; the sign of the thermovoltage is determined by the difference in Seebeck coefficients and the order is reversed on the opposite side. Evenly heating the junctions at the same time causes these voltages to cancel out. Although the resistive heater provides a convenient way to locally heat the thermocouple junctions, these heaters are typically static in location. Therefore, local variation in the thermovoltage response cannot be detected using this method. In the next section, an alternate method using a well-focused laser as a heating source whose location can be scanned to locally probe the thermoelectric response called the photothermoelectric effect will be discussed.

2.3 The Photothermoelectric effect

The basic concept of the photothermoelectric effect, PTE, is the same as the thermoelectric effect, but using a laser as a heating source to probe the temperature-difference-driven photovoltages[26]. One benefit of using a laser as the heating source is that the photovoltage can be measured as a function of heating position, allowing for detection of the local Seebeck response. If a temperature gradient, ∇T is applied somewhere in the middle of the device, Fig. 2.11, with both ends kept at a constant temperature, the open circuit voltage between the ends is

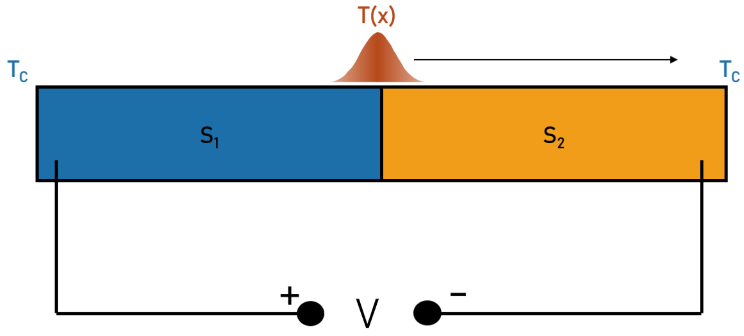

Figure 2.11 : Schematic of the photothermoelectric effect, consisting of a focused laser serving as a heating source with a temperature distribution $T(x)$ heating somewhere in the middle of a device with Seebeck coefficients S_1 and S_2 with the ends of the device kept at a constant temperature T_C.

$$\boxed{V = \int_0^l S(x, T(x)) \nabla T(x) dx} \tag{2.15}$$

Thermoelectric voltage

where T is the local temperature and $S(x, T(x))$ is the local Seebeck coefficient that is a function of position and the temperature distribution.[91] The photothermoelectric effect has been used to characterize nanostructures under focused illumination[26, 87–90, 92–94] including carbon nanotubes[91, 95] and mechanical controllable break junctions.[92, 96–100] Because nanostructures can also be geometrically structured to be plasmonically resonant [92, 101, 102] at certain wavelengths, the photothermoelectric effect is also used as a mechanism for photodetection[26, 92, 96–100, 103, 104] and energy conversion.[105, 106]

Chapter 3

Electronic transport measurements in molecular junctions

3.1 Macroscopic view of electronic transport measurements

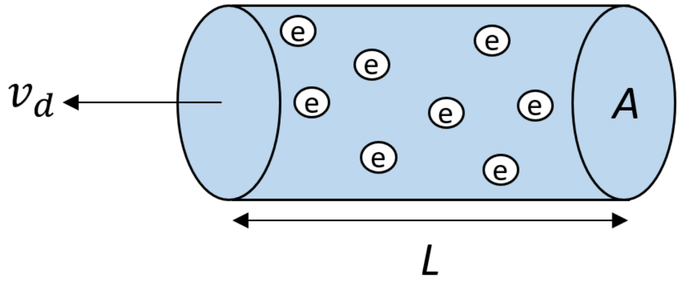

Figure 3.1 : Schematic of a current-carrying wire, of length L, cross-sectional area A, and electrons, e passing through the wire at the drift velocity, v_d.

Imagine a conducting metal wire with of some length, L, and cross-sectional area, A, Fig. 3.1. Because this is a macroscopic wire, we can think of the charge as a classical fluid. If a bias, V, is applied across the wire, the electrons will drift toward the positive terminal. The total charge, Q, in the wire is defined as $Q = neAL$ where e is the electron charge and n is the electron number density. The current, $I = \frac{Q}{t}$, shows the total charge passing through per unit time. The time is set by the drift velocity, defined as $v_d = \frac{L}{t}$. The total current is therefore $I = neAv_d$. Relating this to Ohm's law, $G = \frac{I}{V}$, where G is the total conductance, we see that the conductance increases linearly with the area of the wire. Additionally, the conductance is inversely proportional to the length of the wire.

As the wire gets shorter, the resistance linearly decreases. However, if the wire gets short enough, the resistance plateaus. The length scale associated with this plateau in the resistance is the electron mean free path, λ, or the path the electron can travel before scattering. The length of the wire is then said to be in the ballistic regime, where the electrons can traverse the wire without scattering. The resistance that the resistance plateaus at is called the contact resistance.

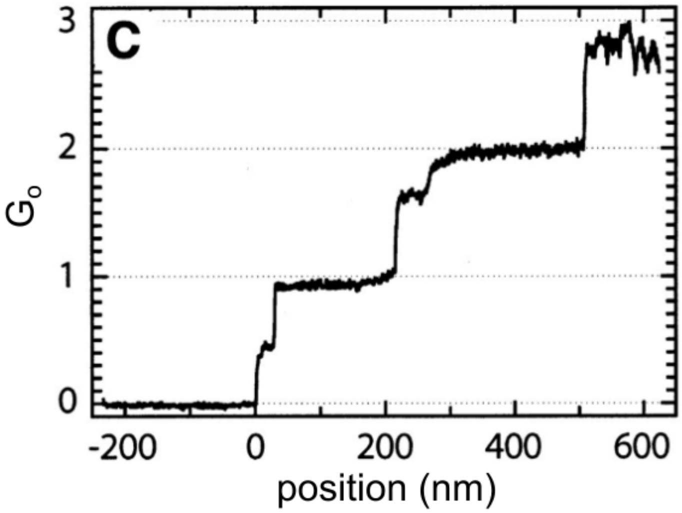

Figure 3.2 : Example of quantized conductance, with the conductance increasing in integer multiples of the conductance quantum, G_o. Adapted with permission from [107]. ©1998 Science

Now, let's decrease the cross-sectional area of the wire. Instead of the conductance decreasing linearly with A, the conductance plateaus as seen in Fig. 3.2, similar to how the resistance plateaued as the wire length decreased. Except this time, as the wire becomes smaller and smaller, there are "steps" in the conductance plateaus with spacing of integer multiples of $\frac{2e^2}{h}$. This is called the conductance quantum, which will be derived in the next section.[108, 109]

3.2 The conductance quantum

Imagine a 1D wire of length L in contact with reservoirs to the left and right with a chemical potential μ_L and μ_R, respectively. This difference in chemical potential can be converted to a voltage, V, by $-\frac{\mu_L-\mu_R}{e}$. The current density, j, of the wire is defined as $j = -ev_d(\mu_L - \mu_R)\frac{\mathrm{d}n}{\mathrm{d}E}$ where $\frac{\mathrm{d}n}{\mathrm{d}E}$ is the density of states. v_d is can be described by the group velocity, $v_d = \frac{1}{\hbar}\frac{\partial E}{\partial k}$ with k as the wave vector. Making these substitutions and recognizing $\frac{\partial E}{\partial k}\frac{\mathrm{d}n}{\mathrm{d}E} = \frac{\mathrm{d}n}{\mathrm{d}k}$, we get $j = -e^2(\frac{(\mu_L-\mu_R)}{-e})v_d\frac{\mathrm{d}n}{\mathrm{d}E} = \frac{e^2V}{\hbar}\frac{\partial E}{\partial k}\frac{\mathrm{d}n}{\mathrm{d}E} = \frac{e^2V}{\hbar}\frac{\mathrm{d}n}{\mathrm{d}k}$. In a 1D system with periodic boundary conditions, the wavefunctions in k-space are separated by $\frac{2\pi}{L}$ *per spin state*. Considering the spin-1/2 degeneracy, $\frac{\mathrm{d}n}{\mathrm{d}k} = \frac{2L}{2\pi}$. This means that the total current is then $I = \frac{2e^2V}{2\pi\hbar} = \frac{2e^2V}{h}$. Therefore the conductance quantum, G_o, is

$$\boxed{G_o = \frac{2e^2}{h}} \tag{3.1}$$

Conductance quantum

which is ∼12.9 kΩ. This equation is true only for a wire with one transmission channel. The Landauer-Buttiker formalism[110] shows that the adding additional channels increases the conductance by integer multiples of Equation 3.1.

3.3 Electronic transport in a molecular junction

Once the wire is broken to have a nanogap, the electronic transport is now dictated by quantum mechanics; we can no longer think about the charges as a classical fluid.[111] The gap serves as an effective barrier and in the classical picture, traversing the gap is forbidden; the electron would be reflected once it reaches the barrier. However, quantum mechanics allows for the electron to tunnel across the gap, from one side to the other through classically forbidden "virtual" states, with a probability of tunneling depending on the height and geometry of the barrier.[112] The conductance from tunneling exponentially decays as the gap gets larger and is defined as

$$\boxed{G = G_o e^{-\beta(d-d_o)}} \tag{3.2}$$

Tunneling conductance of nanogap

where β is the attenuation factor, d is the gap distance, and d_o is the lattice constant. For gold, d_o is around 0.4 nm and β is $\sim 2\text{Å}^{-1}$.[113] The conductance in the gap is dominated where the gap size is the smallest. The conductance drops by a factor of e^2 as the gap increases by β, meaning that the tunneling gaps are in the sub-nanometer regime[114], on the order of a molecular volume.[115]

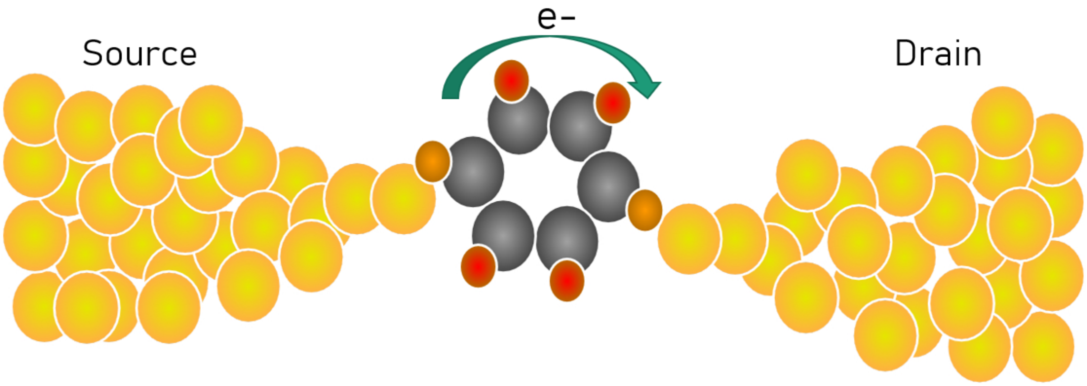

Figure 3.3 : Schematic of a molecular junction, consisting of a molecular between a source and a drain electrode.

Molecules have conductances $\sim 0.006 G_o$[116], dominating the conductance if placed in the gap. As such, molecular junctions, consisting of a molecule in a nanogap between a source and drain electrode depicted in Fig. 3.3, are excellent ways to detect how tunneling electrons interact with the vibrational and electronic states of the molecule. Molecular junctions were first measured in 1974[117] and have recently had a resurgence as molecular electronics gained popularity as a potential way to continue shrinking electronic circuits.[112, 118] Molecular junctions are created using multiple techniques, the most common include STM[116, 119–128], mechanically controllable break junctions[129–141], and electromigration[118, 142–158]. Multiple transport mechanisms can be observed in molecular junctions, including tunneling, vibronic effects[159, 160], and charge hopping[161]. The work in this thesis will focus on tunneling, the dominant transport mechanisms, in electromigrated devices. The electromigration process will be discussed in more details in Sec. 5.3

Electronic transport measurements are an excellent way to detect how the tunneling electrons interact with the molecule as they tunnel from the source to the drain[159]. The molecule itself has two relevant energy levels: the highest occupied molecular orbital, HOMO, and lowest unoccupied molecular orbital, LUMO. In the molecular junction, the molecule serves as effective tunneling barrier[162]; the typical energy spacing between the HOMO and LUMO for a molecule is $\sim$1 eV. The HOMO and LUMO levels of the molecule will be broadened in the molecular junction as they interact conducting states within the electrodes, which obey Fermi-Dirac statistics. The molecular junctions discussed in this work are in the Landauer-Imry regime[163], where the tunneling process is coherent and the chemical potentials of the electrodes is sufficiently far from the HOMO and LUMO levels of the molecule so that molecular charging is not an issue.[159] Additionally, the thermal energy also must be considered in these measurements as thermal fluctuations increase with temperature; the Fermi energy distribution of the source and drain electrodes broadens with temperature, broadening the features from the energy exchanges discussed throughout this section.

When no net bias, V, is applied across the electrodes, the chemical potentials of the source and drain, μ_s and μ_d respectively, are the same. This means that the electrons have equal probability to tunnel from the source to the drain and vice versa as the electrons rearrange themselves to achieve the lowest energy configuration of the system as a whole[112], resulting in no net current, leftmost diagrams of Fig. 3.4a,b. Applying a bias, V, across the electrodes shift the chemical potentials of the source and drain, resulting in a net current from the source to the drain. Depending on the energetic alignment of the molecule to the electrode chemical potentials, the electrons can tunnel through the HOMO or LUMO of the molecule[112] with the LUMO acting as an effective tunneling barrier[162]. Measuring the current, I, as a function of V can provide insight about the interactions that occur between the electrons and the molecule as the electrons undergo a second-order tunneling process, using the LUMO as a virtual state to tunnel across the gap. The rest of the section will focus on how electronic transport measurements can detect some of the most common tunneling mechanisms.

3.3.1 Elastic electron co-tunneling

Most of the time, the unbiased chemical potentials of the source and the drain will be sufficiently far from the HOMO and LUMO levels of the molecule, as seen in the leftmost panel in Fig. 3.4a. Applying V across the electrodes will shift μ_s and μ_d, causing electrons to tunnel from the source, to the LUMO, and again to the drain, middle panel of Fig. 3.4a. Typically, the electron elastically tunnels through the molecule, leaving the molecule with the same amount of energy with which it entered. This is the most common tunneling mechanism and is called *elastic, nonresonant electron co-tunneling*, and can be detected in electronic transport measurements as a

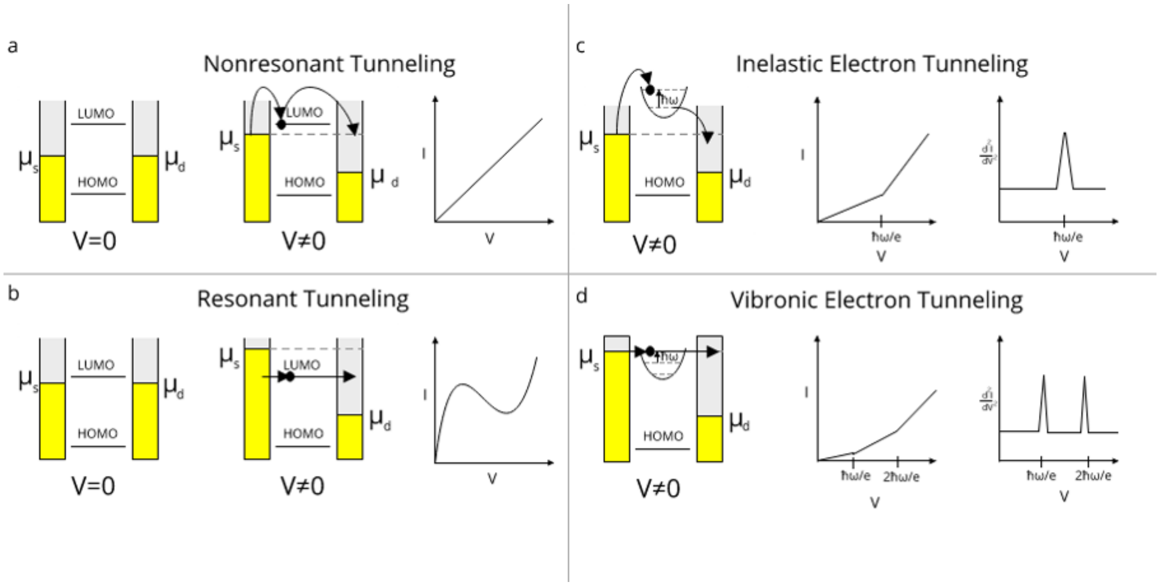

Figure 3.4 : Schematic of electronic tunneling mechanisms through a molecule. *a*: elastic, nonresonant co-tunneling, *b*: resonant tunneling, *c*: inelastic electron tunneling, *d*: vibronic tunneling. μ_s and μ_d is the chemical potential for the source and drain electrodes, respectively.

linear relationship between current and applied bias, rightmost panel of Fig. 3.4a.

If the unbiased chemical potentials of the electrodes are close to the LUMO level, leftmost panel in Fig. 3.4b, *elastic, resonant electron tunneling* is possible. The energy levels of the HOMO and LUMO can be adjusted via gating to achieve resonant tunneling[160, 164, 165]. Leaky gating can cause considerable local heating which can wash out the fine features of molecular junctions, so this method is typically only used to study resonant tunneling.[111] When a bias is applied across the electrodes, μ_d is greater than the LUMO energy which allows for resonant tunneling, middle panel of Fig. 3.4b. In the resonant tunneling regime, the electrons remain coherent during the tunneling process, so quantum interference effects such as negative differential conductance can be observed as dips in the current-voltage measurements, rightmost panel of Fig. 3.4b.[160, 166, 167]

3.3.2 Inelastic electron co-tunneling

Although the elastic tunneling processes are the dominant tunneling mechanisms in the molecular junctions, *inelastic electron tunneling* provides much more interesting information. In inelastic electron tunneling, if a sufficient bias, V, is applied, an electron with $eV \geq \hbar\omega_{vib}$ can tunnel into the molecule and exchange one quanta of vibrational energy, $\hbar\omega_{vib}$, with the molecule before tunneling through the drain, leftmost panel of Fig. 3.4c. From this tunneling process, the electron excites or relaxes the molecule to a different vibrational energy level. Understanding how this energy exchange happens can be described conceptually.[168] When a bias is applied across the electrodes, μ_s and μ_d are shifted. As the electron elastically tunnels from the source to the drain, the electron energy is higher than μ_d. When enough electrons tunnel with this higher energy, the energy distribution of the drain is no longer a simple Fermi-Dirac distribution. Instead, the local effective temperature of the drain at length scales smaller than the electron-electron scattering length will be elevated. This local effective temperature rise will result in bulk phonons in the drain. The electron will tunnel from the source to the molecule and will stay on the molecule for a timescale set by the molecule-lead coupling (which determines the broadening of the molecular electronic states), exchanging $\hbar\omega_{vib}$ with the molecule, before tunneling to the drain. The energy exchange will excite a vibrational mode in the molecule, which will lose energy to the bulk phonons in the electrons at a relaxation timescale set by the coupling of the molecule to the thermal phonons in the leads.[169]

Because the tunneling electron excites a vibrational mode in the molecule, another tunneling channel becomes available which increases the tunneling probability, resulting in a change of slope at the bias where the exchange occurred set by $\frac{\hbar\omega_{vib}}{e}$,[170] middle panel of Fig. 3.4c. This change in the total current is small and is difficult to detect; inelastic processes are much less likely to occur than elastic scattering processes because the timescale of the electron tunneling is much faster than that of the vibrational oscillation, reducing the probability of the inelastic scattering event.[159] As such, this inelastic process can typically be regarded as a weak perturbation. Although directly measuring the current as a function of bias typically doesn't show a clear signal, the differential conductance, $\frac{\mathrm{d}I}{\mathrm{d}V}$, shows a step function while the second derivative, $\frac{\mathrm{d}^2I}{\mathrm{d}V^2}$, shows a peak at the energy where the exchange occurred[171–174], rightmost panel of Fig. 3.4c. Measuring $\frac{\mathrm{d}^2I}{\mathrm{d}V^2}$ is called *inelastic electron tunneling spectroscopy*, IETS, which will be discussed in more detail in the next section. The elastic analog to inelastic electron tunneling is called *vibronic electron tunneling*, Fig. 3.4d, and is seen when μ_s passes through a vibrational energy level of the LUMO. As the bias increases, the peaks in $\frac{\mathrm{d}^2I}{\mathrm{d}V^2}$ are seen at steps of $\Delta V = \frac{\hbar\omega_{vib}}{e}$.[175–178]

3.4 Inelastic electron tunneling spectroscopy

As mentioned in the previous section, inelastic electron tunneling spectroscopy is an electronic transport method to detect where tunneling electrons exchange energy with and excite a vibrational mode in the molecule, by detecting peaks in $\frac{\mathrm{d}^2I}{\mathrm{d}V^2}$. Because the probability of an inelastic event is low, simple I vs. V curves do not highlight these energy exchanges, top panel of Fig. 3.5. Even $\frac{\mathrm{d}I}{\mathrm{d}V}$, middle panel, only highlights some some signal at 0 bias. It isn't until $\frac{\mathrm{d}^2I}{\mathrm{d}V^2}$, bottom panel, that the energy exchanges are clearly detected as peaks. The lineshapes seen in the IETS measurements aren't always peaks but can also be dips;[178] the specific shapes are determined by the energetics of the system as a whole[179] including coherent interference between the elastic and inelastic tunneling electrons.[168]

IETS was first measured in 1966 [180] and has since become a primary technique to identify molecules present in a nanogap.[159, 177, 181, 182] The first IETS measurement of a single molecule wasn't conducted until 1998.[173]. The initial observation of IETS was that it resembled that of Raman or Infrared Absorption spectroscopy.[183] Like Raman and infrared absorption spectroscopies, IETS can detect the molecular vibrations. However, only the molecular vibrations that obey the selection rules will be detected by Raman or infrared absorption, requiring the vibration to change the polarizability or dipole moment, respectively. In centrosymmetric molecules, those with inversion centers, no vibrational mode can be detected by both IR and Raman. While IETS does have some orientation preference,[184] IETS does not have such selection rules and can detect both Raman-active and IR-active vibrational modes,[185] making it a powerful tool to probe the vibrational modes of molecules. Raman spectroscopy will be discussed in Ch. 4.2.

Because the inelastic tunneling events are so rare, it can be challenging to detect the energy exchanges in the total current with sufficient signal-to-noise to detect the peaks via numerical differentiation. Instead, the traditional detection method uses lock-in amplifier techniques, which allows the peaks of $\frac{\mathrm{d}^2 I}{\mathrm{d}V^2}$ to be measured directly using AC modulation.[170] A small AC voltage, $V_{AC}(\omega)$, is applied to the device along the the voltage bias, V_B. Taylor expanding the current yields:[187]

$$\boxed{I(V_B + V_{AC}\cos\omega t) = I(V_B) + \left.\frac{\mathrm{d}I}{\mathrm{d}V}\right|_{V_B} V_{AC}\cos\omega t + \frac{1}{4}\left.\frac{\mathrm{d}^2 I}{\mathrm{d}V^2}\right|_{V_B} V_{AC}^2(1+\cos 2\omega t) + \ldots} \tag{3.3}$$

Lock-in detection of IETS

which means that second harmonic lock-in measurements allow for a quantity directly proportional to $\frac{\mathrm{d}^2 I}{\mathrm{d}V^2}$.[180, 183, 187].

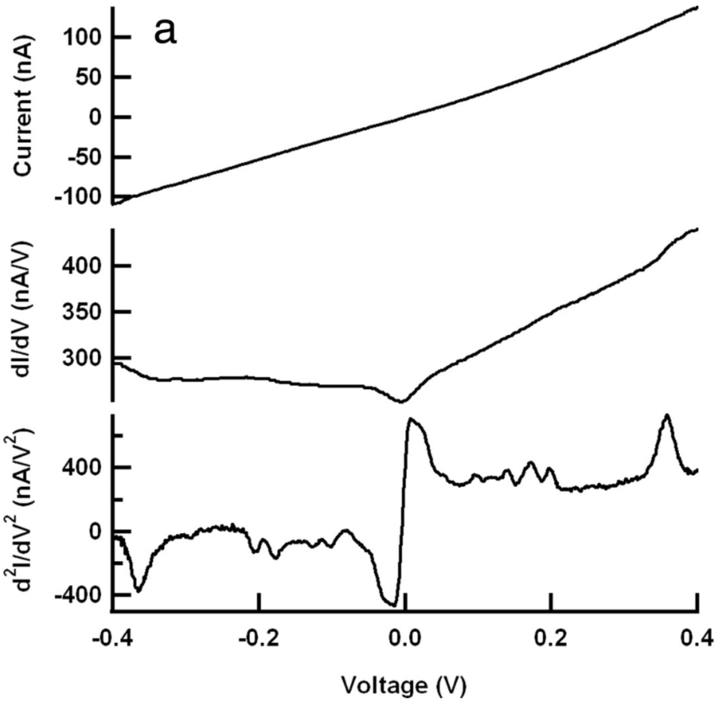

Figure 3.5 : Resolving inelastic tunneling using the second harmonic signal of the electronic transport measurements. *top*: The current (I) vs. voltage (V) curve of a molecular junction looks featureless. *middle*: The first harmonic of the I-V curve shows steps in areas where tunneling electrons exchange energy with the molecule. *bottom*: The second harmonic shows well-resolved peaks where the energy exchanges occur. The second harmonic of the I-V curve is called inelastic electron tunneling spectroscopy. Reprinted with permission from Ref. [186]. ©PNAS 2007.

As mentioned before, one of the energy scales that is important to consider for IETS and other tunneling processes is the thermal energy. When the local temperatures increase, thermal fluctuations become more likely. The HOMO and LUMO energy levels can broaden as they interact with the energy states in the electrodes. As seen in Fig. 3.6, as the temperature increases above 30 K, the signal from the inelastic energy exchange is washed out.[181] The FWHM of the peaks is a function of broadening effects from the thermal energy, the modulation voltage in the lock-in detection method, and the intrinsic linewidth, $W_{intrinsic}$ and is set by:[170, 183, 187, 188]

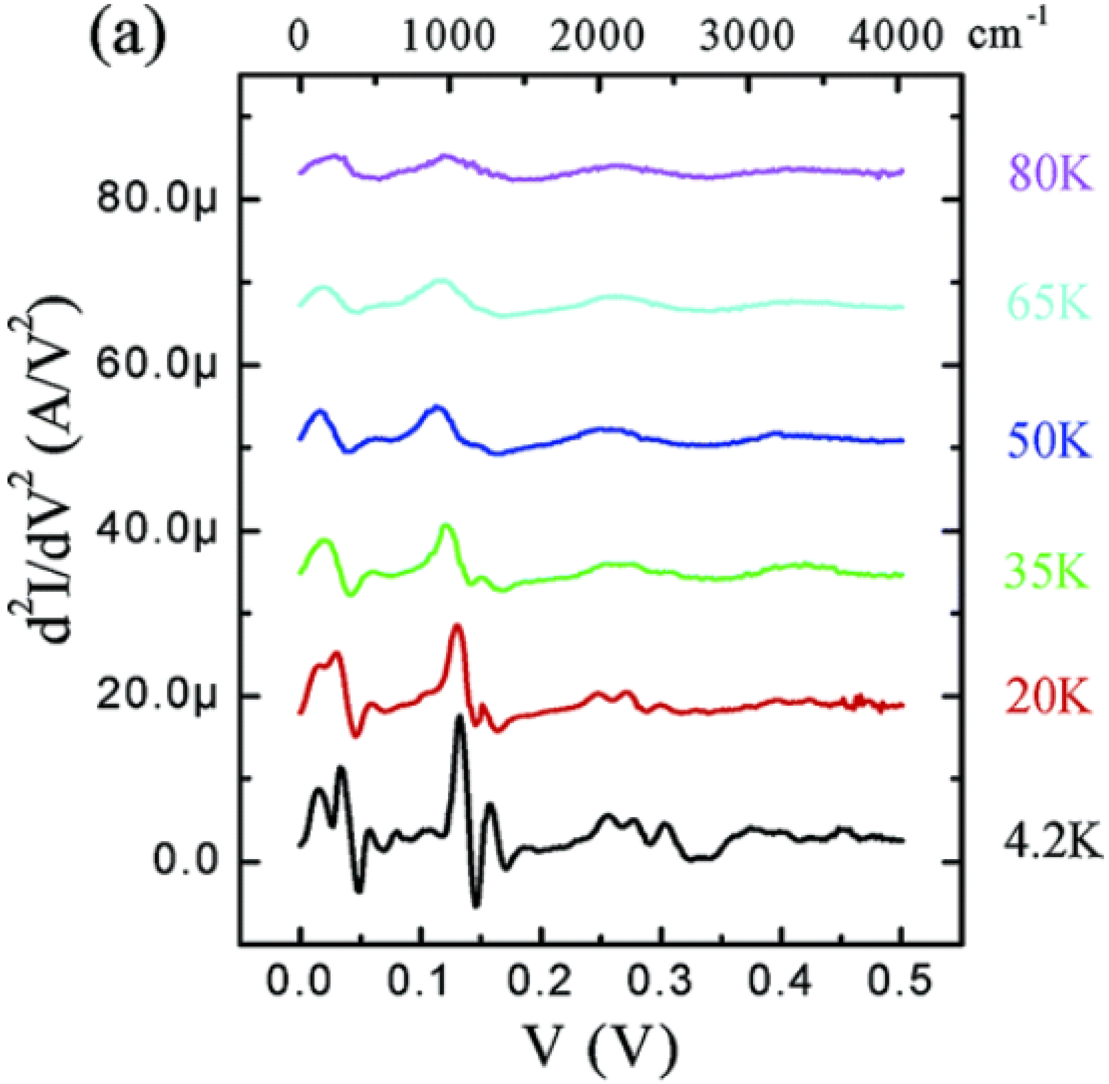

Figure 3.6 : Temperature dependence of inelastic electron tunneling spectroscopy: As the temperature decreases, the peaks become more well-resolved. Reprinted with permission from Ref. [181]. ©2004 American Chemical Society.

$$\boxed{FWHM = \sqrt{W_{intrinsic}^2 + (5.4k_BT/e)^2 + (1.7V_{AC})^2}} \tag{3.4}$$

FWHM of IETS line widths

where $5.4k_BT/e$ is the thermal broadening component[189] and $1.7V_{AC}$ is the broadening component from the AC modulation in the lock-in amplifier.[190] The linewidth dependence on the thermal energy and the modulation voltage can provide a diagnostic tool to determine that the signal is truly IETS. The thermal broadening component from Equation 3.4 shows that cryogenic temperatures must be used to have well-resolved peaks. A linewidth of 5 meV requires a temperature of $T = \frac{5\mathrm{meV}}{5.4*0.86\mathrm{meV/K}} \sim$ 10K![187] Therefore, careful attention must be paid to the *local* temperature of the molecular junction as thermal broadening can wash out the wealth of information IETS can provide.

Chapter 4

Plasmons and surface enhanced Raman spectroscopy

At the core of the gold “bowtie” work discussed in this thesis is trying to get a better understanding about how light interacts with matter, and in particular how light can interact with the free electron gas in gold, resulting in collective oscillation. Just as water molecules can collectively ripple across the surface of a lake, the free electron gas in a metal can be collectively excited under coherent illumination. This is called a plasmon, a quanta of plasma oscillations, just as phonons are a quanta of mechanical vibrations.

In this chapter, plasmons are discussed in more detail. We will first discuss how the optical properties of gold (and other conducting materials, in particular, noble metals) allow for plasmon excitation in the first place. We will then move on to the main types of plasmon: the confined localized surface plasmons (LSP) and the propagating surface plasmon polaritons (SPP). Finally, we will introduce Raman spectroscopy and the role plasmons play in surface enhanced Raman spectroscopy, which can allow for single molecule Raman.

Figure 4.1 : Schematic of a bulk plasmon. *Left:* An initial electric field causes separation of the electron gas and the positively charged lattice. The field is instantaneously turned off. *Middle:* After the field is turned off, the electrons move toward the positively charged lattice due to the electric field caused by that initial separation. *Right:* As the electrons move toward the lattice, they gain momentum from the electric field, causing the electrons to overshoot. This creates an electric field in the opposite direction, resulting in an oscillation of the free electron gas with characteristic frequency ω_p.

4.1 Classical picture of gold's optical properties

4.1.1 The Drude model: free electron theory

The Drude model of conductivity is classically used to describe a metal conductor consisting free electron gas of conducting electrons, free to move around and to collide against the static lattice of positively charged ions. Macroscopically, there is a net zero field, the positive ions in the lattice is neutralized by the surrounding electron gas which rearranges itself to counteract the charge. If a slab of the material is placed in a constant electric field, the electrons in the slab will rearrange themselves to counteract the field and will be displaced from the positive ionic lattice by length $\mathbf{x}$, seen in the leftmost schematic in Fig. 4.1. If the electric field is instantaneously turned off, the separation of the electron gas from the positively charged lattice will result in an electric field that will pull the electrons back toward the lattice, $\mathbf{E} = -en_e\mathbf{x}/\epsilon_o$ with permittivity of free space ϵ_o, number density n_e, and electron charge e. Typical carrier densities for good metals are $\sim 10^{22} - 10^{23}$ carriers/cm^{-1}.[108] As the electrons move back to the lattice, they gain momentum from the field and will overshoot their original position. This, in turn, results in an electric field in the opposite direction which causes the electrons to collectively oscillate akin to simple harmonic motion with an equation of motion without damping of $m_e\frac{\mathrm{d}^2\mathbf{x}}{\mathrm{d}t^2} = -e\mathbf{E} = -\frac{e^2n_e\mathbf{x}}{\epsilon_o} = -k\mathbf{x}$, effective mass of the electron m_e, and spring constant $k = m_e\omega_p$. Substituting for k and rearranging, the ω_p of the collective oscillation of the free electron gas is:

$$\boxed{\omega_p = \sqrt{\frac{e^2n_e}{\epsilon_o m_e}}} \tag{4.1}$$

definition of plasma frequency

ω_p depends only on n_e, the rest of the values are constants. For gold, n_e is around 5.9×10^{22} cm^{-3} which gives $\hbar\omega_p$=8.95 eV. These collective oscillations of the free electron gas are called plasmons, which are quanta of plasma oscillations just as phonons are quanta of mechanical vibrations.[191] The plasma frequency sets the timescale of these bulk plasmons with energy $\hbar\omega_p$.[108, 192]

In the Drude model, the dielectric function ϵ is defined as

$$\boxed{\epsilon_{Drude}(\omega) = 1 - \frac{\omega_p^2}{\omega^2 + i\gamma\omega} = 1 - \frac{\omega_p^2}{\omega^2 + \gamma^2} + i\frac{\gamma\omega_p^2}{\omega(\omega^2 + \gamma^2)}} \tag{4.2}$$

Drude model dielectric function

with damping term γ which is the reciprocal of the relaxation time.[193] For gold, the relaxation time $\sim$ 9.3 fs.[194] In the near-IR, the wavelength is much larger than

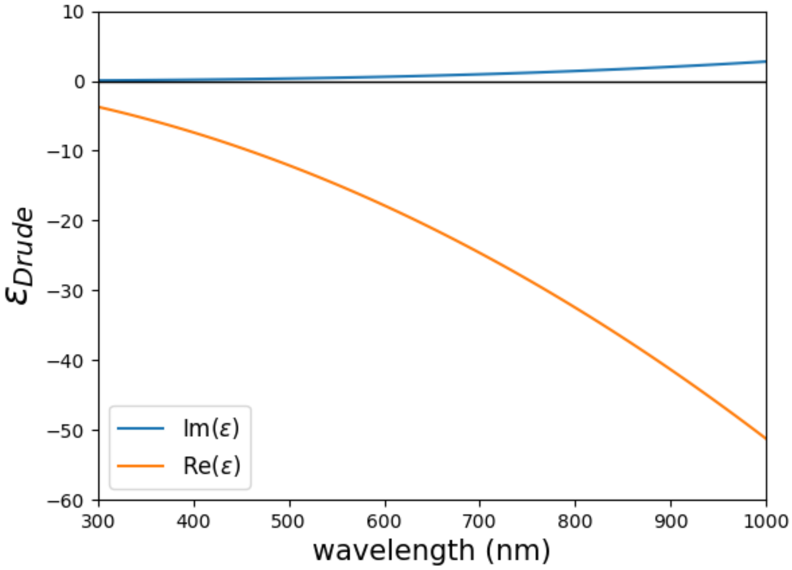

Figure 4.2 : Real and imaginary component of the dielectic function of gold as a function of wavelength using the Drude model.

γ, so Equation 4.2 simplifies to $1 - \frac{\omega_p^2}{\omega^2} + i\frac{\omega_p^2}{\omega^3}\gamma$. Fig. 4.2 plots the real and imaginary parts of Equation 4.2 using values for gold ($\hbar\omega_p$ = 8.95 eV, $\hbar\gamma$ = 65.8 meV). The real part of the dielectric function is negative for the entire visible range, yielding a large imaginary component of the index of refraction, $n = \sqrt{\epsilon}$. Fig. 4.3 shows the real part of ϵ, this time normalized by ω_p. When the frequency of incident light is below that of the plasma frequency, the dielectric function is negative. In a metal, the free electron gas rearranges to cancel an external electric field. When the incident frequency is slower than the plasma frequency, the electrons can keep up with the oscillations to neutralize the field, resulting in total reflection of the light. When the incident light has a frequency faster than the plasma frequency, the free electrons can no longer cancel the oscillating electric field. The dielectric function becomes positive and the metal begins to absorb the incident light. The reflection of the light under the plasma frequency is why metals appear shiny; the visible light according to the Drude model should get reflected due to the negative real component of the dielectric function with only limited electric field penetrating in a length scale called the skin depth. The plasma frequency for metals is typically deep in the UV range.[191]

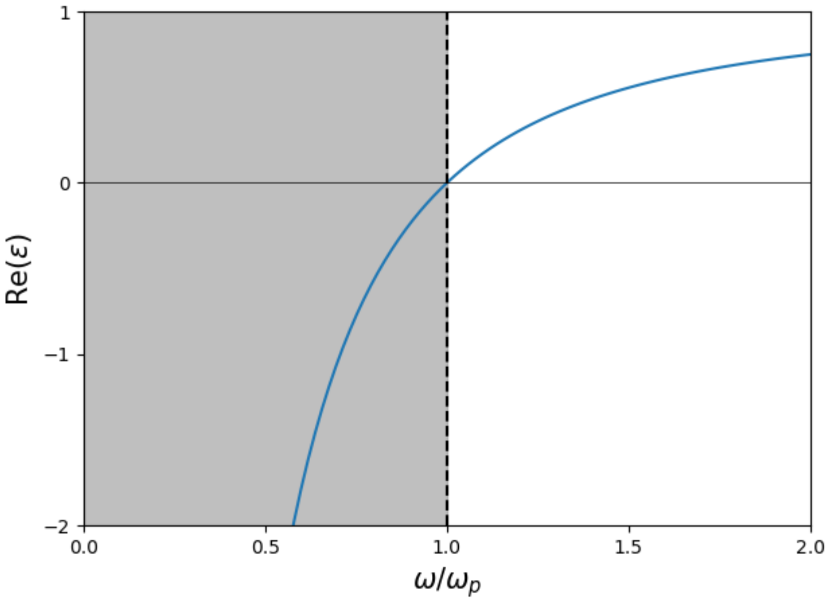

Figure 4.3 : The real component of the gold dielectric function plotted in Fig. 4.2 normalized to the plasma frequency. When the incident frequency is lower than the plasma frequency, the dielectric function is negative and the light is reflected, indicated by the gray rectangle.

However, the Drude model does not capture everything involving the dielectric function of gold, particularly in the visible range. The color of gold is yellow, indicating that the blue frequencies are not reflected as well as the other wavelengths in the visible range. This discrepancy is because the Drude model considers only the free electron gas and not the bound electrons in the system. These bound electrons play a large role in the optical properties of gold and interband transitions must be considered. When high energy photons interact with gold, the electrons in those lower bound states can get promoted to the conduction band.[195–198] The interband transition energy level in gold, promoting $5d$-band electrons to the conduction band is 2.4 eV, which is in the blue range of the visible spectrum.[195, 199] This causes gold to reflect the red and yellow portion of the visible spectrum while absorbing the blue and violet.[200, 201] The interband transition effects are also observed with an energy threshold of 1.8 eV.[202] As seen in Fig. 4.4, the interband transitions cause changes to the dielectric function of gold in the blue.[203] Adding the interband transition contribution to the dielectric function of gold as calculated via the Drude model results in a dielectric function that closely matches the Johnson-Christy measurements.[194] Although gold is more "lossy" (larger imaginary component of ϵ) than silver in the visible and near-infrared (NIR), gold is much more chemically stable under ambient conditions, making it a popular candidate for plasmonics.[204, 205]

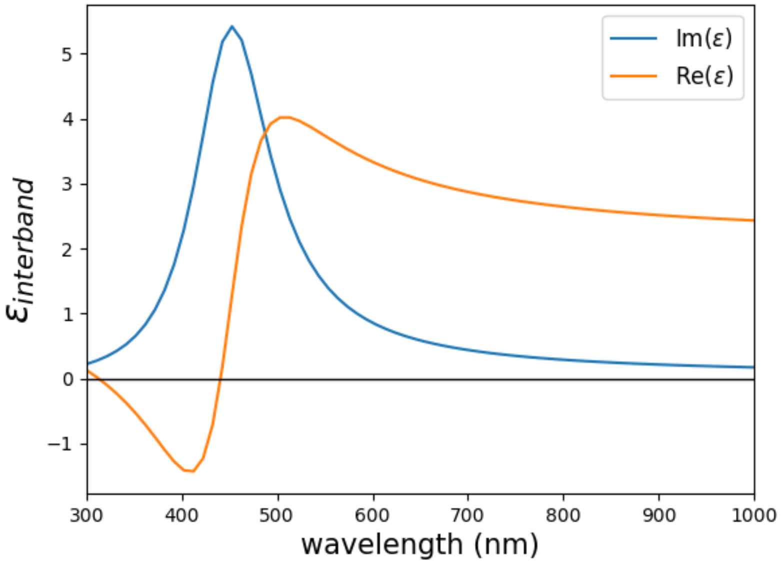

Figure 4.4 : The interband contribution to the dielectric function in gold, considering only a 450 nm incident wavelength. This figure reproduces the plot from Fig. 12.2 in Ref. [191].

4.1.2 Surface plasmon polaritons

In the nanoscale, devices are commonly made with thin metal films on a bulk, planar dielectric substrate such as SiO_2/Si. As mentioned in the previous section, plasmons cannot be excited in a bulk material below the skin depth, as the electric field within a conductor must be zero. As a result, the plasmonic properties of thin films on planar dielectric substrates result in unique plasmonic properties; the plasmonic modes in this case are confined to the metal-dielectric interface. The dielectric function of the substrate, ϵ_d, is real and frequency-independent (negligible ohmic losses) while the dielectric function of the thin metal film, ϵ_m, is a complex, frequency-dependent function described by Equation 4.2 set by $\epsilon_m = \epsilon_m' + i\epsilon_m''$. ϵ_m'' indicates how "lossy" the material is, or how much energy dissipates due to ohmic losses.

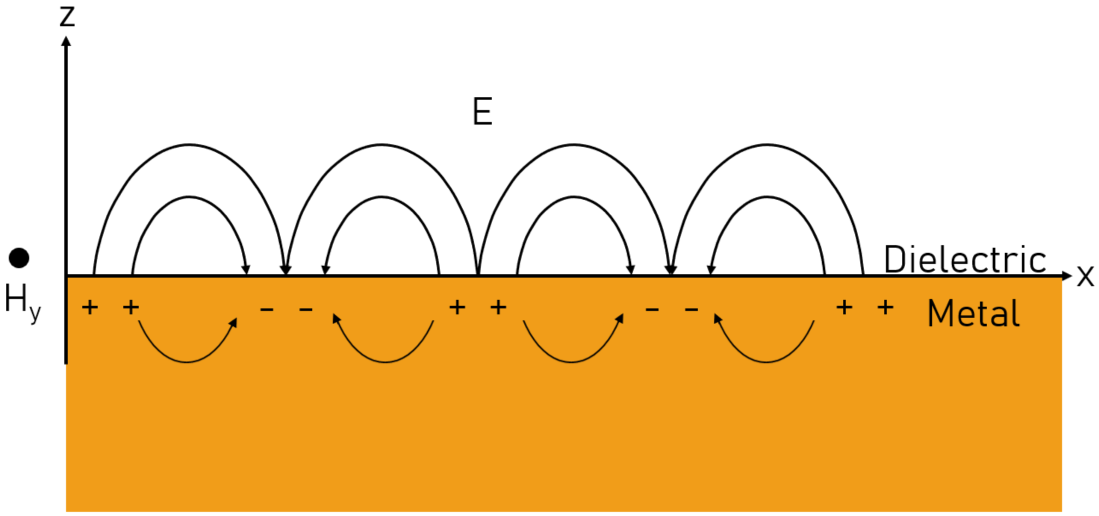

Figure 4.5 : Schematic of a surface plasmon polariton ("propagating plasmon") propagating along a planar metal-dielectric interface due to the periodic oscillation of the charge density.

When an oscillating electric field of a laser interacts with the free electron gas in a metal causing a surface plasmon, the charge density oscillations propagate along the interface of the metal-dielectric surface, Fig. 4.5. The electric fields decay evanescently perpendicularly into the metal and dielectric layers. These propagating plasmonic modes are called surface plasmon polaritons (SPPs) because the collective oscillation of the charge carriers (plasmons) are strongly coupled to the evanescent decay of the electric field confined to the surface (polariton). This propagation of the SPP can be defined with a wave vector $k_x = k_x' + ik_x''$. k_x' indicates the wavelength of the SPP while the k_x'' describes the damping of the SPP as it propagates along the interface of the metal-dielectric interface. The total electric field along the interface, $E(x)$, is

$$\boxed{E(x) = E_o e^{ik_x' x} e^{-k_x'' x}} \tag{4.3}$$

electric field of a SPP along the interface

with the first term being the propagating term and the second term describing the exponential decay along the interface. From Maxwell's equations, it can be shown[191] that the dispersion relation of SPPs is

$$\boxed{k_x' = \frac{\omega}{c}\sqrt{\frac{\epsilon_m' \epsilon_d}{\epsilon_m' + \epsilon_d}} = \frac{1}{\lambda_o}\sqrt{\frac{\epsilon_m' \epsilon_d}{\epsilon_m' + \epsilon_d}}} \tag{4.4}$$

Surface plasmon polariton dispersion relation (Real)

where λ_o is the incident laser wavelength in vacuum. The resonance condition occurs when $\mathrm{Re}(\epsilon_m) = -\epsilon_d$. Neglecting γ in Equation 4.2, the resonant surface plasmon frequency is $\omega_{spp} = \frac{\omega_p}{\sqrt{1+\epsilon_d}}$.[206] The dielectric functions of the dielectric and the metal determine whether SPPs can be excited; one must be negative with the absolute magnitude of the negative dielectric function being larger than the positive dielectric function.[191] Because gold has large, negative real component of ϵ_m[194] as seen in Fig. 4.2, SPPs are frequently detected at the gold-air ($\epsilon_d = 1$) and gold-SiO$_2$ ($\epsilon_d \sim 3.8$) interfaces. The wavelength of the SPP ($\lambda_{spp} = 2\pi/k'_x$) is shorter than the incident laser wavelength, as seen in Fig. 4.6, which means the SPP has more momentum than the incident photon. Due to this momentum mismatch,[207] SPPs cannot be directly excited on a planar film via incident illumination alone. Instead, SPPs can be excited by adding a grating[81, 208–222] or by refracting the light using a prism[223–226]. A grating with correct periodicity a acts as a waveguide by adding a reciprocal lattice vector $G = 2\pi/a$ to the free space wave vector exciting a SPP when $k'_{x_{spp}} = k_{x_{photon}} \sin\theta \pm nG$, where n is an integer and θ is the angle of incidence.[192, 208, 208, 226].

k''_x describes the propagation length of the SPPs, how far they travel before being damped out due to ohmic losses and is defined as[191]

$$\boxed{k''_x = \sqrt{\frac{\epsilon'_m \epsilon_d}{\epsilon'_m + \epsilon_d}} \frac{\epsilon''_m \epsilon_d}{2\epsilon'_m(\epsilon'_m + \epsilon_d)} \frac{\omega}{c}} \tag{4.5}$$

Surface plasmon polariton dispersion relation (Imaginary)

The 1/e propagation length of the electric field is defined as $1/k''_x$ and of the intensity is $1/2k''_x$.[227] Decay lengths in thin gold films are typically ∼ 10 µm.[81, 217, 222, 227–229] The dissipation of the SPPs causes heating in the metal. This heating causes local changes in the conductance of nanoscale devices which can be a way to electronically detect SPP excitation.[209, 214, 218, 227]

Earlier, it was mentioned that the electric field perpendicular to the interface, $E(z)$ decays evanescently into the metal and the dielectric, decaying as

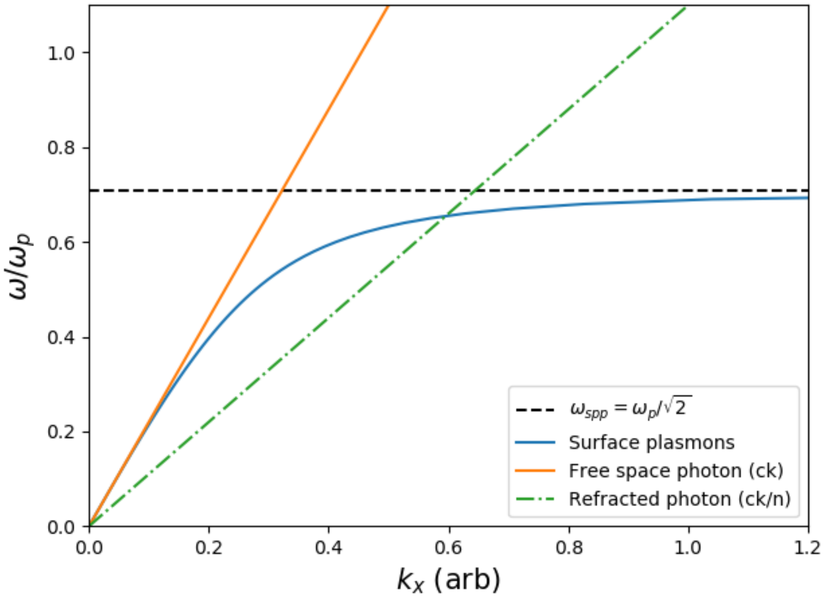

Figure 4.6 : Dispersion relation of *blue line*: SPPs, *orange line*: free space photons, *green line*: refracted photons with index of refraction n. Free space photons do not have the momentum matching conditions to excite SPPs. Instead, increasing the wave vector component of the photons through either a waveguide or a prism with $n > 1$ can allow for SPP excitation. The dashed horizontal line indicates ω_{spp}.

$$\boxed{E(z) = E_o e^{-|\mathrm{Im} k_z||z|}} \tag{4.6}$$

electric field of a SPP along the z-axis

The dispersion relation of the wave vector normal to the metal-dielectric interface is

$$\boxed{k_{j,z}^2 = \frac{\epsilon_j^2}{\epsilon_m + \epsilon_d}\frac{\omega^2}{c^2}} \tag{4.7}$$

SPP dispersion relation (normal component)

where j is the material of interest. As seen in Fig. 4.7, the electric field decays much more rapidly in the metal than in the dielectric. The 1/e decay length is called the skin depth and is defined as $1/\mathrm{Im}(k_z)$. For gold under 785 nm, $\epsilon_m = -22.86 + i1.42$[194] and $\epsilon_d = 1$, the skin depth into the gold is $\sim$ 25 nm. In the thin film limit, the electric field can penetrate beyond the thickness of the film![230] If the SPP propagates to a break in symmetry, such as another grating or the edge of the material serving as an antenna-type structure, free photons can be emitted.[207, 213, 216, 219, 229, 231–234]

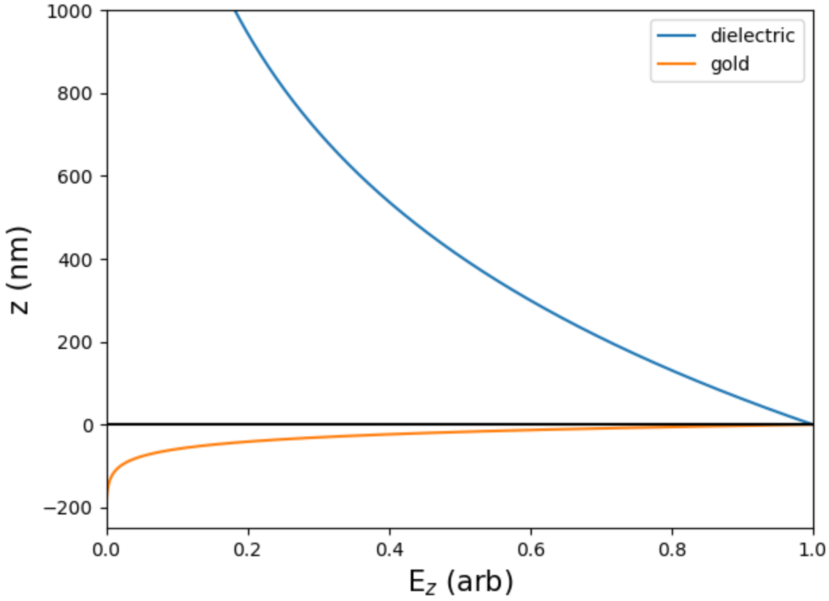

Figure 4.7 : Evanescent decay of SPP electric field into dielectric and metal layer. The decay length into the metal layer is much shorter than that into the dielectric.

4.1.3 Local surface plasmons

At the nanoscale, plasmonic properties become even more interesting as the effects of bulk plasmons and surface plasmons become less distinct. If a spherical nanoparticle is sufficiently smaller than the incident wavelength, the incident oscillating electric field is confined to the nanoparticle and will induce resonant local surface plasmon "standing wave" oscillations, Fig. 4.8, that do not propagate. For sufficiently small

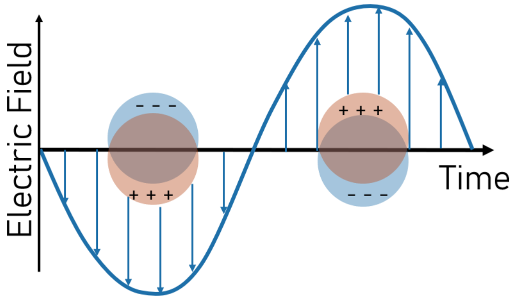

Figure 4.8 : Schematic of a dipolar local surface plasmon resonance. The oscillating electric field of the incident light results in surface plasmons confined within the nanoparticle. The electron cloud oscillates relative to the positively charged ions in the metal sphere. Figure recreated from Ref. [235]

nanoparticles, this coherent oscillation of the electron cloud called the dipole plasmon mode dominates the system. This dipolar mode is considered a “bright” mode; an excited dipolar mode will decay radiatively, emitting photons of the characteristic plasmon frequency.[236, 237] Higher order “dark” modes can exist, e.g. the quadripole mode where half the electron cloud moves with the oscillating field while the other half moves against it, which decay non-radiatively.[73, 238, 239]

For a sufficiently small nanosphere with volume V and dielectric function $\epsilon_m(\omega) = \epsilon'_m(\omega)+i\epsilon''_m(\omega)$ in a dielectric environment with frequency-independent dielectric function ϵ_d, Mie theory solves Maxwell's equations with appropriate boundary conditions in order to calculate the total extinction cross-section σ_{ext} (the total cross-section of absorption and scattering) considering only the dipolar mode:[240]

$$\boxed{\sigma_{ext} = \frac{9V\epsilon_d^{3/2}}{c}\frac{\omega\epsilon''_m}{(\epsilon'_m + 2\epsilon_d)^2 + \epsilon''^2_m}} \tag{4.8}$$

Mie theory extinction cross section for a nanosphere

When $\epsilon'_m \sim -2\epsilon_d$ and $\epsilon''_m << 0$, resonance conditions for a large σ_{ext} are met. This resonance occurs at the Mie frequency, $\omega_{Mie} = \frac{\omega_p}{\sqrt{3}}$.[206]

Mie theory neglects the interband transition terms of the dielectric in gold, so the Mie frequency doesn't accurately describe the local surface plasmon resonance frequency.[198] Adding in the interband transition contribution, ϵ_b, to the dielectric function of gold, the polarizability α (which describes how easily the dipole mode is excited) of a sphere with radius R, in vacuum is defined as

$$\boxed{\alpha = R^3 \frac{\epsilon - 1}{\epsilon + 2} = \frac{R^3(\epsilon_b \omega^2 - \omega_p^2) + i\omega\gamma\epsilon_b}{((\epsilon_b + 3)\omega^2 - \omega_p^2]) + i\omega\gamma(\epsilon_b + 3)}} \tag{4.9}$$

Polarizability of nanosphere including interband transitions

which has a resonance frequency ω_R condition when $\omega_R = \frac{\omega_p}{\sqrt{\epsilon_b + 3}}$ with a width set by $\gamma(\epsilon_b + 3)$.[198] The figure-of-merit (Q-factor) indicates how well the resonance maintains its energy content and is determined through the ratio of the plasmon energy and the full width at half maximum of the band.[241] The larger the Q-factor, the better the plasmonic resonance is with larger local electric field enhancements, longer lifetimes, and weaker damping.[242] This means that when the electron mean free path is low, either because of poor conductivity or because the size of the nanoparticle is so small that surface scattering dominates the mean free path, γ becomes large, reducing the quality of the plasmon resonance. Large interband transition contributions of the dielectric function additionally degrade the plasmon resonance. The effects of conductivity and interband transitions on the plasmonic resonance are why transition metals are poor candidates for plasmonics. The interband transitions are also why the dipolar plasmon resonance for gold is shifted to the visible ($\sim$ 520 nm) despite the plasma frequency being in the deep UV. γ also indicates that although the size of the nanoparticles must be smaller than the wavelength of the incident illumination for localized surface plasmons, the nanoparticles cannot be so small that surface scattering dominates the mean free path. Therefore, typical gold nanoparticles used in plasmonics are $\sim$ 10-100 nm in diameter.[198] Factors that affect the plasmon energy include size and geometry of the nanoparticles and the dielectric environment surrounding the nanoparticle.[206, 239, 240] From Equations 4.8, changing the dielectric environment changes the extinction cross section and can cause the plasmon energy to shift. Because the dielectric function for gold decreases with wavelength, Fig. 4.2, the resonance red-shifts when placed in an environment with higher index of refraction.[205] Changing the size and shape of the nanoparticle also shifts the plasmon energy. The resonance red-shifts as the particles become more oblong if the electric field polarization is along the major axis as there will be one plasmonic mode per unique axis.[239] Additionally, the particle size has clear effects on the plasmonic energy, having a 1/R relationship.[240]

Because of the collective oscillations of the free electron gas, the induced electric field near the surface of the nanoparticle is enhanced. This local electric field can be enhanced even further if two nanoparticles are brought together, known as dimers. The polarization dependence of the incident illumination is important, Fig. 4.9. If the laser is in the optimal polarization, the charge distributions due to the plasmonic oscillations in the nanoparticle can allow for large local enhancements.[120, 236] As the particles get closer together, the field enhancements can get closer together, increasing by $\sim d^{-8}$.[198] As seen in the next section, these local field enhancements can allow for Raman enhancements $\sim 10^{11}$. These field enhancements are *near-field*, meaning that the fields decay rapidly away from the interparticle gap. Bringing these particles together causes the plasmon resonances to shift, red-shifting in the top case of Fig. 4.9 and blue-shifting in the bottom case due to Coloumb interactions.[205] This

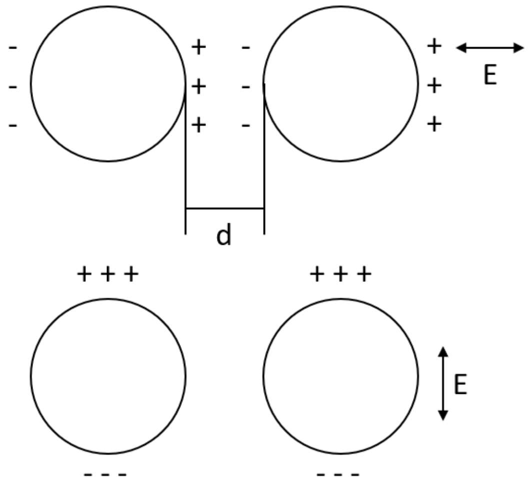

Figure 4.9 : Schematic of plasmonic dimers, consisting of two nanoparticles brought close together with an interparticle gap d under incident laser illumination, demonstrating the importance of incident laser polarization. *top*: When the laser polarization goes along the length of d, the charge distribution due to the plasmonic resonance allows for localized electric field enhancements in the gap, increasing as d shrinks. *bottom* When the laser polarization is oriented perpendicular to the length of d, the charge distributions due to the plasmonic oscillations do not create the local field enhancements between the particles. Figure recreated from Ref. [198].

shifting is called hybridization, where the plasmonic modes in distinct nanoparticles interact with each other.[243] As we will discuss in the next section, these large local enhancements of the electric field can be utilized to enhance inelastic light scattering in single molecule junctions.

4.1.4 Decay mechanisms of plasmons

The dipolar plasmonic mode was previously called a “bright” mode and the higher-order multipolar modes were called “dark” modes. Here, we will discuss both the radiative (“bright”) and non-radiative (“dark”) decay mechanisms of plasmons. Recently, pulsed lasers have been used to probe the relaxation times of the plasmonic

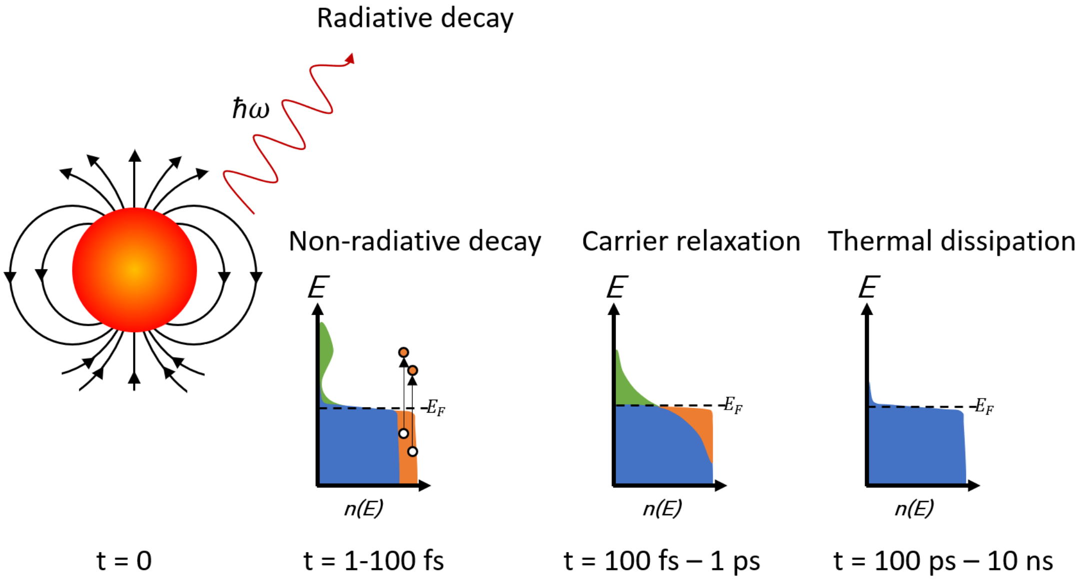

Figure 4.10 : Excitation and relaxation of local surface plasmons after a laser pulse. From left to right is a time axis. *t=0*: the incident illumination excites an LSPR which redirects the Poynting vector towards the nanoparticle. t = *1 - 100 fs*: The LSPR decays, either radiatively via re-emitted photons ($\hbar\omega$) or non-radiatively via the excitation of non-thermal "hot" carriers through either interband or intraband transitions. The hot electron distribution is seen in green and the hot hole distribution is seen in orange. t = *100 fs - 1 ps*: "hot" carriers relax via electron-electron scattering, redistributing their energy distributions as they begin to thermalize. t = *100 ps - 10 ns*: The local heating from the LSPR thermally dissipates through the substrate as the system relaxes to thermal equilibrium.

decay.[73, 215, 244–248] As seen in Fig. 4.10, after a local surface plasmon resonance is excited in a nanoparticle, the free electron oscillations begins to become damped with a dephasing timscale $\sim$ 2-50 fs[205] and will either decay radiatively emitting coherent photons or non-radiatively by exciting non-thermal "hot" electron-hole pairs, depending on the specifics of the excited plasmonic mode.[198] The "hot" electrons[92, 98, 100, 249, 250] get excited to energy levels above the Fermi energy from either intra- or interband transitions[195] changing the Fermi distribution to have a non-thermal, high-energy tail. The timescale for these non-thermal excitations is $\sim 1 - 100$ fs. The excitation efficiency and energy distribution is determined by the specifics of the plasmonic resonance including particle size, plasmon energy, electronic structure, and density of states of the material.[73] If the hot electron energy, $E = E_F + k_b T_{el}$ where E_F is the Fermi energy and T_{el} is the effective temperature of the hot electron, is larger than the work function of the material, the electrons may be emitted due to photoemission.[196, 251–254] Otherwise, between $\sim$ 100 fs - 1 ps, the hot carriers begin to thermalize, rearranging to a "quasi" equilibrium distribution as the carriers relax due to electron-electron, electron-phonon, electron-defect, or surface scattering.[205] After $\sim$ 100 ps-1 ns, the system reaches thermal equilibrium as the local heat dissipates through the surrounding substrate via phonon-phonon scattering. Although the lifetimes of these hot carriers are quite short, non-radiative decay of local surface plasmon resonances can be used beyond just local heating such as energy conversion,[255] photodetection,[92, 98, 256] and photochemistry.[73] The hot electrons can play a role in plasmon-assisted transport[81, 229, 257–260] and have been shown to add additional photocurrent in molecular and tunnel junctions.[258, 261, 262] As a result, care should be taken when attributing signal from electronic transport of plasmonically resonant molecular or tunneling junctions under laser illumination.

4.2 Raman spectroscopy

Ch. 3 discussed how electronic transport measurements can probe the energy exchanges between tunneling electrons and molecular electronic and vibrational states in a molecular junction. In this section, we will discuss molecular vibrations and how we can probe them using the frequency of scattered light, in a method called Ra-

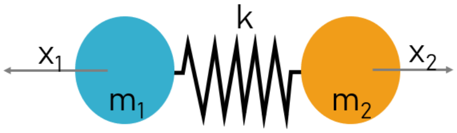

Figure 4.11 : Schematic of a diatomic molecule, consisting of two masses, m_1 and m_2, on a spring with spring constant, k.

man spectroscopy. Consider a diatomic molecule consisting of two atoms covalently bonded. This molecule can be simplified to two masses, m_1 and m_2, on a spring with some spring constant, k, whose value represents the strength of the chemical bond, as seen in Fig. 4.11. The displacement of the atoms in the molecule q can be described from using Hooke's law, $\mu\frac{\mathrm{d}^2 q}{\mathrm{d}t^2} = -kq$, where $\mu = \frac{m_1 m_2}{m_1+m_2}$ is the effective mass of the molecule. Solving for q gives $q = q_o \cos\omega_{vib} t$ where $\omega_{vib} = \sqrt{\frac{k}{\mu}}$ is the characteristic vibrational frequency. If an incident electric field oscillating at some frequency ω_o, $E = E_o \cos\omega_o t$, interacts with the molecule, the molecule can also oscillate inducing a dipole moment, p, described by $p = E \cdot \alpha = E_o \cos\omega_o t \cdot \alpha$, where α is the polarizability tensor of the molecule which describes how easily a dipole moment can be induced in the molecule. Because α changes as the molecule vibrates, α depends on q. For small q, α can be described as a function of q using the small amplitude approximation, which to the first order is $\alpha(q) = \alpha_o + \frac{\partial\alpha}{\partial q} \cdot q$. $\alpha(q)$ can then be substituted into the equation for p, yielding

$$\boxed{p = \alpha_o E_o \cos\omega_o t + \frac{\partial\alpha}{\partial q} q E_o (\cos(w_o - w_{vib})t + \cos(\omega_o + \omega_{vib})t)} \tag{4.10}$$

dipole moment for Rayleigh and Raman scattering

Equation 4.10 describes the possible frequencies the incident photon can be scattered to before being re-emitted, depicted in Fig. 4.12. The first term is the elastic scattering event called Rayleigh scattering, where the re-emitted photon has exactly the same energy as the incident photon. The second and third terms describe inelastic scattering processes. The second term describes Stokes scattering, where the photon *loses* energy to the molecule, leaving with $\hbar\omega_o - \omega_{vib}$ of energy, exciting the molecule from the ground state to an excited vibrational state. The third term describes Anti-Stokes scattering, where the photon *gains* energy from the molecule, re-emitting with $\hbar\omega_o + \omega_{vib}$ of energy, relaxing the molecule from an excited state back to the ground state. Therefore, the frequency of the scattered light can be used as a probe to determine the molecular vibrations in the molecule. The next two subsections will go into these scattering mechanisms in more detail.

4.2.1 Rayleigh scattering

The dominant scattering mechanism is the elastic Rayleigh scattering. Generally, intensity from Rayleigh scattering is $\sim 0.1\%$ of the incident light. In this mechanism, an incident photon is absorbed by the molecule, which is then excited to a virtual state, before it is re-emitted at exactly the same energy as the incident photon. The molecule essentially acts an an antenna oscillating at the same frequency as the incident electric field. The Rayleigh scattering cross-section is inversely proportional to λ^4, where λ is the incident wavelength. Because of the strong wavelength dependence of the Rayleigh cross-section, shorter wavelengths are scattered more strongly than longer wavelengths.[191] This wavelength dependence is why the sky is blue during daylight.

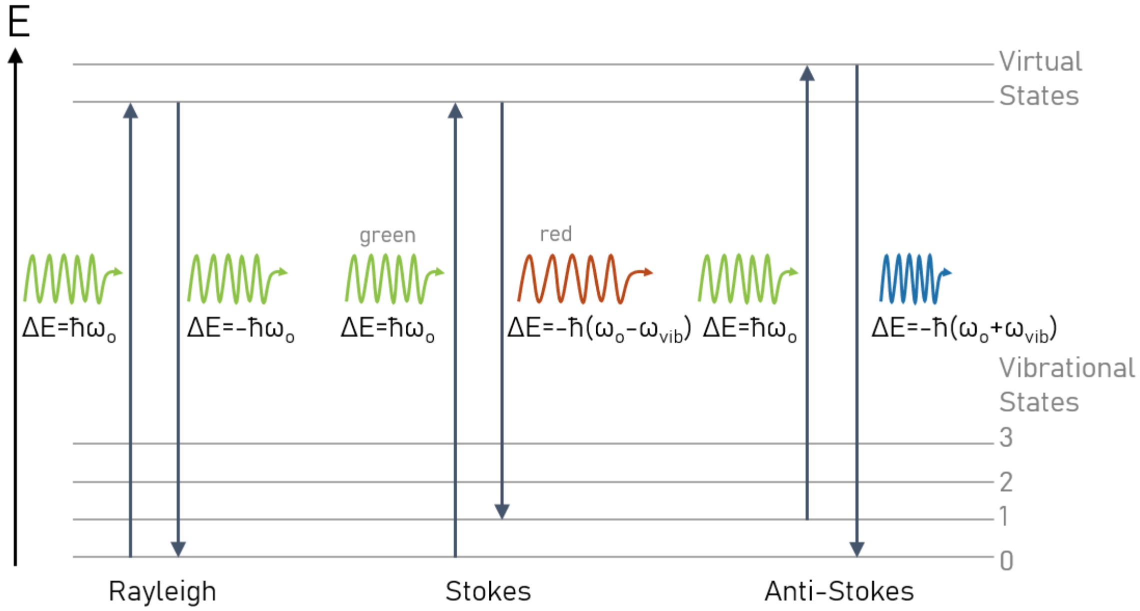

Figure 4.12 : Schematic of Rayleigh and Raman scattering. A molecule absorbs an incident photon of energy $\hbar\omega_o$, gets excited to a virtual state, before re-emitting the photon which is either elastically or inelastically scattered. *Left*: Rayleigh scattering, the elastic scattering event where both the molecule and photon energies remain unchanged. *Middle*: Stokes scattering, where the incoming photon loses energy to the molecule, exciting it to an excited vibrational state. *Right*: Anti-Stokes scattering, where the incoming photon gains energy from the molecule, relaxing it to a ground state.

4.2.2 Stokes and Anti-Stokes scattering

Although Rayleigh scattering is the dominant scattering mechanism, about 1 in 10 million photons[263, 264] are scattered inelastically, exchanging energy with the molecular vibrational modes. These vibrational modes are quantized and can be approximated as a quantum harmonic oscillator, with evenly spaced energy levels described by $E_n = \hbar\omega(n + \frac{1}{2})$, for low integers n. Because Raman spectroscopy looks at energy shifts, it is often easier to consider the energy in terms of wavenumber, cm^{-1}, defined as cm$^{-1} = \frac{1}{\lambda}$ instead of ω. The Raman shift can be converted from wavelength to wavenumber by

$$\boxed{\mathrm{cm}^{-1} = \frac{1}{\lambda_{incident}\mathrm{nm}} - \frac{1}{\lambda_{scattered}\mathrm{nm}} \times \frac{10^7\mathrm{nm}}{\mathrm{cm}}} \tag{4.11}$$

Raman shift conversion from wavelength to wavenumber

For reference, 1 eV = 8086 $\mathrm{cm}^{-1} \sim$ 242THz.

Stokes scattering refers to when a molecule in the ground state absorbs an incident photon, gets excited to a virtual state, and relaxes back down to an excited vibrational state, receiving $\hbar\omega_{vib}$ of energy from the photon, before re-emitting the scattered photon with less energy than the incident photon. Anti-Stokes scattering refers to when a molecule is already in an excited vibrational state when it absorbs an incident photon, gets excited to a virtual state, and relaxes back down to the ground state, giving $\hbar\omega_{vib}$ to the re-emitted photon. Because the Fermi energy is much higher than the thermal energy at experimental temperatures (the Fermi energy of gold is 5.53 eV or 64,200 K),[108] the energy distribution of the system is degenerate with the lower states dominating the local vibrational population. As such, at finite temperatures, the Stokes signal will be much larger than the Anti-Stokes signal. The Stokes scattering will largely be temperature independent while the Anti-Stokes scattering intensity will increase with local temperature. Due to this temperature dependence of the Raman scattering intensity, the ratio of the Anti-Stokes to the Stokes intensity, I_{AS} and I_S respectively, can be used as a way to probe the local, vibrational effective temperature of a particular vibrational mode, T_ν^{eff} as

$$\boxed{\frac{I_{AS}}{I_S} = (\frac{\sigma_{AS}}{\sigma_S})(\frac{g(\omega_{AS})}{g(\omega_S)})^2(\frac{\omega_{AS}}{\omega_S})^4 \exp\left\{\frac{-\hbar(\delta\omega)}{k_B T_\nu^{eff}}\right\}} \tag{4.12}$$

Probing temperature with ratio of Anti-Stokes to Stokes intensities for the following parameters with subscripts AS and S indicating the values for Anti-Stokes and Stokes emission respectively: cross-section σ,[265] scattered photon frequency ω, electric field enhancement factor from plasmons $g(\omega)$, and the Raman shift $\delta\omega$.[266, 267] Note that this describes the *effective* temperature of an *individual* vibrational mode; different modes can have different effective temperatures.[266–268] Additionally, if Stokes scattering occurs at a rate faster than the vibrational relaxation timescale, the Raman scattering process itself can drive the local vibrational temperature to become elevated in a process called optical pumping. In general, the Raman intensity scales linearly with incident laser intensity, however under the presence of optical pumping, the Anti-Stokes signal scales quadratically with incident intensity. These concepts will be discussed in further detail in Ch. 5.6. Because inelastic light scattering events are so rare, spontaneous Raman scattering is challenging to detect without enhancement.[263, 264] The electric field enhancement of plasmonic nanosystems can significantly increase the Raman scattering intensity in a process called surface-enhanced Raman spectroscopy (SERS), which will be discussed in in Sec. 4.2.3.

From Equation dipole moment for Rayleigh and Raman scattering, both the Stokes and Anti-Stokes scattering require $\left.\frac{\partial \alpha}{\partial q}\right|_{q=0} \neq 0$, which means that for a vibrational mode to be Raman active the polarizability must change with time. A similar spectroscopic technique called infrared (IR) spectroscopy, which looks at the absorption, transmission, and reflectance of IR illumination to probe the vibrational modes, requires a change in the dipole moment, $\left.\frac{\partial p}{\partial t}\right|_{q=0} \neq 0$, to be IR active. The rule of mutual exclusion states that if a molecule has a center of symmetry, no vibrational mode can be both IR and Raman active, seen in Fig. 4.13. IETS does not have such limitations in detecting these vibrations.

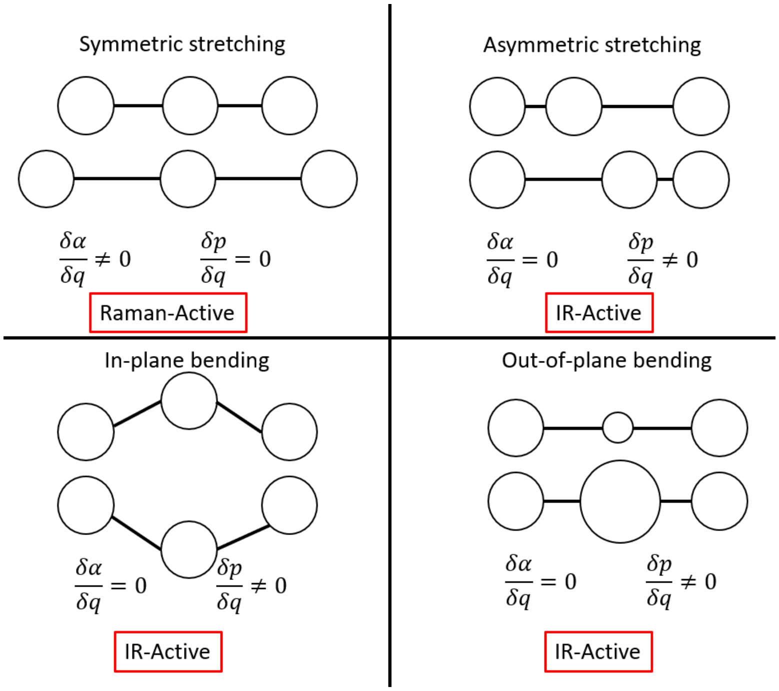

Figure 4.13 : Schematic of Raman and IR active modes in a centrosymmetric molecule, demonstrating rule of mutual exclusion.

4.2.3 Surface-enhanced Raman spectroscopy

Because inelastic light scattering events are so rare, spontaneous Raman scattering is challenging to detect. In the 1970s, the first reports of surface-enhanced Raman spectroscopy (SERS), where the plasmonic enhancement of the local electromagnetic field from roughened metal substrates strongly modified the Raman scattering rate, were published. There are two different mechanisms that are attributed to these enhancements: electromagnetic and the chemical theory[269], with the former being discussed in further detail in this section. The general concept of SERS from electromagnetic enhancement from plasmons is depicted in Fig. 4.14 and can be described as follows: a molecule is present on a roughened metal substrate and is under incident laser illumination with electric field $E = E_o$, frequency ω, and intensity I_o. The local plasmonic modes in the substrate increase the local electric field by a factor of $g(\omega)$ to $E = g(\omega)E_o$. The molecule then scatters the light, re-emitting a photon of frequency ω'. The electric field is again enhanced by the local plasmons, this time by a factor of $g(\omega')$. The total electric field is then $E = \alpha g(\omega)g(\omega')E_o$, where α is the polarizability tensor of the molecule. For low shift wavenumbers, $g(\omega') \sim g(\omega)$. Therefore, the total intensity of the SERS signal is $I \propto g^4 I_o$, which scales to the fourth power with g but *linearly* with I_o.[198]

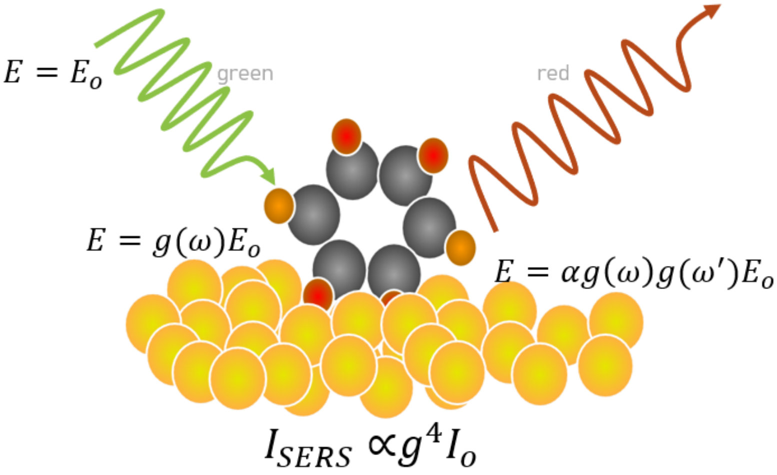

Figure 4.14 : Schematic of surface-enhanced Raman spectroscopy. A molecule is present on a roughened metal substrate. The electric field of the incident laser illumination, $E = E_o$, is enhanced by some factor $g(\omega)$ due to the plasmonc modes in the substrate. The molecule scatters the enhanced, incident photons, re-emitting the scattered photon whose electric field is again enhanced by $g(\omega')$, where ω' is the frequency of the scattered light. For low wavenumbers, $g(\omega') \sim g(\omega)$, so the overall intensity of the Raman signal, $I_{SERS} \propto g^4 I_o$, where I_o is the incident intensity.

The total SERS enhancement factor is defined as:

$$\boxed{G = |\frac{\alpha_R}{\alpha_{Ro}}|^2 |gg'|^2} \tag{4.13}$$

where α_R describes the polarizability tensor of the Raman tensor of the entire system and α_{Ro} is the polarizability tensor of the isolated molecule. These values can vary because the interaction of the molecule with the SERS substrate can affect the resonant properties and vibrational details of the molecular modes compare to that of the isolated molecule. SERS enhancement factors $\sim 10^5 - 10^{11}$ are commonly reported,[198, 239, 270] with single molecule SERS sensitivity requiring an enhancement $\sim 10^8$.[145, 271, 272] For gold and silver under resonant wavelengths, $g >> 1$, which allows for large G values due to the g^4 dependence.[198] For example, if $g \sim 10$, $G \sim 10^4 - 10^5$.[270] G can be determined experimentally by comparing the ratio of the SERS intensity and the normal Raman intensity, adjusting for the number of molecules in the excitation volume.[273]

When measuring SERS in the single- to few-molecule regime, there are some key indicators. The first is “blinking”,[145, 269, 274, 275] where the intensity of individual vibrational modes change suddenly and independently, indicating that the molecule is re-arranging within the plasmonically-enhanced electric field. As the molecule re-arranges, the coupling of the specific vibrational modes to the enhanced local field changes with time causing the changes to Raman signal. Another indication of single- to few-molecule SERS signal is spectral diffusion,[145, 168, 238, 271, 274, 275] where the specific mode energy shifts with time. As the molecule re-arranges, the changing interactions between the molecule, disorder in the metal, and the plasmonic resonances can cause the the energy levels to shift slightly, typically $\sim 20\text{cm}^{-1}$. Such re-arrangements of the molecules would be averaged out for a large ensemble of molecules.[238] A final indication of single- to few-molecule SERS measurements is signal from the low wavenumber Anti-Stokes continuum staying constant as the “blinking” and spectral diffusion effects are observed. This continuum is commonly seen in SERS and is attributed to the Raman scattering by the conduction electrons in the electrodes[168, 198, 268, 274, 276–279] and the the interaction of these electrons with the adsorbed molecules.[280, 281] When changes in the Raman signal due to “blinking” and spectral diffusion effects are observed, this low-wavenumber Anti-Stokes continuum can serve as an indication that the rest of the system remains constant with time, providing further evidence that the changing signal is from single- to few-molecules.[238]

SERS is commonly conducted in aggregated nanoparticle clusters[198], nanogaps formed by electromigration[145, 168] or mechanically controllable break junctions[139, 141] or via a sharp STM-style tip being brought in close proximity to a roughened metal substrate in a process called tip enhanced Raman spectroscopy, TERS.[282–285] Adding a grating to serve as a waveguide on the tip can allow for SPPs to propagate along the tip before emitting highly confined light at the tip,[216] which provides a way for nonlocal excitation of TERS for higher spatial resolution.[211] This technique is not limited to TERS, however. SPPs have been used to remotely excite nanogaps for SERS measurements[286, 287] in which SPPs are excited by shining on a grating[81] or the end of a nanowire[288, 289] which then propagate along the device before emitting light when scattering off the nanoscale molecular junction nanogap.

Chapter 5

Previous work: Single molecule sensitivity, but high local heating

5.1 Motivation: Understanding how energy dissipates through a single molecule through simultaneous electronic transport and optical measurements

As technology advances, development of electronic devices strives to make the devices smaller, more portable, and faster. These sorts of demands have pushed electrical components to the single-molecule scale. Although Chapter 3 discusses how molecular junctions have been widely studied, one major open question remains: how does heat dissipate through a single molecule? Heat dissipation is well understood in the macroscopic limit, but there is a lack of quantitative data that shows how energy exchanges between electronic and vibrational states of a molecule. By studying simultaneous IETS and SERS measurements, quantifying these energy exchanges is possible and learning how to drive and manipulate these exchanges can be explored. Measuring these energy exchanges is no simple task - single molecule SERS sensitivity requires resonant plasmonic enhancement which typically comes with high local heating due to the collective oscillation of the electrons while the IETS measurements require cryogenic temperatures for well-resolved peaks highlighting the inelastic energy exchanges. In this chapter, previous results of lithographically-defined plasmonically-active single molecule junctions with single molecule SERS enhancement with the ability for simultaneous electronic transport measurements will be discussed along with some of the challenges of achieving true low temperature measurements due to local temperature rises from plasmonically active modes in the wire. Finally, experimental methods for the experiments described in the rest of the chapters will be discussed.

5.2 Intact gold "bowtie" devices have a resonant transverse plasmon mode

A significant amount of work discussed in this thesis, and in numerous publications in the Natelson lab including Refs. [113, 150, 151, 168, 243, 266, 268, 274, 290–292], has been conducted using gold "bowtie" devices; devices consisting of a thin film, polycrystalline gold nanowire between two "fan-out" electrodes, seen in Fig. 5.1 with gratings in the electrode design, which are discussed in more detail in Chapter 9 and are not always present. These electrodes extend out to bonding pads which allow for electronic transport measurements. Information regarding the fabrication of these bowties is seen in Sec. 5.8.1. The nanowire geometry is optimized to have a resonant transverse plasmon mode (perpendicular to the length of the wire) under 785 nm free space CW laser illumination [290].

The intact nanowire under 785 nm illumination experiences a temperature rise due to this plasmonic resonance, which can be detected via electronic transport measurements. Because the nanowire is so much smaller than the connecting electrodes, the nanowire dominates the conductance measurements of the entire device. Therefore, changes in the conductance measurements can be attributed to changes in the nanowire itself. A study of the incident laser polarization dependence of the dif-

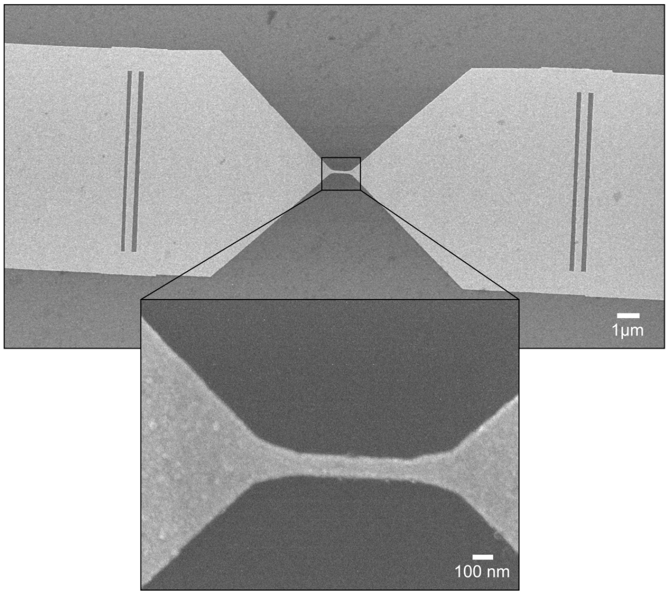

Figure 5.1 : SEM image of a gold "bowtie" device with gratings in the electrode design. Inset: zoomed-in image of the nanowire

ferential conductance of nanowire provides evidence of the excitation of the local, transverse plasmon mode in the wire, Fig. 5.2. The differential conductance has the largest magnitude when the laser is in the transverse polarization, and the smallest change when the laser is in the longitudinal polarization.

The temperature rise of the nanowire under laser illumination can be quantified using a bolometric technique, as discussed in Ref. [290]. Ohm's law relates a voltage, V, to a resistance, R, and current, I, as:

$$\boxed{V = IR} \tag{5.1}$$

Ohm's Law

Relating a small change in R to a small change in I by taking a derivative of Equation 5.1 then results in:

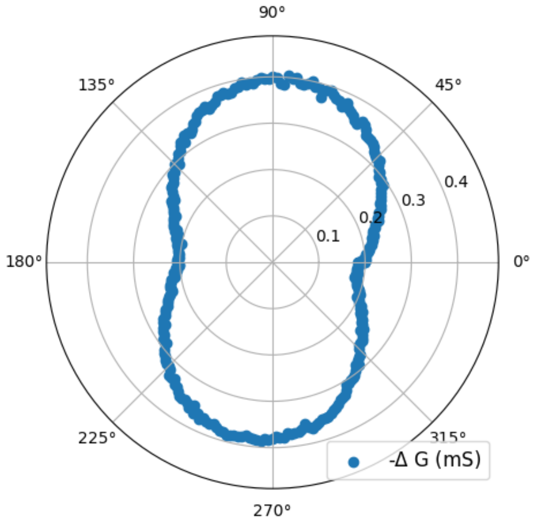

Figure 5.2 : Polar plot of the incident laser polarization dependence of the nanowire differential conductance (ΔG). Δ G has the largest magnitude when the laser is in the transverse (90°) polarization due to the excitation of the resonant transverse plasmon mode.

$$\boxed{\mathrm{d}R = -(\frac{R^2}{V})\mathrm{d}I} \tag{5.2}$$

Differential Ohm's Law

Using the relation $\mathrm{d}R = \mathrm{d}R\frac{\mathrm{d}T}{\mathrm{d}T} = \mathrm{d}T\frac{\mathrm{d}R}{\mathrm{d}T}$, the temperature rise of the nanowire, ΔT, can be estimated using the differential conductance, $\Delta G = \frac{\mathrm{d}I}{V}$, by:

$$\boxed{\Delta T = \frac{-R^2 \Delta G}{\frac{\mathrm{d}R}{\mathrm{d}T}}} \tag{5.3}$$

Conversion of differential conductance to temperature rise

where $\frac{\mathrm{d}R}{\mathrm{d}T}$ is the slope of the substrate temperature dependence of the total device resistance and R is the total device resistance at the measurement substrate temperature. This conversion is true at substrate temperatures where $\frac{\mathrm{d}R}{\mathrm{d}T}$ is linear, which is generally above 30 K, Fig. 5.3. At lower substrate temperatures, Equation 5.3 should no longer be used. Quantifying the temperature rise at lower substrate temperatures will be discussed in more detail in Sec. 5.7. At room temperature, the typical temperature rise of a standard nanowire on a 200 nm SiO_2/Si substrate under a focused 785 nm laser with FWHM of 1.8 µm with power ∼ 20 mW in the transverse polarization is on the order of 1 K[290].

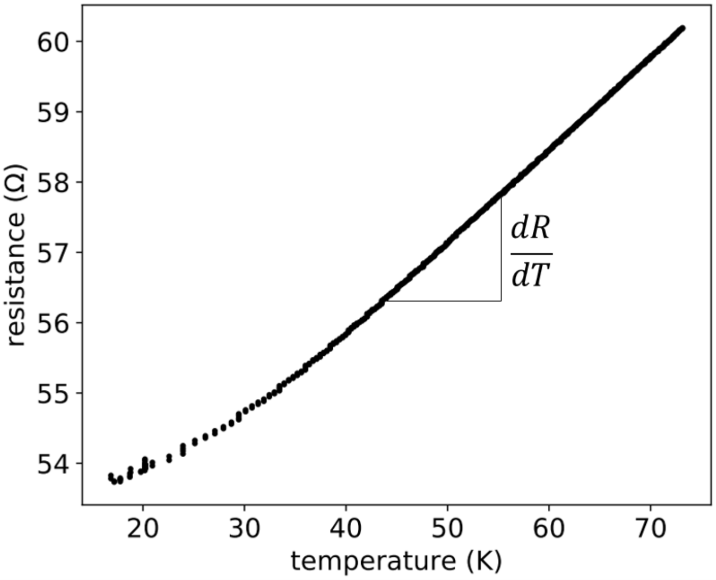

Figure 5.3 : Device resistance, R, as a function of substrate temperature, T. The relationship is linear to around 30K, and so the temperature dependence of the resistance can be estimated by the slope, $\mathrm{d}R/\mathrm{d}T$.

5.3 Broken nanowires have high local enhancements of the electric field, specific to the details in the nanogap

Creating a nanogap in the nanowire within the bowtie devices allow for a molecular tunnel junction, Fig. 5.4. The nanogap is created in one of two ways: the "self-aligned" fabrication technique where the gap is created in a two-step lithography process or through electromigration in an intact wire. The work in this thesis utilizes electromigration because it allows for the wire to be intact for initial conductance measurements without a tunneling gap.

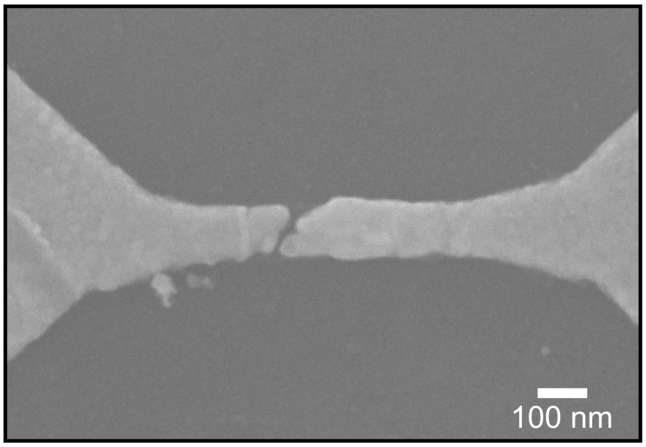

Figure 5.4 : SEM image of a bowtie device with an electromigrated nanogap

The "self-aligned" gaps are created during device fabrication which can allow for small gaps to be fabricated in bulk.[293–295] These gaps can be well-controlled geometrically, and the gap sizes can be smaller than what is achievable during fabrication.[295] The self-aligned fabrication process, detailed in Fig. 5.5, consists of a two-step lithography technique. An initial lithography step patterns half of the device and has an initial deposition of the Au layer, with an additional Cr layer over the Au film. The Cr oxidizes and expands beyond the Au layered pattern. An additional lithography step patterns the second half of the device, which overlaps with the previously-deposited pattern, and a final Au layer is deposited. After lift-off, the Cr is etched away, resulting in a nanogap within the wire where the Cr expanded.

Although the self-aligned gap fabrication allows for arrays of devices to be fabricated with nanogaps, the devices in this work have gaps created through electromigra-

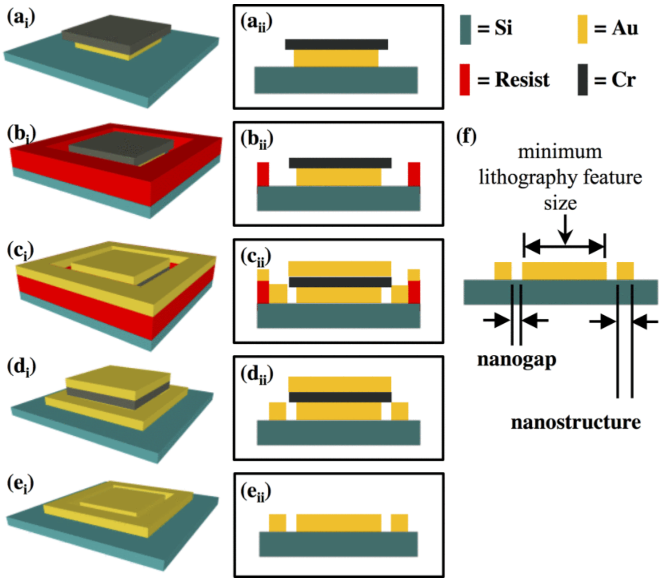

Figure 5.5 : Schematic of self-aligned fabrication process. *first column*: 3D schematic. *second column*: 2D cross-section. *a*: After the initial lithography step and development, a layer of Au is deposited. A layer of Cr is then deposited over the Au layer. The Cr layer oxidizes, expanding beyond the Au layer after lift-off. *b*: After the second step of lithography, the resist is developed to show the lithographically created pattern. *c*: The final Au film is deposited via e-beam evaporation. *d*: After lift-off, only the Au and Cr layers remain. *e*: The Cr layer is etched away using a wet Cr etch, leaving behind only the gold films that were directly evaporated onto the substrate. *f*: Comparison of gap sizes of self-aligned structures vs. lithographically defined features. Figure reprinted with permission from Ref. [295]. ©2011 IEEE.

tion. Although considered a failure in traditional circuit design[296, 297], the process can be used to create nanoscale gaps in nanowires. The concept of electromigration is simple: when a large current density (typically higher than 10^8A/cm^2) is pushed through a conducting wire due to an applied bias, charge carriers travel through the wire. As the charge carriers move through the wire, they move past and interact with the stationary ions in the conductor. Momentum exchanges between the charge carriers and the ions can cause the charge carriers to physically push the ions out of the way, resulting in a nanogap, called the electron wind force. Additionally, due to the high electric fields during the electromigration process, charge defects can be pushed along wire causing further separation.[298] These momentum exchanges most commonly occur when the charge carriers scatter of defects, such as grain boundaries or structural defects. When an ion begins to diffuse, the local current density at that location increases, resulting in more scattering and therefore more momentum transfer at that specific location.[142, 296, 299–301] Using electromigration in a controlled way can allow for consistent nanoscale gap formations in nanowires.

The electromigration process in these bowtie devices is as follows: a National Instruments DAQ is controlled via computer to apply a bias across the device. The bias is linearly ramped up while the total current is monitored. Joule heating, where a conductor is heated as a current passes through, will cause an increased resistance as the voltage increases. Dynamically measuring the change in resistance as the voltage ramps allows for controlled electromigration; the process is terminated when a change in resistance is larger than what is expected due to Joule heating. This process is repeated until the total device resistance is larger than that of the conductance quantum, $G_o = 3.8E - 5\text{S} = \frac{2e^2}{h}$, ∼12.9 kΩ.

The specific details of the nanogap can allow for large enhancements of the local electric field, Fig. 5.6. In Ref. [243], COMSOL Multiphysics was used to model the electric field enhancement of the nanogap system. As expected, when the laser is in the longitudinal polarization, the electric field enhancement and charge distribution are relatively weak. The largest response occurs when the laser is in the transverse polarization, exciting that local mode within the nanowire; within the gap, there is large, local enhancements of the electric field specific to the device geometry which is a result of the hybridization of the local transverse plasmon mode with the multipolar modes within the gap.

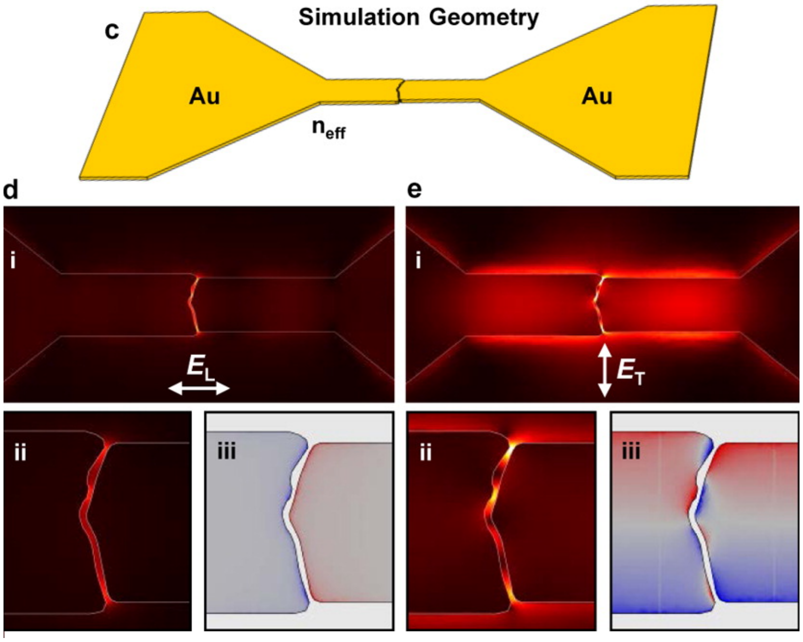

Figure 5.6 : Simulation of *i, ii* electric field enhancement and *iii* charge distribution in nanogaps. *c*: Example of simulation geometry used in finite-element modeling using COMSOL. *d*, *e*: results of the simulation of the gap under illumination in the longitudinal, E_L, and transverse, E_T, polarization, respectively. The local field enhancement within the wire is largest when the laser is in the transverse polarization because of the resonant local transverse plasmon mode in the nanowire. Within the gap, very large local enhancements of the electric field is seen under the transverse polarization, indicating hybridization of the transverse plasmon with multipolar modes within the gap. Reprinted with permission from Ref. [243]. ©2013 American Chemical Society.

5.4 The large field enhancements in the nanogaps allow for SERS measurements

The large field enhancements from the hybridization of the local, multipolar modes within the gap and the local surface plasmon resonance from the nanowire allow for detection of single molecular Raman scattering via SERS. As seen in Fig. 5.7c,d, 2D maps of the integrated Raman signal of the characteristic Si peak (510-520 cm^2) as a function of laser position were conducted with the laser in the transverse and longitudinal polarization, respectively. The maps are nearly identical regardless of polarization; the Si peak is not enhanced due to the local modes within the gap. The signal is largest when the laser is incident on the substrate and smallest when the laser is incident on the gold bowtie. When looking at the characteristic peaks around 1500-1600 cm^2 of the applied self-assembled monolayer of BPE (*trans*-1,2-bis(4-pyridyl)-ethlyene), the maps look much different. When the laser is in the transverse polarization, Fig. 5.7e, there is a "hotspot" of signal within the nanogap, with no detectable signal anywhere else. This hotspot is completely absent when the laser is in the longitudinal polarization, Fig. 5.7f, indicating that the signal is detected due to SERS. In Ref. [113], the electric field was experimentally determined to be enhanced by a factor of 1000.[266]

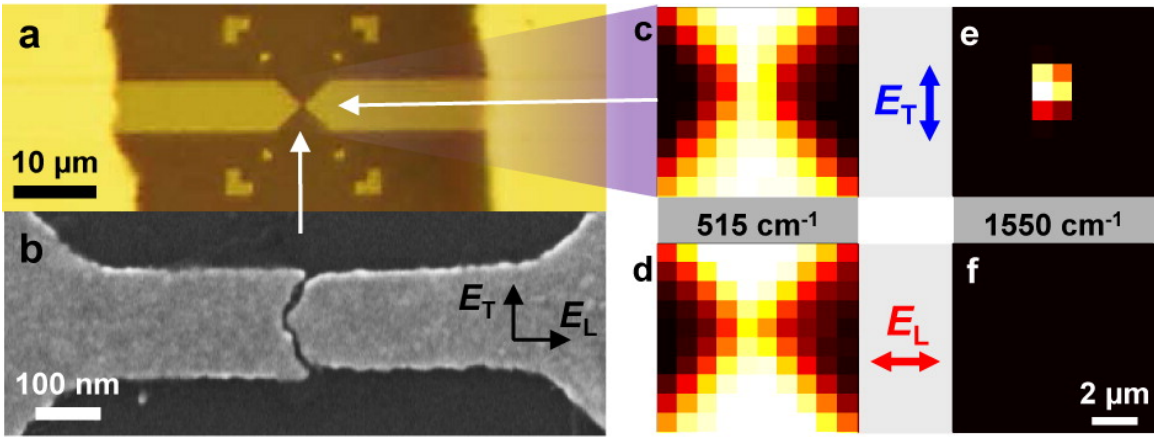

Figure 5.7 : Simulation of *i, ii* electric field enhancement and *iii* charge distribution in nanogaps. *c*: Example of simulation geometry used in finite-element modeling using COMSOL. *d*, *e*: results of the simulation of the gap under illumination in the longitudinal, E_L, and transverse, E_T, polarization, respectively. The local field enhancement within the wire is largest when the laser is in the transverse polarization because of the resonant local transverse plasmon mode in the nanowire. Within the gap, very large local enhancements of the electric field is seen under the transverse polarization, indicating hybridization of the transverse plasmon with multipolar modes within the gap. Reprinted with permission from Ref. [243]. ©2013 American Chemical Society.

A plot comparing the Raman intensity within the hotspot under the transverse and longitudinal polarization, respectively, is seen in Fig. 5.8. The characteristic BPE signals are clearly visible when the laser is in the transverse polarization and are not detected at all in the longitudinal polarization. This indicates that the high local field enhancement due to the plasmonic modes within the gap is responsible for the SERS signal.

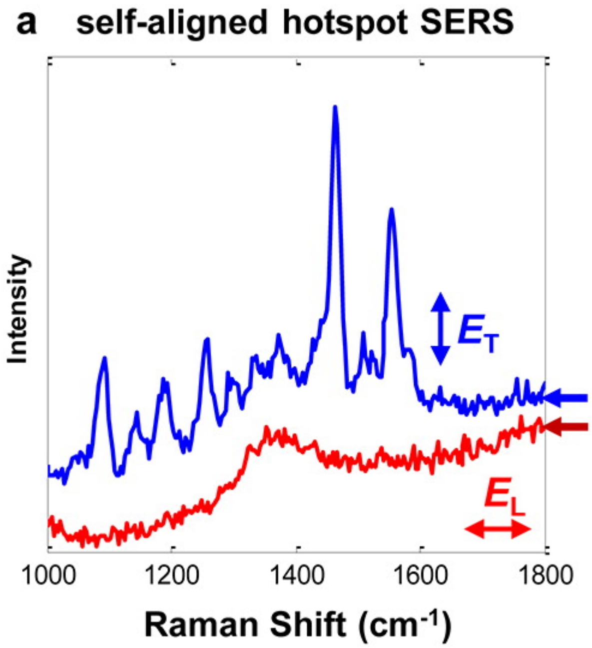

Figure 5.8 : Comparison of Raman signal in nanogap in the longitudinal, E_L, and transverse, E_T, polarizations. Well-defined peaks are detected under E_T that are not detected under E_L. Reprinted with permission from Ref. [243]. ©2013 American Chemical Society.

5.5 Simultaneous single molecule SERS and electronic transport measurements

The SERS enhancement within the gold bowtie devices can allow for single molecule Raman measurements. In Ref. [274], simultaneous Raman and differential conductance measurements were conducted in single molecule junctions with para-mercaptoaniline (pMA) and a fluorinated oligophenylyne (FOPE), seen in the bottom panel of Fig. 5.9a,b respectively. As seen in the top rows in Fig. 5.9, the Raman intensity of specific peaks can have sudden drops in the measured intesnity, with the amplitudes of the different vibrational modes varying independently. This "blinking" of the Raman signal is attributed to that of the single- to few-molecule regime; it is unlikely that large ensemble of molecules would show temporal fluctuations as this.[170, 238, 272] Instead, this "blinking" is thought to capture the movement and rearrangement of a single molecule, with different vibrational modes being enhanced as the molecular orientation changes.[269, 275, 302] Additionally, as seen in Fig. 5.9b, individual vibrational modes experience a Raman shift by as much as ± 20 cm^{-1}. This strong spectral diffusion further indicates that the signal is due to the details of the molecular environment while the low wavenumber continuum remains constant with time.[271, 274] Both the "blinking" and spectral diffusion are routinely observed in these junctions.[145, 150, 151, 168, 266]

As discussed in Chapter 3, the conductance as a function of applied bias can provide insight about when a tunneling electron exchanges energy with a molecule, exciting a vibrational mode in the molecule. Because the IETS signal detects Raman-active modes (as well as modes that Raman can't detect!), simultaneous electronic transport and Raman measurements can provide additional information about the

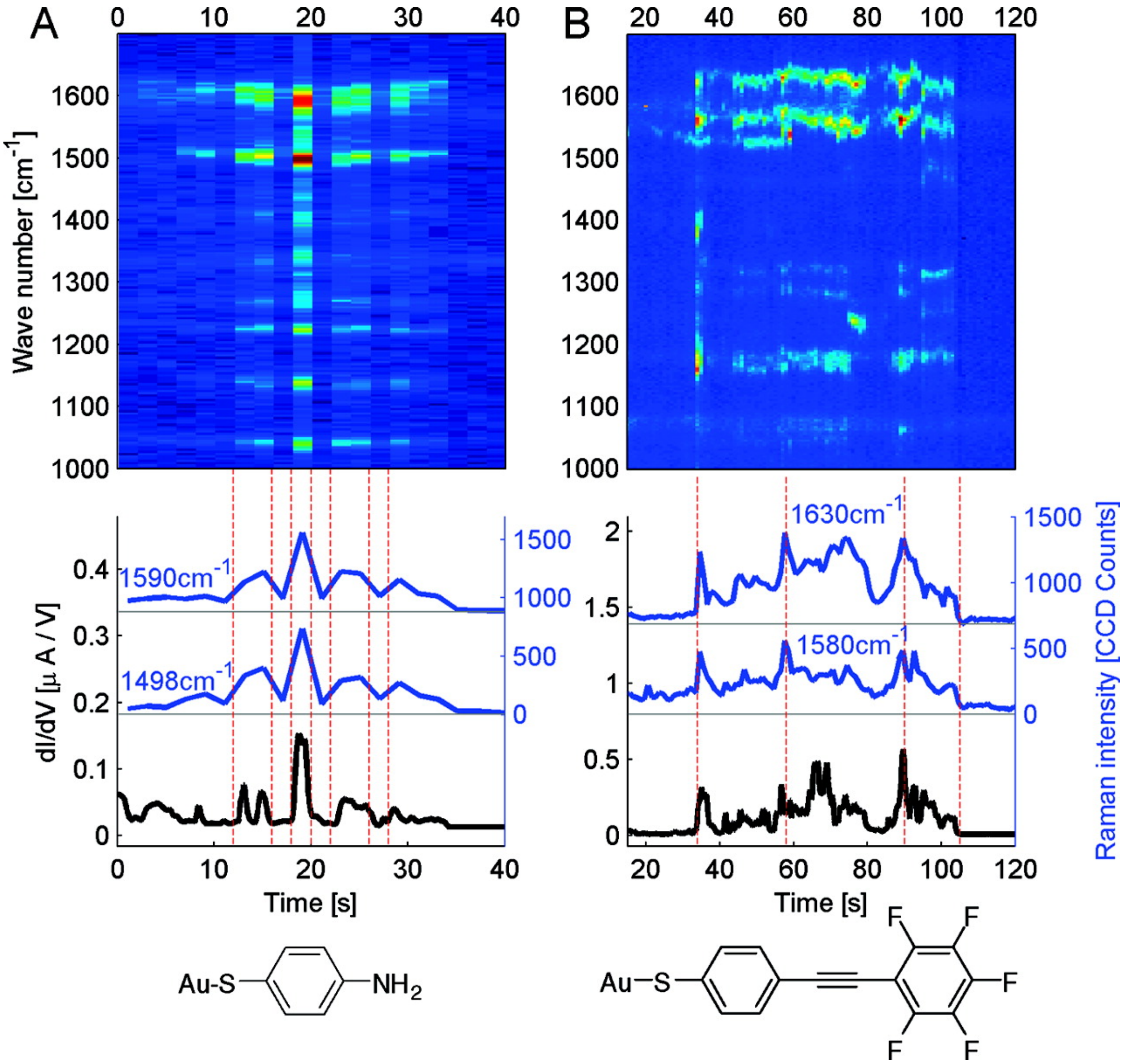

Figure 5.9 : Simultaneous measurements of Raman and differential conductance of single molecular junctions. *a*, *b*: Measurements of molecular junctions with pMA and FOPE, respectively. *top row*: Colormap of the Raman intensity as a function of time (x-axis) and wavenumber (y-axis). The colorscale indicates the intensity of the Raman peaks. The "blinking" of signal of specific modes indicates the one- to few-molecule regime. *b*: *black line, left axis*: Differential conductance measurement as a function of time. *blue lines, right axis*: Intensity of specific characteristic Raman peaks as a function of time. The vertical red dashed lines indicate times where changes within the electronic transport and Raman intensity measurements changed rapidly. Reprinted with permission from Ref. [274]. ©2008 American Chemical Society.

specifics of the molecular environment, including the molecular orientation.[141, 141, 145, 168, 172, 268, 274, 303–308] As seen in Fig. 5.9, there is strong correlation in the temporal changes in the differential conductance and Raman measurements; when a vibrational mode becomes active, both the differential conductance and the Raman intensity increase, further indicating the single-molecule sensitivity. This correlation was seen in ∼10% of the devices measured.[274] Although these room temperature measurements show that the signals detected in these devices are in the single- to few-molecule regime, quantifying the energy exchanges between the tunneling electrons and the electronic and vibrational states in the molecule require cryogenic temperatures for well-resolved IETS peaks.

5.6 Anti-Stokes signal hints at local heating in the junction

In Chapter 4.2, it was shown that the ratio of Anti-Stokes to Stokes intensity provides an indication of the local temperature distribution. Raman scattering itself can drive the vibrational population out of thermal equilibrium. If the Stokes scattering events, exciting the molecule vibrational modes from the ground state to an excited state, occur more quickly than the time for the vibration to relax to the bulk phonon modes, the excited vibrational population will exceed the equilibrium population, resulting in an effective vibrational temperature above the substrate temperature, T_{ν}^{eff}.[113, 266, 267, 309] In this regime, the intensity of the Anti-Stokes signal scales quadratically with the incident laser intensity while the Stokes intensity scales linearly.[267, 309] In Ref. [268], a systematic study of the Raman response of a three-ring oligophenylene vinyelene terminating in amine functional groups (OPV3) under bias was conducted which showed both optical and electronic pumping. Seen in Fig. 5.10, the Stokes signal (left) stays constant under applied bias as expected; at the measurement temperature

(80 K), the system is degenerate. The Anti-Stokes signal of the low wavenumber continuum, however, *does* increase even with moderate applied biases, indicating an effective vibrational temperature that increases with applied bias. Additionally, an Anti-Stokes mode $\sim 1800\text{cm}^{-1}$ (223 meV) shows clear signal at zero bias, which means that the local temperature of this mode is significantly elevated above the substrate temperature. The signal doesn't increase until the applied bias exceeds the vibrational mode energy $\hbar\omega_\nu$ which indicates current-driven vibrational pumping.[266] Further studies involving the bias-dependence of Raman spectra in single molecule junctions is discussed in more detail in Refs. [150] and [151]. Because the effective vibrational temperatures exceeded the substrate temperature by several orders of magnitude under optical illumination[268], further study to probe the local temperature rise of the system was required.

5.7 High local heating in gold nanowires

Because the effective vibrational temperature of some modes were $\sim 100-1000$ times larger than the substrate temperature at a substrate temperature of 80 K, attempting to conduct simultaneous IETS and SERS measurements at cryogenic temperatures posed some significant challenges. The IETS peaks were softened and widened when measured under laser illumination compared to when the laser was off with a substrate temperature of 5 K, implying thermal broadening due to local heating. This prompted a study of the local heating of the nanowire due to the presence of the wire, which was published in [292]. Gold bowtie devices, Fig. 5.11a, were measured on various substrates. Using a lock-in amplifier, the differential conductance of the device under chopped optical illumination was measured. Because the device's conductance is dominated by the constriction, it is assumed that all measured change

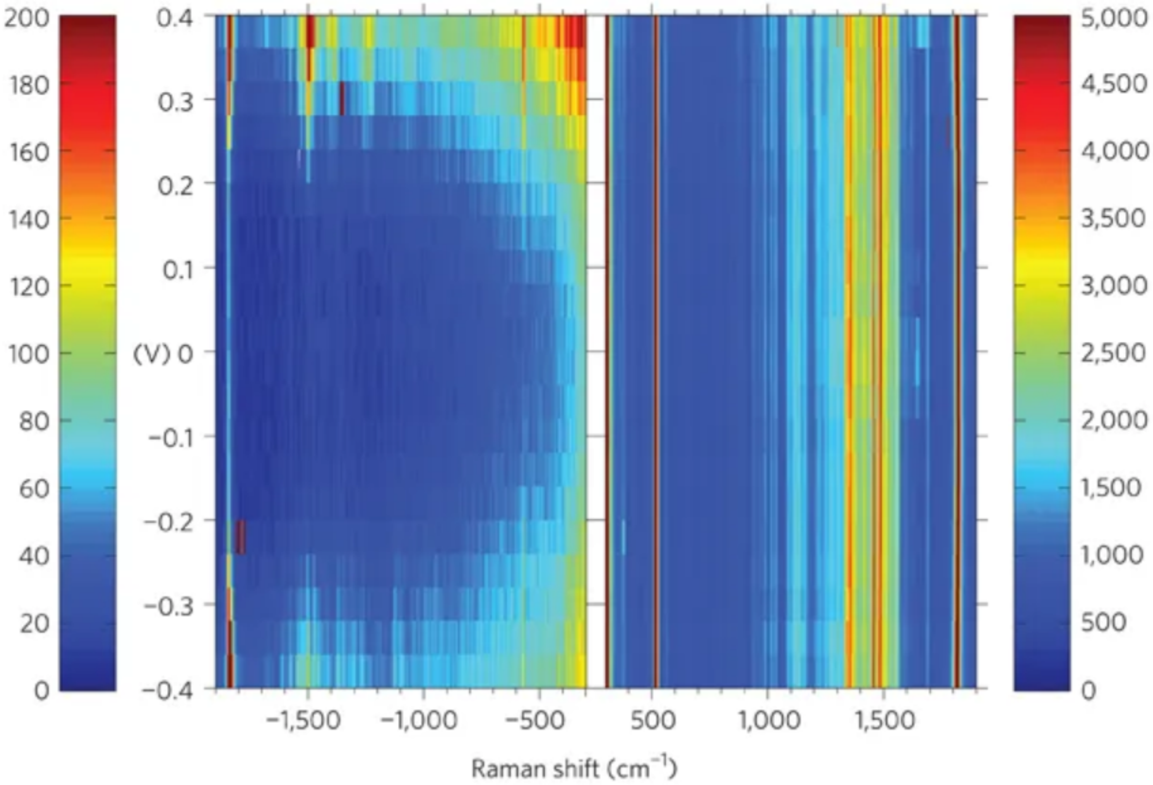

Figure 5.10 : Heating apparent in single molecule Anti-Stokes signal of molecular junction under moderate bias. The Raman response of a OPV3 molecular junction as a function of applied bias. The Stokes signal, *left*, remains constant under applied bias. The Anti-Stokes signal of the low wavenumber continuum increases with applied bias. A measurable mode around 1800 cm^{-1} at zero bias shows an elevated effective vibrational temperature, with the intensity increasing after the applied bias exceeds $\hbar\omega_\nu$ of that mode. Note that the color bars for the Stokes and Anti-Stokes signal have different magnitudes. Reprinted with permission from Ref. [268]. ©2011 Nature Nanotechnology.

in the conductance occurs at the constriction. From the measured change of conductance, the temperature rise was inferred using bolometric techniques and assuming Ohm's law, as discussed in [290]. A study of the polarization and incident laser intensity dependence of the inferred temperature rise of the bowtie constriction on various substrates and at various substrate temperatures was conducted. As seen

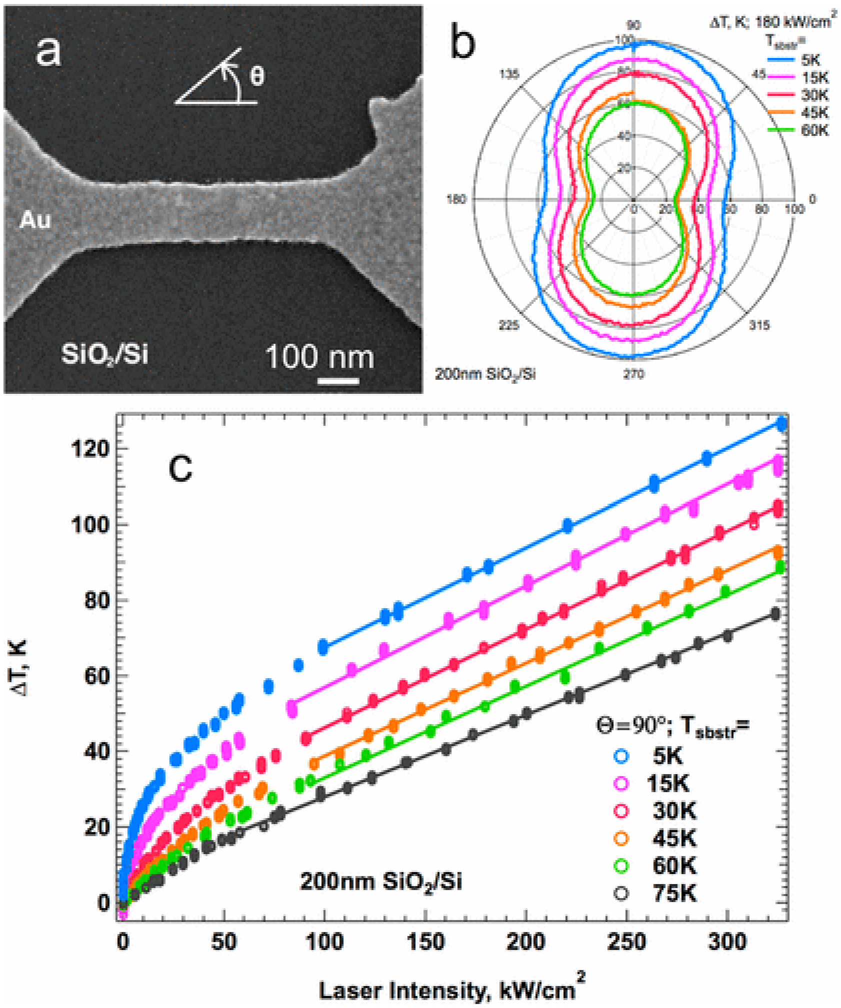

Figure 5.11 : *a*: SEM image of a typical gold bowtie device. *b*: polarization dependence of the temperature rise of the constriction under direct illumination at various substrate temperatures. The maximum heating occurs when the laser is in the transverse polarization, exciting the local surface plasmon resonance in the nanowire. The heating of the wire increases as the substrate temperature decreases. *c*: Intensity dependence of the temperature rise of the constriction under direct illumination at various substrate temperatures. As the substrate temperature increases, the intensity dependence becomes more linear. At lower substrate temperatures, the temperature rise of the constriction's becomes more nonlinear at low intensities, but becomes linear at around 75 kW/cm^2. Reprinted with permission from [292]. ©2016 American Chemical Society.

in Fig. 5.11b, the temperature rise has a strong polarization dependence, with the transverse polarization (perpendicular to the length of the wire) having the largest response. This is indicative of the excitation of the transverse local surface plasmon resonance that couples in with the multipolar "dark" modes that allow for SERS. As the substrate temperature lowers from 60 K to 5 K, the temperature rise of the constriction increases. The inferred temperature rise of the nanowire under transverse laser illumination with a 200 nm SiO_2 substrate of temperature 5 K is around 100 K! As seen in Fig. 3.6, for IETS signal to have well-resolved peaks to see this energy exchange, the local temperature must be at least below 20 K! As with Ref. [290], the measured differential conductance is linear with the substrate temperature for temperatures above 40K. Below 40K, however, the constriction temperature rise (negative differential conductance) increases nonlinearly with substrate temperature, and therefore the temperature rise had to be calculated using curve-fitting routines instead of a simple linear equation as before. Additionally, the intensity dependence, Fig. 5.11c shows the intensity dependence of the constriction temperature rise. When the substrate temperature is 75 K, the relationship between temperature rise and laser intensity is linear. Below 75K, however, the relationship becomes more nonlinear as the intensity decreases. The thermal conductivity of substrates at low temperatures is normally nonmonotonic and nonlinear, and phonon thermal boundary resistance due to the mismatch of the acoustic phonons at low temperatures contributes to these large temperature rises.

One approach to try to reduce this large temperature rise is by using a substrate with better thermal conductivity than 200 nm SiO_2/Si. At 5K, the thermal conductivity of quartz and sapphire is on the order of 10^3 times better than that of Silicon. However, as seen in Fig. 5.12, the temperature rise is only reduced by around a factor

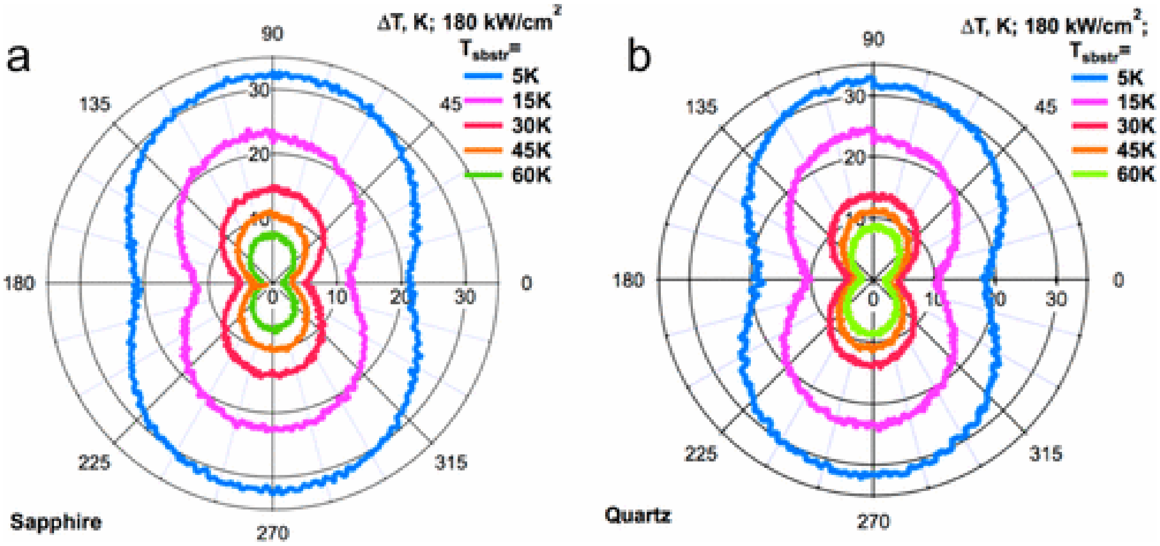

Figure 5.12 : Comparison of local heating of the nanowire constriction due to direct laser illumination using (a) sapphire and (b) quartz substrates. Although the thermal conductivity of these substrates is around a factor of 10^3 better than that of silicon, the temperature rise is only reduced by around a factor of 3. Reprinted with permission from [292].©2016 American Chemical Society

of 3 for both substrates, which suggests that the temperature rise is predominantly determined by the thermal boundary resistance, preventing thermal transport from the nanowire into the substrate.[244] This study indicated that a simple change of substrate could not reduce the local temperature enough to obtain well-resolved IETS peaks. Instead, in Chapter 9 will discuss an alternate approach to reduce the local effective temperature using surface plasmon polaritions to *remotely* excite the nanowire constriction for both SERS and electronic transport measurements in a similar approach as Refs. [81, 211, 214, 286, 287].

5.8 Experimental methods

5.8.1 Gold "bowtie" fabrication process and naming convention

Devices were fabricated on silicon wafers with 200 nm - 2 µm thermally grown oxide. Bonding pads and a common ground were deposited using a shadow mask and electron beam (E-Beam) evaporation. 5 nm Ti/50 nm Au was found to be the optimal metal deposition thickness to reduce complications during wire bonding (see Sec. A.2 for more information). Refer to Sec. A.1 for the number of bonding pads and naming convention.

Prior to electron beam lithography, chips are sonicated in acetone and rinsed in isopropyl alcohol (IPA) and blown dry. Using an in-house Harrick PDC-32 G plasma cleaner, the chip undergoes 2 minutes of O_2 plasma cleaning on the "high" setting. Using single-layer polymethyl methacrylate (PMMA) 495 A4 in Anisole (Microchem) and spinning at 3000 RPM for 40 seconds over the entire chip, the chip is annealed at 180 for 90 seconds. (Tip: the hot plate temperature dial has poor calibration. The hot plate reaches 180 when the hotplate is set to around 215 .) The gold "bowtie" devices are lithographically defined using the JEOL 6500 and Nabity software.

The standard bowties consist of a nanowire, approximately 120 nm wide and 600 nm long sandwiched between two fan-out electrodes that extend out at 45ngles until reaching the width of 10 µm. Then the electrodes extend out with 10 µm thickness until reaching the bonding pad. "Long" bowties consist of a nanowire that is still approximately 120 nm wide but has an extended length, typically 5-10 µm long. In the case of "bowties with gratings", two rectangular slits are also designed in the rectangular electrode design. After lithography, the devices are developed in 3:1 IPA : methyl isobutyl ketone (MIBK) for 40 seconds, rinsed with IPA and blown dry with

N_2, and undergo O_2 plasma cleaning on "low" for 5 seconds prior to electron beam evaporation in the Edwards FL 400. During evaporation, 1 nm of Ti (Cr if specially noted) is deposited as an adhesion layer and between 15-30 nm of Au is deposited afterward, at an average rate of 1 Å/s. The sample is then soaked in acetone for "lift off" before being sonicated, rinsed in IPA, and blown dry.

Throughout this work, different terminologies are used to delineate the various styles of bowtie devices. Unless otherwise specified, the term *standard bowtie* is the typical bowtie configuration described above (with the nanowire of dimensions 120 nm wide, 600 nm long) made with 15 nm Au/1 nm Ti on a silicon wafer with 200 nm thermally grown oxide. The term *long bowtie* indicates the same conditions of the standard bowtie device but with an extended nanowire length. The term *bowtie with gratings* has the same conditions as the standard bowtie configuration but with 2 rectangular holes (8 µm length, 300 nm width spaced 0.5 µm apart) in the electrode design and with 30 nm Au/1 nm Ti on 2 µm thermally grown oxide.

The chip is then mounted to the chip carrier, as discussed in Sec. A.1, using N grease before being wire bonded with 25 µm gold wires. In the case of optical measurements at low temperatures (<70 K), the chip must be elevated on the chip carrier using a piece of copper between 1-2 mm thick to account for the reduced range of motion of the piezo controlled stage.

5.8.2 Home built Raman microscope

A home-built Raman microscope with a raster-scanning laser was used for this measurement, illustrated in Fig. 5.13. Since 2018, the Toptica iBeam Smart WS 785 nm free space wavelength continuous wavelength, turn-key diode laser in the TEM 00 mode was used. Prior to this, the Ondax SureLock RO 785 nm laser was used. The laser is isolated using an external optical isolator which the beam is steered into using two mirrors. I recommend that the isolator be upgraded as the opening to the isolator is on the order of the laser spot size which results in some diffraction. After the isolator, the OptiGrate BragGrate$^{\text{TM}}$ Spatial Filter (BSF) is sometimes used to clean the beam mode for ultra low wavenumber Raman measurements. The Bragg style grating in the BSF diverts wavelengths not at the specified 785 nm wavelength and reflects cleaned beam completely and the position is adjusted through the incident angle. However, due to the BSF extreme sensitivity to wavelength, the positional stability of the laser position was not within tolerance of the pinhole placement between power cycles. In order to extend the laser lifetime, the BSF is removed when such measurements are not required so that the laser can be turned off during off-experiment hours without needing to adjust the pinhole placement. After 2018, these were just completely removed as the pinhole is sufficient as the BSF is more appropriate for paths where a pinhole isn't feasible (high intensity pulsed lasers, for example). After the BSF and/or mirror, an attenuator wheel that can be controlled using the NI DAQ is placed along with an optical chopper before being steered with another mirror. An 100 µm optical pinhole in a beam expander configuration cleans the beam mode. The laser is then placed through a polarizer and a controllable angle $\lambda/2$ waveplate is placed. The laser is then steered by two mirrors and reflects off a notch filter to allow for the incident and exiting beam from the sample to travel the same path. The notch filters used to reduce the Rayleigh peak from Raman measurements were OptiGrate's BragGrate$^{\text{TM}}$ Notch Filters. Like the BSF, these filters are particularly sensitive in positional placement. The notch filters are aligned in the same way, except this time, only the light that is *not* 785 nm is allowed to pass through the notch filter without affecting its path. After reflecting off the notch filter, the laser passes through a final beam expander, this time the first lens is controlled using Newport's NPC3SG 3 channel, closed loop, piezo nanopositioner controller. The laser is then steered through a cage system before being focused by a 50x (NA=0.7) objective lens down through the low working distance optical window of the cryostation. The laser is focused on the chip by adjusting the chip height using piezo controlled stage movement. The laser then reflects off the silicon chip, and travels back through the same beam expander as before, but this time, scattered light not at 785 nm is not reflected by the notch filter. Instead, the laser will continue through an additional two notch filters and into the Horiba Jobin Yvon iHR 320 spectrometer with Synapse CCD. A removable beam splitter is placed between the cage and the final beam expander to allow for white light illumination and imaging via a CCD camera. The spot size of the laser is approximately 1.8 µm full width half maximum and is around 20 mW incident intensity without additional attenuation. All measurements are under high vacuum ($< 10^{-7}$ bar).

5.8.3 Motion control using the piezo controlled lens

Just a quick note regarding motion control of the NPC3SG piezo controller. The LabVIEW software that came with the controller doesn't actually allow read/write permissions. I did some extensive debugging by communicating with the device in a terminal and found that there's an error with the flow control via USB communication in general. To bypass this unreliable USB software connection, I bypassed the USB entirely by using analog control by sending voltages to the piezo controller directly to the back panel via the NI DAQ and then reading the voltages in via the DAQ once again. In order to use the Python software I wrote, discussed in Chapter A, LabVIEW MUST be installed to properly connect to the DAQ. Motion control using

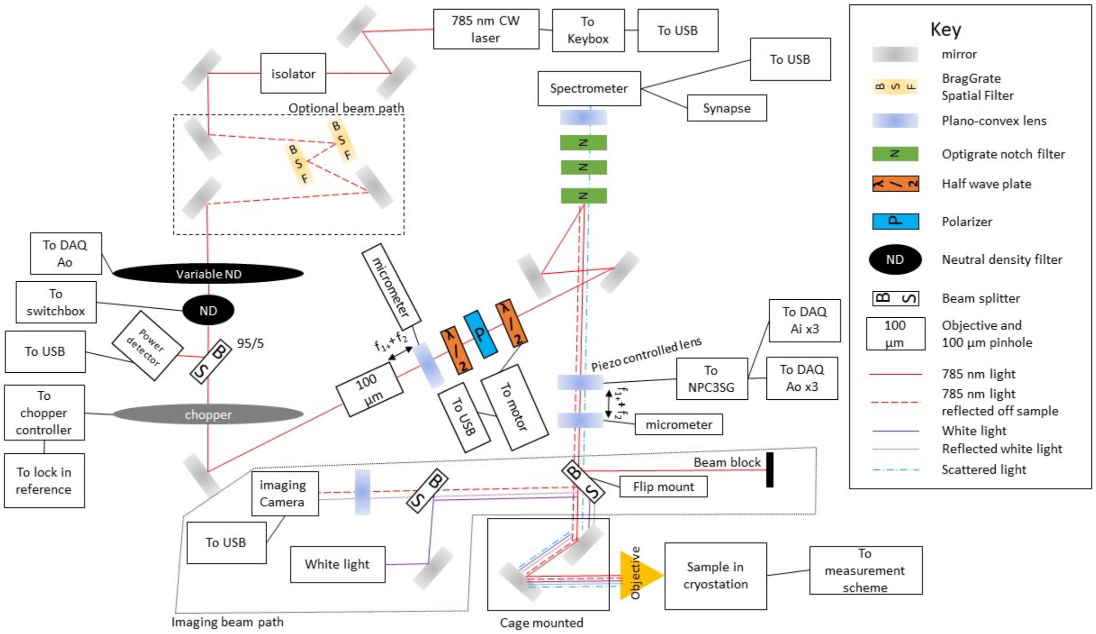

Figure 5.13 : Schematic of the homemade Raman microscope alignment

the sample stage isn't nearly as stable or retraceable as using the piezo controlled lens and is not recommended.

5.8.4 Photothermoelectric effect measurement methods

An optical chopper is used to modulate the light intensity of a frequency around 367 Hz, which is much slower than the thermalization time scale of the devices.[81, 210] The integrated, steady-state voltage at each end of the device was probed using the SR560 voltage amplifier (100 MΩ input impedance) with the potential difference between the two ends being measured as the input of a SR7270 lock-in amplifier while under high vacuum. Unless otherwise specified, the measurements were conducted at room temperature. The schematic of the measurement setup is seen in Fig. 5.14. In devices electromigrated to very large resistances (∼ 100MΩ), the capacitive phase shifts could be sufficiently large during lock-in detection. In these cases, the photovoltages were instead detected via DC measurements using the NI DAQ instead of the lock-in amplifier (and without optical chopping).

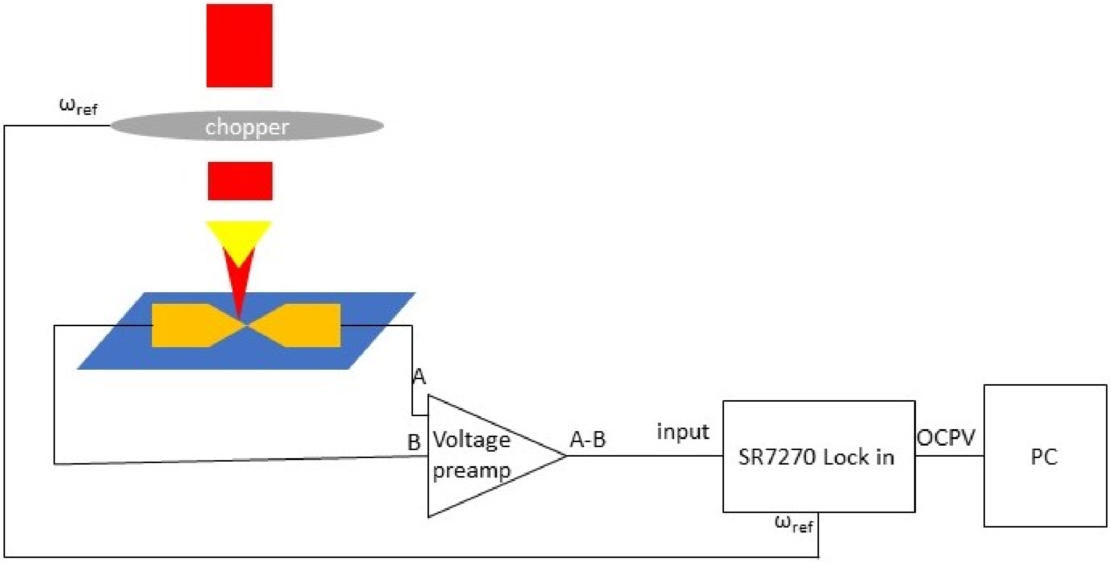

Figure 5.14 : Schematic of the photothermoelectric effect measurement

5.8.5 Photocurrent "heating" measurement methods

An optical chopper is used to modulate the light intensity of a frequency around 367 Hz, which is much slower than the thermalization time scale of the devices.[81, 210] Two lock-in amplifiers are used for this measurement. The first applies a small AC voltage to measure the first and second harmonic response of this applied AC bias for IETS measurements. The second lock-in amplifier is set to measure the steady-state amplified current as a response of the chopped laser illumination. During the measurements discussed in Chapter 9, a DC bias of 5 mV is applied across the device. A schematic of the measurement setup is seen in Fig. 5.15

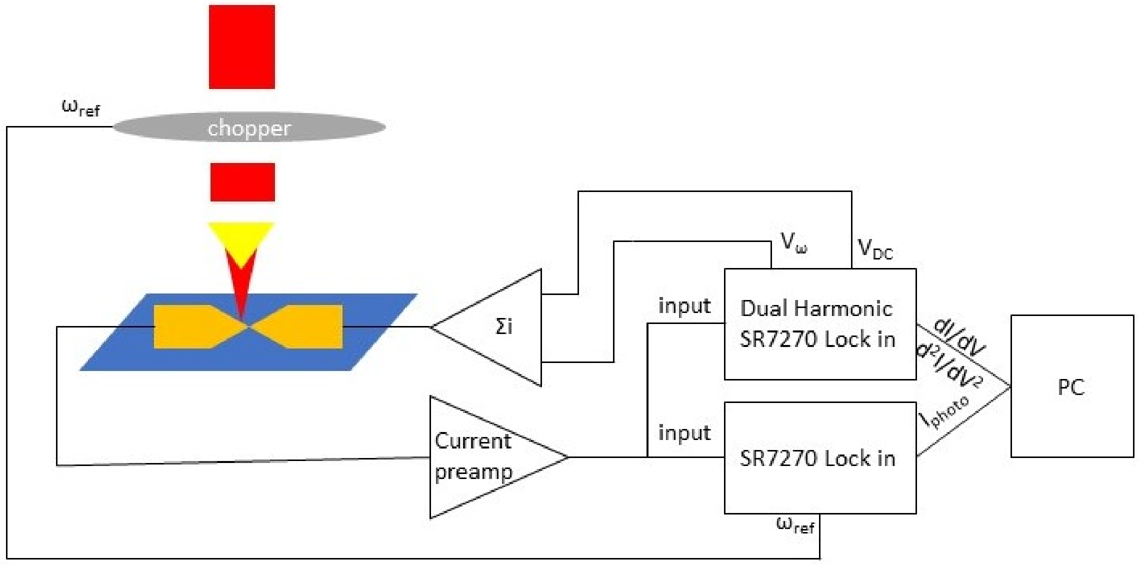

Figure 5.15 : Schematic of the photocurrent measurement

Chapter 6

Thermoelectric effects in intact polycrystalline gold nanowires

6.1 Motivation: Creating single metal thermocouples via nanostructuring

As discussed in Section 2.2.1, the electronic component of the S in metals depends on σ. σ can be manipulated locally in nanoscale devices via changes in the geometric structure. This means that nanostructuring the devices can result in local control of S, resulting in single metal thermocouples. In the work done by Sun, W. *et al.* [82], single metal thin film devices consisting of two parallel wires of different widths with large bonding pads on one side and a connecting joint on the other were measured, as sketched in Fig. 6.1. The bonding pads were kept at the substrate temperature and the junction of the two wires were heated using a resistive heater. As the heater temperature increased, the open circuit voltage (OCV) measured linearly increased. A series of devices were tested; the larger wire width was kept at a constant 100 µm but the more narrow wire's dimension varied between 3-50 µm (much larger than the electronic mean free path). As the more narrow wire's width decreased, the slope of the OCV vs. heater temperature increased. This was experimentally demonstrative that locally changing σ via nanostructuring can result in single metal thermocouples.

However, because the geometric changes were still much larger than the electronic mean free path and because the static placement of the heater was relatively close to

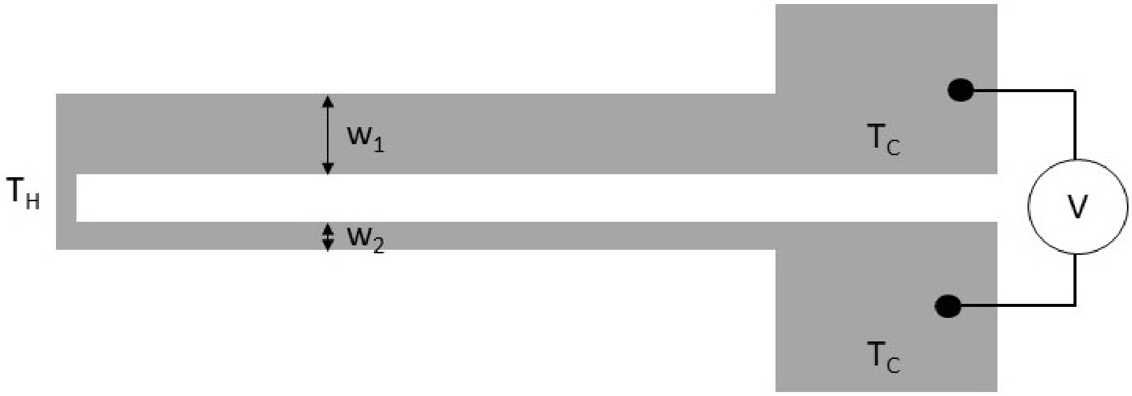

Figure 6.1 : Sketch of single metal thermocouple measured by Sun, W. *et al.*: A thin film single metal thermocouple consisting two parallel wires of different widths, w_1 and w_2, are in contact with each other at one end. The OCV is probed between the two free ends kept at the cold substrate temperature, T_C, while the joined end is heated with a resistive heater to temperature T_H. Figure adapted with permission from Ref. [82]. ©2011, American Institute of Physics.

the bonding pads, there was some debate of the source of the signal. A comment from Notre Dame [83] raised concern that rather than the signal occurring from the width dependence of the wires, the response was actually from asymmetric thermal transport that unequally heated the bonding pads resulting in stray OCV from parasitic leads. Sun, W. [310] responded to the comment dismissing these claims.

Because the ongoing nature of this conversation, we decided to see for ourselves if we could detect OCV signal in our gold bowtie devices. Our particular set up had some inherent differences from the previous measurements that would be beneficial to advancing the conversation forward: our bowtie devices were symmetric, the geometry change was significantly farther away from the probing ends eliminating the potential for asymmetric heating of the leads, and our well-focused laser beam which would serve our heating source could be raster-scanned providing position-dependent measurements of the open circuit photovoltage (OCPV) in the photothermoelectric effect (PTE).

6.2 The experiment: Position-dependent photothermoelectric voltages of a uniform nanowire as a function of laser position

From Section 2.2.2, how nanostructuring can allow for single metal thermocouples was discussed. Changing the geometry of a nanoscale device can change the local boundary scattering, therefore changing the local Seebeck coefficient. Because the gold "bowtie" devices consist of a nanowire between two fan out electrodes, there should be a measurable signal when the interface of the fan-out electrode and the nanowire is illuminated. Illuminating the other side of the nanowire should result in a voltage of the same magnitude, but of the opposite sign. In this section, the surprising results of this simple experiment of gold bowtie devices with an extended length nanowire will be discussed. This closely follows Reference [90].

6.2.1 Experimental details

A schematic of the experimental setup is seen in Fig. 6.2b. The steady-state, integrated open circuit photovoltage of the device was measured as a function of a 785 nm CW laser position, whose position was moved by a piezo controlled lens. The laser illumination was modulated using an optical chopper, whose frequency was the input reference for the lock-in amplifier. The open circuit voltage was measured as the difference in potential between the two ends of the device and was amplified by a voltage amplifier prior to lock-in amplifier detection. Details of the measurement scheme is detailed further in Section 5.8.4. The measurements of the gold bowtie devices were conducted at room temperature under high vacuum within the closed cycle optical cryostat. The fabrication technique to create the bowties described in this section is detailed in Section 5.8.1. Both standard and long bowties were studied.

6.3 Results: Substantial local variation of the local Seebeck coefficient in polycrystalline nanowires

6.3.1 Standard “bowtie” device: maximum signal at the interface of the nanowire and electrode design

Initially, the standard ”bowtie” devices with a nanowire with a length around 600 nm were measured, Fig. 6.2a. The steady-state, integrated open circuit photovoltage of the device was measured as a function of laser position, which was raster scanned around the nanowire and fan-out electrodes. The map of this measurement is seen in Fig. 6.2c. As expected, shining the laser at the interface of the fan-out electrode and the nanowire resulted in a change of photovoltage, because at that location, the electronic mean free path changes due to the change in nanostructuring. Shining the laser on the opposite end of the the nanowire shows a similar magnitude of photovoltage, but of the opposite polarity, indicating that this is due to the change in local Seebeck coefficient. To better highlight these observations, a scatter plot of the PTE voltage along the length of the wire is seen in Fig. 6.2d. Regardless of the polarization, the PTE signal when the laser is illuminating either interface of the nanowire and fan-out electrode results in photovoltages of roughly the same magnitude, but of opposite polarity. The transverse polarization (perpendicular to the nanowire) results in a slightly more elevated signal, likely because of the resonant local surface plasmon within the nanowire.

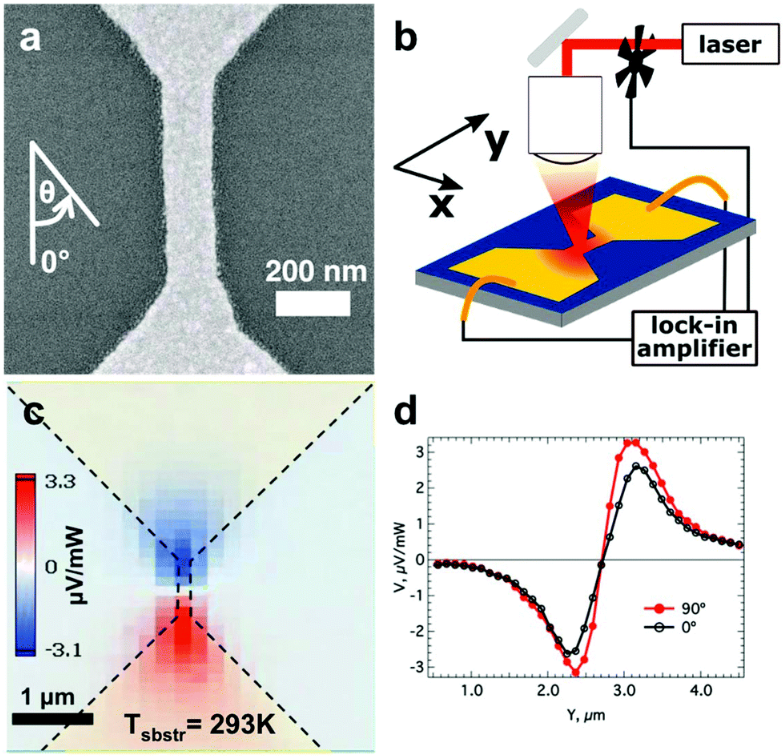

Figure 6.2 : Photothermoelectric measurements of a standard gold bowtie device. *a*: an SEM image of a standard device, *b*: schematic of the measurement setup. *c*: 2D PTE map of the standard gold bowtie device. *d*: Scatter plot of *c*, showing the PTE signal along the length of the device. The black line shows PTE signal when the laser is in the longitudinal polarization (along the length of the nanowire), whereas the red line indicates the transverse polarization (perpendicular to the nanowire). Reprinted with permission from [90]. ©2017 Nanoscale.

6.3.2 Extended "bowtie" device: surprising local variation of the photovoltage response with length scales smaller than the laser spot size

Because the length of the wire is only 600 nm, whereas the laser spot size is around 1.8μm, the signal could not be completely resolved to be only as an effect of heating the interface of the fan-out electrodes and the nanowire. In order to resolve this effect, the length of the nanowire was extended from 600 nm to 10 μm. It was expected that

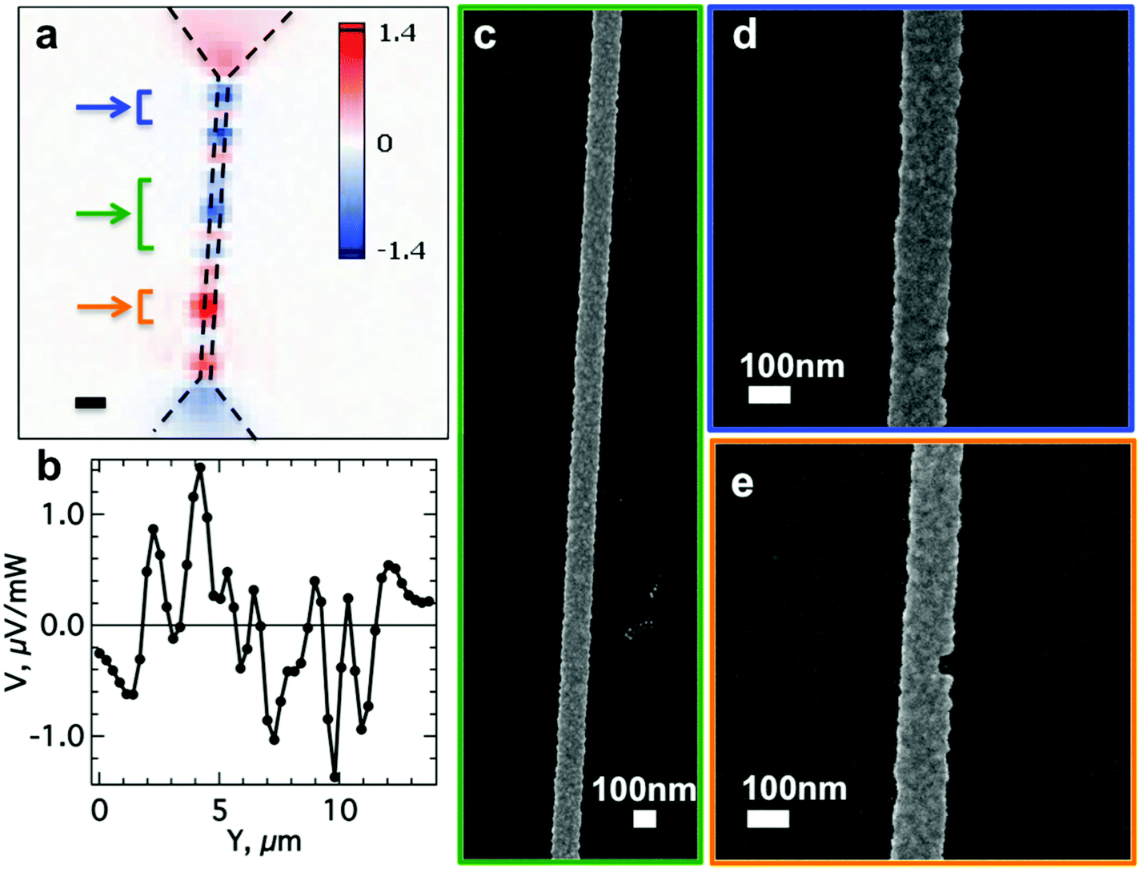

Figure 6.3 : Photothermoelectric measurements of an extended gold bowtie device. *a*: 2D PTE map of a bowtie device with a 10 μm long nanowire. The scale bar shows 1 μm. The units of the colormap is μV/mW. *b*: Scatter plot of the PTE signal along the length of the device. *c*-*e*: SEM images along the length of the device. The displayed area is highlighted by brackets in *a* that are the same color as the boxed outline. Reprinted with permission from [90]. ©2017 Nanoscale.

the features in Fig. 6.2c would simply spread out; traditional theory of nanostructured single metal thermocouples consider devices of uniform width and thickness to have a constant Seebeck coefficient. Therefore, the PTE signal along the length of the extended nanowire should be completely featureless. Instead, the PTE map showed surprising local variations along the length of the wire, Fig. 6.3a. The PTE signal not only varied in magnitude but also in polarity. As seen in Fig. 6.3b, these changes were observed within the spot size of the laser! In some cases, the variation in signal could be explained by a defect in the wire, as seen in Fig. 6.3e, but for the most part, there was no obvious explanation to the inhomogeneity of the photovoltage response due to SEM images alone, Figs. 6.3c,d. This spatial variation of the photovoltage is not specific only to gold, bowties made of Ni and Au/Pd showed similar results, Fig. 6.4. Bulk Ni has a Seebeck coefficient of -20 μV/K (compared to 6.5 μV/K of gold), resulting in larger photovoltages. The AuPd with Ti adhesion layer has an anomalously low photovoltage signal compared to the room temperature Seebeck coefficient of AuPd of approximately -35 μV/K, which can possibly be because the AuPd alloyed with the Ti.

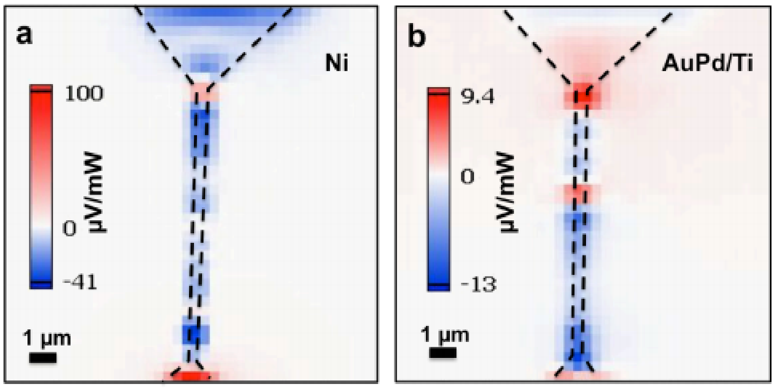

Figure 6.4 : Photothermoelectric measurements of an extended bowtie devices made of Ni (a) and AuPd with Ti adhesion layer (b) which shows that this spatial variation of the photovoltage is not unique to only gold films. Reprinted with permission from [90]. ©2017 Nanoscale.

6.3.3 Annealing the device yields changes in the variation in photovoltage response

The variation in the extended bowties was consistently seen, but the specific pattern was unique to each device. Comparing the pattern before and after annealing could probe the dependence of the pattern to the local grain structure. Fig. 6.5a shows a 5 µm device prior to annealing. Afterward, the device was current annealed by running a current through the nanowire while monitoring the resistance to avoid electromigration. After the resistance dropped by around 2%, the measurement was repeated, Fig. 6.5b. The magnitude of the PTE signal was reduced by roughly a factor of 5. Current annealing can have some undesirable consequences, such as physically moving gold atoms through electromigration, so another device was measured by annealing on a hotplate. Fig. 6.5c shows a 10 µm long device prior to annealing, and Fig. 6.5d shows the same device after annealing on a hotplate at 200 °C for 3 hours under an Ar atmosphere. Once again, the variation in the photovoltage response changed. This time, while the signal near the interface of the fan-out electrodes and the nanowire constriction stays roughly the same magnitude, the magnitude of the signal along the nanowire decreases and overall pattern of the spatial variation changes. The change of pattern and magnitude indicates that the variation in photovoltage is sensitive to the crystalline structure of the device.

6.3.4 Small perturbations in Seebeck coefficient can result in similar spatial variations of the photovoltage signal

The spatial variation of the photovoltages observed along the length of the wire could be explained by local perturbations of the Seebeck coefficient. By varying the local Seebeck coefficient, Fig. 6.6a, and assuming a Gaussian heating source, the resulting

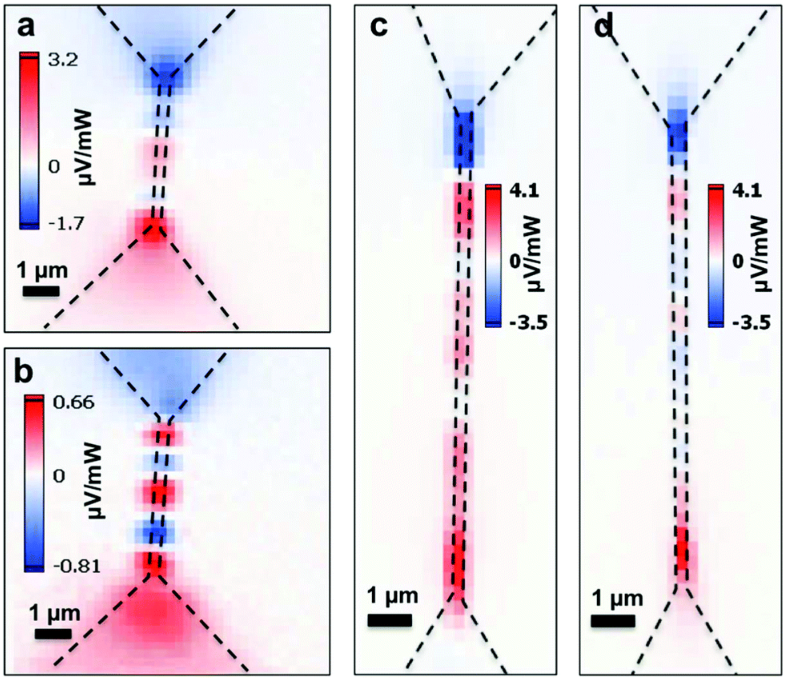

Figure 6.5 : Photothermoelectric measurements of extended gold bowtie devices before and after annealing *a*: 2D PTE map of a bowtie device with a 5 µm long nanowire prior to annealing. *b*: PTE map of the same device in *a* after current annealing. *c*: PTE map of a bowtie device with a 10 µm long nanowire prior to annealing. *d*: PTE map of the same device in *d* after annealing at 200 °C for 3 hours in Ar. Reprinted with permission from [90]. ©2017 Nanoscale.

calculated voltages, 6.6b, could be compared to the measured values to determine the change of Seebeck coefficient required to observe the spatial variation of the photovoltages. As seen from the calculation, the change of the Seebeck coefficient due to the interface of the nanowire and the electrodes (around offset = -5 and 5 µm) results in a change in voltage of opposite polarity, but of the same magnitude. Perturbing the Seebeck coefficient somewhere in the middle by a few percent yields changes in the spatial variation of the photovoltages seen in experiment. Using such a toy model, the Seebeck coefficient needs to change on the order of 10% to reach magnitudes observed in experiment.

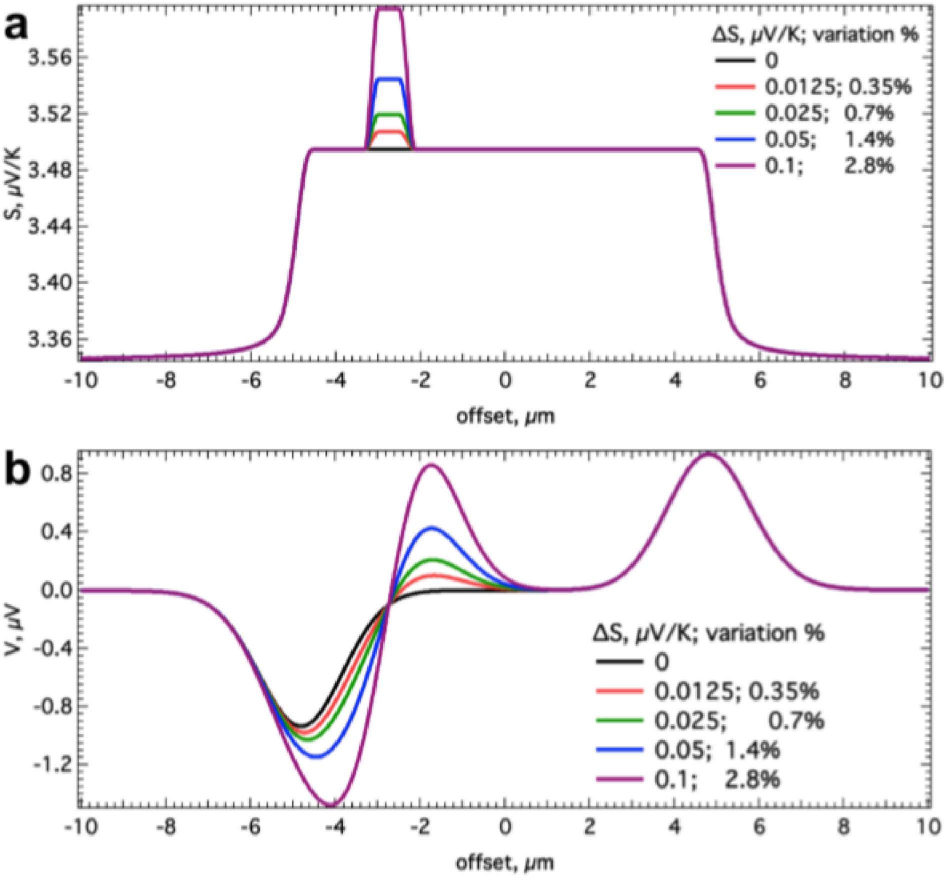

Figure 6.6 : COMSOL simulation perturbing the local Seebeck coefficient. *a*: The local Seebeck coefficient is perturbed along the length of the device. *b*: The photovoltage calculated from the variation in Seebeck coefficient in *a*. Reprinted with permission from [90]. ©2017 Nanoscale.

6.4 Discussion and Conclusions: Does grain structure have a significant effect on the Seebeck coefficient?

In this chapter, the PTE signal of intact gold "bowtie" devices as a function of laser position was discussed. Standard bowties resulted in signal that follows traditional theory of nanostructured single metal thermocouples: local changes in geometry change the local electrical conductivity, and therefore result in a local change in Seebeck coefficient. Heating the interface of the two different widths results in an open circuit voltage. In an effort to better resolve the effect at the width changes, the nanowire was extended to be much longer than the laser spot size. Instead of being featureless long the length of the wire, as expected for a nanowire of uniform width and thickness, the photovoltage varied in magnitude and polarity along the nanowire with length scales smaller than the laser spot size. Annealing the devices caused a change in the overall pattern. Because the pattern varied from device-to-device and and changed after annealing, a natural candidate to consider for this variation is a change in Seebeck coefficient due to crystallographic orientation or grain boundaries. The electronic portion of the Seebeck coefficient depends on the energy dependence of the electrical conductivity; grain boundaries and defects in crystalline structures can affect the diffusive electronic transport through the material and the specifics of these structures can change with annealing.[32, 55, 66] Additionally, the Fermi energy change across grain boundaries can be abrupt, which can additionally contribute to the local Seebeck coefficient.[311, 312] Finally, this work indicates that although nanostructuring can result in single metal thermocouples, local details of the Seebeck coefficient due to intrinsic changes within the wire which would otherwise be difficult to detect should be considered, particularly in devices with large Seebeck coefficients and in devices with large device-to-device variation.

6.5 Surface modification of gold bowtie devices shows promise of tuning thermoelectric response

In thin films, the bulk electron mean free path can be comparable to the film thickness, resulting in surface scattering and therefore reducing the electron mean free path on the order of the film thickness. As such, surface conditions can have an effect of the thermoelectric properties of the material. In Refs. [90] and [313], the thermoelectric response due to different surface conditions were studied. First, in Ref. [90], the effect of using a self-assembled monolayer on an extended bowtie device was observed. Then, in both Refs. [90] and [313], the decomposition of gold oxide from oxygen plasma cleaning was detected. Here, we will briefly discuss both of these findings as future work will likely focus on the importance of surface modification for tuning the thermoelectric response.

6.5.1 Surface modification using self-assembled monolayers

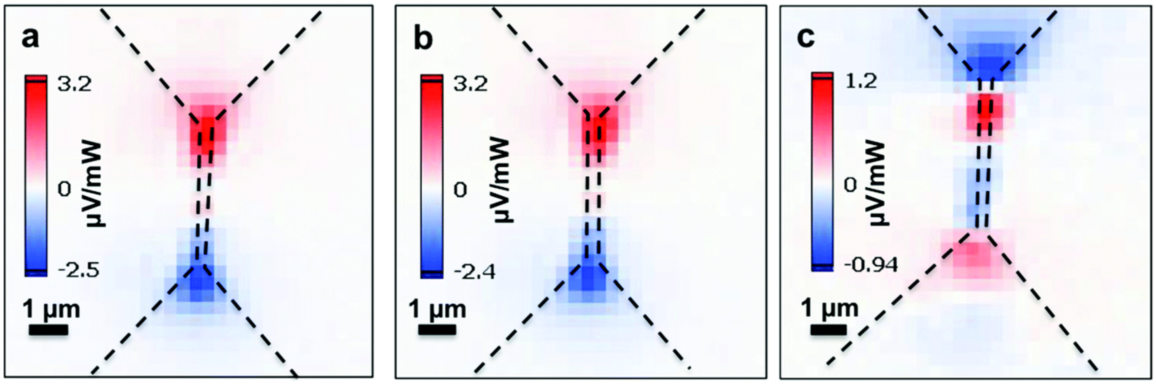

Figure 6.7 : *a, b*: 2D photothermoelectric maps of gold bowtie devices with benzyl mercaptan SAM before and after annealing, respectively. The photovoltage signal does not change with annealing. *c*: 2D photothermoelectric map of the same device after the SAM is removed, changing the pattern and magnitude of the photovoltages. These measurements were taking at 5K. Reprinted with permission from [90]. ©2017 Nanoscale.

The photothermoelectric properties of the gold bowtie devices can be affected by adding a self-assembled monolayer (SAM) on the device. Adding a SAM to gold can tune the work function[314, 315], affecting the Fermi energy and the Seebeck coefficient.[316, 317] Fig. 6.7 shows the photothermoelectric maps of devices with benzyl mercaptan SAM. The photovoltage pattern of the device with the SAM does not change before and after annealing, Fig. 6.7a,b. Once the SAM is removed using dilute $NaBH_4$, the magnitude and the pattern of the detected voltages change significantly, Fig. 6.7c.

6.5.2 Detecting the decomposition of gold oxide using the photothermoelectric effect

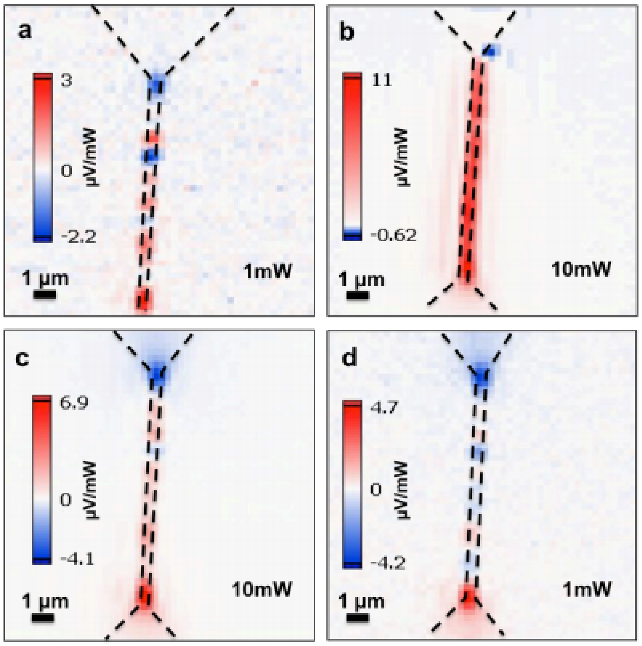

Figure 6.8 : *a*: 2D photovoltage map of a bowtie device after O_2 plasma clean under 1 mW laser illumination. *b*: photovoltage map of the same device in *a* in a subsequent scan under 10 mW laser illumination. *c, d*: Additional scans after *b* under 10 mW and 1 mW laser illumination, respectively. Reprinted with permission from [90]. ©2017 Nanoscale.

Prior to measurement, the devices are cleaned using oxygen plasma treatment. The initial photothermoelectric effect scan of long bowtie devices were different than any subsequent scans. Instead of having spatial variation of changing magnitudes and polarities along the length of the device, the initial photovoltage scan showed something completely different, Figs. 6.8b and 6.9. These initial scans show a nearly constant photovoltage along the length of the device, with a constant polarity. Subsequent scans show the spatial variation as discussed before, Figs. 6.8c,d and the second column of Fig. 6.9. Treating the same device with oxygen plasma again results in the similar first-scan measurements. Both Refs. [90] and [313] attribute this signal due to the photodecomposition of the unstable gold oxide layer that is deposited during the oxygen plasma cleaning process. Supporting this is the observation that the polarity of the photovoltage of the first scan is determined by the scanning direction, affecting the direction of the photodecomposition, Fig. 6.9. Subsequent scans are identical regardless of scan direction.

Both results discussed in this section provide evidence that the photothermoelectric effect can be affected by the surface conditions of nanostructured devices. Further studies are currently underway to explore these effects in more detail.

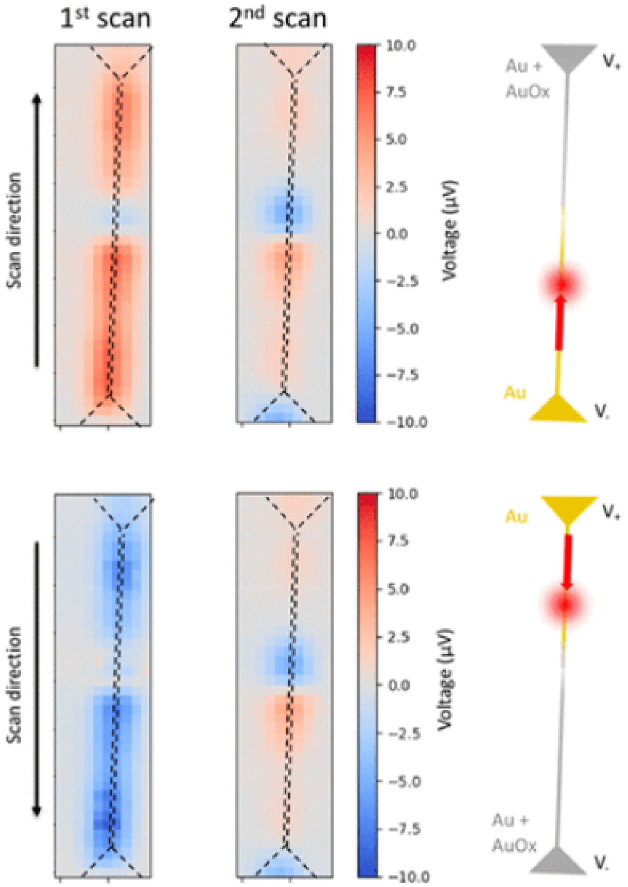

Figure 6.9 : *top row*: *1st scan*: Initial photovoltage measurement after O_2 plasma cleaning. *2nd scan*: Subsequent scan, showing that the spatial variation returns to normal. *schematic*: Schematic showing the direction of the Au/AuO_x photodecomposition during the laser scan. *bottom row*: Same measurements as before, but with the opposite scanning direction. The photovoltage of the first scan after O_2 plasma cleaning results in a photovoltage of the opposite polarity, but the subsequent scan is the same regardless of scanning direction. Reprinted with permission from [313]. ©2018 American Chemical Society.

Chapter 7

Photothermoelectric detection of local strain variations and defects in gold single-crystal and bicrystal stripes

7.1 Motivation: Determine the importance of grain structure in the Seebeck coefficient

The surprising local variation in the Seebeck coefficient in polycrystalline nanowires of uniform width and thickness discussed in Ch. 6 changed in pattern and magnitude after annealing. Ref. [90] discussed a natural candidate for this local variation: that individual grains have their own unique Seebeck coefficients. The Fermi surface of gold, seen in Fig. 2.7, has necks that extend to the Brillouin zone, which can result in abrupt changes in the Fermi energy at grain boundaries. The electronic component of the Seebeck coefficient described by the Mott-Jones equation, Equation 2.8, is determined by the energy dependence of the electrical conductance which is a function of the electron mean free path and the Fermi area. Simplifying the study to single crystalline nanowires and devices consisting of two single crystals in contact with each other at an individual grain boundary henceforth called a “bicrystal” can elucidate the importance of grain structure of the Seebeck coefficient.

Refs. [319] and [318] describe methods to fabricate long single- and bi-crystal microscale wires on silicon chips using a high temperature annealing process. The process of the bicrystal growth is described in further detail in Fig. 7.1, although the

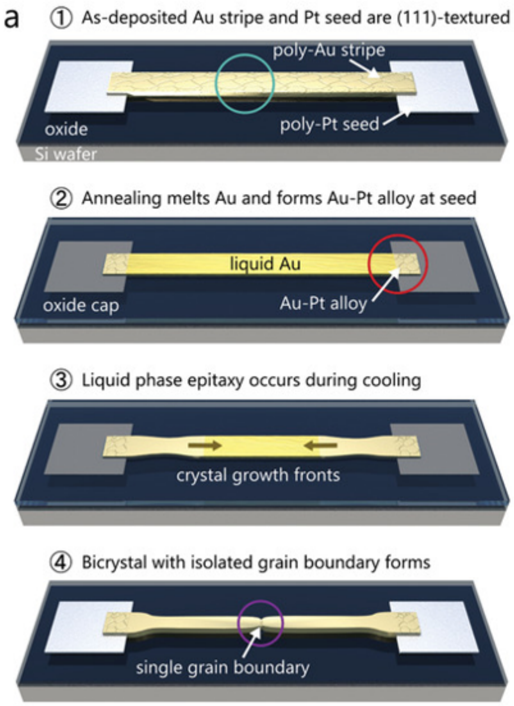

Figure 7.1 : Schematic of the bicrystal fabrication process. *1*: A polycrystalline gold stripe is deposited using electron beam evaporation overlapping pre-deposited platinum seeds on either side evaporated on a silicon chip. *2*: A silicon dioxide cap is deposited over the entire chip, serving as a crucible. The temperature of the entire chip is then ramped up, heating the chip to just above the melting point of the gold, but below the melting point of the platinum-gold alloy. *3*: The chip is then cooled, with the platinum seed serving as the driving mechanism of crystallization. The gold crystallizes in the $\langle 111 \rangle$ direction in the z-axis as it cools. *4*: An individual grain boundary forms in the middle of the device. Single crystals are similarly fabricated using only one platinum seed. Reprinted with permission from [318]. ©2019 Advanced Materials.

process for the single crystalline growth is similar. A study of the photothermoelectric signal in single and bicrystal devices can demonstrate the effects of crystalline structure on the Seebeck coefficient. If the crystollographic orientation affects the Seebeck coefficient, individual grain boundaries will behave as a thermocouple in that heating the individual grain will result in a maximum in open circuit photovoltage magnitude.

Additionally, the photovoltage signal should be relatively featureless along the length of a single crystalline wire. Comparison of the photothermoelectric measurements to that of electron backscatter diffraction (EBSD) measurements which can probe the crystallographic orientations of the wires can provide a way to correlate photovoltage measurements to the grain structure in the wires. The next two chapters will discuss the surprising sensitivity of the photothermoelectric effect to both local variations of strain and platinum concentration which provides a larger contribution to the Seebeck coefficient than differences in crystallographic orientations. The work in this chapter is pending publication at the time this thesis was written.

7.2 The experiment: Compare photovoltage measurements to electron backscatter diffraction measurements to determine a correlation between the Seebeck coefficient and grain structure

The devices discussed in this chapter are the single- and bi-crystal wires on 200 nm SiO_2/Si substrates described in Refs. [319] and [318], respectively. The wires are then milled to a uniform width $\sim$ 600 nm before contact pads for wire bonding are deposited. In this chapter, the platinum seeds are sufficiently far ($\sim$ 100 µm) from the portion of the wire being measured to prevent platinum diffusion into the wire. An example of a single crystalline wire is seen in Fig. 7.2b.

Electron back-scatter diffraction (EBSD) is a technique used to probe the crystallographic information about a sample. When an electron beam interacts with the tilted sample, the electrons are diffracted. These diffracted electrons are then imaged by a detector and the pattern of the diffracted electrons can be used to characterize the crystallographic details of the sample.[320] EBSD measurements demonstrate that the device shown in Fig. 7.2b is single crystalline, Fig. 7.2c. The z-axis shows a ⟨111⟩ crystalline orientation which was observed in the previous works.[318, 319] The same photothermoelectric mapping techniques discussed in Ref. [90] was used and is depicted in Fig. 7.2a.

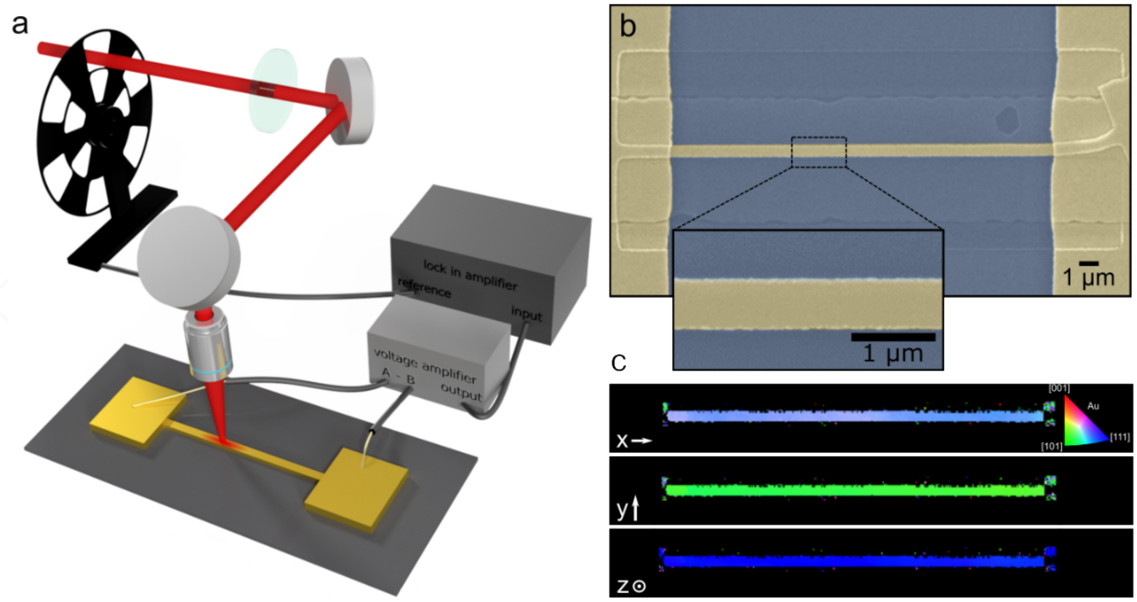

Figure 7.2 : *a*: Schematic of the experimental setup. *b*: False-colored SEM image of the single crystalline wire, with a zoomed-in image of the wire on the inset. There are no discernible features along the length of the wire. *c*: Electron back-scatter diffraction image of the device shown in *b* which demonstrates that the device is single crystalline. The z-axis is in the ⟨111⟩ orientation.

EBSD not only probes the crystalline orientation but also probes variations in strain and local defects. Using cross-correlation techniques, relative local stresses can be detected although determining the absolute strain can be challenging.[321, 322] Even minor misalignments in the microscope can cause large, nonphysical “phantom” strains to be detected.[323] Although measuring the absolute strain using EBSD is nearly impossible without a strain-free reference, EBSD serves as a powerful tool to detect misorientations of the crystal along the length of the wire.[324] Using the reference orientation deviation (ROD) approach,[325], the local deviation of an individual point in a crystal from the average orientation of the grain is used as a metric to probe the local strain distribution within the wire.[324] An advantage to this approach is that each grain is analyzed individually, so grain boundaries and an anomalously strained grain does not affect the local misorientation distributions of other grains.

7.3 Results: Grain boundaries do not behave as thermocouples, but the Seebeck coefficient is sensitive to crystallographic misorientation

7.3.1 Spatial variation of OCPV along a single crystal is correlated to the local crystallographic misorientation

If the spatial variation of the OCPV observed in the polycrstalline wires in Ref. [90] was due to grain-to-grain differences in the Seebeck coefficient, the OCPV signal of a single crystalline wire should be relatively featureless. As seen in the top panel of Fig. 7.3a, the OCPV map of the device in Fig. 7.2b shows variation of signal along the length of the wire. Although the OCPV does not change signs as observed previously[90], the magnitude of the signal varies along the length of the wire with length scales on the order of the laser spot size. As seen in Fig. 7.2b, the wire is of uniform width and thickness with no discernible topological features that would cause changes to the local Seebeck coefficient. This variation in the OCPV maps was observed in the 55 single crystals measured. The top panel of Fig. 7.3b shows the OCPV of another single crystal device showing similar variation. The magnitude of this variation is ∼10 nV/mW. ROD analysis for the single crystal devices

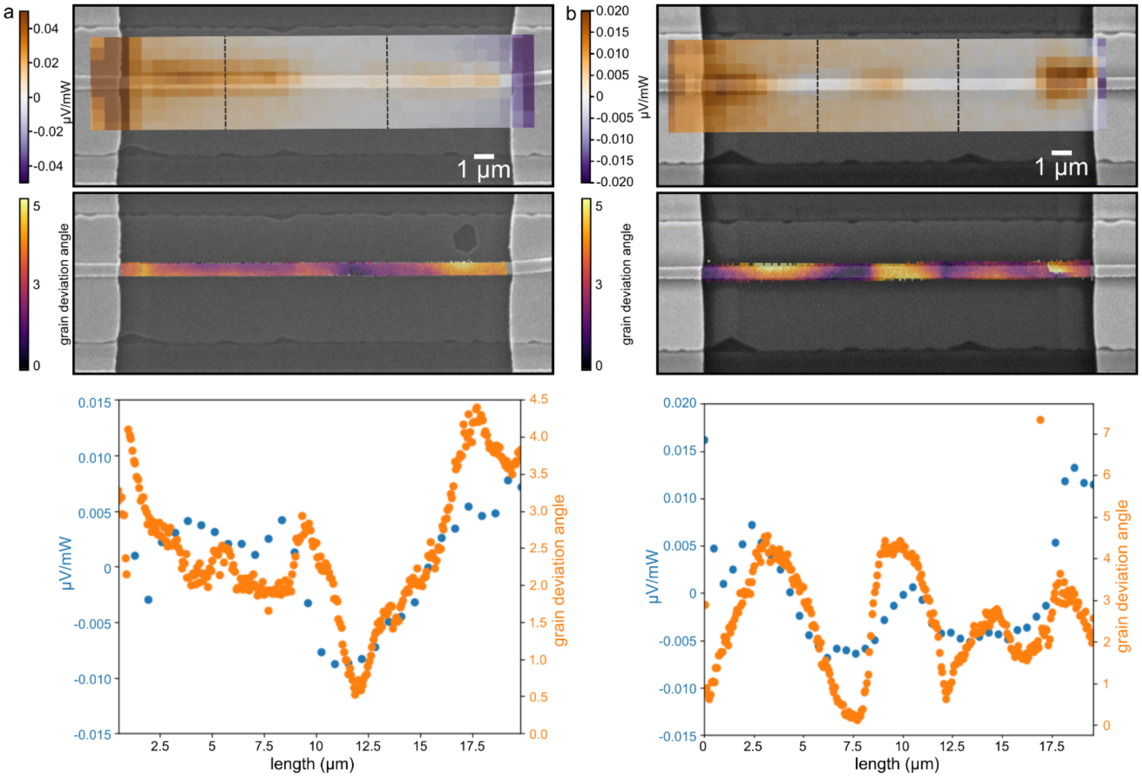

Figure 7.3 : Comparison of OCPV and EBSD measurements for *a* the device shown in Fig. 7.2b and *b* of another single crystalline device. *top panel*: OCPV maps of the single crystals show spatial variations on the order of the laser spot size. *middle panel*: ROD maps showing the local misorientation angle along the length of the crystal. *bottom panel*: scatter plot comparison showing the average OCPV (blue) and misorientatioin angle (orange) across the width of the wire. The OCPV measurements have the linear background subtracted for linear correlation statistics. The r-value was 0.64 and 0.62 for *a, b* respectively. The vertical dashed lines indicates locations where the OCPV maps were spliced together.

demonstrated that while the wires have a $\langle 111 \rangle$ crystallographic orientation along the z-axis, there is notable misorientation along the length of the wire in the x- and y-axes. The ROD maps for both devices are shown in the middle panels of Fig. 7.3. To directly compare the signal between the OCPV and the grain deviation angles detected by ROD, the average signal across the wire was plotted as a function of device length, bottom panels of Fig. 7.3. Because the OCPV measurements have a linear background with a negative slope due to the voltage measurement measurement requiring opposite polarities at the each of the pads, Fig. 7.4, this background was subtracted from the OCPV scatter plots in the bottom panel of Fig. 7.3 to highlight the variations in the OCPV not due to this background but does not change the overall agreement between the OCPV and ROD measurements. This background subtraction also allows for linear correlation statistics. The Pearson coefficient[326] r-value was used to determine the correlation between the OCPV and ROD measurements using interpolation methods at even intervals. The r-values were found to be 0.64 and 0.62 for the devices in Fig. 7.3a,b respectively, which shows that the OCPV and ROD measurements have good correlation.

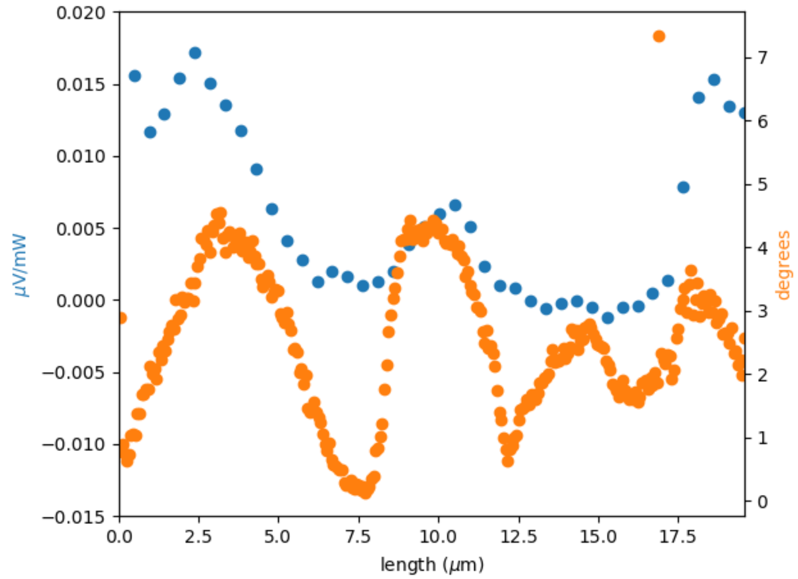

Figure 7.4 : Comparison of OCPV and EBSD measurements in Fig. 7.3b without the linear subtraction. The background subtraction does not affect the overall agreement between the OCPV and ROD measurements but allows for correlation statistics.

The effects of elastic strain on the Seebeck coefficient were discussed in Ch. 2.2.1

and in Refs. [54, 60, 327]. These studies considered the long-range effects of strain on the Seebeck coefficient of gold polycrstalline wires which varies ~ 6.3×10^{-6} V/K per unit strain. The correlation between the OCPV and the ROD measurements indicates that the local Seebeck coefficient is sensitive to short-range effects of strain and other defects detected by ROD measurements.[324] Simulations are currently underway to estimate the variation in Seebeck coefficients that would yield the magnitude of voltages observed in experiments. From this, the magnitude of strain can be estimated from both the ROD misorientation angles and the simulated Seebeck coefficients.

7.3.2 Local grain misorientation contributes more to the Seebeck coefficient than individual grain boundaries

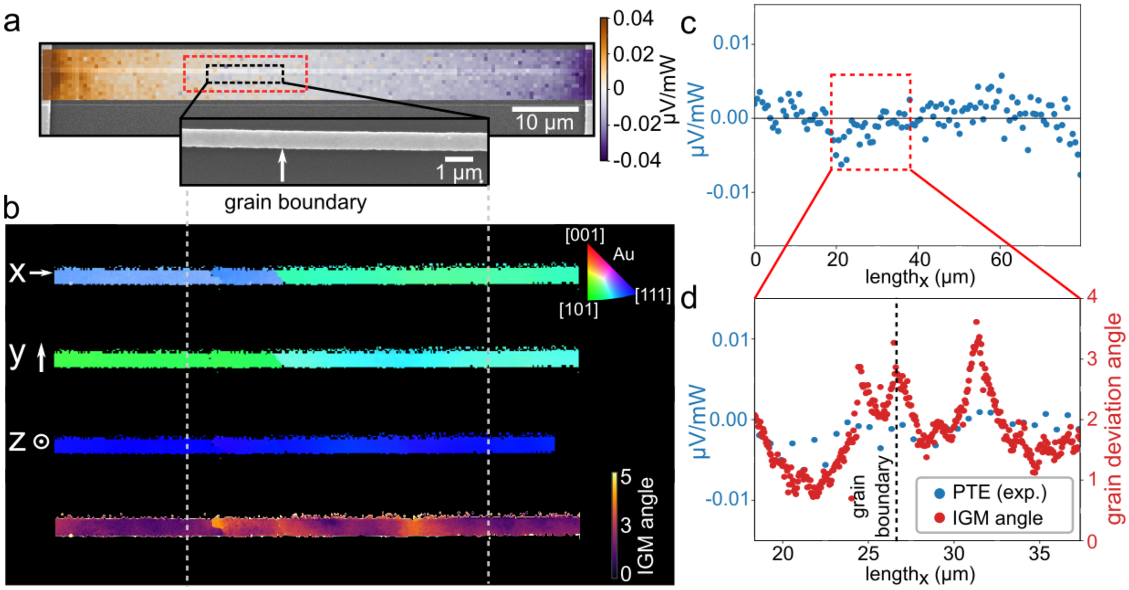

Figure 7.5 : *a*: OCPV map of a bicystal device. *inset*: Zoomed-in image of the black dashed box highlighting the individual grain boundary which can be seen by the change of contrast. *b*: EBSD and ROD map of the device in the red box in *a*. The scale bar is shared with the inset of *a*. *c*: Scatter plot of the OCPV along the length of the device. *d*: Comparison of the OCPV and misorientation angles within the red dashed box in *c*.

In order to determine whether differing grain crystallographic orientations have different Seebeck coefficients, the study was extended to study bicrystal devices. One such example of a bicrystal is shown in Fig. 7.5a. The SEM image is relatively featureless along the device, with the exception of a change of contrast at the location of the grain boundary, inset. Fig. 7.5b shows the EBSD and ROD measurements around the grain boundary marked by the red box in Fig. 7.5a. The ROD measurements were taken only in this field-of-view to reduce noise. As before, the z-axis is in the $\langle 111 \rangle$ crystallographic orientation. However, the x- and y-axes have their own unique orientation for each grain demonstrating a well-behaved grain boundary. To reduce the local variation in strain along the length of the device, the bicrystal was annealed at 300°C prior to measurement. The OCPV map and scatter plots, Fig. 7.5a,c, are relatively featureless along the length of the device. There is no discernible OCPV signal when the grain boundary is heated. The comparison of the OCPV and ROD measurements around the grain boundary is seen in Fig. 7.5d. Unlike what was observed in the unannealed single crystals in Fig. 7.3, although there is considerable misorientation across the grain boundary, the OCPV signal does not change at the grain boundary. These observations indicate that the variation of the Seebeck coefficients in Ref. [90] was likely due to strain gradients in the nanowire as opposed to the grain structure of the wire itself. An unannealed bicrystal, Fig. 7.6, shows larger magnitudes and more spatial variation in the OCPV but still no discernible signal at the grain boundary itself.

A histogram comparing the difference between the maximum signal of unannealed vs. annealed bicrystals is shown in Fig. 7.7. The unannealed bicrystal devices consistently have larger photovoltages than annealed devices, with the signal being a factor of 2.7× larger.

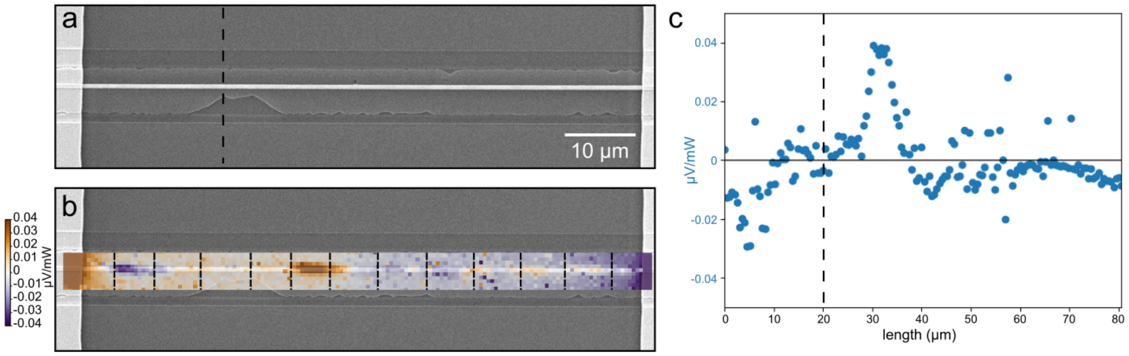

Figure 7.6 : *a*: SEM image of an unannealed bicrystal with the grain boundary marked with a black dashed line. *b,c*: 2D map and scatter plot of the OCPV along the unannealed bicrystal, respectively. The dashed black line marks the location of the grain boundary in the scatter plot.

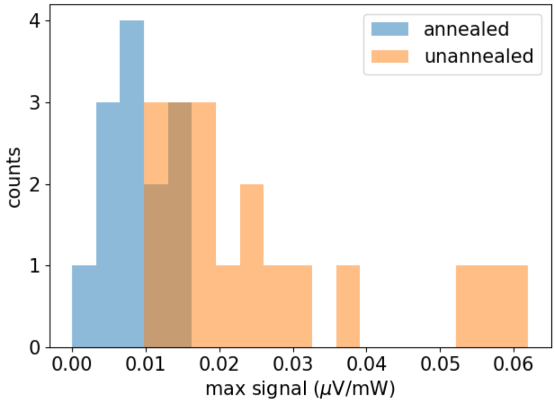

Figure 7.7 : Histogram of photovoltages along annealed and unannealed bicrystals.

7.3.3 Structural defects or geometry changes also change the local Seebeck coefficient

Fig. 7.8a shows an OCVP map of an annealed bicrystal with a structural defect on one side. As before, the EBSD and ROD maps, Fig. 7.8b, demonstrate a well-behaved grain boundary with a ⟨111⟩ crystallographic orientation in the z-axis. This time, however, both the ROD and OCPV measurements near the grain boundary do

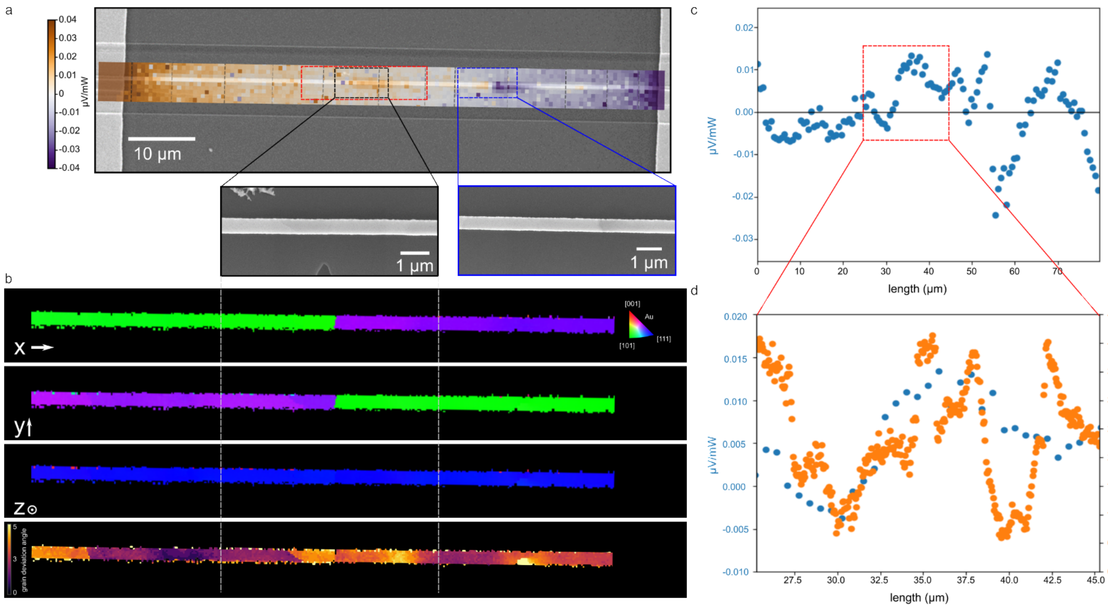

Figure 7.8 : *a*: OCPV map of a bicystal device with a defect. *black inset*: Zoomed-in image of the black dashed box highlighting the individual grain boundary which can be seen by the change of contrast. *blue inset*: Zoomed-in image of the blue dashed box highlighting a defect noted by the change of contrast. *b*: EBSD and ROD map of the device in the red box in *a*. The scale bar is shared with the inset of *a*. *c*: Scatter plot of the OCPV along the length of the device. *d*: Comparison of the OCPV and misorientation angles within the red dashed box in *c*.

show some correlation, Fig. 7.8d. Although there is an overall positive photovoltage detected near the grain boundary, this signal is likely from residual strain as opposed to the grain orientations themselves, as the OCPV and ROD measurements agree for much longer length scales than the laser spot size. This signal near the grain boundary is smaller than that observed near the structural defect. At the defect, the thickness of the wire is abruptly changed and the photovoltage signal changes polarity on either side and becomes relatively large. This change of sign at this defect is consistently observed at the defects that result in a change of wire thickness but not of width, Fig. 7.9. From simulations, the change of polarity in the OCPV occurs when the Seebeck coefficient change is large and abrupt.

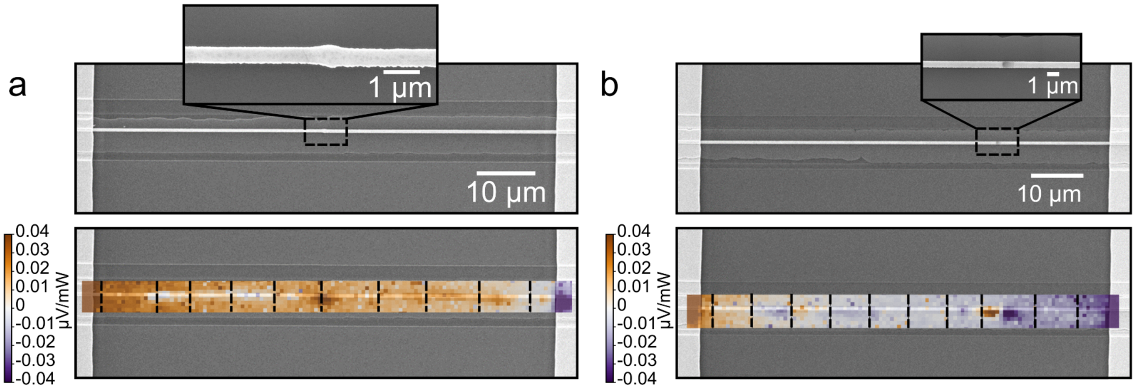

Figure 7.9 : *a*: SEM and OCPV map of a device with a defect that changes the wire width. The signal provides a maximum in the OCPV but does not change sign. *b*: SEM and OCPV map of a device with a defect that changes the wire thickness. The signal changes sign at the defect and becomes large on either side.

A further indication that the Seebeck coefficient is more affected by geometric defects than by the crystalline structure is seen in Fig. 7.10. The wire thickness is compromised, marked by a change in contrast in the SEM image in Fig. 7.10a and width in the EBSD images of Fig. 7.10d. The EBSD images show that the device has many distinct grains along the wire. However, the OCPV signal, Fig. 7.10b,c, is dominated by the effects of the defect; no changes in the signal is observed at grain boundaries.

7.4 Discussion and conclusions: Photovoltages are sensitive to local defects and strain variation, but not significantly impacted by granular structure

In this chapter, the OCPV of single and bicystal wires was studied to determine the sensitivity of the Seebeck coefficient to granular structures. Surprisingly, simplifying

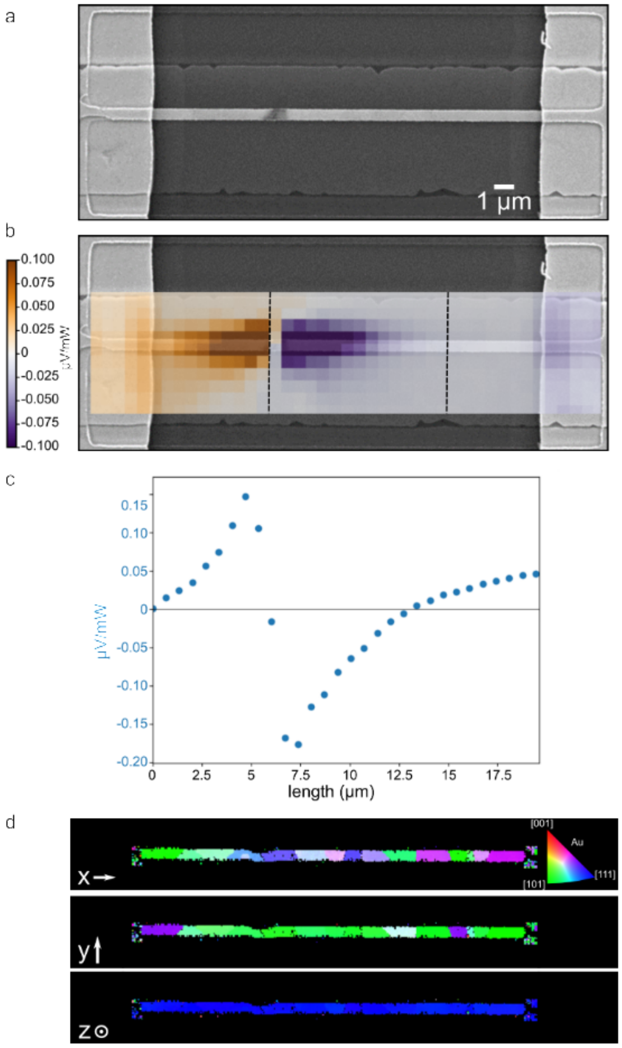

Figure 7.10 : *a*: SEM image of a device with a large structural defect and multiple grain boundaries. *b,c*: 2D map and scatter plot of the OCPV of the device, respectively. *d*: EBSD image of the device detailing a change in device thickness and multiple grain boundaries.

the measurements described in Ref. [90] to single crystals of uniform width and thickness did not result in featureless photovoltage signals. Instead the photovoltages had spatial variations that correlated with the local misorientation of the wire as detected via EBSD. The photovoltages were significantly more sensitive to the variations in the misorientation angle than to grain boundaries. The unannealed bicrystal had larger phohtovoltage signals than the annealed bicystals discussed in this work, but none had large photovoltages when the grain boundary was heated. These observations indicates that the variations in the polycrystalline wires in Ref. [90] were likely from residual strain than from the granular structure itself.[328] Although the photovoltage signal was sensitive to structure defects that changed either the width or thickness of the device, the residual strain in the wire can produce comparable photovoltages.

Although it is well-known and well-studied that the Seebeck coefficient is sensitive to changes in the electronic conductivity and the Fermi area, it is typically considered to be a constant in areas of uniform thickness and width. This study demonstrates that care must be used when attributing changes of the Seebeck coefficient in single material thermocouples to local changes in geometry, especially when the geometric changes are much larger than the electron mean free path. It also shows that the scanning probe method is an effective tool to detect intrinsic variations within a nanoscale device that would otherwise be challenging to detect using traditional electronic transport methods. Additional caution should be used when nanostructuring in devices of materials with large ZT scores, as the effects of local strain and defects could produce even larger effects demonstrated here.

Chapter 8

Detection of trace platinum impurities in gold single- and bi-crystal devices via the photothermoelectric effect

8.1 Motivation: Determine the effect of platinum concentration on the Seebeck coefficient in gold single- and bi-crystals

In Ref. [318], the individual grain boundaries in the bicystals fabricated in the method described in Fig. 7.1 were consistently found to be in the middle of the wire. Fig. 8.1a shows a histogram of the relative location of the grain boundary between the two platinum seeds. The grain boundary position has a highly localized normal distribution around the center of the wire. Figs. 7.5 and 7.8 show that while the z-axis crystallographic orientation is in the ⟨111⟩ direction, each crystal is randomly oriented in the x- and y-axes. Different crystallographic orientations tend to have different growth rates as the preferential orientation for solidification tends to minimize the surface and interface energies,[329, 330] so that these randomly-oriented bicrystals consistently resulted in a grain boundary in the center position indicates that the driving mechanism of crystallization cannot be explained by crystalline growth kinetics alone. Instead, the driving mechanism was determined to be a platinum gradient within the wire. The local distribution of platinum composition along the wire was measured using NanoSIMS (Nanoscale secondary ion mass spectroscopy).[331] NanoSIMS is a highly specialized and sensitive measurement technique that allows for the chemical composition of nanoscale devices to be detected. In this measurement technique, the sample is sputtered using a focused cesium ion beam. The ejected secondary 194Pt ions were then measured using a mass spectrometer. Fig. 8.1b shows symmetric negative platinum gradients from the platinum seeds to the center of the wire. Platinum impurities in gold changes the solidus temperature, Fig. 8.1c. The gold closest to the platinum seeds solidifies first as the system cools, resulting in a solidification front starting at the seeds to the middle of the wire. Because the platinum seeds result in nearly symmetric platinum gradients, Fig. 8.1b, the grain boundary consistently forms in the center of the wire.

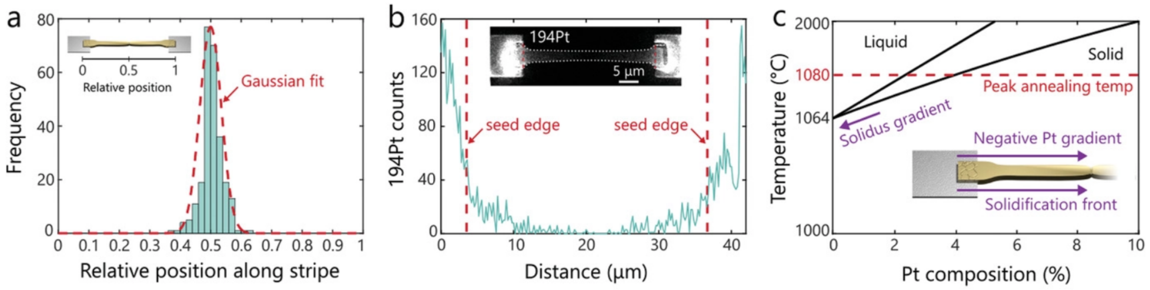

Figure 8.1 : *a*: Histogram of the grain boundary position in the bicrystal devices. *b*: NanoSIMS data detailing a negative platinum gradient from the seeds to the center of the wire. *c*: Phase diagram highlighting that the gradient in platinum concentration affects the temperature of solidification. The negative platinum gradient into the wire serves as the crystal growth mechanism as it dictates the directionality of solidification. Reprinted with permission from Ref. [318]. ©2019 Advanced Materials.

Because the platinum gradient is the driving mechanism of crystallization, these bicrystals are a natural candidate to study the effects of a platinum gradient in the photothermoelectric measurements. Fig. 2.8 demonstrates that platinum impurities can have drastic effects on the Seebeck coefficient of gold.[46–48] By changing the distance between the platinum seeds, the extent of the platinum gradient can be adjusted. A study of bicrystals with large platinum gradients due to close seeds will be discussed below, however a more in-depth study of the photothermoelectric effect of bicrystals with varying platinum seed distances is currently underway at the time of this thesis writing. Some preliminary results will also be detailed.

8.2 The experiment: Measuring the photothermoelectric effect in bicrystals with various platinum seed distances

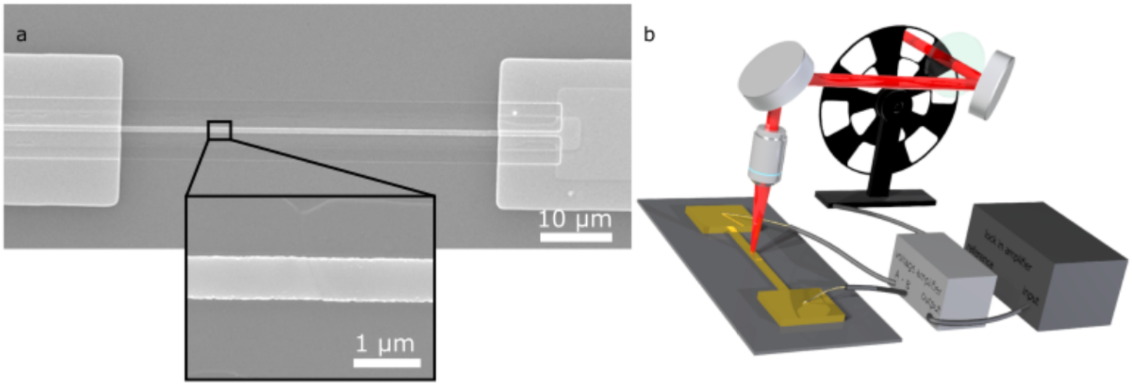

Figure 8.2 : *a*: SEM image of a gold bicrystal. The platinum seed is located in the large square in the rightmost bonding pad. *inset*: zoomed-in image of the grain boundary which can be seen by the change of contrast. *b*: Schematic of the experimental setup.

The devices studied in the chapter are the bicrystals detailed in Ref. [318], but this time the platinum seeds are much closer ($\sim$ 20 μm) away from the bonding pads. As before, the grain boundary can be identified by a change of contrast in SEM imaging, Fig. 8.2a. The bonding pads on this device are asymmetrically placed. The platinum seed is seen in the square in the rightmost pad, whereas the platinum seed on the left is out of the field-of-view in the SEM image. As a result of the bonding pad placements, the grain boundary is located on the left hand side of the measurements although the grain boundary is centered between the two platinum seeds. The measurement setup is the same as that detailed in Chapters 6 and 7 and is depicted in Fig. 8.2b. A cross-sectional TEM image of a typical grain boundary is shown in Fig. 8.3 and shows that the grain boundary is abrupt and that grooves form normal to substrate surface. This groove is seen in the change of contrast in the inset of Fig. 8.2a.

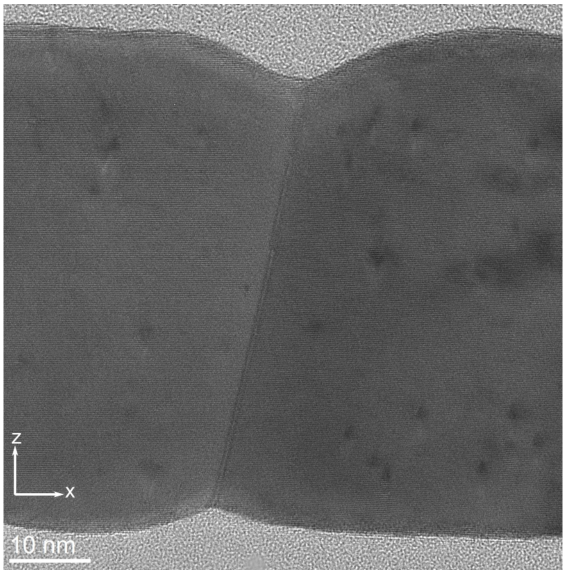

Figure 8.3 : Cross-sectional TEM image of an individual grain boundary in a bicrystal device. The grain boundary is abrupt and grooves form normal to the substrate surface. Image taken by R. Traylor.

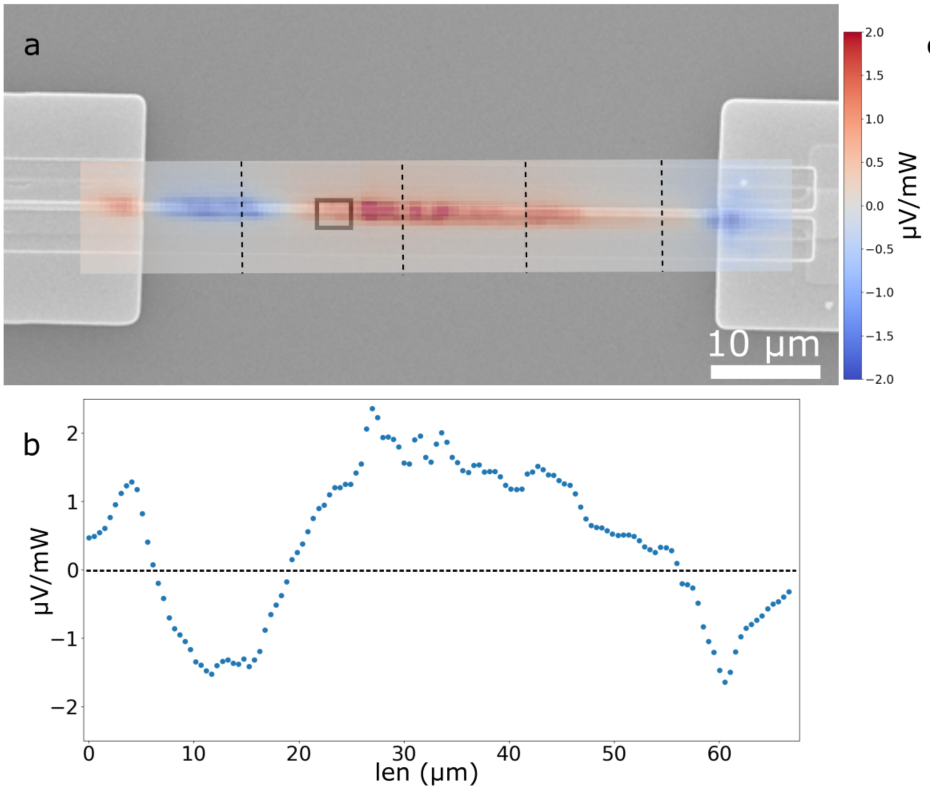

Figure 8.4 : *a*: 2D map and *b*: scatter plot of the OCPV along the unannealed bicrystal with close platinum seeds seen in Fig. 8.2a. The location of the grain boundary is depicted by the black box. The dashed vertical lines indicate locations where individual maps were stitched together.

8.3 Results: Platinum concentration has much larger effects on the Seebeck coefficient than residual strain

8.3.1 Large platinum gradients result in photovoltages ~ 100 times larger than the signal from the previously-discussed local strain variations

The OCPV map and scatter plot of the bicrystal seen in Fig. 8.2a is shown in Fig.8.4a,b respectively. The OCPV maps are significantly different than the maps seen in bicystals with platinum seeds much farther away in Ch. 8. As before, the signal near the grain boundary is around zero. On either side of the grain boundary, the OCPV is of opposite polarity and slowly varies with length scales ∼ 10 µm, more than 5× the FWHM of the focused laser spot size. The largest magnitude of signal occurs approximately 5 µm on either side of the grain boundary. Finite-element modeling suggests a 1.8 µm FWHM focused beam diameter should not appreciably heat the grain boundary beyond 3-4 µm away from the boundary, which indicates that this maximum signal is not set neither the grain boundary nor the laser spot size. The overall magnitude of the OCPVs detected in this device is $\sim 1\ \mu$V/mW, which is ∼ 100× larger than the magnitudes observed in the devices discussed in Ch. 7.

8.3.2 Annealed bicrystals have different OCPV signatures compared to unannealed bicrystals

Annealing metal wires can affect a multitude of internal features not optically visible such as the grain structure, impurity locations, and internal stresses and strains.. During the fabrication process, the devices were cooled to room temperature from 300 °C within two hours. Due to interactions with the substrate and surrounding (at the time of fabrication) oxide, internal stresses could form as the metal is rapidly cooled. An additional set of annealed devices was prepared with the cooling time slowed to a full 24 hours. The results of an annealed device is seen in Fig. 8.5. This time, the contact pads are symmetrically placed so the grain boundary appears in the center of the device. As before, the signal near the grain boundary is around zero and the OCPV is of opposite polarity on either side of the boundary. This time, however, the maximum signal is not ∼ 5 µm from either side of the grain boundary and instead appears closest to the bonding pads ∼ 20 µm from the grain boundary. The differences in the OCPV signatures between the unannealed and annealed devices

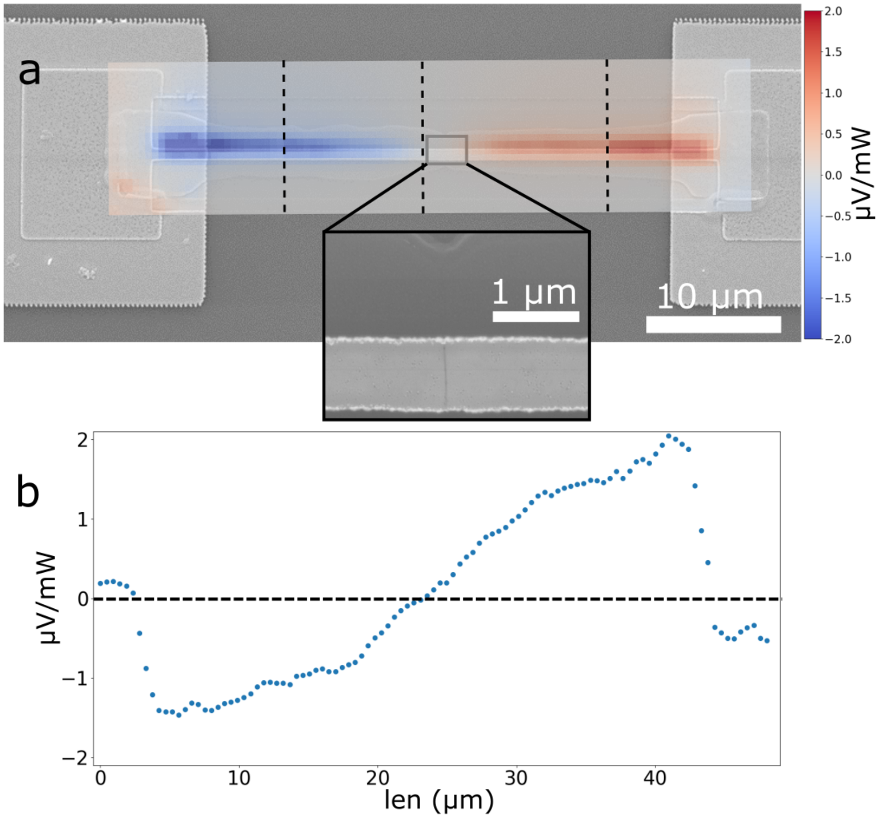

Figure 8.5 : *a*: 2D map and *b*: scatter plot of the OCPV along the annealed bicrystal with close platinum seeds shown in the squares on both contact pads. The location of the grain boundary is depicted by the black box. The dashed vertical lines indicate locations where individual maps were stitched together. *Inset*: zoomed-in image of the grain boundary which has a notable change of contrast.

are consistently observed, Fig. 8.6. The unannealed devices consistently show the maximum signal occurring $\sim$ 5 μm from the grain boundary whereas the maximum signal occurs $\sim$ 20 μm from the grain boundary in annealed devices. This difference in the length scales of the OCPV cannot be explained by platinum diffusion during the annealing process, as the expected diffusion length is $\sim$ 500 nm.[332, 333] Instead, the differences are likely explained by the relief of local strain within the wire during the annealing process as described in Ch. 7.

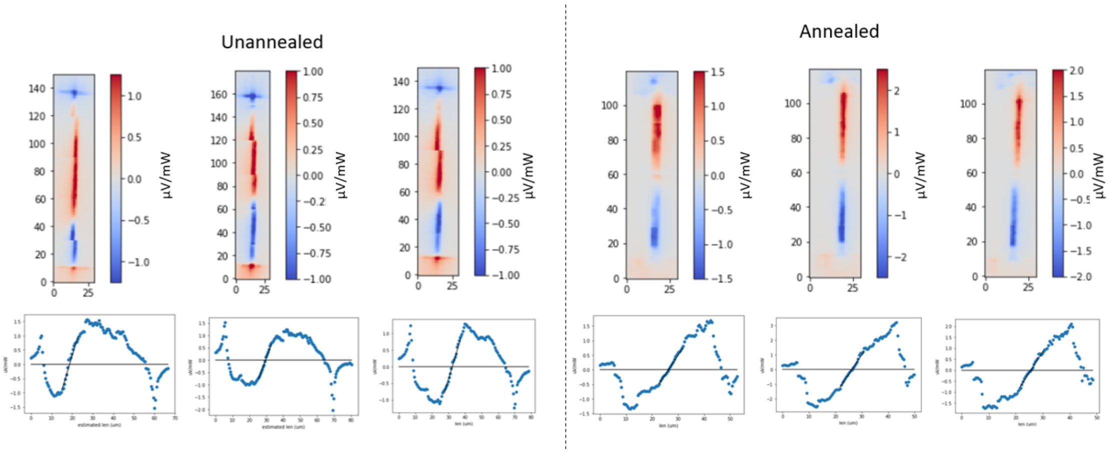

Figure 8.6 : Comparison of OCPV variation in *left* unannealed and *right* annealed bicrystal devices.

8.3.3 NanoSIMS does not have the resolution to detect the platinum gradient far from the platinum seeds, but the photovoltage signal is still sensitive to the impurities

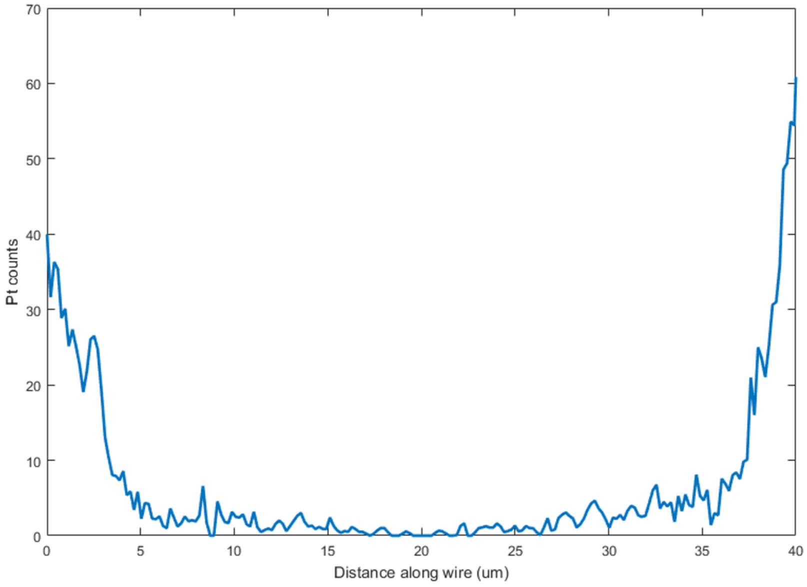

Figure 8.7 : Platinum counts detected via NanoSIMS along the length of a 40 µm long bicrystal. Measurements by L. Gan.

In Ref. [318], NanoSIMS was used to determine the 194Pt composition of the bicrystal wires. An example of the 194Pt compositon along the length of these short bowties is seen in Fig. 8.7. Near the platinum seeds, high platinum counts are detected. However, the NanoSIMS reaches the noise floor ∼ 10 μm from the seeds. Although 194Pt was selected because it is the most common platinum isotope, the total counts are relatively low making it challenging to adequately detect the platinum concentration along the devices. Fig. 8.8 shows a bicrystal twice as long as the one in Fig. 8.7. No platinum is detected before reaching the center of the device.

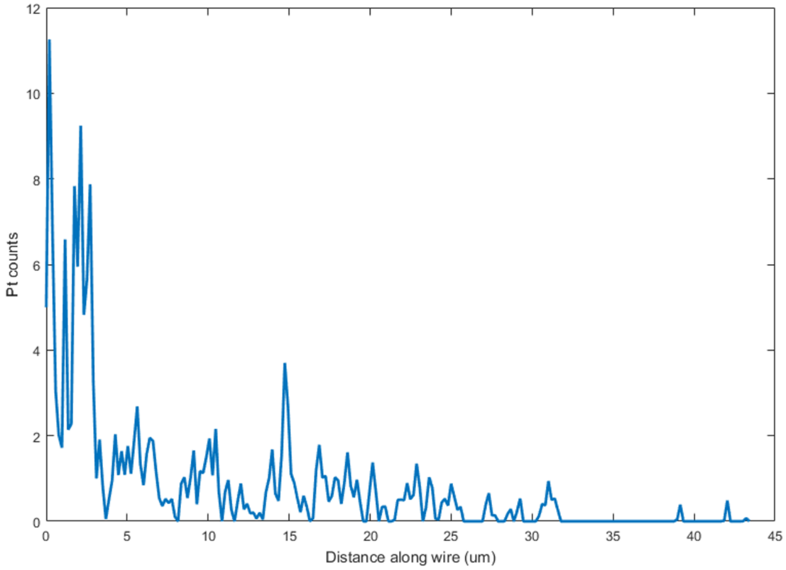

Figure 8.8 : Platinum counts detected via NanoSIMS along the length of a 100 μm long bicrystal. Measurements by L. Gan.

Although the platinum concentration in these wires is sufficiently low that detection via NanoSIMS is challenging, the OCPV is still quite sensitive to the impurities. A study of the OCPV signal of single crystals with varying platinum seed distances is currently underway. Fig. 8.9 shows preliminary OCPV maps of the single crystals with platinum seeds 50, 200, 350, and 400 μm away from the left contact pad.

In general, the magnitude of the OCPV is decreases as the distance of the platinum seed increases while the spatial variation increases with platinum seed distance. NanoSIMS and EBSD measurements are currently underway to compare these findings. However, the larger magnitude of the OCPV detected for the devices closest to the platinum seeds is likely because of the larger platinum gradient in the devices, resulting in large changes to gold's Seebeck coefficient.[46–48] Additionally, because the negative platinum gradient is the driving mechanism of crystalline growth in these devices[318], the quality of the single crystals likely degrades as the platinum gradient comes negligible. A thorough comparison of the NanoSIMS and EBSD measurements will be able to corroborate these findings.

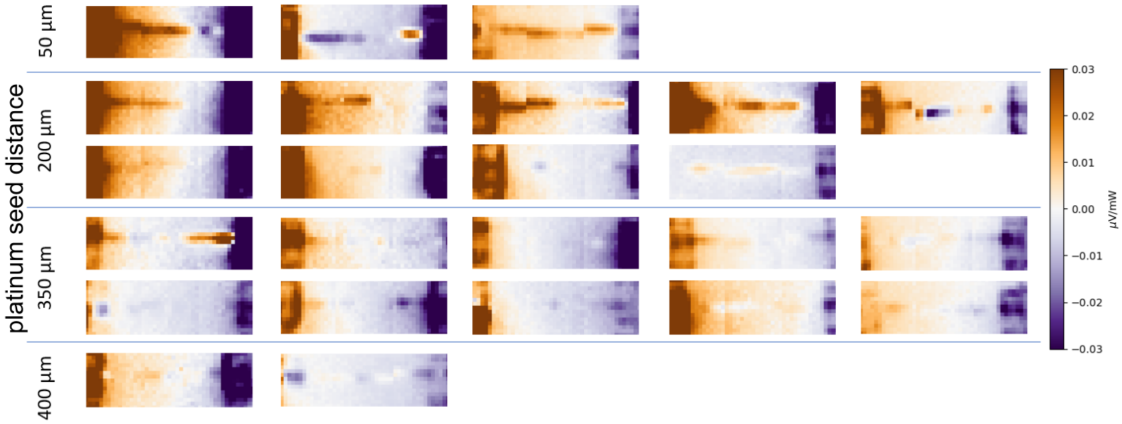

Figure 8.9 : OCPV maps of single crystals at varying distances from the platinum seed. These maps are set to the same color scale for direct comparison.

Initial finite element modeling has shown that the length scales and magnitudes of the OCPV observed in these experiments can be attributed to a gradient in the Seebeck coefficient. Variation of the Seebeck coefficient $\sim 0.01\mu\text{V/K}$ per 250 nm can result in OCPVs of the magnitudes observed in this work. Previous works have shown that increasing the platinum concentration in gold from 0.11% to 0.5% changes the Seebeck coefficient of gold by $\sim 1.7\mu\text{V/K}$.[46–48] Using those values, the initial simulations suggest that variations in platinum $\sim 0.01\%$ per 1 µm have substantial impact on the observed OCPV magnitudes.

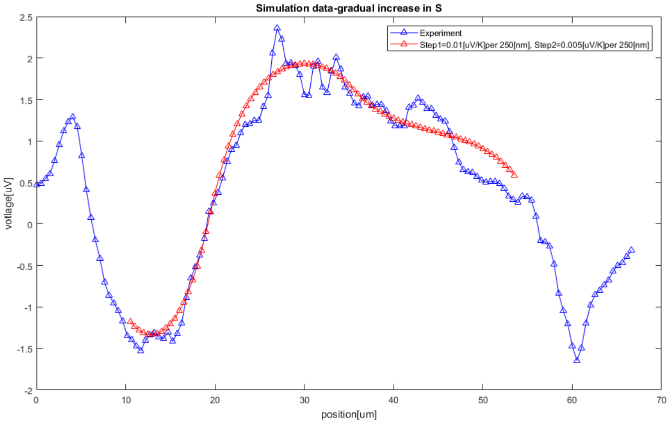

Figure 8.10 : Simulations of the OCPV due to a gradient in Seebeck coefficient $\sim 0.01\mu\text{V/K}$ per 250 nm provide magnitudes and length scales similar to that observed in experiment.

8.4 Discussion and conclusions: Photovoltages are sensitive to platinum impurities in gold that can be challenging to detect using conventional means

Because the driving mechanism of crystal growth in the single and bicrystal devices studied in this and the previous chapter is a negative platinum gradient,[318] these systems are natural candidates to study the effects of platinum impurities on the local Seebeck coefficient of gold. The photovoltages are highly sensitive to changes in the platinum concentration that even NanoSIMS has difficulty detecting. The photovoltages detected in short bicrystals have magnitudes $\sim 100\times$ larger than the long devices measured in Ch. 7. Annealed devices have different signatures than unannealed devices which indicate that even in devices with high platinum concentration are (likely) still sensitive to residual strain. Further work is currently being conducted to compare the platinum concentration detected via NanoSIMS and crystalline quality determined via EBSD to the OCPV measurements of single crystalline wires at varying distances from the platinum seed. Preliminary modeling indicates that the OCPV signal can be attributed to gradients in the Seebeck coefficients that correspond to trace variations in the platinum concentration along the length of the wire. The sensitivity of the Seebeck coefficient in gold to both impurity concentration and strain demonstrates that the photothermoelectric effect can be used as a powerful diagnostic tool that can probe intrinsic properties of a nanoscale device that can otherwise be challenging to detect.

Chapter 9

Quantifying remote heating from propagating surface plasmon polaritons

9.1 Motivation: reduce local heating at nanowire constriction for simultaneous SERS and IETS

As discussed in Sec. 5.7, the plasmonic resonances in the gold bowtie nanowires that make single-molecule Raman sensitivity possible also result in high local heating at substrate temperatures that are low enough for well-resolved IETS peaks. Reducing the temperature rise of the constriction under laser illumination is imperative to be able to probe simultaneous IETS and Raman measurements. Remotely exciting the nanogap via SPPs by including a periodic grating into the electrode design can allow for the majority of the heating to occur in the electrodes, away from the resonant constriction, yet provide the benefit of plasmonic coupling between the propagating and local modes in the gap. In order to determine if such an approach would reduce the local temperature of the constriction enough for well-resolved IETS measurements, a study was conducted to estimate the temperature rise of the intact wire. This chapter closely follows Ref. [334].

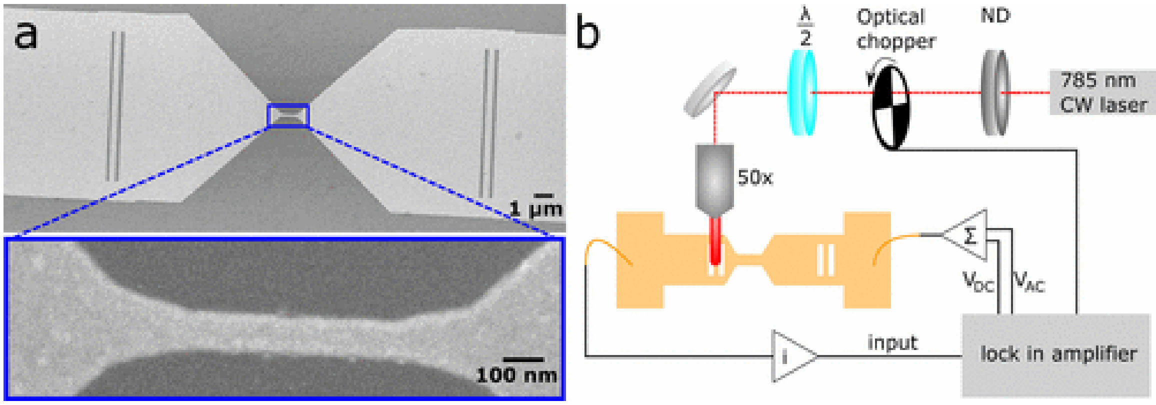

Figure 9.1 : *a*: SEM image of bowtie with grating. *b*: Schematic of experimental setup. Reprinted with permission from [334]. ©2017 American Chemical Society.

9.2 The experiment: Measure the temperature rise of the constriction as a function of grating position

The devices in this work were the bowties with gratings, Fig. 9.1a. The gold thickness was increased from 15 nm Au to 30 nm to extend the SPP decay length. Two rectangular holes, which we will call "gratings", were included in the electrode design during a one-step lithography step. The distance of the grating from the constriction was varied, from 5 µm to 13 µm away. The dimensions of the rectangular holes were experimentally determined to maximize signal and fabrication yield, which are close the theoretical optimal values as determined by the collaborators in the Dr. Nordlander group, Fig. 9.2. Unless otherwise specified, the substrate was 2 µm SiO_2/Si, in order to reduce damping of the SPP, which will be discussed later on in this chapter. The measurement scheme closely follows that of Refs. [290] and [292]. The schematic of the device is seen in Fig. 9.1b. The steady-state differential conductance of the device as a function of laser position is measured using lock-in techniques. In order to avoid the nonlinear temperature rise, the substrate temperature was at 40 K, which was the lowest temperature within the linear regime, Fig. 9.3. The device was biased with 5 mV DC signal and the laser was modulated using an optical chopper at 339 Hz. More information is seen in Sec. 5.8.5.

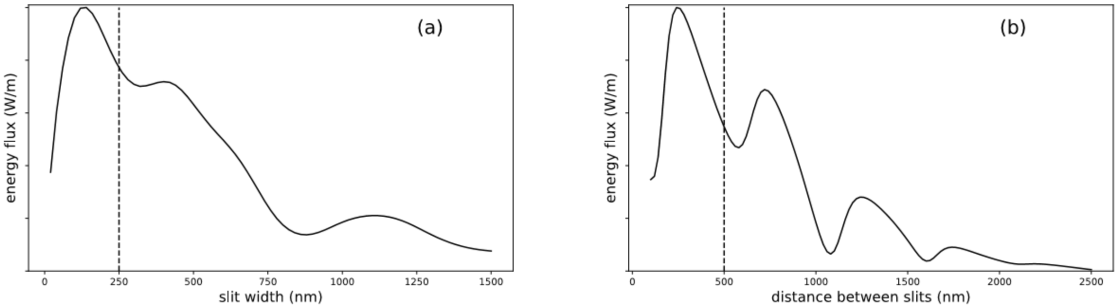

Figure 9.2 : The calculated energy flux of the device based on the following grating parameters: *a*: slit width *b*: distance between slits. The experimentally used values are marked by the dashed lines. Reprinted with permission from [334]. ©2017 American Chemical Society.

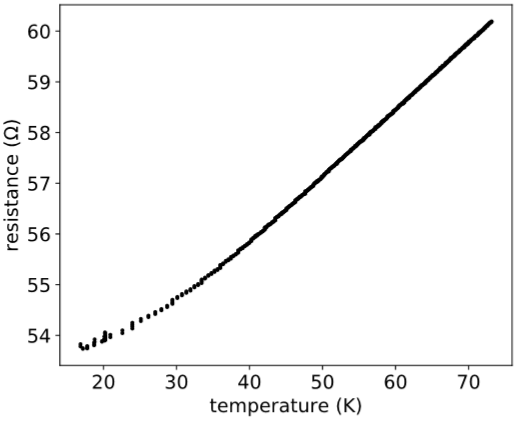

Figure 9.3 : Substrate temperature dependence of device resistance: The relation is linear to around 35 K. Reprinted with permission from [334]. ©2017 American Chemical Society.

9.3 Results: Remote excitation reduces local heating well within IETS limitations

9.3.1 The efficiency of SPP propagation depends strongly on oxide thickness

Rastering the beam around an area of interest, the steady-state differential conductance of the entire device was measured as a function of laser position. Shining the laser directly on the nanowire resulted in the largest change of differential conductance, regardless of polarization, Fig. 9.4 top row. When the laser was in the transverse polarization, Fig. 9.4a, the resonant local surface plasmon in the nanowire was excited resulting in a larger signal compared to the longitudinal polarization, Fig. 9.4b. The polarization dependence of the differential conductance of the device when incident on the constriction is seen in Fig. 9.4c. As seen in Fig. 5.11b, the polarization dependence shows the largest signal when in the transverse polarization due to the plasmon resonance. The signal has less polarization dependence than seen in previous works because the gold thickness change shifted the plasmon resonance, and the nanowire width was not adjusted to account for this change. Rastering the laser around the grating changes the observations significantly. When the laser is in the transverse polarization (parallel to the grating), Fig. 9.4d, there is no signal detected regardless of laser position. In the longitudinal polarization, Fig. 9.4e, maximum signal is seen when the laser is incident on the grating. Fig. 9.4f shows the polarization dependence of the differential conductance when the laser is incident on the grating. The maximum signal occurs when the laser illumination is in the longitudinal polarization, the opposite of what was seen in the constriction case. This is indicative of excitation of SPPs. Although adding additional rectangular holes to exceed the laser

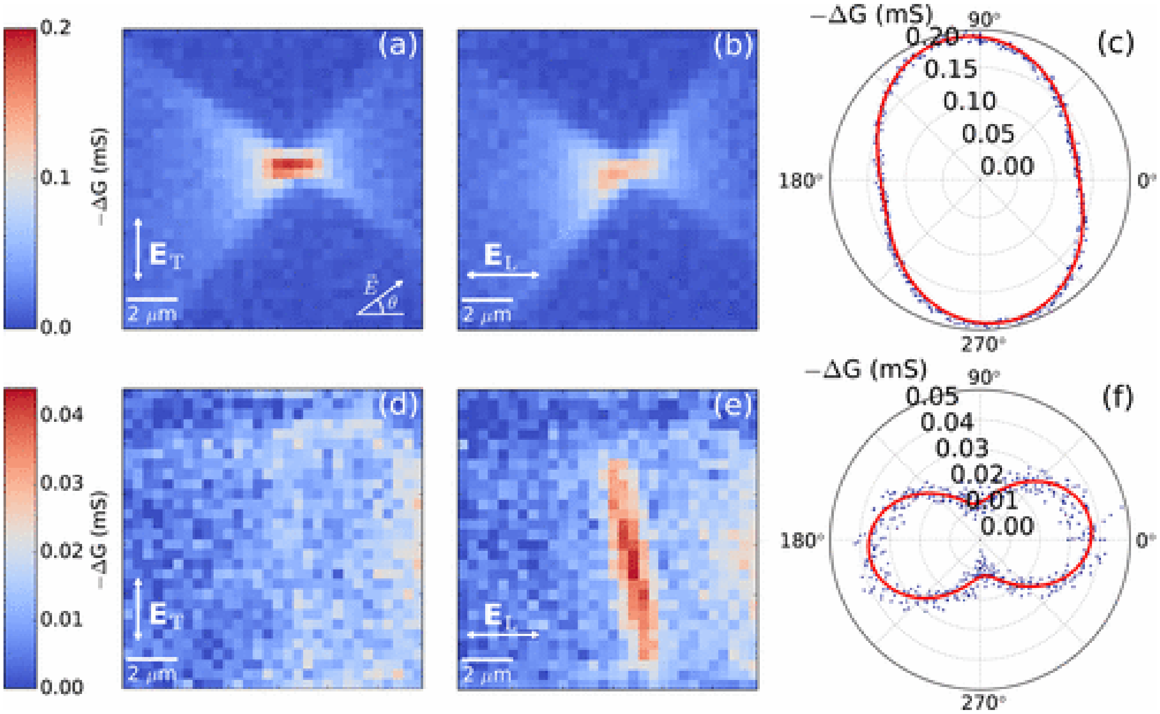

Figure 9.4 : Differential conductance maps and polarization dependence of bowties with gratings on 2 µm SiO_2/Si substrates: *a, b*: 2D map of the differential conductance as a function of laser position scanning around the nanowire constriction under transverse and longitudinal polarization, respectively. The signal is largest when the laser is incident on the nanowire constriction and in the transverse polarization. *c*: Polarization dependence of the differential conductance when the nanowire constriction is illuminated. The transverse polarization has the largest signal because of the local surface plasmon resonance in the nanowire. *d, e*: 2D map of the differential conductance as a function of laser position scanning around the grating in the electrode design under transverse and longitudinal polarization, respectively. The differential conductance is almost featureless even when the laser is incident on the grating when the laser is in the transverse polarization. When the laser is in the longitudinal polarization, the largest response occurs when the laser is incident on the grating. *f*: Polarization dependence of the differential conductance when the laser is incident on the grating. The signal is largest when the laser is in the longitudinal polarization, indicating the excitation of surface plasmon polaritons. Reprinted with permission from [334]. ©2017 American Chemical Society.

spot size increased signal by around 10%, the overall useable yield during fabrication dropped by around 25% due to defects from the proximity effect in the lithography process, Fig. 9.5. Compared to direct laser illumination, the differential conductance of the device measured when the laser was illuminating a grating 8.8 µm from the constriction as seen in Fig. 9.4 decreased by a factor of 4.5.

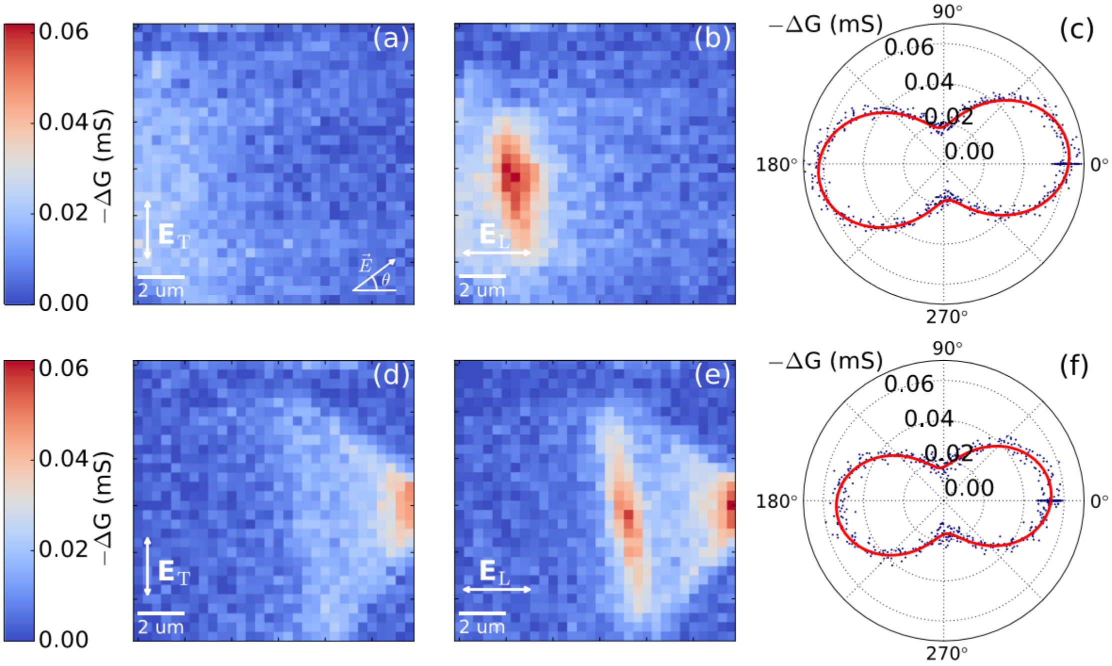

Figure 9.5 : Comparison of signal in devices with larger grating areas: *a*, *b*: 2D differential conductance maps around the grating in a device with 14 rectangular slits in the electrode design, under transverse and longitudinal polarization, respectively. *c*: Polarization dependence of the differential conductance when the laser is incident on the larger grating. *d*, *e*: 2D differential conductance maps around the grating in a standard bowtie with grating device under the transverse and longitudinal polarization, respectively. *f*: Polarization dependence of the differential conductance while the laser is incident on the standard grating. Although the signal is around 10% larger in the devices with a larger grating, the yield during fabrication dropped by 25%. Reprinted with permission from [334]. ©2017 American Chemical Society.

As mentioned in the introduction, plasmon resonance has a large dependence on the dielectric conditions. Changing the substrate from 2 µm to 200 nm SiO_2 on Si dramatically changes the results. Fig. 9.6 shows the same measurements as that of Fig. 9.3 but on a substrate with 200 nm SiO_2. While the observations around the constriction are the same as before, where shining the laser on the constriction while in the transverse polarization has the largest result, the signal at the grating completely loses its polarization dependence. In order to detect any signal at the gratings, the DC bias must be increased to 100 mV, and even so, only the corners of the grating have any appreciable signal, regardless of the polarization. Various grating parameters were used to measure signal on 200 nm SiO_2, and these results were consistently seen.

Simulations, conducted by the collaborators in the Dr. Peter Nordlander group, were able to explain this observation, Fig. 9.7. Fig. 9.7a shows that as the oxide thickness increases, the energy flux oscillates. Changing the substrate thickness by around 100 nm can result in the energy flux being a maximum to a minimum, prematurely damping the SPP propagation. The oscillations have a period of 272 nm, which closely matches the half wavelength of the 785 nm free space wavelength laser light in silica (n=1.45) of 720 nm which indicates a Fabry-Perot resonance.[335] Fig. 9.7b shows the simulated electric field amplitude of the device with an oxide thickness that is a maximum in the Fabry-Perot oscillation, 1.53 µm, whereas Fig. 9.7c shows the simulated electric field amplitude of the device with an oxide thickness that is a minimum in the Fabry-Perot oscillation, 1.63 µm. The interface of the SiO_2/Au shows the electric fields related to SPP propagation. When the oxide thickness is a maximum in the Fabry-Perot oscillation, the electric fields associated with SPP propagation propagate much farther than when the oxide thickness is a minimum.

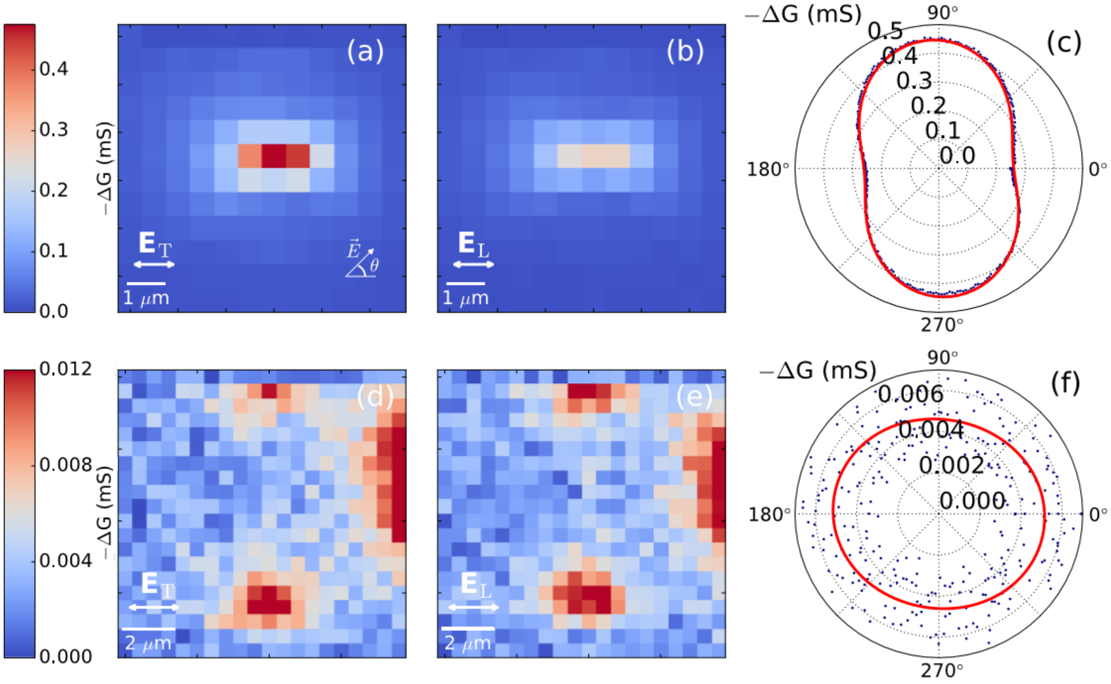

Figure 9.6 : Differential conductance maps and polarization dependence of bowties with gratings on 200 nm SiO_2/Si substrates: *a, b*: 2D differential conductance map around the constriction under transverse and longitudinal polarization, respectively. *c*: Polarization dependence of the differential conductance when the laser is incident on the nanowire constriction. The observations when scanning around the nanowire constriction is the same regardless of substrate; the local surface plasmon mode that is resonant with the incident laser illumination is excited under transverse polarization. *d, e*: 2D differential conductance maps around the grating in the electrode design in the transverse and longitudinal polarization, respectively. Unlike in Fig. 9.4, the signal at the grating occurs only at the corners of the grating regardless of polarization. *f*: Polarization dependence of the differential conductance when the laser is incident on the grating, showing no notable polarization dependence. Reprinted with permission from [334]. ©2017 American Chemical Society.

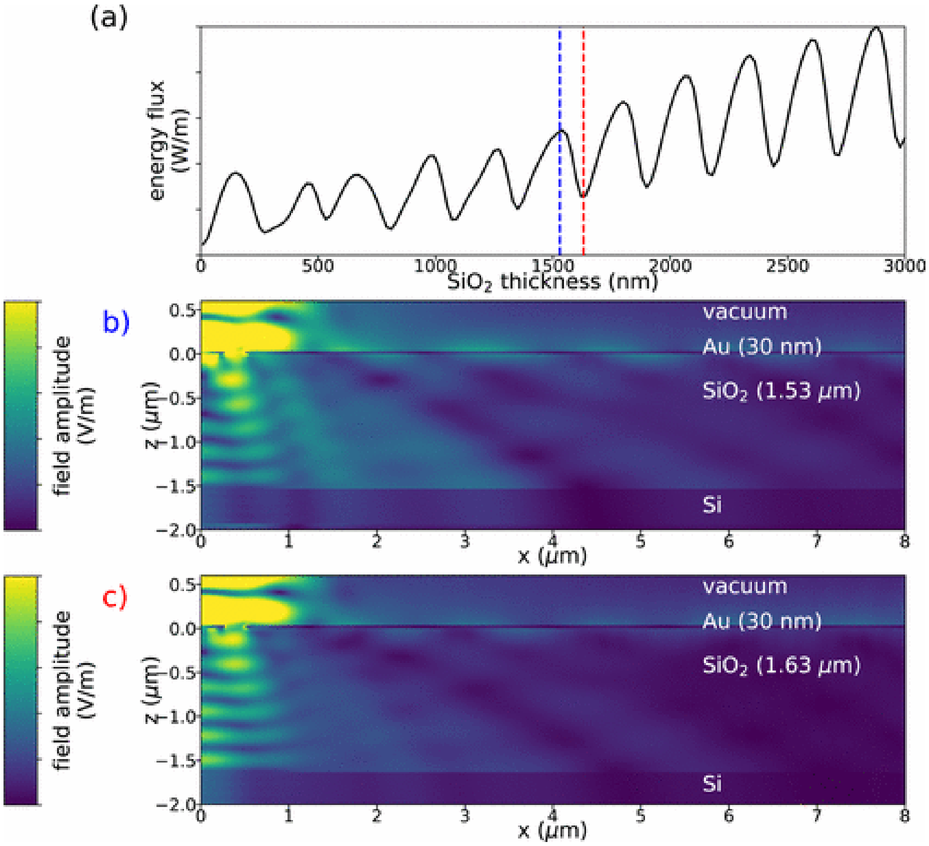

Figure 9.7 : *a*: The calculated energy flux propagating through the device as a function of SiO_2 thickness. As the oxide thickness increases, the energy flux oscillates with a period of 272 nm indicative of a Fabry-Perot cavity. *b*: The calculated electric field amplitude in the device with 1.53 µm SiO_2, a maximum seen in *a* indicated by the blue dashed line. The SPP is seen at the interface of the SiO_2/Au interface. *c*: The calculated electric field amplitude in the device with 1.63 µm SiO_2 thickness, a minimum seen in *a* noted by the red dashed line. The electric field damps out more quickly than seen in *b*. Reprinted with permission from [334]. ©2017 American Chemical Society.

9.3.2 The temperature rise of the constriction is decreased by up to a factor of 60 when comparing remote excitation to direct illumination of the nanowire

Like Refs. [290] and [292], the temperature rise of the constriction when the laser is incident on the nanowire can be detected using a bolometric technique using the

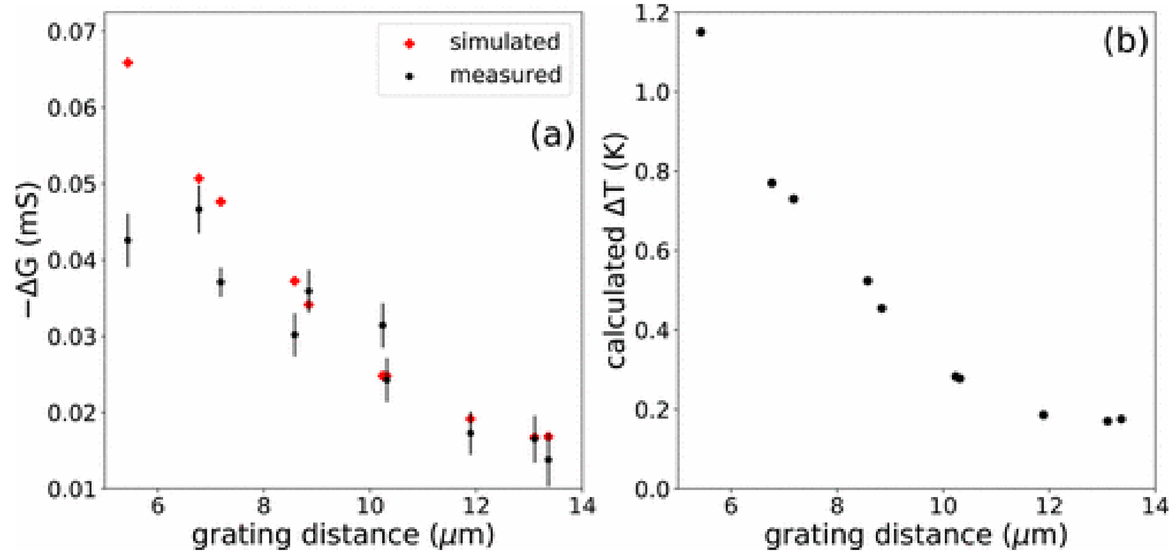

Figure 9.8 : Simulated temperature rise of the nanowire constriction from the measured differential conductance: *a*: Comparison of the experimentally measured and simulated differential conductance of the device as a function of grating distance. *b*: The calculated temperature rise of the nanowire constriction due to excitation from SPPs as a function of grating distance. Reprinted with permission from [334].

slope of the temperature dependence of the device as a first order estimate, Fig. 9.3. When the laser is incident on the gratings, however, the temperature rise of the constriction due to the remote excitation from SPPs should not be estimated using the bolometric technique as the measurement is less straightforward. While the maximum temperature rise occurs at the grating, the grating increases absorption within the electrode design, compared to an intact electrode without the rectangular holes. Illuminating the grating additionally excites the propagating SPPs that will additionally heat the nanowire constriction. In order to determine that the main excitation of the nanowire is from remote excitation due to SPPs and *not* due to increased absorption, theoretical computations were conducted to estimate the temperature rise.

Using COMSOL Multiphysics, the collaborators in the Dr. Nordlander group compared the experimentally measured and theoretically calculated differential conductance of the device with the grating under laser illumination as a function of grating distance, Fig. 9.8a. The simulated geometry matched well with experiment. Using an exponential fit, the decay length of the SPPs was determined to be 7.7 ± 0.8 µm, which agrees with previously published results[209, 218, 227]. Using the same geometry, the total temperature rise of the constriction when the grating was illuminated was calculated, Fig. 9.8b. Using these calculated values, the experimentally measured differential conductance due to grating illumination can be converted to the temperature rise in the constriction. Illuminating the gratings closest to the constriction (immediately after the fan-out electrodes, 5 µm away from the constriction) resulted in a temperature rise in the constriction that was a factor of 11 smaller compared to that of direct illumination. Illuminating the farthest gratings, approximately 13 µm away from the constriction, resulted in a temperature rise in the constriction that was a factor of 60 smaller compared to that of direct illumination. Despite the fact that the farthest gratings were nearly a factor of two longer than the decay length of the SPP as determined in Fig. 9.8a, there was still a clear change in differential conductance when the gratings were illuminated.

In order to confirm that the temperature rise of the constriction was due to remote excitation from SPPs as opposed to increased absorption from the grating, Fig. 9.9 shows the calculated temperature rise of the constriction due to *only* SPP dissipation was calculated with and without gratings, eliminating both heating from absorption and heating from the fan-out electrodes. The temperature rise with the presence of the grating is larger by more than an order of magnitude compared to that with no gratings, which suggests that the temperature rise is driven by the SPP excitation. Although the temperature rise of the constriction seen in Fig. 9.9 is almost an order of magnitude smaller than that seen in Fig. 9.8b, this temperature rise neglects the

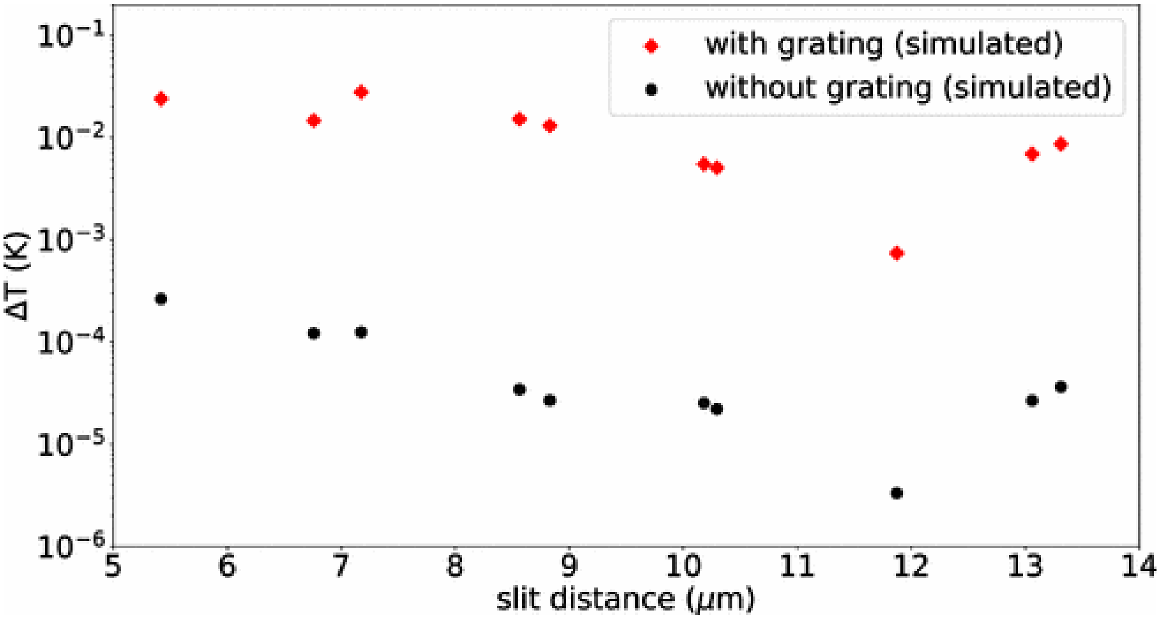

Figure 9.9 : Simulated temperature rise considering only SPP dissipation in the nanowire: the temperature rise of the nanowire due to only SPP dissipation, neglecting heating effects from direct absorption and from the connecting fan-out electrodes, with (red points) and without (black points) the grating in the electrode design. The temperature rise of the constriction is more than an order of two larger when the gratings are present, indicating that the temperature rise is driven by SPP as opposed to a simple absorption increase. Reprinted with permission from [334]. ©2017 American Chemical Society.

effects due to the fan-out electrodes. When the dissipation of the SPPs in the fan-out electrodes is included, while still excluding the heating from direct absorption, the calculated temperatures closely match what was detected using the previous model, Fig. 9.10.

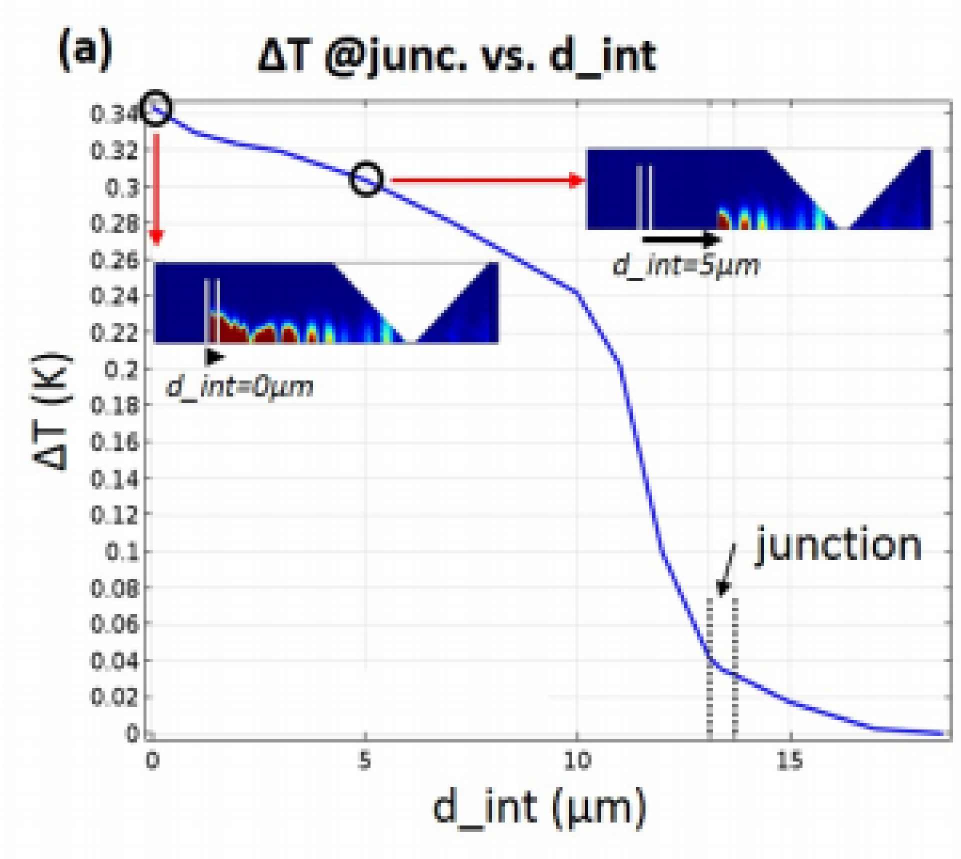

Figure 9.10 : Simulation of nanowire heating due to SPP dissipation: the temperature rise of the nanowire constriction is calculated considering the SPP dissipation the area between the parameter d_{int} and the constriction. d_{int} is measured from the distance of the grating located 13.4 µm from the constriction. Insets include examples d_{int} is 0 µm and 5 µm, which is at the grating and 8.4 µm away from the constriction. When the area of dissipation excludes only the beam (d_{int} = 1.8 µm) the temperature rise of the constriction is hardly affected. The largest temperature decrease is detected when the dissipation from the fan-out electrodes is excluded (d_{int} between 10 and 13.4 µm). The temperature rise considering the dissipation from the fan-out electrodes to the constriction closely matches what was calculated from the differential conductance measurement, indicating that the heating of the constriction is primarily from SPP dissipation. Reprinted with permission from [334]. ©2017 American Chemical Society.

9.4 Discussion and conclusions: Remote excitation of the nanowire via SPPs can reduce local temperature rises by up to a factor of 60

In this chapter, the differential conductance of the device was compared when the laser was directly illuminating the nanowire constriction to when the laser was illuminating a grating in the electrode design. The polarization dependence of the differential conductance during direct illumination of the nanowire showed a maximum response when the laser was in the transverse polarization, exciting the local surface plasmon resonance within the nanowire constriction. When the laser was shining on the grating, the maximum response occurred when the laser was in the longitudinal polarization, which indicated that SPPs were launched from the grating and propagated to the nanowire constriction, heating it up. The efficiency of SPP excitation was shown to be strongly dependent on the thermal oxide layer, changing this thickness by 100 nm could almost entirely damp out the signal. To determine the temperature rise due to the remote excitation of the SPPs, theoretical calculations of the differential conductance were compared to that of experiment, which were in close agreement and the temperature rise of the nanowire considering SPP dissipation and thermal diffusion due to increased absorption at the grating site was considered. Considering the temperature rise from SPP dissipation alone, neglecting that from increased absorption at the grating site, indicates that the temperature rise is driven by the remote excitation of the SPPs. The temperature rise of nanoconstriction due to remote excitation was a factor of 11 lower for gratings around 5 µm away from the constriction and a factor of 60 lower for gratings around 13 µm away from the constriction, when compared to that of direct excitation. This indicates that the addition of gratings in the electrode design allows significant reduction in the local temperature of the nanowire due to SPP excitation which can be readily detected using electronic transport methods, which provides potential for low temperature electronic transport and optical measurements.

Chapter 10

Detecting hot electrons in directly and remotely excited nanogaps via enhanced photovoltages

10.1 Motivation: elucidate tunneling mechanisms in illuminated nanogaps and probe the coupling of surface plasmon polaritons to local multipolar modes in nanogaps using open circuit photovoltages

As mentioned in Ch. 9, gratings were added to the electrode design in the bowtie devices to allow for remote excitation for simultaneous SERS and IETS measurements, in order to prevent the high local heating from the plasmonic mode in the nanowire under direct illumination that makes single molecule Raman possible. Remotely exciting the nanowire via SPPs launched from the grating design reduced the local temperature at the nanowire enough to where IETS spectra would still have well-resolved peaks. Electromigrating the nanogap for these measurements add additional complications to the electronic transport measurements not considered in Ref. [334], the addition of the nanogap requires the consideration of tunneling mechanisms not included in the previous bolometric measurements, such as photo-assisted tunneling,[81, 210, 336, 337] internal photoemission,[196, 252–254] rectification[92, 113, 266, 338], and hot electron current.[257, 258, 261, 262] Conducting open circuit photovoltage (OCPV) measurements can help discern between these different mechanisms and can provide insight on how remotely excited SPPs couple to local modes at the nanogap. This chapter will closely follow three references: Ref. [102] for direct excitation of the nanogap, Ref. [339] for remote excitation of the nanogap using SPPs, and Ref. [340] for discussion.

10.2 The experiment: comparing open circuit photovoltage signal of both directly and remotely excited bowtie devices before and after electromigration

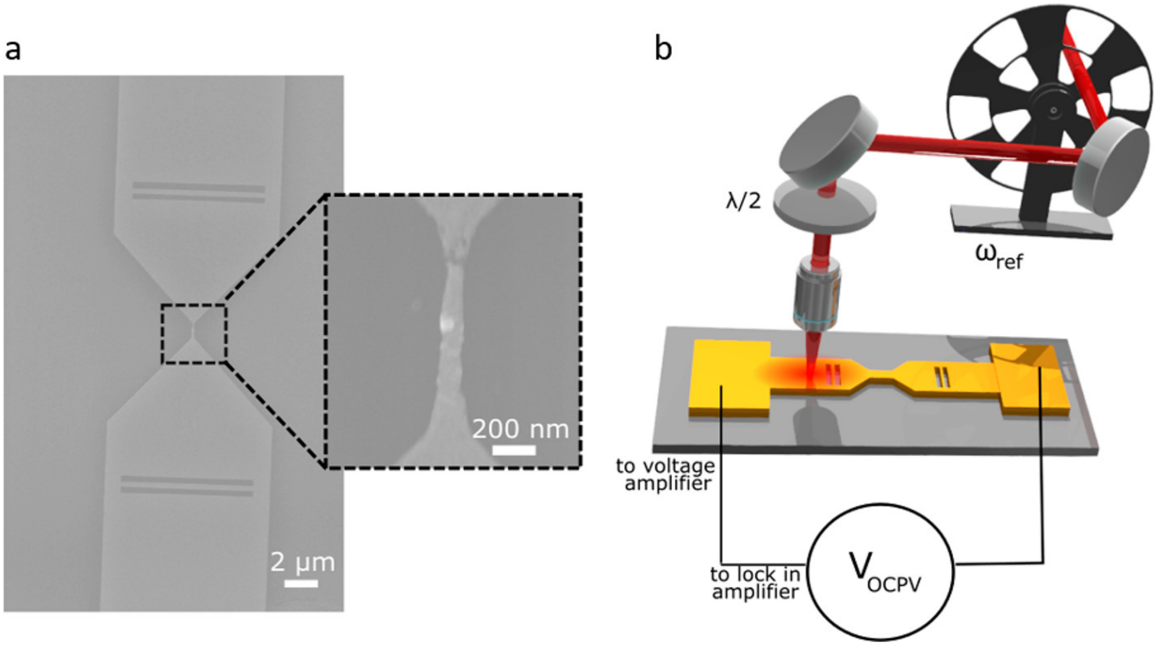

Figure 10.1 : *a*: SEM image of an electromigrated bowtie with grating. *b*: Schematic of experimental setup. Reprinted with permission from [339]. ©2019 American Chemical Society.

The devices studied in this chapter are both standard bowties[102] and bowties with gratings[339]. Nanogaps were formed in the nanowire constriction via electromigration, Fig. 10.1a, following the procedure detailed in Ch. 5.3. Because the gold thickness of the bowties with gratings is twice as thick as devices previously published

(Refs. [102, 113, 150, 151, 268, 274]), the electromigration process was slightly different. The NI DAQ could not source enough current to begin the electromigration process, so the Keithley 2400 SourceMeter was initially used until the device resistance reached around 100 Ω, and then the electromigration procedure was continued using the NI DAQ until the electrical conduction dropped below the conductance quanta, $2e^2/h = 12.9$ kΩ. The experimental setup measuring the OCPV is the same setup discussed in Ch. 6, with the schematic shown in Fig. 10.1b. The OCPV measurements were measured before and after electromigration for a series of devices with different grating distances between 5.2 μm and 10.2 μm from the nanowire.

10.3 Results: Enhanced photovoltages due to hot electron photocurrent in both directly and remotely excited plasmonically-active nanogaps

10.3.1 Electromigrating the nanowire: open circuit photovoltages in the nanogap enhanced around a factor of 1000

Scanning a standard bowtie prior to electromigration shows the same results discussed in Ch. 6, where the largest signal occurs at the interface of the nanowire constriction and the fan-out electrodes, Fig. 10.2a. This signal occurs because the Seebeck coefficient changes at the geometric change, resulting in a single metal thermocouple, which can be explained via the traditional Seebeck effect. A systematic study of the OCPV signal during the electromigration process was conducted. Because the stability of the intermediate resistances before gap formation improves at lower temperature, the measurements in Fig. 10.2 are conducted at 5 K unless specially noted. When the resistance was increased from the initial 61 Ω to 106 Ω, the OCPV map didn't change

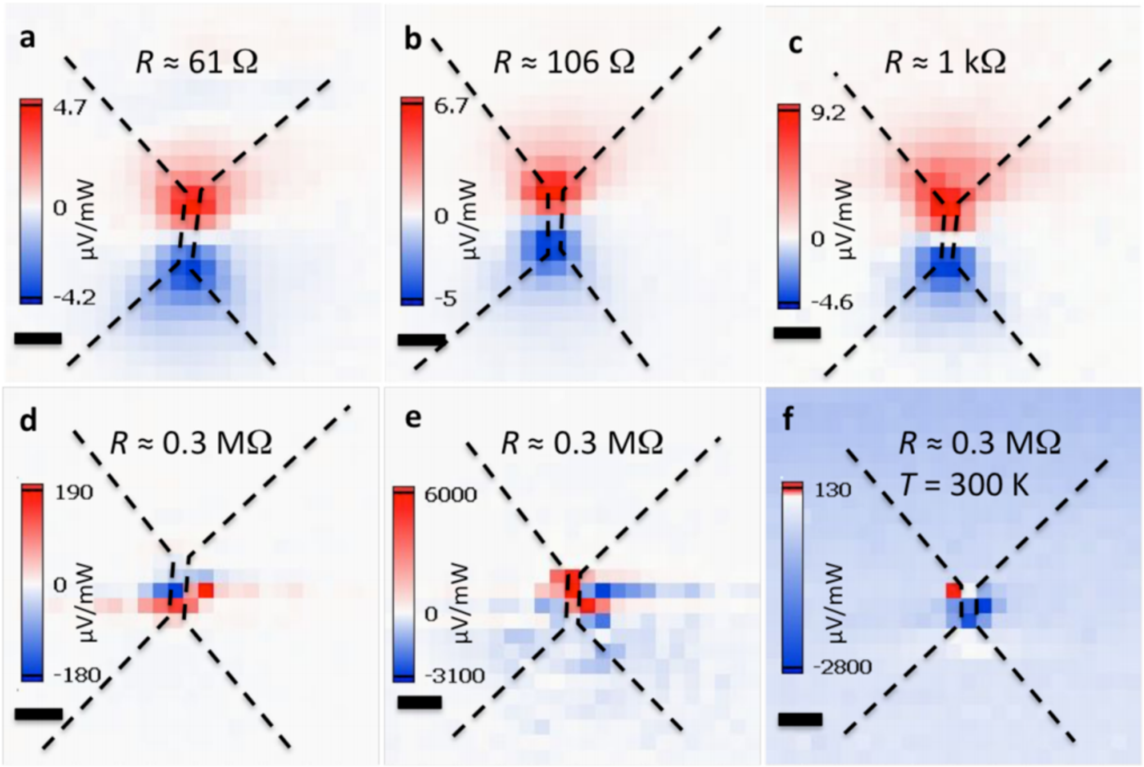

Figure 10.2 : Evolution of OCPV maps of nanowire constriction in a standard bowtie device without Ti adhesion layer during the electromigration process with a substrate temperature of 5 K. *a*: Initial scan prior to the eletromigration process. *b*-*d*: Subsequent scans of the same device, electromigrated to higher resistances. *e*: Subsequent scan of the device electromigrated to the same resistance as *d*. *f*: Subsequent scan of device at the same resistance as *d*, *e* with a substrate temperature at room temperature. The scale bars are 1 μm. The incident laser illumination is in the transverse polarization, perpendicular to the length of the nanowire. Reprinted with permission from [102]. ©2017 American Chemical Society.

very much, Fig. 10.2b. When the resistance increased to 1 kΩ, Fig. 10.2c, the spatial variation remained the same, with the largest signal occurring at the geometric change, but the signal magnitude was larger near the top electrode because the gap typically forms near the ground electrode during the electromigration process. This OCPV magnitude increased by a factor ~2 during this process.

Electromigrating the device above the conductance quantum will yield a nanoscale gap in the nanowire constriction. The OCPV response near the nanogap is significantly different than that of the unbroken case, Fig. 10.2d. Now, the OCPV signal is highly localized to the gap, with the length scale of the signal smaller than the spot size of the laser and no signal is observed at the geometric changes. The local OCPV is enhanced by $\sim 20\times$. Subsequent scans without further electromigration results in even larger OCPV enhancements, $\sim 1000\times$ larger than the pre-migrated case, Fig. 10.2e. Typically, subsequent scans had a dominant voltage in the nanogap, with one polarity dominating in the gap. The OCPV measured in these gaps were on the order of 10 mV *per mW* of incident laser power! Warming the device to room temperature did not change the observed pattern, Fig. 10.2f. The signal once again was confined to the nanogap.

The evolution of the OCPV signal during the electromigration process was also observed in the short circuit photocurrent measurements, top and bottom row of Fig. 10.3 respectively. In both cases, the pre-electromigrated device, Fig. 10.3a,d, have nearly symmetric spatial distribution of the OCPV and short-circuit photocurrent, respectively, at the interface of the nanowire and the fan-out electrodes. Once the electromigration begins but before the creation of the nanogap, the signal becomes enhanced on the side nearest the nanogap, Fig. 10.3b,e. Once the gap is formed, the signal becomes highly localized to the gap, Fig. 10.3c,f.

10.3.2 The enhanced open circuit photovoltages in the gap strongly depend on the plasmonic resonances and gap details

The signal in the nanogap is highly sensitive to the laser polarization, Fig. 10.4b. Under high power, the spatial variation of the OCPV changes scan-to-scan. The signal is highly localized to the gap with length scales on the order of one pixel

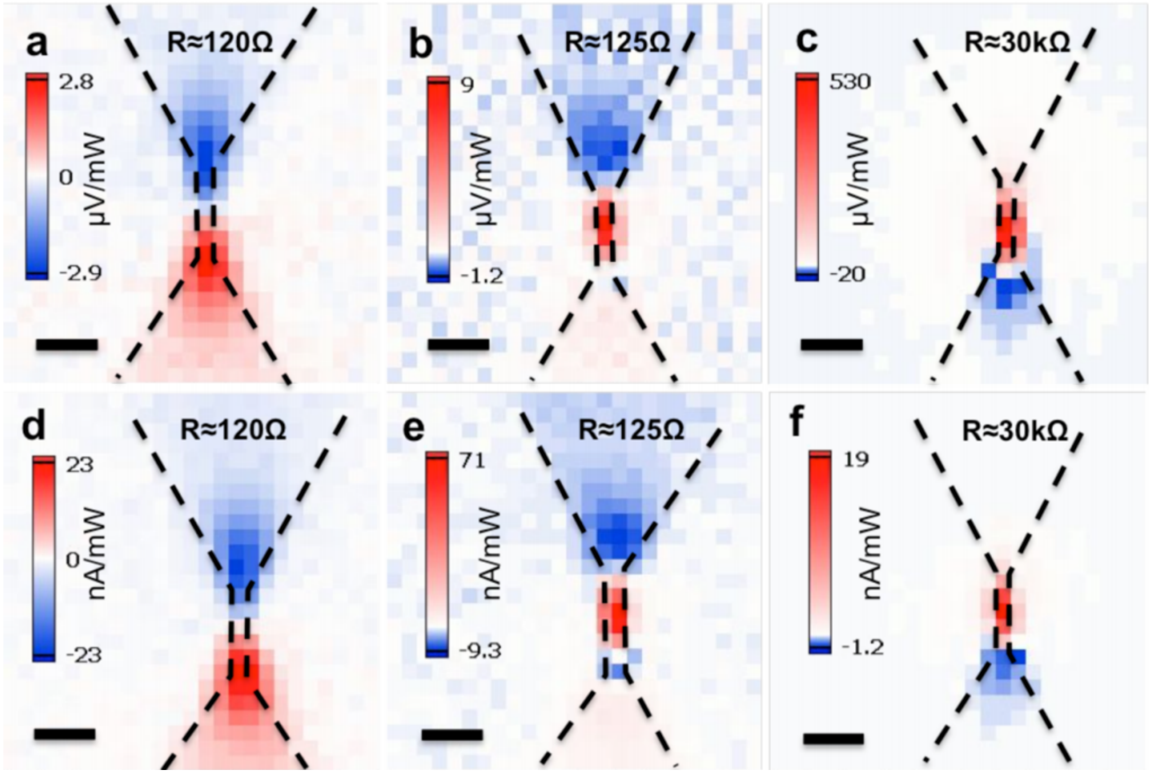

Figure 10.3 : Comparison of *top row* open circuit photovoltage measurements to *bottom row* short circuit current measurements during the electromigration process at room temperature. The scale bars are 1 µm. The incident laser illumination is in the transverse polarization, perpendicular to the length of the nanowire. Reprinted with permission from [102]. ©2017 American Chemical Society.

(∼ 0.3 µm) which is much smaller than the laser spot size. The instability of the scan-to-scan measurements indicates that the signal is sensitive to the local details of the nanogap. The strong polarization dependence suggests that the localized OCPV in the gap is enhanced due to the resonant plasmonic modes in the wire. Devices made of nickel do not have the transverse plasmon resonance, Fig. 10.5. Although there is localized OCPV signal in the nanogap after electromigration, the large enhancement factors of ∼ 1000× seen in the gold nanogaps are not observed in the nickel devices. Instead, the enhancement in the electromigrated nickel devices is ∼ 10× larger than

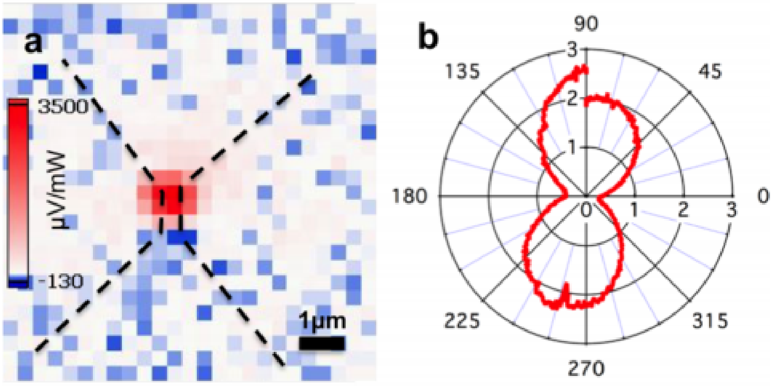

Figure 10.4 : *a*: OCPV map of an electromigrated device under 1 mW incident power. The lower power allowed for greater scan-to-scan stability. The scale bar is 1 μm. The incident laser illumination is in the transverse polarization, perpendicular to the length of the nanowire. *b*: polarization dependence of the OCPV in the nanogap. 90 degrees indicates the transverse polarization (perpendicular to the nanowire). Reprinted with permission from [102]. ©2017 American Chemical Society.

the pre-electromigrated case. This reduction in the OCPV enhancement within the gap is also observed in AuPd devices.[102]

10.3.3 The enhanced open circuit photovoltages cannot be described using traditional photothermoelectric effect arguments

In the devices without the nanogap, the traditional photothermoelectric effect is responsible for the spatial variation in the OCPV maps. The interface of the fan-out electrodes and the nanowire acts as an effective thermocouple as the change in geometry changes the local Seebeck coefficient. Heating this interface results in an open circuit OCPV meant to counteract the diffusion of electrons due to the applied temperature gradient from the incident laser. In the case of the electromigrated devices, the large enhancements of the OCPV cannot be explained solely using the traditional photothermoelectric effect, Fig. 10.6a. If one electrode is heated to a higher tem-

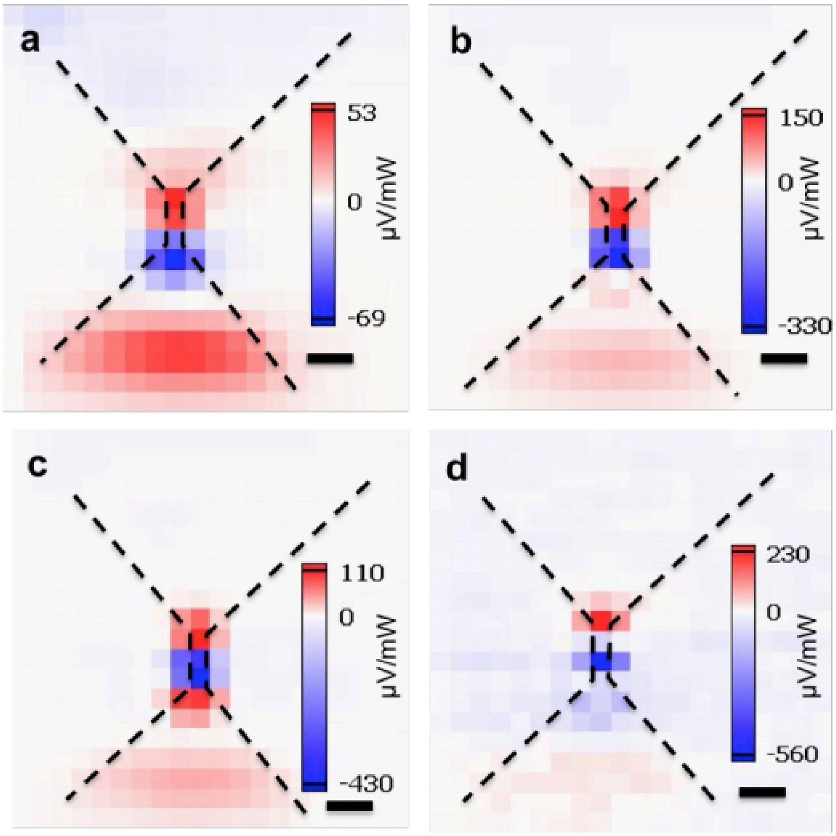

Figure 10.5 : Evolution of OCPV maps during the electromigration process of a Ni device. The device resistance in each panel was *a*: 190 Ω, *b*: 744 Ω, *c*: 2.9 kΩ, *d*: 48 kΩ. Reprinted with permission from [102]. ©2017 American Chemical Society.

perature than the other electrode, charge carriers will tunnel through the gap with an energy-dependent transmission probability. An open circuit voltage will build up to counteract this tunneling and will be set by the differences in Seebeck coefficients of the electrode and of the gap. The Seebeck coefficient of tunnel[341–343] and molecular[257, 344, 345] junctions is on the order of 10 μV/K, which would yield a significantly smaller response than what is observed. The nanogap likely has a Seebeck coefficient around that of atomic-scale junctions, which is even smaller than that of tunnel and molecular junctions.[346] Even accounting for potential contaminants and adsorbates in the nanogap using exaggerated Seebeck coefficients of 100 μV/K with a temperature rise of 10 K across the nanogap (with the substrate at room temperature), the maximum contribution from contamination is around an order of magnitude smaller than what is observed in plasmonic nanogaps.[102, 347, 348] Although the titanium adhension layer can oxidize which can have large effects on the Seebeck coefficient[349, 350] and can affect the conductance measurements of the device, the enhanced OCPV are seen in devices without the Ti adhesion layer, Fig. 10.2, and therefore cannot be the dominant mechanism for this enhancement.

Ref. [340] discusses some other potential causes of the enhanced OCPV in the nanogaps. In Ref. [292], it was shown that thermal boundary resistance can result in high local heating of the nanowire due to the plasmonic resonances within the wire. Direct illumination of the nanogap can result in high local heating in the electrodes. Thermal expansion of the electrodes can change the gap size which may affect the tunneling barrier, Fig. 10.6b. As the interelectrode spacing changes, so too does the zero-bias conductance. As a consequence, thermal expansion of the electrodes cannot be responsible for the enhanced OCPV which require no net current at zero bias. The incident photons can also exchange energy with the tunneling electrons in a process called photon-assisted transport, Fig. 10.6c. This energy exchange can allow for the electrons to tunnel through effective tunneling barriers that they otherwise would be unable to cross.[259, 261, 336, 351, 352] This increase of tunneling occurs in discrete steps of $V_{bias} = \hbar\omega/e$ due to the energy exchange with the incident photons.[351] which can result in transient photocurrent at zero-bias from the zero-bias current.[336] The photons can instead be absorbed by the metal electrodes, exciting a photoelectron through the photoelectric effect. If the photoelectron has enough energy to escape the electrode *and* has momentum toward the gap, these electrons can tunnel across

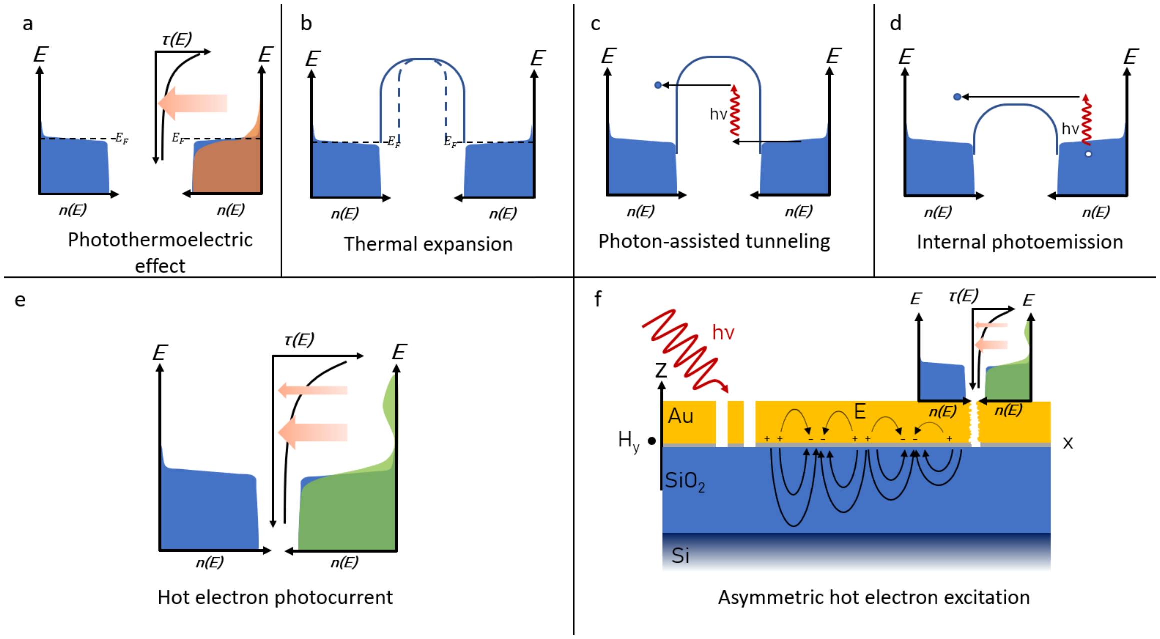

Figure 10.6 : Examples of photo-activated processes in tunnel junctions. *a*: Photothermoelectric effect. If one electrode is heated more than the other, the temperature-dependent Seebeck coefficient and energy distribution of the charge carriers will vary between the two electrodes. The energy-dependent transmission probability, $\tau(E)$, sets the magnitude of the effect. *b*: Thermal expansion. The inter-electrode separation can change under laser illumination due to a temperature rise, which changes the effective tunneling barrier. *c*: Photon-assisted tunneling. An electron gains energy from a photon as it tunnels across the the gap in conditions where tunneling is otherwise forbidden. *d*: Internal photoemission. A photon is absorbed by the metal electrode which excites a photoelectron with appropriate momentum directionality and energy to overcome the tunneling barrier to tunnel across the gap. *e*: Hot carrier photocurrent. The incident laser illumination excites a non-thermal distribution of charge carriers. The "hot" carriers with energy $\sim \hbar\omega$ can tunnel across the gap prior to relaxation. *f*: Remote excitation of hot electron from SPPs. SPPs propagate from a grating to the nanogap, exciting hot electrons which can tunnel across the gap. Asymmetric hot electron excitation, pictured, can occur when hot electrons are preferentially excited on the opposite side of the gap as the excited SPP. Figure adapted from Ref. [340]

the barrier, Fig. 10.6d.

A similar mechanism that likely is the biggest player in the enhanced OCPV is hot electron photocurrent, Fig. 10.6e. When the local plasmonic modes are excited under direct illumination, they can decay non-radiatively resulting in "hot" electron generation. The energy distribution in this case is non-thermal, and some of the hot carriers can tunnel across the gap prior to relaxing to thermal equilibrium.[353] Unlike photoemitted electrons, these "hot" carriers are excited from the local plasmons resulting in different energy distributions and do not have the same momentum directionality constraints that the photoemitted electrons have particularly at normal incidence. These hot electrons must tunnel across the gap before thermally relaxing to equilibrium which is not the case in photon-assisted tunneling. The OCPV expected from photon-assisted tunneling are expected to be orders of magnitude smaller than that of hot electron photocurrent.[261] As we will discuss later, hot electrons can be remotely excited via SPPs which propagate to the gap couple to the local modes before decaying nonradiately generating the hot electrons which can then tunnel across the gap. The OCPV measurements can provide insight on the details of how the SPPs couple to the local modes, such as asymmetric excitation of hot electrons where the SPPs more efficiently excite hot carriers on the opposite side of the gap, Fig. 10.6f.

10.3.4 Reasonable estimates of hot electron current yield similar open circuit photovoltage enhancements

In the previous section, several different photo-mediated tunneling processes were discussed as possible candidates for causing the large enhancements of the OCPV in the nanogaps. The OCPV measurements provided a way to eliminate several candidates as those mechanisms could not result in a zero-bias photocurrent. Other candidates were eliminated for either being irrelevant or of little significance. The most likely candidate for contributing the majority of the OCPV enhancement was hot electron photocurrent. In this particular mechanism, Fig. 10.6e, the electron energy distributions vary between the source and the drain. This difference in hot electron excitation can be due to asymmetric illumination between the electrodes and differences in local multipolar modes in the gap hybridizing with the dipolar resonance in the nanowire decaying non-radiatively on either side of the gap. If one side more efficiently excites "hot" electrons than the other, there will be a net photocurrent of hot electrons tunneling in one direction across the gap. A photovoltage will therefore be detected in the open circuit voltage measurement configuration due to the charge buildup that counteracts this tunneling.

In Ch. 3.2, the Landauer-Buttiker approach was used to describe electronic transport and define the conductance quantum. The Landauer-Buttiker approach can also be used to describe the hot electron photocurrent in a method that closely follows Ref. [353]. The photocurrent, I_p, of hot electrons tunneling from the source to the drain with electronic energy distributions $f_S(\epsilon)$ and $f_D(\epsilon)$, respectively, can be described by

$$\boxed{I = \frac{2e}{h}\int_{-\infty}^{\infty} d\epsilon [f_S(\epsilon) - f_D(\epsilon)]\tau(\epsilon)} \tag{10.1}$$

Landauer-Buttiker expression of current

where $\tau(\epsilon)$ is the energy-dependent transmission function. If the source electrode is illuminated, the time-dependent electronic energy distribution can be written as $f_S(\epsilon, t) = f_{S_{eq}}(\epsilon, t) + f_{S_p}(\epsilon, t)$, where the first term is the equilibrium Fermi-Dirac distribution and the second term accounts for the non-equilibrium effects from the light absorption. From this, $f_S(\epsilon) - f_D(\epsilon) = f_{S_{eq}}(\epsilon, t) - f_{D_{eq}}(\epsilon) + f_{S_p}(\epsilon, t)$. $f_{S_{eq}}(\epsilon, t) - f_{D_{eq}}(\epsilon)$ just shows the difference in the equilibrium temperatures of the source and drain electrodes and accounts for the standard photothermoelectric effect where $f_{D_{eq}}(\epsilon) =$

$[e^{\epsilon-\mu/k_BT_e}+1]^{-1}$ with electronic temperature T_e and chemical potential μ.

More interestingly is the non-equilibrium contribution to the photocurrent induced by the light absorption, $f_{D_p}(\epsilon,t)$. Because timescales of these experiments are much longer than the thermalization[81], considering the non-equilibrium photocurrent, I_p, due to steady state, CW illumination of frequency ω_I incident on *only the source electrode* provides the upper limit of the hot electron photocurrent. I_p is described by

$$\boxed{I_p = \frac{2e}{h}\frac{\dot{N}_I}{\hbar\omega_I}L(\omega_I)\int_{-\infty}^{\infty} d\epsilon \frac{\tau_e(\epsilon)}{\rho(\epsilon)}\frac{\tanh\left(\epsilon/2k_BT_e\right)}{1+e^{-\hbar\omega_I/k_BT_e}\cosh(\epsilon/k_BT_e)}\tau(\epsilon)} \tag{10.2}$$

non-equilibrium photocurrent from hot carriers under CW illumination

with photons per second per atom $\dot{N}_I$, absorption linewidth $L(\omega_I)$ that depends on the specifics of the geometry, composition, and environment of the nanogap, relaxation time of the non-equilibrium distribution $\tau_e(\epsilon)$, density of states per atom $\rho(\epsilon)$, and energy-dependent transmission function $\tau(\epsilon)$. For a simple tunnel junction with one conductance channel, $\tau(\epsilon)=\Gamma_S\Gamma_D[(\epsilon-\epsilon_o)^2+(1/4)(\Gamma_S\Gamma_D)^2]^{-1}$ with resonance energy ϵ_o and resonance widths of the source and drain electrodes, Γ_S and Γ_D respectively. If Γ is small compared to $\epsilon-\epsilon_o$ and $\epsilon_o/k_BT >> 1$, I_p can be simplified to

$$\boxed{I_p \sim \frac{e}{\hbar}\frac{\dot{N}_I}{\hbar\omega_I}L(\omega_I)\frac{\tau_e(\epsilon_o)}{\rho(\epsilon_o)}\frac{1}{1+\frac{1}{2}e^{\epsilon_o-\hbar\omega_I/k_BT_e}}\frac{\Gamma_S\Gamma_D}{\Gamma_S+\Gamma_D}} \tag{10.3}$$

simplified non-equilibrium photocurrent from hot carriers under CW illumination

Considering the OCPV configuration to counteract I_p yields

$$\boxed{I_p = -\frac{2e^2}{h}\tau(\epsilon=0)V_{OCPV}} \tag{10.4}$$

photovoltage response to non-equilibrium photocurrent

From Equation 10.4, V_p can be estimated. Γ can be estimated via resistance measurements of the nanogap without laser illumination. Typical values are ~ 0.1 for a 10 MΩ device, with resonance energy $\epsilon_o \sim 2.7$ eV. Considering the 10 mW incident power (400 kW/cm^2) with 10^{19} atoms per m^2 amounts to 4×10^{-10} W/atom. Considering 785 nm laser illumination (1.57 eV), $\dot{N}_I = 1.6 \times 10^9$ photons/atom/second. The density of states can be estimated using the free elecron model, $\rho(\epsilon) \sim 0.1\mathrm{eV}^{-1}$.[353] From COMSOL simulations $L(\omega_I) \sim 0.05$. Conservative estimates of $\tau_e \sim 10^{-14}$ s which gives $I_p \sim 0.5$ nA or $V_p \sim 5$ mV where $V_p = I_p / \frac{\mathrm{d}I}{\mathrm{d}V}$ where $\frac{\mathrm{d}I}{\mathrm{d}V}$ is the zero-bias conductance of the device. OCPVs of this magnitude were observed in the nanogaps and have been reported by other groups.[258, 261, 262]

As shown in Fig. 10.5, although the OCPV signal is localized to the gap of a non-plasmonically resonant device, the signal is significantly smaller than that of a plasmonically resonant device. This, coupled with the strong polarization dependence in Fig. 10.4 and the device-to-device variation and temporal fluctuations indicate that the OCPV are extremely sensitive to the plasmonic details in the gap. The specific details of the nanogap set the resonant energy and the local effective electronic temperatures, which exponentially affect I_p. As the atomic-scale details change under illumination, so too does the plasmonic resonances and therefore the measured V_p.

10.3.5 Remote excitation of hot electrons via surface plasmon polaritons enhance open circuit photovoltages by a factor of 100

Adding gratings to the electrode design allows for propagating SPPs to be launched toward the nanogap. As discussed in Ch. 9, the SPPs in devices with an intact nanowire could be detected using electronic transport measurements. OCPVs could provide indication of how the SPPs couple with the local modes in the nanogap. The OCPV signal of a device with gratings 9.2 µm and 10.2 µm away from the nanowire constriction was measured before and after electromigration to a resistance of 100 kΩ, Fig. 10.7. Scanning around the nanowire constriction prior to electromigration, middle panel in Fig. 10.7a, behaved as a single metal thermocouple, as observed in Ch. 6, where heating the interface of the electrodes and the nanowire has the largest response due to the geometric nanostructuring. The polarization dependence of the OCPV near the unbroken nanowire does not have as much polarization dependence as seen in Ch. 6 because the thickness of the device shifts the local surface plasmon resonance within the nanowire. Additionally, the polarization data is taken where the OCPV signal is largest, at the interface of the electrodes and the nanowire, as opposed to centered on the nanowire itself. However, the transverse polarization still has a larger response than that of the longitudinal polarization. The sign of the OCPV is determined by the sign of the local temperature gradient; shining the laser on the side nearest the ground (oriented at the bottom of Fig. 10.7) results in a negative voltage.

When the gratings on either side of the constriction are illuminated with longitudinally polarized light instead, a slight increase in the OCPV is detected. The magnitude of the signal is approximately two times larger when the laser is incident on the grating, as opposed to when the laser is present elsewhere on the gold. The small OCPV signal can be explained because the temperature rise due to SPPs is small, on the order of 0.3 K, as determined by Ref. [334]. When the gratings are illuminated with light in the longitudinal polarization, SPPs are excited along the length of the device. The SPP remotely excites the nanowire constriction and the dissipation of the SPP in the electrodes and nanowire result in an assymmetric heating profile; the

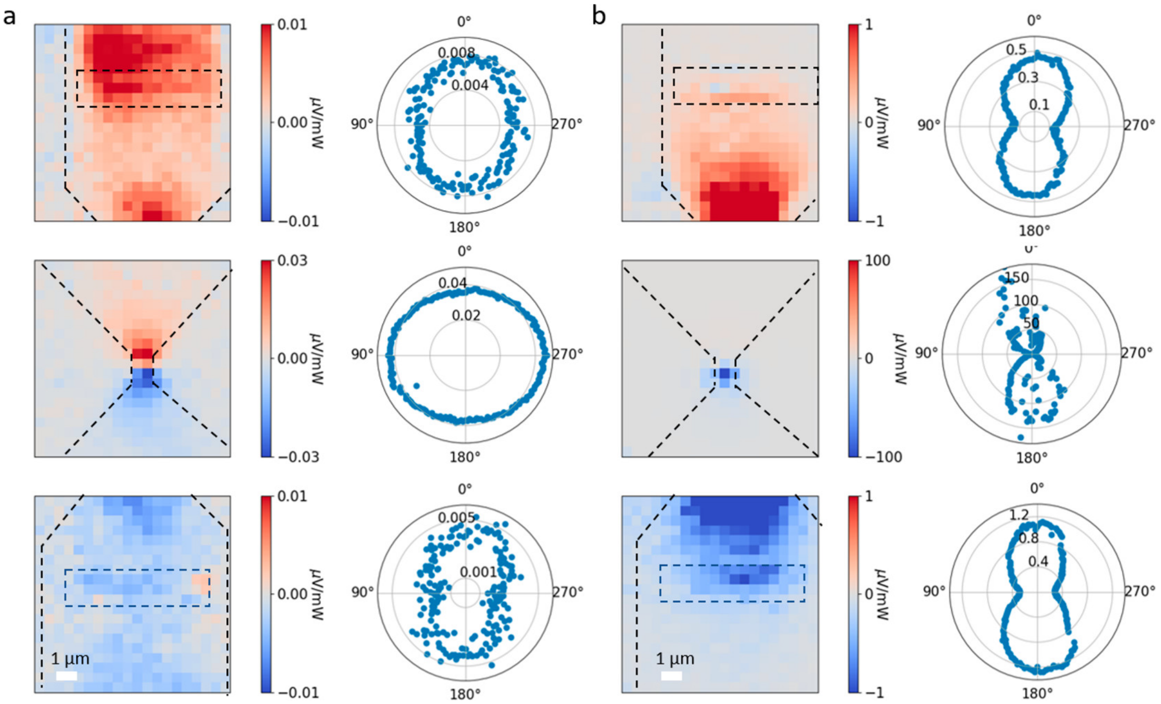

Figure 10.7 : *a, b*: Comparison of OCPV maps at constriction and grating before and after electromigration to 100 kΩ, respectively. The top row shows the 2D OCPV map of the top grating and the polarization dependence of the OCPV with the laser incident on the top grating. The middle row shows the 2D maps and polarization dependence around the constriction. The bottom row shows the measurements for the bottom grating. All OCPV maps were measured with the laser under the longitudinal polarization (perpendicular to the grating, parallel along the length of the device) to excite the SPP modes. The signal at the junction is enhanced by a factor of 3000 after electromigration, whereas the signal at the gratings is enhanced by a factor of 100. Reprinted with permission from [339]. ©2019 American Chemical Society.

nanowire is heated more on the side of the illuminated grating due to this dissplation. Therefore, the OCPV detected when the laser illuminates the grating has the same sign as the OCPV detected at the interface of the same side electrode and nanowire interface. In other words, illuminating the grating near the ground results in a negative OCPV signal. The polarization dependence of the OCPV when the grating is illuminated is much more pronounced than when the constriction is illuminated. The maximum signal occurs when the laser is in the longitudinal polarization due to the excitation of the SPPs, as previously discussed in Ch. 9.

Electromigrating the device above the conductance quantum will yield a nanoscale gap in the nanowire constriction. Fig. 10.7b shows the OCPV response near the nanogap and gratings after electromigrating to 100 kΩ. The OCPV response near the nanogap is significantly different than that of the unbroken case. Now, the OCPV signal is highly localized to the gap, with the length scale of the signal smaller than the spot size of the laser. Additionally, only one sign of the OCPV is detected. The signal at the nanogap is *3000 times* larger after than prior to electromigration. As discussed in Sec. 10.3.3, this signal cannot be attributed entirely on the thermoelectric effect; the Seebeck coefficient of tunnel[341] and molecular[257, 344, 345] junctions is on the order of 10 μV/K, which would yield a significantly smaller response than what is observed. The nanogap likely has a Seebeck coefficient around that of atomic-scale junctions, which is even smaller than that of tunnel and molecular junctions.[346] Additionally, as the laser spot size is 1.8 µm in diameter, significantly larger than the nanogap, the temperature distribution across the gap should be fairly uniform. Both of these considerations make it clear that the OCPV enhancement cannot be explained using the traditional thermoelectric effect. Instead, as discussed in Sec. 10.3.3, the enhancement of the OCPV is likely the response to counteract the hot electrons, excited by the resonant plasmonic modes in the nanogap, tunneling across the gap.[102, 353] The single polarity of OCPV at the nanogap, therefore, indicates that the specific details of the nanogap (and therefore the local plasmonic modes) make hot electron generation more preferable on one side than the other, resulting in a net current from one side to the other.[255, 256, 354, 355] To support that the signal is from hot electron tunneling, with one side preferentially generating more hot electrons with momentum suitable for tunneling due to the atomic details of the nanogap as opposed to some vastly different transmission probability between the electrodes, Fig. 10.8 shows that although the hot electron tunneling may be asymmetric, the differential conductance measurements are symmetric indicating that the source-drain transmission probabilities are nearly identical. The symmetry in the differential conductance measurements and lack of correlation between the electronic transport measurements to the OCPVs additionally eliminate optical rectification[92, 113, 266, 338, 340] as the dominant mechanism.

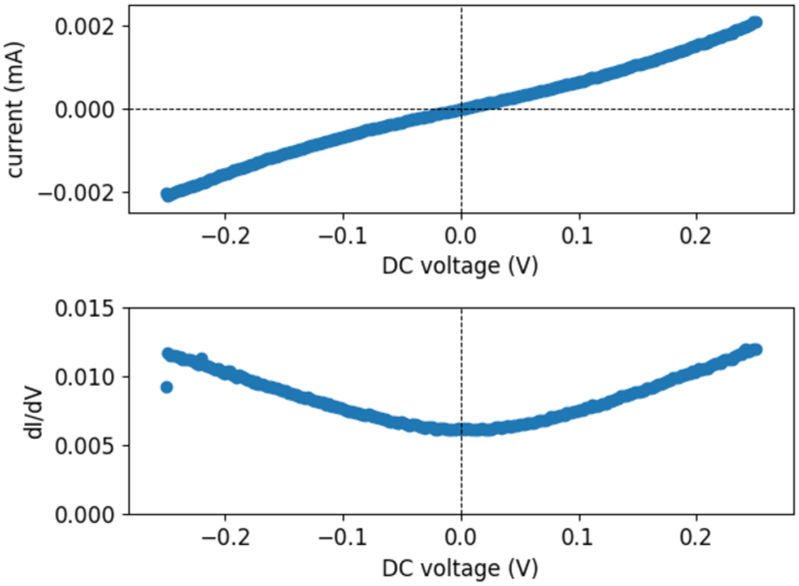

Figure 10.8 : Differential conductance of a device with a nanogap: The symmetry about 0 V indicates that the transmission probabilities between the source and drain are identical, and not the culprit for the asymmetric hot electron tunneling across the gap. Reprinted with permission from [339]. ©2019 American Chemical Society.

The polarization dependence of the OCPV when the laser is incident on the gap provides some additional information. First the dominant polarization varies device-to-device. As seen in the middle row of Fig. 10.7b, the OCPVs show maximum signal when the laser is in the longitudinal polarization, the ”lightning rod” mode. Fig. 10.4 shows the OCPVs having maximum signal in the transverse polarization. This strong, but varying, polarization dependence indicates that the OCPVs are a result of the incident laser coupling with the local plasmonic modes, specific to the details of the nanowire geometry and atomic-scale details of the gap. Fig. 10.9 shows a scatter plot indicating the ratios of the OCPV as a function of electromigrated resistances, indicating that the details of the gap leading to multipolar plasmonic modes play an important role in the hot electron generation, which then tunnel across the gap. Under laser illumination, the atomic-scale details of the nanogap can change with time. When this happens, the multipolar plasmonic modes, and therefore the enhancement of the OCPVs, change as well. The polarization dependence of the OCPV of the gap shows instability, Fig. 10.7b, providing further evidence that the plasmonic coupling plays the dominant role in OCPV enhancement.

When the laser is incident on the gratings after electromigration, the signal at the gratings is additionally enhanced, top and bottom panels of Fig. 10.7b. The polarization dependence shows strong response when the laser is in the longitudinal polarization, indicating that the signal is primarily a response of remote SPP excitation. When the laser is incident on the grating in the longitudinal polarization, clear response is shown as seen in the maps of Fig. 10.7b. The signal at the gratings is enhanced by around *100 times* after electromigration, compared to the signal before electromigration. As evidenced in the intact case, and in Ch. 9, the temperature rise from the SPPs cannot be responsible for the temperature rise alone. Although heating from SPPs can result in thermal expansion near the gap, changing the geometric details of the gap, the zero-bias differential conductance would be nonzero in this scenario, which cannot produce a zero-bias OCPV. Instead, the SPPs can

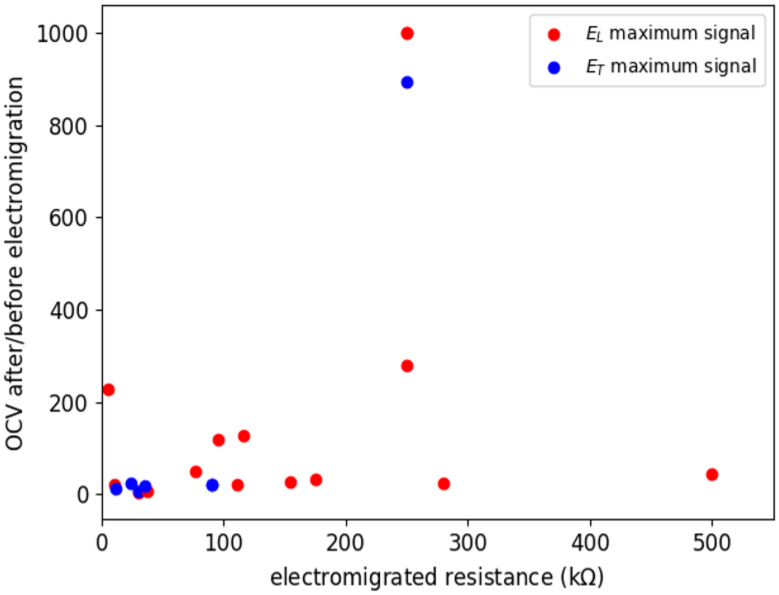

Figure 10.9 : Ratios of the OCPV detected at the nanogap after and before electromigration as a function of electromigrated resistance. The red data shows devices with maximum signal under longitudinal polarization whereas the blue data shows devices with maximum signal under transverse polarization. Reprinted with permission from [339]. ©2019 American Chemical Society.

hybridize with the local modes in the nanogap and the resonant local dipole mode in the wire which can decay radiatively, emitting a photon, or non-radiatively to excite hot electrons. The excited hot electrons with the correct directionality of momentum can then tunnel across the gap, resulting in an OCPV to counteract the hot electron current.

10.3.6 Asymmetric hot electron excitation via surface plasmon polaritons detected

The OCPV measurements can provide details about how the SPP couples with the local modes of the nanogap. In Fig. 10.10a, a device has an anomalously close bonding pad near the bottom grating. When the nanowire is intact, *left*, the top grating has the same OCPV polarity as the same side of the nanowire constriction as observed in Fig. 10.7, which demonstrates that the SPP most efficiently couples with and locally heats that side of the nanowire constriction.[334] The bottom grating, however, has the opposite polarity of signal compared to the same size of the nanowire constriction. This time, the excited SPPs more efficiently couple with and heat the contact pad/device interface compared to the nanowire constriction. After electromigration, *right*, the bottom grating's signal polarity changes. This time, the polarity matches that of the nanowire constriction indicating that the excitation of hot electrons that tunnel across the gap has a much larger contribution to the OCPV than the heating of the contact pad-device interface. The polarity of the top grating does not change, the SPPs couple to the local modes in the nanogap and excite hot electrons that tunnel across the gap, albeit in the opposite direction than the preferential direction of direct gap illumination.

Fig. 10.10b shows a different scenario. Like in Fig. 10.10a, a contact pad is anomalously close, this time near the top grating which is readily apparent in the case of the intact wire, *left*. This time, the SPPs excited via illumination on the top grating more efficiently couples with the contact pad than with the nanowire constriction whereas those excited via illumination of the bottom grating couple with and locally heat the nanowire. After electromigration, *right*, the signal at *both* gratings have the *same* polarity as the OCPV at the nanogap! This means regardless of which direction the SPPs excite the nanogap, the hot electron current flows in a *single* direction. In this case, direct illumination of the nanogap results in preferential hot electron current toward the bottom electrode. Illuminating the top grating excites hot electrons on the same side of the nanogap, with the largest contribution to the OCPV coming from the coupling with the local modes in the nanogap than with the bonding pad as

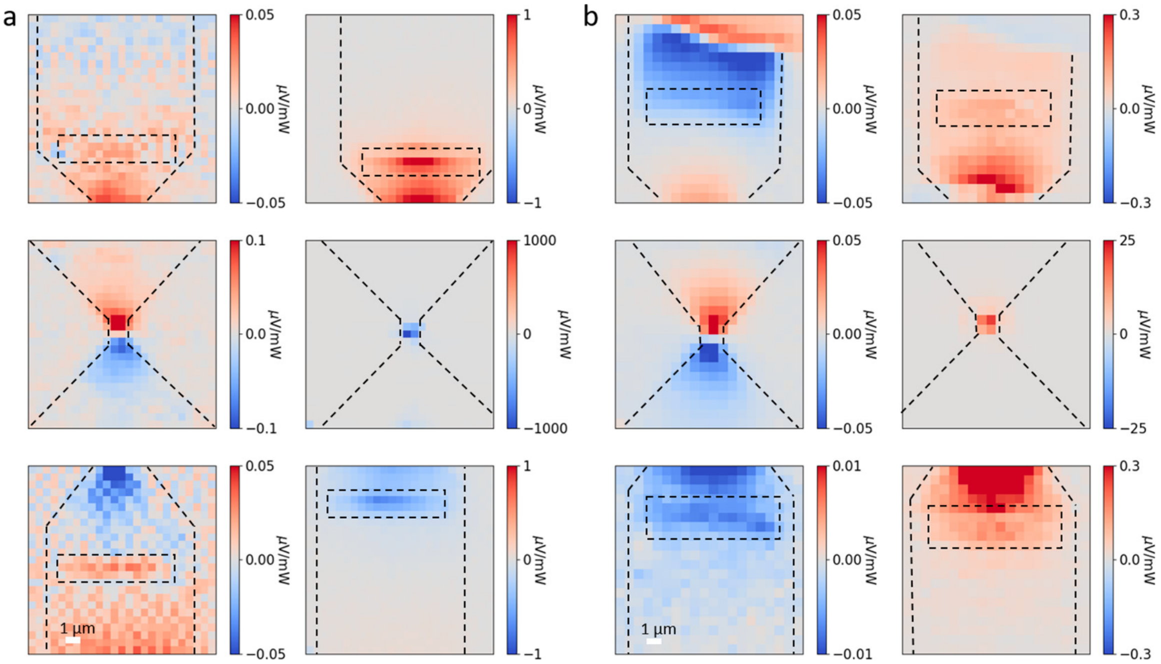

Figure 10.10 : Asymmetryic hot electron generation from surface plasmon polaritons. *a*: *left*: OCPV maps of a device prior to electromigration with an anomalously close bonding pad on the bottom. The top grating has an OCPV whose polarity matches that of the same side of the nanowire-electrode interface, indicating efficient heating of the nanowire. The bottom grating more efficiently heats the bonding pad below it than the nanowire constriction resulting in the opposite polarity of OCPV compared to that of the nanowire-electrode interface. *right*: OCPV maps of the same device after electromigration. The bottom grating this time has a negative OCPV signal which indicates that OCPV contribution of the SPPs exciting hot electrons in the gap exceeds that of the SPPs heating the bonding pad. *b*: OCPV of a device prior to electromigration with a close bonding pad on the top. The bottom grating has OCPV polarity as the nanowire constriction, but the top grating better couples with the bonding pad instead of the nanowire constriction. *right*: After electromigration, both gratings have the same polarity of OCPV as the nanogap, indicating asymmetric hot electron excitation. The incident polarization in all of these figures is in the longitudinal polarization. Reprinted with permission from [339]. ©2019 American Chemical Society.

in the pre-electromigrated case, which tunnel across toward to the bottom electrode which has been observed in Fig. 10.7 and Fig. 10.10a. Illuminating the bottom grating more efficiently excites hot electrons *on the opposite side of the nanogap* counter to the thermal gradient, as depicted in Fig. 10.6f. This surprising result indicates that the hot electron generation is from the decay of the hybridization of the SPPs with the local modes in the gap as opposed to simply the decay due to the SPPs themselves!

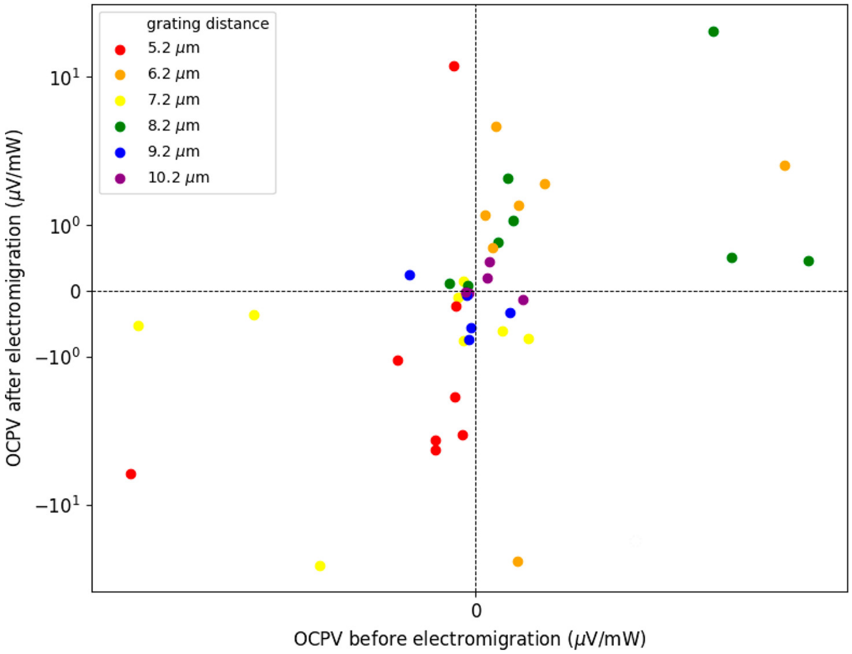

Figure 10.11 : Log-log scatter plot comparing the OCPV signal at the grating before and after electromigration. Quadrants I and III show gratings whose OCPV polarities remained unchanged before and after electromigration, whereas Quadrants II and IV show gratings whose OCPV change after electromigration. Reprinted with permission from [339]. ©2019 American Chemical Society.

To demonstrate the frequency of the OCPV at the gratings changing polarity after electromigration, a log-log scatter plot of the OCPV of all 42 gratings measured after vs. before electromigration is seen in Fig. 10.11. Quadrants I and III show the 32 gratings that did not change polarity after electromigration. In these quadrants, the gratings more efficiently heated the nanowire constriction prior to electromigration *and also* excited hot electrons on the same side of nanogap as the SPP. Quadrants II and IV, however, show the 10 gratings whose OCPV polarities changed after electromigration. Gratings in these quadrants *either* more efficiently excited the bonding pad than the nanowire prior to electromigration but then coupled more efficiently with the local modes in the nanogap exciting hot electrons on the same side as the excited SPP that tunnel across the gap *or* gratings that asymmetrically excite hot electrons on the opposite side of the gap after electromigration. Fig. 10.11 also shows the large variation of device-to-device OCPV measurements. This variation is due to the exponential dependence of the resonant energy and effective temperatures of the non-thermal carriers in Equation 10.3 and the specifics how the SPPs can couple to the local modes of the nanogap which vary due to the atomic-scale details of the gap.

10.4 Discussion and conclusion: open circuit photovoltages provide a wealth of information about plasmonically-active nanoscale devices

In the case of the gold bowtie devices with an intact wire, the OCPV signal observed at both the nanowire and the gratings is due to the traditional thermoelectric effect. Heating either the geometric change at the nanowire or the grating results in asymmetric temperature gradient across the gap. The change of Seebeck coefficient at the geometric change results in a single metal thermocouple with an OCPV due to the applied temperature gradient. Once a nanogap is formed in the nanowire due to electromigration, the dominant mechanism is no longer the traditional thermoelectric effect. Instead, when the nanowire is directly illuminated, the OCPV is largely enhanced by $\sim 1000\times$ with the observed enhancements due to direct illumination shown in a histogram in Fig. 10.12. Although many different tunneling mechanisms can occur in an illuminated tunnel junction, the dominant contribution of the OCPV enhancement is likely due to charge distributions working to counteract hot electron photocurrent excited due to the plasmonic modes in the nanogap.

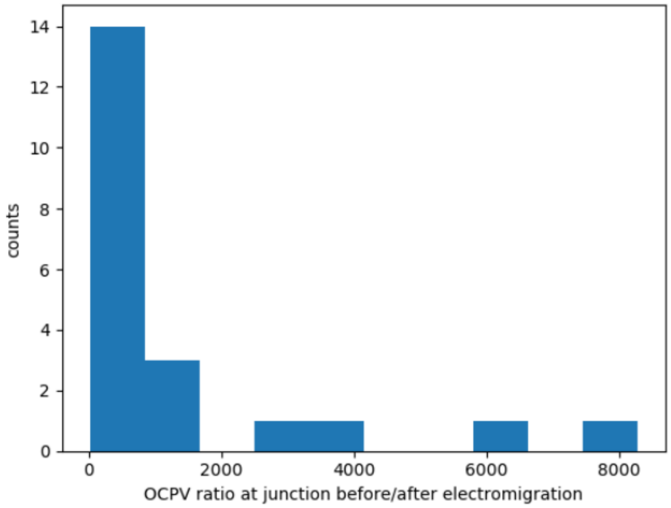

Figure 10.12 : Histogram of the ratio of OCPV observed in the nanogap before and after electromigration. The OCPV is largely enhanced in the nanogap after electromigration. Reprinted with permission from [339]. ©2019 American Chemical Society.

Illuminating gratings instead allows for the excitation of SPPs which then propagate to the nanogap and hybridize with the local modes in the nanogap. The OCPV measurements provide insight on how the SPPs couple with the local modes of the nanogap, with asymmetric hot electron generation detected in 3 out of 21 devices. The OCPV signal at the grating is enhanced after electromigration, $\sim 100\times$ larger prior to electromigration, Fig. 10.13. Although the enhancement is much smaller than that of direct illumination, this OCPV enhancement at the gratings demonstrates that the SPPs efficiently couple with the local modes in the nanogap which excite hot electrons with appropriate momentum to tunnel across the gap.[255, 256, 354, 355]

The asymmetric generation of hot electrons also indicates that this enhancement is due to the hybridization of the SPP and local gap modes.

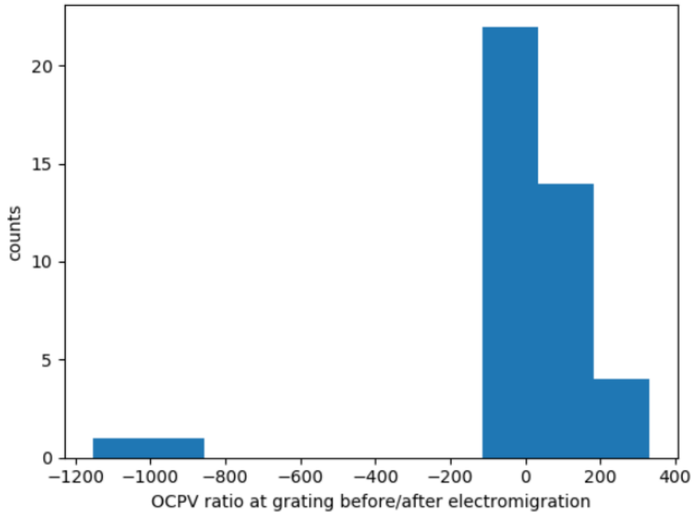

Figure 10.13 : Histogram of the ratio of OCPV observed in the grating before and after electromigration. The OCPV is enhanced in the grating after electromigration though to a lesser extent than that of direct illumination of the gap. The OCPV can also change polarity after electromigration. Reprinted with permission from [339]. ©2019 American Chemical Society.

These studies show that open circuit photovoltages are not only a way to probe intrinsic variations such as strain or impurities or local changes in geometry within nanoscale devices but also an excellent way to elucidate the tunneling mechanisms occurring in nanoscale, plasmonically-active tunnel junctions. These photovoltages are sensitive to the plasmonic resonances within the gap, the resonant energy in the gap, and the effective electronic temperature. The same techniques allow for detection of remote hot carrier excitation from surface plasmon polaritons and provides details on the coupling of the propagating SPPs to the local multipolar modes in the nanogap and dipolar mode within the nanowire.

Chapter 11

Conclusions

In this thesis, the photothermoelectric effect and electronic transport measurements were used to characterize gold nanoscale devices under laser illumination. Nanostructuring devices can allow for single metal thermocouples, which can allow for wavelength-specific photodetection when the device is structured with plasmonically resonant structures. Although the photothermoelectric effect can be used to determine the location of geometric changes in a nanoscale device, the results in this thesis show that this measurement is sensitive to more subtle changes, such as strain and platinum impurities, that can be challenging to detect using other electronic transport or conventional imaging techniques. The photovoltage measurements additionally provide insight on the specific details within a plasmonically-active nanogap; enhanced photovoltages, highly localized within a nanogap from electromigration, can indicate which side of a nanogap more efficiently generates non-thermal "hot" electrons which tunnel across the gap when under laser illumination of a specific polarization. Remote excitation of hot electrons via surface plasmon polaritons, which propagate from a grating in the electrode design to the nanogap, is also detected using photovoltage measurements. The plasmonic resonances within the nanowire, which allow for the hot electron generation and the single-molecule sensitivity for Raman spectroscopy, and high thermal boundary resistance, can result in high local heating of the nanowire when under direct illumination at low substrate temperatures, making it impossible to take true low temperature optical measurements. Electronic transport measurements allow for an estimation of this temperature rise, and additionally, provide evidence that remotely exciting the nanowire using surface plasmon polaritons can sufficiently reduce that temperature rise while still coupling to the local modes within the gap. The photovoltage measurements provide details of how the surface plasmon polaritons specifically couple to the local modes in the nanogap, particularly in the case of asymmetric hot electron generation.

11.1 Possible future directions

11.1.1 Photothermoelectric effect

Current work is underway looking at the effect of surface modification on the photothermoelectric effect, using self-assembled monolayers to shift the work function of the gold. Simplifying the underlying nanostructure to a single crystalline device can reduce the background photovoltage signal due to the strain profile in the polycrystalline wire. Additionally, work is currently being conducted to use nanostructuring of devices to create wavelength-sensitive photodetectors. Extending this work to include waveguides on substrates of varying oxide thicknesses can allow for better-resolved wavelength detection; the excitation of surface plasmon polaritons is highly sensitive to the dielectric environment as well the specifics of the particular wavelength coupling into the particular geometry of the gratings.

As seen in the contact design of the single- and bi-crystal devices, the phothothermoelectric voltages can be used to map out surface features of thin films. This photovoltage mapping could be extended to include more complicated geometries; adding the photovoltages detected under two perpendicular polarizations may provide full details of the film's surface!

Polycrystalline gold nanowires have surprising spatial variation in detected photovoltages; likely due to the specifics of the variation in strain of the film. The specific details of metal deposition during electron beam evaporation affects the strain profiles in thin films, which has been studied extensively in noble metals.[66, 67] A thorough study of photovoltage signal due to deposition conditions, including rates, temperatures, thickness, and vacuum levels, could be conducted for various metals. These effects from strain could become significantly more pronounced in materials with large ZT values. Graphene nanoribbons with optimized patterns show promise of high ZT values[356, 357]. Studies of strain engineering graphene devices have shown that graphene can withstand elastic strains on the order of 20%[64], which can significantly change the thermal conductivity[65] and the band gap[358, 359], therefore affecting the ZT value. Extending the photovoltage measurements to strain engineered graphene nanoribbons can provide ways to tune the thermoelectric response.

Enhanced photovoltages are detected in electromigrated nanowires which can be attributed to the hot electrons, generated from the plasmonic resonances sensitive to the specific atomic details of the gap, which then tunnel across the nanogap. Mechanically controllable break junctions can allow for a systemic study of well-defined gaps[114]. Asymmetric hot electron generation in these junctions has been detected[360]. A comprehensive study of the photovoltage signal as a function of gap size in a mechanical break junction can provide insight on the specific details of hot electron generation in these systems.

11.1.2 Remote excitation of nanpgap systems

Understanding how electronic and vibration states exchange energy in single molecule junctions through simultaneous electronic transport and optical measurements is a challenging but important task to understanding heat flow in nanoelectronics. The gold bowtie devices allow for both optical and electronic transport measurements to be conducted, however the local heating due to plasmonic resonances and thermal boundary resistance make detecting these interactions at low temperatures challenging to detect. Remotely exciting the nanogap using surface plasmon polaritons from gratings in the electrode design reduces the temperature rise of the gap by up to a factor of 60 while still having clear electronically detectable signal. The photovoltages detected at the grating after electromigration is enhanced by a factor of 100, compared to that before electromigration. As such, this remote excitation technique appears to be a promising path forward for true, low temperature simultaneous optical and electronic transport measurements.

Using the remote excitation route has some challenges that must be overcome. First, the light emitted at the nanogap from remote excitation cannot be detected using confocal microscopy, where a spatial filter in the form of a pinhole is placed to eliminate out-of-focus light. This technique is frequently used to increase resolution and contrast in imaging.[361] Additionally, the light detected at the nanogap will be less intense than what is detected at the grating. Furthermore, rough edges at the grating can provide SERS enhancement of molecules or contamination at the grating. One potential way to mitigate these issues is to take Raman spatial maps before and after electromigration and subtracting the two images. The SERS enhancement at the grating should be unaffected by the electromigration process, whereas the signal enhancement at the nanogap should only appear after electromigration. Conducting Raman measurements of clean junctions, looking for an increase of low wavenumber Raman signal can reduce the complications of signal at the grating; although there is no molecular junction in this case for electronic transport measurements, this could provide a way to determine whether the light emitted at the nanogap is at detectable levels.

Appendix A

Experimental methods and software

A.1 Cryostation and device naming convention

Around 2015, the cryostation changed from a small optical cryostat to the Montana Instruments closed cycle cryostation with an optical window. In all cases, the measurements were taken under high vacuum with an Edwards T-Station 75 turbo pump. The major difference is that the older cryostat was cooled with an open flow and did not have the temperature control and stability of the Montana Instruments cryostation. The chip carrier of the two systems were different, also, with the Montana Instruments cryostation having a LCC 28 (leadless chip carrier) specially made by Montana Instruments whereas the older cryostat used a CERDIP (CERamic Dual In-line Package) carrier with 16 total pins. By the way, the ground pin of the chip carrier for the old cryostat should be bent slightly before insertion as the connection to the cryostation is usually faulty there. I am the last student who used the older cryostat for the “main setup” measurements. The easiest way to tell if a data set was taken with which cryostat is by the nomenclature of the device. Each chip had a common ground with two columns of bonding pads. The older chips had 7 in each column (totaling 14 devices), whereas the newer chips had 12 in each (24 total devices). I referred to individual devices in a numbering convention that first referred to the column (1 or 2), then a dash, and then the particular row of the device (1 through 7 or 12 depending on the carrier). For example, column 1, row 3 would be device 1-3. Therefore, any number after the dash that was greater than 7 indicates that the entire chip therefore was measured on the Montana Instruments cryostation. The wiring diagram for the Montana Instruments LCC 28 is seen below in Figure A.1.

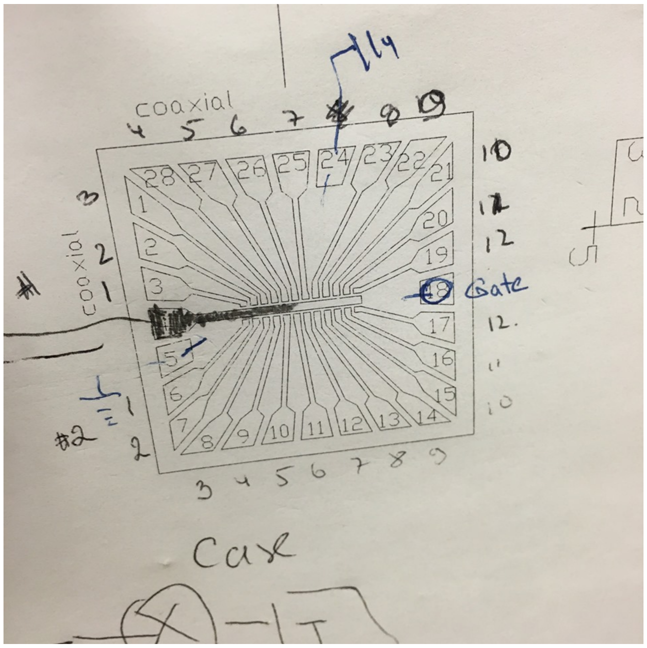

Figure A.1 : Montana Instruments LCC 28 wiring diagram: The squares indicate the bonding pads that surround the common ground, pad 4 highlighed in black. Bonding pad 18 is used for gating while pads 4 and 24 are grounded and are normally skipped during wire bonding. The numbers hand-written in black ink that surround the chip indicate the nomenclature of the device row number. The top half of the devices refer to Column 1 and the bottom half refer to Column 2 in the naming convention described in Section A.1 and correspond to the “break out” coax cable box for wiring.

The low working distance optical window for the Montana Instruments cryostation frequently leaks, resulting in a slow leak in the vacuum. While Montana Instruments has instructions on how to fix this with epoxy, I found that cleanly fixing this window is challenging. I instead began repairing the window using VacSeal High Vacuum Leak Sealant which was just as effective but also is removable and easier to apply.

A.2 Wire bonding considerations

Although the majority of this work uses 2 µm SiO_2, devices with 200 nm thick oxide should be bonded with care using the K&S 4526 wire bonder. The "force" setting should not exceed 2/10 to prevent "piercing through" the oxide layer, resulting in stray electronic signal.

The samples on the LCC 28 chip carriers that will be measured at room temperature (and thus not needing the copper piece underneath) can be wire bonded using standard tip height. The chips that need to be measured at low temperature will need to have a buffer piece of copper between the device and the chip carrier. This copper piece results in the chip to be too high for the back of the wire bonding tip. The tip should be lowered slightly to allow for proper bonding.

Finally, the tips that I have found to be the best are DeWeyl Tool Company's MASOD-1/16/-750-45-CG-2520-M. The lead time for these can be quite long (>4 weeks)!

A.3 Experimental software

The experimental code can be seen in Refs. [362] and [363] for the main experiment and the photodetection experiment, respectively. The code is written using the Anaconda distribution of Python 3 and uses an Anaconda environment. Here, I will detail the different packages within the optics distribution. In order for the Raman system to run, the system must be ran using 32 bit (more on this later). If the Raman system is not going to be used, either 32 or 64 bit is compatible.

Although this uses Python, the DAQ controller REQUIRES National Instruments' LabVIEW to be installed. The Thorlabs TDC001 and KDC101 polarizer controllers

REQUIRE Thorlabs Kinesis installes. Finally, the Raman spectrometer REQUIRES Horiba Jobin Yvon SynerJY software, the software developer key (SDK), *and* the physical key (USB with green light).

Other libraries required include: pyDAQmx[364], PyVISA (visa)[365], PM100[366], pyUSB[367][368], and pythonnet (clr)[369].

A.3.1 Graphical User Interface (GUI)

The graphical user interface (GUI) package consists of the GUIs used for the experiment built using tkinter package ("Tk interface") which is the standard GUI for Python. This may not translate well using a different operating system than Windows. This package consists of four different py files:

1. base_gui: Tk "widgets" to easily create GUI for different equipment
2. daq_break_gui: GUI for only using DAQ for electromigration
3. k2400_gui: GUI for only using the Keithley K2400 for electromigration
4. main_lockin_gui: Full software suite

You likely will only use the main lockin GUI.

Upon start up, the main lockin GUI identifies which equipment is connected to the system. Only measurements that have all required equipment show up. Peripheral equipment (polarizer controller, power meter, etc.) will not interrupt measurements. The main GUI for the photodetection computer is seen in Fig. A.2. In this case, the stepper motor is not connected, so the map scan measurements are disabled.

Clicking on one of the measurements will have another GUI pop up to ask for the relevant information for the measurement. Fig. A.3 shows the GUI for the

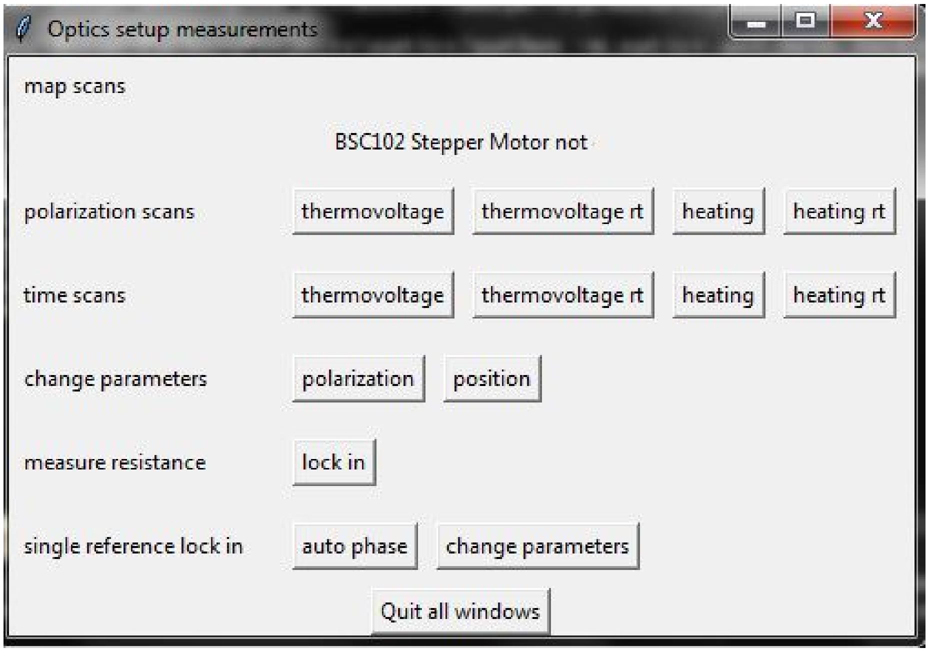

BSC102 Stepper Motor not

Figure A.2 : Main lockin GUI: Displays the different instruments that the system can run. Measurements that require a particular instrument will be disabled if that equipment is not identified.

thermovoltage vs. time information. Use the browse button to show where you want the files to be saved. The file name of each scan typically has this structure: device_measurement type_polarization_scan, where *device* is the string you input into the GUI, *measurement type* is a descriptor (in this case, it would be 'time scan'), *polarization* is the polarization of the incident beam read by the polarizer controller (omitted if not connected), and *scan* is the integer in the "scan" box in the GUI. This number auto-enumerates and files do not overwrite, so you likely don't need to change this number unless you need to skip a value for some reason. Once you press "run", the measurement will start. This will pop up as a Matplotlib canvas which will dynamically plot data in a window. Do not click in this window during measurement, or you will lose access to seeing the real-time data plotting. After the measurement is complete, a screenshot of this window will additionally be saved under the save file name in jpeg format. After measurement, some of these windows remain dynamically active. Clicking on individual pixels of a map scan, for instance, will move the laser beam to that location.

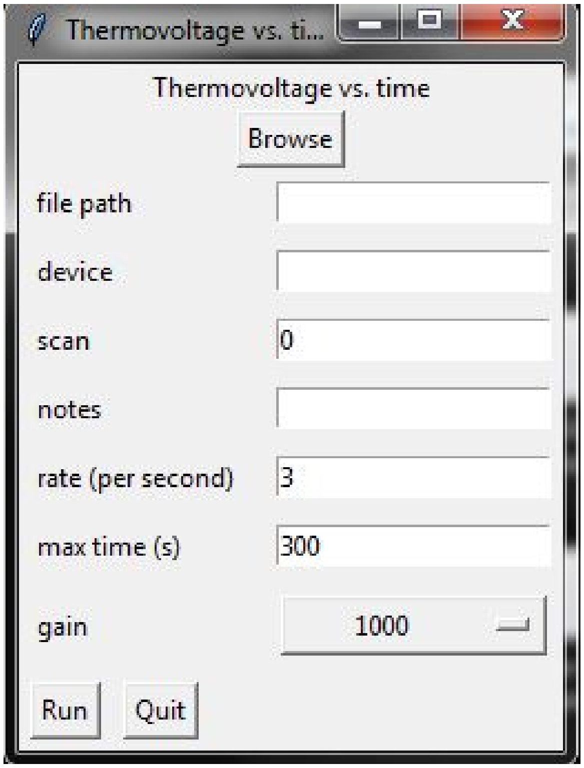

file path
device
scan 0
notes
rate (per second) 3
max time (s) 300
gain 1000

Figure A.3 : Measurement GUI example. Fill in the blanks and select *run* when ready.

I tried my best to make sure that things can quit gracefully without hanging indefinitely. Clicking “abort” or “quit” instead of the red X will ensure that this happens.

A.3.2 Hardware control

The hardware control package controls the communication between the computer and the hardware. I will go through each one here. **Note: you should only need to change things in the hardware_addresses_and_constants file!** This is where all the IP addresses, ports, scaling factors, etc. are handled.

As much as I could help it, I had the computer communicate as simply as possible. This means bypassing proprietary software and sending direct USB/GPIB/ethernet commands. These are all context managed,[370] so that canceling actions results in proper shut down procedures instead of "hanging" - shutting down and starting up can take about 30 seconds.

1. hardware_addresses_and_constants: **This is the only file you should need to edit**. This is where all the IP addresses, port locations, serial numbers,m etc. are located. This is also where the scaling factor for the power meter is fed into (total power on the sample divided by the power read from the beam sampler)

2. daq: controls the NI DAQ. **This requires PyDAQmx which requires LabVIEW to be installed**

3. annenuator_wheel: controls the circular ND filter that is rotated using the NI DAQ. This requires PyDAQmx to be installed to control the NI DAQ

4. keithley_k2400: Controls the Keithley source meter. Uses PyVISA (visa) over GPIB.

5. npc3sg: Controls the NPC3SG piezo controller. The USB communication of this device is very poor - XONXOFF handshakes randomly fail which result

in hanging (but ignoring the handshakes also results in errors). The native LabVIEW software doesn't work, either. This is actually controlled using the NI DAQ using analog output voltages, and the positions are read in using input voltages.

6. pm100d: Controls the Thorlabs PM100D power meter. This requires the correct serial number of the detector and the power factor (ratio of total power to the power read at the beam sampler) to get correct readings. By the way, this uses the library ThorlabsPM100 - I couldn't get around it.

7. sr7270: Controls the SR7270 lock in amplifiers. This uses pyUSB and simply uses the USB commands to control the lock in.

8. polarizercontroller: This controls the polarizer controller. This requires Thorlabs Kinesis to be installed and requires the DOTNET (x64) DLLs added to the PATH. To do this, you must use pythonnet (clr). You will frequently need to HOME the polarizer controller - the KDC101 has a known issue to slip and have a large offset between the read and actual polarization angle. This software tries its best to account for this slippage. Thorlabs knows of this issue. The TDC001 seems to behave much better with this regard.

9. topica_ibeam_smart: **USE THIS INSTEAD OF THE PROPRIETARY SYSTEM**. This controls the Topica laser. Actually using this instead of the proprietary software is better because it sets everything to directly to the recommended specs with correct timing. It also shuts down the laser property and puts it into standby mode. Also, every hour, it sends a status check to the laser log path, set in the hardware address and constants file. This is controlled directly via COM control.

10. ccd_controller: **IN BETA**. This controls the SynerJY CCD controller for the Raman spectrometer. This requires pythonnet (clr) and for the SynerJY DLLs to be added to PATH (you actually need the SynderJY software installed). Horiba's software for 64 bit computers basically uses a COM interface to use 32 bit DLLs on a 64 bit server - very, very slow and causes intermittent hanging. Both the CCD and mono controllers is why this system uses 32 bit software. By the way - that green glowing SynerJY USB stick must be connected to the computer to use the hardware - it's the authentication key. One more thing - for this software to work (or even the LabVIEW software), you need a "SDK" key authorized on Horiba's side. I got this by telling customer service that I couldn't connect via LabVIEW.
11. mono_controller: Controls the mono controller for the Raman spectrometer. The same caveats discussed in ccd_controller apply.

A.3.3 Measurements

In order to make creating new measurement software as easy as possible, I created base measurements under the measurements package. ALL measurements result in a CSV file with headers that give information about the systematics (laser intensity, polarization, notes, etc.). The final line of this header has "end of header" for easy parsing. Then, an additional header gives the title and units of each column. These labels are the same between measurements for easy data processing.

1. base_measurement: the foundation for all lockin measurements
2. base_intensity: base measurement for measuring some value as a function of incident laser position, controlled using the attenuator wheel

3. base_map: base measurement for measureing some value as a function of laser position, creating a 2D map. Clicking on a pixel after the scan is complete moves the laser to that position. Note: the map is reflected compared to what you see on the camera because of the way matplotlib defines the origin - clicking on the pixel does put it in the corresponding position according to the map.

4. base_polarization: base measurement for measuring some value as a function of incident laser polarization, rotated using the waveplate

5. base_time: base measurement for measuring some value as a function of time

These are extended for "heating" measurements (applying a DC bias and measuring the current) in the heating_measurements package or the thermovoltage measurements in the thermovoltage_measurements package. The thermovoltage measurements with DC in the name correspond to a DC measurement using the DAQ for a very broken gap.

The current vs. voltage measurements are seen in current_vs_voltage package. The current_vs_voltage_vs_gate allows for a "waterfall" plot to show a color map of the IV curves at different gates. The current_vs_voltage file simply creates a scatter plot of the current as the voltage ramps.

The electromigration package allows for the K2400 and DAQ electromigration using k2400_break and daq_break, respectively.

A.3.4 Raman

This is in beta and is unstable. Clicking the Raman tab will load the spectrometer for measurements and launch the Raman GUI. Many of these show scatter plots of the integrated signal between two points of the total spectrum (e.g. highlights one peak). Clicking on a point of the scatter plot shows the entire spectrum at that point. These plots can be replotted for another peak after acquisition.

1. raman_gui: The main GUI for the Raman measurements
2. raman_intensity: Looks at Raman signal as a function of incident laser intensity as a scatter plot integrated between two points. Clicking on a point on the scatter plot shows the entire Raman scan at that point
3. raman_map: Plots a designated Raman peak as a function of laser position. Clicking a pixel moves the laser to the corresponding position and shows the total Raman signal at that location. The map can be replotted using a different start/stop position for the peak!
4. raman_outgoing_polarization: Shows at the Raman signal of a peak as a polarizer is rotated in the *scattered* beam path. Clicking a point on the scatter plot shows the entire spectrum at that point
5. raman_polarization: Shows at the Raman signal of a peak as a function of *incident* laser position. Clicking a point on the scatter plot shows the entire spectrum at that point
6. raman_time: Shows the Raman signal of a peak as a function of time
7. raman_voltage_waterfall: Shows the entire Raman spectrum as a function of applied bias in a color map. Clicking a point shows the line plot of the entire spectrum at that point.
8. single_spectrum: Shows the entire spectrum at a single point
9. unit_conversions: Converts units for the Raman measurement

10. raman_iets: Takes Raman spectra at the same time as current-voltage curves

A.3.5 Plots

The packages thermovoltage_plot and heating_plot are the “widgets” to dynamically plot the values during the measurements described above

A.3.6 Miscellaneous

The misc_utility package has more helper “widgets”.

1. conversions: completes conversions for measurements, such as converting the signal of the lock in amplifier from a sine wave to a square wave
2. curve_fit_equations: has functions of the different curves used for fits
3. parser_tool: contains tools to parse out bad strings in USB communication
4. scanner: determines the locations to scan for map measurements
5. : tkinter_utilities: small “widgets” for the main GUIs.

Bibliography

[1] F. J. DiSalvo, "Thermoelectric Cooling and Power Generation," *Science*, vol. 285, no. 5428, pp. 703–706, Jul. 1999. [Online]. Available: https://science.sciencemag.org/content/285/5428/703

[2] L. E. Bell, "Cooling, Heating, Generating Power, and Recovering Waste Heat with Thermoelectric Systems," *Science*, vol. 321, no. 5895, pp. 1457–1461, Sep. 2008. [Online]. Available: https://science.sciencemag.org/content/321/5895/1457

[3] W.-H. Chen, C.-Y. Liao, and C.-I. Hung, "A numerical study on the performance of miniature thermoelectric cooler affected by Thomson effect," *Applied Energy*, vol. 89, no. 1, pp. 464–473, Jan. 2012. [Online]. Available: http://www.sciencedirect.com/science/article/pii/S0306261911005186

[4] R. P. Huebener, "Thermoelectric Power of Aluminum and Dilute Aluminum Alloys," *Physical Review*, vol. 171, no. 3, pp. 634–641, Jul. 1968. [Online]. Available: https://link.aps.org/doi/10.1103/PhysRev.171.634

[5] M. Cutler and N. F. Mott, "Observation of Anderson Localization in an Electron Gas," *Physical Review*, vol. 181, no. 3, pp. 1336–1340, May 1969. [Online]. Available: https://link.aps.org/doi/10.1103/PhysRev.181.1336

[6] E. M. Levin, "Charge carrier effective mass and concentration derived from combination of Seebeck coefficient and $^{125}\mathrm{Te}$ NMR measurements in complex tellurides," *Physical Review B*, vol. 93, no. 24, p. 245202, Jun. 2016. [Online]. Available: https://link.aps.org/doi/10.1103/PhysRevB.93.245202

[7] D. Kraemer, B. Poudel, H.-P. Feng, J. C. Caylor, B. Yu, X. Yan, Y. Ma, X. Wang, D. Wang, A. Muto, K. McEnaney, M. Chiesa, Z. Ren, and G. Chen, "High-performance flat-panel solar thermoelectric generators with high thermal concentration," *Nature Materials*, vol. 10, no. 7, pp. 532–538, Jul. 2011. [Online]. Available: https://www.nature.com/articles/nmat3013

[8] C. Lasance, "The Seebeck Coefficient," *Electronics Cooling*, Nov. 2006. [Online]. Available: https://www.electronics-cooling.com/2006/11/the-seebeck-coefficient/

[9] L. D. Hicks and M. S. Dresselhaus, “Thermoelectric figure of merit of a one-dimensional conductor,” *Physical Review B*, vol. 47, no. 24, pp. 16 631–16 634, Jun. 1993. [Online]. Available: https://link.aps.org/doi/10.1103/PhysRevB.47.16631

[10] G. J. Snyder and E. S. Toberer, “Complex thermoelectric materials,” *Nature Materials*, vol. 7, no. 2, pp. 105–114, Feb. 2008. [Online]. Available: https://search.ebscohost.com/login.aspx?direct=true&db=a9h&AN=28611002&site=ehost-live&scope=site

[11] A. I. Boukai, Y. Bunimovich, Jamil Tahir-Kheli, Jen-Kan Yu, W. A. Goddard III, and J. R. Heath, “Silicon nanowires as efficient thermoelectric materials,” *Nature*, vol. 451, no. 7175, pp. 168–171, Jan. 2008. [Online]. Available: https://search.ebscohost.com/login.aspx?direct=true&db=a9h&AN=28331152&site=ehost-live&scope=site

[12] A. I. Hochbaum, Renkun Chen, R. D. Delgado, Wenjie Liang, E. C. Garnett, M. Najarian, A. Majumdar, and Peidong Yang, “Enhanced thermoelectric performance of rough silicon nanowires,” *Nature*, vol. 451, no. 7175, pp. 163–167, Jan. 2008. [Online]. Available: https://search.ebscohost.com/login.aspx?direct=true&db=a9h&AN=28331158&site=ehost-live&scope=site

[13] S. Kwon, M. C. Wingert, J. Zheng, J. Xiang, and R. Chen, “Thermal transport in Si and Ge nanostructures in the ‘confinement’ regime,” *Nanoscale*, vol. 8, no. 27, pp. 13 155–13 167, Jul. 2016. [Online]. Available: http://pubs.rsc.org/en/content/articlelanding/2016/nr/c6nr03634a

[14] S.-Y. Lee, G.-S. Kim, J. Lim, S. Han, B. Li, J. T. L. Thong, Y.-G. Yoon, and S.-K. Lee, “Control of surface morphology and crystal structure of silicon nanowires and their coherent phonon transport characteristics,” *Acta Materialia*, vol. 64, pp. 62–71, Feb. 2014. [Online]. Available: http://www.sciencedirect.com/science/article/pii/S1359645413009002

[15] G. Joshi, H. Lee, Y. Lan, X. Wang, G. Zhu, D. Wang, R. W. Gould, D. C. Cuff, M. Y. Tang, M. S. Dresselhaus, G. Chen, and Z. Ren, “Enhanced Thermoelectric Figure-of-Merit in Nanostructured p-type Silicon Germanium Bulk Alloys,” *Nano Letters*, vol. 8, no. 12, pp. 4670–4674, Dec. 2008. [Online]. Available: https://doi.org/10.1021/nl8026795

[16] J. R. Szczech, J. M. Higgins, and S. Jin, “Enhancement of the thermoelectric properties in nanoscale and nanostructured materials,” *Journal of Materials Chemistry*, vol. 21, no. 12, pp. 4037–4055, Mar. 2011. [Online]. Available: https://pubs.rsc.org/en/content/articlelanding/2011/jm/c0jm02755c

[17] A. Burkov, “Metals at High Temperatures: Thermoelectric Power,” in *Encyclopedia of Materials: Science and Technology.* Elsevier, 2001, pp. 5548–5554. [Online]. Available: https://linkinghub.elsevier.com/retrieve/pii/B0080431526009700

[18] J. P. Moore and R. S. Graves, “Absolute Seebeck coefficient of platinum from 80 to 340 K and the thermal and electrical conductivities of lead from 80 to 400 K,” *Journal of Applied Physics*, vol. 44, no. 3, pp. 1174–1178, Mar. 1973. [Online]. Available: https://aip.scitation.org/doi/10.1063/1.1662324

[19] C. Herring, “Theory of the Thermoelectric Power of Semiconductors,” *Physical Review*, vol. 96, no. 5, pp. 1163–1187, Dec. 1954. [Online]. Available: https://link.aps.org/doi/10.1103/PhysRev.96.1163

[20] P. G. Klemens, “The Contribution of Phonons to the Thomson Coefficient,” *Australian Journal of Physics*, vol. 7, no. 3, pp. 520–522, 1954. [Online]. Available: https://www.publish.csiro.au/ph/ph540520

[21] R. P. Huebener, “Size Effect on Phonon Drag in Platinum,” *Physical Review*, vol. 140, no. 5A, pp. A1834–A1844, Nov. 1965. [Online]. Available: https://link.aps.org/doi/10.1103/PhysRev.140.A1834

[22] P. G. Klemens, “Theory of phonon drag thermopower,” in *Fifteenth International Conference on Thermoelectrics. Proceedings ICT ’96*, Mar. 1996, pp. 206–208.

[23] N. Cusack and P. Kendall, “The Absolute Scale of Thermoelectric Power at High Temperature,” *Proceedings of the Physical Society*, vol. 72, no. 5, pp. 898–901, Nov. 1958. [Online]. Available: https://doi.org/10.1088%2F0370-1328%2F72%2F5%2F429

[24] H. H. Andersen and M. Nielsen, “Thermo-electricity in gold at low temperatures,” *Physics Letters*, vol. 6, no. 1, pp. 17–18, Aug. 1963. [Online]. Available: http://www.sciencedirect.com/science/article/pii/0031916363902026

[25] W. Worobey, P. Lindenfeld, and B. Serin, “Thermoelectric power of gold,” *Physics Letters*, vol. 16, no. 1, pp. 15–16, May 1965. [Online]. Available: http://www.sciencedirect.com/science/article/pii/003191636590377X

[26] X. Lu, L. Sun, P. Jiang, and X. Bao, “Progress of Photodetectors Based on the Photothermoelectric Effect,” *Advanced Materials*, vol. 0, no. 0, p. 1902044. [Online]. Available: https://onlinelibrary.wiley.com/doi/abs/10.1002/adma.201902044

[27] R. P. Huebener, “Thermoelectric Size Effect in Pure Gold,” *Physical Review*, vol. 136, no. 6A, pp. A1740–A1744, Dec. 1964. [Online]. Available: https://link.aps.org/doi/10.1103/PhysRev.136.A1740

[28] O. Dreirach, “The electrical resistivity and thermopower of solid noble metals,” *Journal of Physics F: Metal Physics*, vol. 3, no. 3, pp. 577–584, Mar. 1973. [Online]. Available: https://doi.org/10.1088%2F0305-4608%2F3%2F3%2F016

[29] J. E. Robinson, “Thermoelectric Power in the Nearly-Free-Electron Model,” *Physical Review*, vol. 161, no. 3, pp. 533–539, Sep. 1967. [Online]. Available: https://link.aps.org/doi/10.1103/PhysRev.161.533

[30] “3d (VRML) Fermi Surface Database.” [Online]. Available: http://www.phys.ufl.edu/fermisurface/

[31] T.-S. Choy, J. Naset, S. Hershfield, C. J. Stanton, and J. Chen, “A Database of Fermi Surfaces in Virtual Reality Modeling Language,” vol. 45(1):L36. Bulletin of The American Physical Society, 2000, p. 42. [Online]. Available: http://www.phys.ufl.edu/fermisurface/

[32] S. F. Lin and W. F. Leonard, “Thermoelectric Power of Thin Gold Films,” *Journal of Applied Physics*, vol. 42, no. 9, pp. 3634–3639, Aug. 1971. [Online]. Available: https://aip.scitation.org/doi/abs/10.1063/1.1660781

[33] M. Cattani, M. C. Salvadori, A. R. Vaz, F. S. Teixeira, and I. G. Brown, “Thermoelectric power in very thin film thermocouples: Quantum size effects,” *Journal of Applied Physics*, vol. 100, no. 11, p. 114905, Dec. 2006. [Online]. Available: https://aip.scitation.org/doi/full/10.1063/1.2388046

[34] D. Kojda, R. Mitdank, M. Handwerg, A. Mogilatenko, M. Albrecht, Z. Wang, J. Ruhhammer, M. Kroener, P. Woias, and S. F. Fischer, “Temperature-dependent thermoelectric properties of individual silver nanowires,” *Physical Review B*, vol. 91, no. 2, p. 024302, Jan. 2015. [Online]. Available: https://link.aps.org/doi/10.1103/PhysRevB.91.024302

[35] A. D. Avery, R. Sultan, D. Bassett, D. Wei, and B. L. Zink, “Thermopower and resistivity in ferromagnetic thin films near room temperature,” *Physical Review B*, vol. 83, no. 10, p. 100401, Mar. 2011. [Online]. Available: https://link.aps.org/doi/10.1103/PhysRevB.83.100401

[36] E. Shapira, A. Tsukernik, and Y. Selzer, “Thermopower measurements on individual 30 nm nickel nanowires,” *Nanotechnology*, vol. 18, no. 48, p. 485703, Dec. 2007. [Online]. Available: http://stacks.iop.org/0957-4484/18/i=48/a=485703?key=crossref.80fab8f4f19b047fb4a61d403c9981dd

[37] D. De, S. K. Bandyopadhyay, S. Chaudhuri, and A. K. Pal, “Thermoelectric power of aluminum films,” *Journal of Applied Physics*, vol. 54, no. 7, pp. 4022–4027, Jul. 1983. [Online]. Available: https://aip.scitation.org/doi/abs/10.1063/1.332583

[38] S. B. Soffer, “Statistical Model for the Size Effect in Electrical Conduction,” *Journal of Applied Physics*, vol. 38, no. 4, pp. 1710–1715, Mar. 1967. [Online]. Available: https://aip.scitation.org/doi/abs/10.1063/1.1709746

[39] H. Yu and W. F. Leonard, “Thermoelectric power of thin silver films,” *Journal of Applied Physics*, vol. 44, no. 12, pp. 5324–5327, Dec. 1973. [Online]. Available: https://aip.scitation.org/doi/abs/10.1063/1.1662151

[40] W. F. Leonard and H. Yu, “Thermoelectric power of thin copper films,” *Journal of Applied Physics*, vol. 44, no. 12, pp. 5320–5323, Dec. 1973. [Online]. Available: https://aip.scitation.org/doi/abs/10.1063/1.1662150

[41] M. A. Angadi and L. A. Udachan, “Thermopower measurements in chromium films,” *Journal of Materials Science Letters*, vol. 1, no. 12, pp. 539–541, Dec. 1982. [Online]. Available: https://doi.org/10.1007/BF00724741

[42] V. D. Das and N. Soundararajan, “Size and temperature effects on the Seebeck coefficient of thin bismuth films,” *Physical Review B*, vol. 35, no. 12, pp. 5990–5996, Apr. 1987. [Online]. Available: https://link.aps.org/doi/10.1103/PhysRevB.35.5990

[43] R. Schepis and K. Schröder, “Thermopower of thin iron films,” *Journal of Magnetism and Magnetic Materials*, vol. 104-107, pp. 1757–1759, Feb. 1992. [Online]. Available: http://www.sciencedirect.com/science/article/pii/0304885392915363

[44] M. J. Burns and P. M. Chaikin, “Thermoelectric power of two-dimensional Pd and Pd-Au films,” *Physical Review B*, vol. 27, no. 10, pp. 5924–5933, May 1983. [Online]. Available: https://link.aps.org/doi/10.1103/PhysRevB.27.5924

[45] B. L. Melnichuk, A. I. Lopatinsky, and Z. V. Stasyuk, “The Thermoelectric Power in Transition Metal Thin Films,” *physica status solidi (a)*, vol. 171, no. 2, pp. 495–500, 1999. [Online]. Available: https://onlinelibrary.wiley.com/doi/abs/10.1002/%28SICI%291521-396X%28199902%29171%3A2%3C495%3A%3AAID-PSSA495%3E3.0.CO%3B2-4

[46] F. A. Otter, “Thermoelectric Power and Electrical Resistivity of Dilute Alloys of Mn, Pd, and Pt in Cu, Ag, and Au,” *Journal of Applied Physics*, vol. 27, no. 3, pp. 197–200, Mar. 1956. [Online]. Available: https://aip.scitation.org/doi/abs/10.1063/1.1722342

[47] R. P. Huebener and C. van Baarle, “Thermoelectric Power of Annealed and Quenched Gold-Platinum Alloys,” *Physical Review*, vol. 159, no. 3, pp. 564–571, Jul. 1967. [Online]. Available: https://link.aps.org/doi/10.1103/PhysRev.159.564

[48] R. P. Huebner and C. Van Baarle, “Thermoelectric power of annealed and quenched gold-platinum alloys at low temperatures,” *Physics Letters*, vol. 23, no. 3, pp. 189–190, Oct. 1966. [Online]. Available: http://www.sciencedirect.com/science/article/pii/0031916366908572

[49] E. L. Christenson, “Effects of Transition Metal Solutes on the Thermoelectric Power of Copper and Gold,” *Journal of Applied Physics*, vol. 34, no. 5, pp. 1485–1491, May 1963. [Online]. Available: https://aip.scitation.org/doi/10.1063/1.1729605

[50] C. A. Domenicali and F. A. Otter, “Thermoelectric Power and Electron Scattering in Metal Alloys,” *Physical Review*, vol. 95, no. 5, pp. 1134–1142, Sep. 1954. [Online]. Available: https://link.aps.org/doi/10.1103/PhysRev.95.1134

[51] M. Bailyn, “Phonon-Drag Part of the Thermoelectric Power in Metals,” *Physical Review*, vol. 157, no. 3, pp. 480–485, May 1967. [Online]. Available: https://link.aps.org/doi/10.1103/PhysRev.157.480

[52] C. Van Baarle, “Anisotropy of electron relaxation time and phonon-drag thermopower,” *Physica*, vol. 33, no. 2, pp. 424–428, Jan. 1967. [Online]. Available: http://www.sciencedirect.com/science/article/pii/0031891467901747

[53] J. S. Dugdale and M. Bailyn, “Anisotropy of Relaxation Times and Phonon Drag in the Noble Metals,” *Physical Review*, vol. 157, no. 3, pp. 485–490, May 1967. [Online]. Available: https://link.aps.org/doi/10.1103/PhysRev.157.485

[54] A. J. Mortlock, “The Effect of Tension on the Thermoelectric Properties of Metals,” *Australian Journal of Physics*, vol. 6, no. 4, pp. 410–419, 1953. [Online]. Available: https://www.publish.csiro.au/ph/ph530410

[55] J. Blatt, *Thermoelectric Power of Metals*. Springer Science & Business Media, Dec. 2012, google-Books-ID: sfXjBwAAQBAJ.

[56] D. Shoenberg and B. R. Watts, “The effect of tension on the Fermi surfaces of the noble metals,” *The Philosophical Magazine: A Journal of Theoretical Experimental and Applied Physics*, vol. 15, no. 138, pp. 1275–1288, Jun. 1967. [Online]. Available: https://doi.org/10.1080/14786436708222763

[57] D. Gamble and B. R. Watts, “The effect of uniaxial stress on the Fermi surface neck of gold,” *Physics Letters A*, vol. 40, no. 1, p. 22, Jun.

1972. [Online]. Available: http://www.sciencedirect.com/science/article/pii/0375960172901806

[58] D. S. Tan, “The effect of elastic deformation on the Fermi surface of copper,” *Journal of Physics and Chemistry of Solids*, vol. 26, no. 10, pp. 1623–1624, Oct. 1965. [Online]. Available: http://www.sciencedirect.com/science/article/pii/002236976590096X

[59] J. K. A. Amuzu and P. K. Addoli, “Relative changes in the Fermi surfaces of the noble metals due to uniaxial tension,” *Journal of Physics F: Metal Physics*, vol. 12, no. 8, pp. 1637–1639, Aug. 1982. [Online]. Available: https://doi.org/10.1088%2F0305-4608%2F12%2F8%2F010

[60] X. Kleber, P. Roux, and M. Morin, “Sensitivity of the thermoelectric power of metallic materials to an elastic uniaxial strain,” *Philosophical Magazine Letters*, vol. 89, no. 9, pp. 565–572, Sep. 2009. [Online]. Available: https://doi.org/10.1080/09500830903170567

[61] A. N. May and J. K. A. Amuzu, “Measurement of the longitudinal piezo-thermoelectric effect in polycrystalline wires of the noble metals,” *Journal of Physics F: Metal Physics*, vol. 3, no. 9, pp. L154–L155, Sep. 1973. [Online]. Available: https://doi.org/10.1088%2F0305-4608%2F3%2F9%2F002

[62] J. K. A. Amuzu, “Measurement of the shear piezo-thermoelectric effect in copper and silver,” *Journal of Physics F: Metal Physics*, vol. 17, no. 11, pp. 2261–2265, Nov. 1987. [Online]. Available: https://doi.org/10.1088%2F0305-4608%2F17%2F11%2F014

[63] H. Shioya, M. F. Craciun, S. Russo, M. Yamamoto, and S. Tarucha, “Straining Graphene Using Thin Film Shrinkage Methods,” *Nano Letters*, vol. 14, no. 3, pp. 1158–1163, Mar. 2014. [Online]. Available: https://doi.org/10.1021/nl403679f

[64] C. Si, Z. Sun, and F. Liu, “Strain engineering of graphene: a review,” *Nanoscale*, vol. 8, no. 6, pp. 3207–3217, Feb. 2016. [Online]. Available: https://pubs.rsc.org/en/content/articlelanding/2016/nr/c5nr07755a

[65] N. Wei, L. Xu, H.-Q. Wang, and J.-C. Zheng, “Strain engineering of thermal conductivity in graphene sheets and nanoribbons: a demonstration of magic flexibility,” *Nanotechnology*, vol. 22, no. 10, p. 105705, Feb. 2011. [Online]. Available: https://doi.org/10.1088%2F0957-4484%2F22%2F10%2F105705

[66] R. Abermann and R. Koch, “The internal stress in thin silver, copper and gold films,” *Thin Solid Films*, vol. 129, no. 1, pp. 71–78, Jul. 1985. [Online]. Available: http://www.sciencedirect.com/science/article/pii/0040609085900963

[67] C. A. Neugebauer, “Tensile Properties of Thin, Evaporated Gold Films,” *Journal of Applied Physics*, vol. 31, no. 6, pp. 1096–1101, Jun. 1960. [Online]. Available: https://aip.scitation.org/doi/abs/10.1063/1.1735751

[68] P. A. Kinzie and L. G. Rubin, “Thermocouple Temperature Measurement,” *Physics Today*, vol. 26, no. 11, p. 52, Dec. 2008. [Online]. Available: https://physicstoday.scitation.org/doi/abs/10.1063/1.3128323

[69] Committee E-20, Ed., *Manual on the Use of Thermocouples in Temperature Measurement.* 100 Barr Harbor Drive, PO Box C700, West Conshohocken, PA 19428-2959: ASTM International, Jan. 1981. [Online]. Available: http://www.astm.org/doiLink.cgi?STP470B-EB

[70] N. Shukla, S. K. Tripathi, A. Banerjee, A. S. V. Ramana, N. S. Rajput, and V. N. Kulkarni, “Study of temperature rise during focused Ga ion beam irradiation using nanothermo-probe,” *Applied Surface Science*, vol. 256, no. 2, pp. 475–479, Oct. 2009. [Online]. Available: http://www.sciencedirect.com/science/article/pii/S0169433209010186

[71] E. Aldrete-Vidrio, D. Mateo, and J. Altet, “Differential Temperature Sensors Fully Compatible With a 0.35-μm CMOS Process,” *IEEE Transactions on Components and Packaging Technologies*, vol. 30, no. 4, pp. 618–626, Dec. 2007.

[72] R. J. M. Vullers, R. van Schaijk, I. Doms, C. Van Hoof, and R. Mertens, “Micropower energy harvesting,” *Solid-State Electronics*, vol. 53, no. 7, pp. 684–693, Jul. 2009. [Online]. Available: http://www.sciencedirect.com/science/article/pii/S0038110109000720

[73] M. L. Brongersma, N. J. Halas, and P. Nordlander, “Plasmon-induced hot carrier science and technology,” *Nature Nanotechnology*, vol. 10, no. 1, pp. 25–34, Jan. 2015. [Online]. Available: https://www.nature.com/articles/nnano.2014.311

[74] P. M. Krenz, B. Tiwari, G. P. Szakmany, A. O. Orlov, F. J. Gonzalez, G. D. Boreman, and W. Porod, “Response Increase of IR Antenna-Coupled Thermocouple Using Impedance Matching,” *IEEE Journal of Quantum Electronics*, vol. 48, no. 5, pp. 659–664, May 2012.

[75] G. P. Szakmany, P. M. Krenz, A. O. Orlov, G. H. Bernstein, and W. Porod, “Antenna-Coupled Nanowire Thermocouples for Infrared Detection,” *IEEE Transactions on Nanotechnology*, vol. 12, no. 2, pp. 163–167, Mar. 2013.

[76] S. Sadat, A. Tan, Y. J. Chua, and P. Reddy, “Nanoscale Thermometry Using Point Contact Thermocouples,” *Nano Letters*, vol. 10, no. 7, pp. 2613–2617, Jul. 2010. [Online]. Available: https://doi.org/10.1021/nl101354e

[77] K. Luo, Z. Shi, J. Varesi, and A. Majumdar, “Sensor nanofabrication, performance, and conduction mechanisms in scanning thermal microscopy,” *Journal of Vacuum Science & Technology B: Microelectronics and Nanometer Structures Processing, Measurement, and Phenomena*, vol. 15, no. 2, pp. 349–360, Mar. 1997. [Online]. Available: https://avs.scitation.org/doi/abs/10.1116/1.589319

[78] X. Zhang, H. Choi, A. Datta, and X. Li, “Design, fabrication and characterization of metal embedded thin film thermocouples with various film thicknesses and junction sizes,” *Journal of Micromechanics and Microengineering*, vol. 16, no. 5, pp. 900–905, Mar. 2006. [Online]. Available: https://doi.org/10.1088%2F0960-1317%2F16%2F5%2F004

[79] M. E. Bourg, W. E. van der Veer, A. G. Grüell, and R. M. Penner, “Electrodeposited Submicron Thermocouples with Microsecond Response Times,” *Nano Letters*, vol. 7, no. 10, pp. 3208–3213, Oct. 2007. [Online]. Available: https://doi.org/10.1021/nl071990q

[80] E. Shapira, D. Marchak, A. Tsukernik, and Y. Selzer, “Segmented metal nanowires as nanoscale thermocouples,” *Nanotechnology*, vol. 19, no. 12, p. 125501, Feb. 2008. [Online]. Available: https://doi.org/10.1088%2F0957-4484%2F19%2F12%2F125501

[81] D. Benner, J. Boneberg, P. Nürnberger, R. Waitz, P. Leiderer, and E. Scheer, “Lateral and Temporal Dependence of the Transport through an Atomic Gold Contact under Light Irradiation: Signature of Propagating Surface Plasmon Polaritons,” *Nano Letters*, vol. 14, no. 9, pp. 5218–5223, Sep. 2014. [Online]. Available: https://doi.org/10.1021/nl502165y

[82] W. Sun, H. Liu, W. Gong, L.-M. Peng, and S.-Y. Xu, “Unexpected size effect in the thermopower of thin-film stripes,” *Journal of Applied Physics*, vol. 110, no. 8, p. 083709, Oct. 2011. [Online]. Available: https://aip.scitation.org/doi/10.1063/1.3653824

[83] G. P. Szakmany, A. O. Orlov, G. H. Bernstein, and W. Porod, “Comment on “Unexpected size effect in the thermopower of thin-film stripes” [J. Appl. Phys. 110, 083709 (2011)],” *Journal of Applied Physics*, vol. 115, no. 23, p. 236101, Jun. 2014. [Online]. Available: https://aip.scitation.org/doi/full/10.1063/1.4884735

[84] ——, “Shape engineering of antenna-coupled single-metal nanothermocouples,” *Infrared Physics & Technology*, vol. 72, pp. 101–105, Sep. 2015. [Online]. Available: http://www.sciencedirect.com/science/article/pii/S1350449515001711

[85] ——, “Single-Metal Nanoscale Thermocouples,” *IEEE Transactions on Nanotechnology*, vol. 13, no. 6, pp. 1234–1239, Nov. 2014.

[86] H. Liu, W. Sun, and S. Xu, “An Extremely Simple Thermocouple Made of a Single Layer of Metal,” *Advanced Materials*, vol. 24, no. 24, pp. 3275–3279, 2012. [Online]. Available: https://onlinelibrary.wiley.com/doi/abs/10.1002/adma.201200644

[87] G. P. Szakmany, A. O. Orlov, G. H. Bernstein, and W. Porod, “Novel Nanoscale Single-Metal Polarization-Sensitive Infrared Detectors,” *IEEE Transactions on Nanotechnology*, vol. 14, no. 2, pp. 379–383, Mar. 2015.

[88] A. Harzheim, J. Spiece, C. Evangeli, E. McCann, V. Falko, Y. Sheng, J. H. Warner, G. A. D. Briggs, J. A. Mol, P. Gehring, and O. V. Kolosov, “Geometrically Enhanced Thermoelectric Effects in Graphene Nanoconstrictions,” *Nano Letters*, vol. 18, no. 12, pp. 7719–7725, Dec. 2018. [Online]. Available: https://doi.org/10.1021/acs.nanolett.8b03406

[89] M.-M. Mennemanteuil, G. Colas-des Francs, M. Buret, A. Dasgupta, A. Cuadrado, J. Alda, and A. Bouhelier, “Laser-induced thermoelectric effects in electrically biased nanoscale constrictions,” *Nanophotonics*, vol. 7, no. 12, pp. 1917–1927, Nov. 2018. [Online]. Available: http://www.degruyter.com/view/j/nanoph.2018.7.issue-12/nanoph-2018-0083/nanoph-2018-0083.xml

[90] P. Zolotavin, C. I. Evans, and D. Natelson, “Substantial local variation of the Seebeck coefficient in gold nanowires,” *Nanoscale*, vol. 9, no. 26, pp. 9160–9166, Jul. 2017. [Online]. Available: https://pubs.rsc.org/en/content/articlelanding/2017/nr/c7nr02678a

[91] B. C. St-Antoine, D. Ménard, and R. Martel, “Position Sensitive Photothermoelectric Effect in Suspended Single-Walled Carbon Nanotube Films,” *Nano Letters*, vol. 9, no. 10, pp. 3503–3508, Oct. 2009. [Online]. Available: https://pubs.acs.org/doi/10.1021/nl901696j

[92] S.-F. Shi, X. Xu, D. C. Ralph, and P. L. McEuen, “Plasmon Resonance in Individual Nanogap Electrodes Studied Using Graphene Nanoconstrictions as Photodetectors,” *Nano Letters*, vol. 11, no. 4, pp. 1814–1818, Apr. 2011. [Online]. Available: https://doi.org/10.1021/nl200522t

[93] L. Gravier, A. Fábián, A. Rudolf, A. Cachin, K. Hjort, and J.-P. Ansermet, “Thermopower measurement of single isolated metallic nanostructures,” *Measurement Science and Technology*, vol. 15, no. 2, pp. 420–424, Jan. 2004. [Online]. Available: https://doi.org/10.1088%2F0957-0233%2F15%2F2%2F015

[94] T. Borca-Tasciuc and G. Chen, “Thin-Film Thermophysical Property Characterization by Scanning Laser Thermoelectric Microscope,” *International Journal of Thermophysics*, vol. 19, no. 2, pp. 557–567, Mar. 1998. [Online]. Available: https://doi.org/10.1023/A:1022586032424

[95] T. DeBorde, L. Aspitarte, T. Sharf, J. W. Kevek, and E. D. Minot, “Photothermoelectric Effect in Suspended Semiconducting Carbon Nanotubes,” *ACS Nano*, vol. 8, no. 1, pp. 216–221, Jan. 2014. [Online]. Available: https://doi.org/10.1021/nn403137a

[96] X. Xu, N. M. Gabor, J. S. Alden, A. M. van der Zande, and P. L. McEuen, “Photo-Thermoelectric Effect at a Graphene Interface Junction,” *Nano Letters*, vol. 10, no. 2, pp. 562–566, Feb. 2010. [Online]. Available: https://doi.org/10.1021/nl903451y

[97] Y. Zhang, H. Li, L. Wang, H. Wang, X. Xie, S.-L. Zhang, R. Liu, and Z.-J. Qiu, “Photothermoelectric and photovoltaic effects both present in MoS_2,” *Scientific Reports*, vol. 5, p. 7938, Jan. 2015. [Online]. Available: https://www.nature.com/articles/srep07938

[98] F. H. L. Koppens, T. Mueller, P. Avouris, A. C. Ferrari, M. S. Vitiello, and M. Polini, “Photodetectors based on graphene, other two-dimensional materials and hybrid systems,” *Nature Nanotechnology*, vol. 9, no. 10, pp. 780–793, Oct. 2014. [Online]. Available: https://www.nature.com/articles/nnano.2014.215

[99] J. Park, Y. H. Ahn, and C. Ruiz-Vargas, “Imaging of Photocurrent Generation and Collection in Single-Layer Graphene,” *Nano Letters*, vol. 9, no. 5, pp. 1742–1746, May 2009. [Online]. Available: https://doi.org/10.1021/nl8029493

[100] M. Buscema, M. Barkelid, V. Zwiller, H. S. J. van der Zant, G. A. Steele, and A. Castellanos-Gomez, “Large and Tunable Photothermoelectric Effect in Single-Layer MoS2,” *Nano Letters*, vol. 13, no. 2, pp. 358–363, Feb. 2013. [Online]. Available: https://doi.org/10.1021/nl303321g

[101] R. Yang, A. Narayanaswamy, and G. Chen, “Surface-Plasmon Coupled Nonequilibrium Thermoelectric Refrigerators and Power Generators,” Mar. 2005. [Online]. Available: https://www.ingentaconnect.com/content/asp/jctn/2005/00000002/00000001/art00006

[102] P. Zolotavin, C. Evans, and D. Natelson, “Photothermoelectric Effects and Large Photovoltages in Plasmonic Au Nanowires with Nanogaps,” *The Journal of Physical Chemistry Letters*, vol. 8, no. 8, pp. 1739–1744, Apr. 2017. [Online]. Available: https://doi.org/10.1021/acs.jpclett.7b00507

[103] N. M. Gabor, J. C. W. Song, Q. Ma, N. L. Nair, T. Taychatanapat, K. Watanabe, T. Taniguchi, L. S. Levitov, and P. Jarillo-Herrero, "Hot Carrier–Assisted Intrinsic Photoresponse in Graphene," *Science*, vol. 334, no. 6056, pp. 648–652, Nov. 2011. [Online]. Available: https://science.sciencemag.org/content/334/6056/648

[104] D. Wu, K. Yan, Y. Zhou, H. Wang, L. Lin, H. Peng, and Z. Liu, "Plasmon-Enhanced Photothermoelectric Conversion in Chemical Vapor Deposited Graphene p–n Junctions," *Journal of the American Chemical Society*, vol. 135, no. 30, pp. 10 926–10 929, Jul. 2013. [Online]. Available: https://doi.org/10.1021/ja404890n

[105] C. Wood, "Materials for thermoelectric energy conversion," *Reports on Progress in Physics*, vol. 51, no. 4, pp. 459–539, Apr. 1988. [Online]. Available: http://stacks.iop.org/0034-4885/51/i=4/a=001?key=crossref.8a0fcbbd4590f73612fa08a02674e70a

[106] A. J. Minnich, M. S. Dresselhaus, Z. F. Ren, and G. Chen, "Bulk nanostructured thermoelectric materials: current research and future prospects," *Energy & Environmental Science*, vol. 2, no. 5, pp. 466–479, 2009. [Online]. Available: https://pubs.rsc.org/en/content/articlelanding/2009/ee/b822664b

[107] S. Frank, "Carbon Nanotube Quantum Resistors," *Science*, vol. 280, no. 5370, pp. 1744–1746, Jun. 1998. [Online]. Available: http://www.sciencemag.org/cgi/doi/10.1126/science.280.5370.1744

[108] D. Natelson, *Nanostructures and Nanotechnology.* Cambridge University Press, Jun. 2015, google-Books-ID: A6umCQAAQBAJ.

[109] M. Di Ventra, "Electrical Transport in Nanoscale Systems," *Electrical Transport in Nanoscale Systems*, Aug. 2008. [Online]. Available: https://ui.adsabs.harvard.edu/2008etns.book.....D/abstract

[110] S. Datta, "Exclusion principle and the Landauer-Büttiker formalism," *Physical Review B*, vol. 45, no. 3, pp. 1347–1362, Jan. 1992. [Online]. Available: https://link.aps.org/doi/10.1103/PhysRevB.45.1347

[111] M. L. Perrin, E. Burzurí, and H. S. J. v. d. Zant, "Single-molecule transistors," *Chemical Society Reviews*, vol. 44, no. 4, pp. 902–919, Feb. 2015. [Online]. Available: https://pubs.rsc.org/en/content/articlelanding/2015/cs/c4cs00231h

[112] D. Natelson, "Towards the ultimate transistor," *Physics World*, vol. 22, no. 06, pp. 27–31, Jun. 2009. [Online]. Available: https://doi.org/10.1088%2F2058-7058%2F22%2F06%2F37

[113] D. R. Ward, F. Hüser, F. Pauly, J. C. Cuevas, and D. Natelson, "Optical rectification and field enhancement in a plasmonic nanogap," *Nature Nanotechnology*, vol. 5, no. 10, pp. 732–736, Oct. 2010. [Online]. Available: https://www.nature.com/articles/nnano.2010.176

[114] D. Natelson, "Mechanical Break Junctions: Enormous Information in a Nanoscale Package," *ACS Nano*, vol. 6, no. 4, pp. 2871–2876, Apr. 2012. [Online]. Available: https://doi.org/10.1021/nn301323u

[115] A. Goel, J. B. Howard, and J. B. Vander Sande, "Size analysis of single fullerene molecules by electron microscopy," *Carbon*, vol. 42, no. 10, pp. 1907–1915, 2004. [Online]. Available: https://linkinghub.elsevier.com/retrieve/pii/S0008622304002180

[116] L. Venkataraman, J. E. Klare, I. W. Tam, C. Nuckolls, M. S. Hybertsen, and M. L. Steigerwald, "Single-Molecule Circuits with Well-Defined Molecular Conductance," *Nano Letters*, vol. 6, no. 3, pp. 458–462, Mar. 2006. [Online]. Available: https://doi.org/10.1021/nl052373+

[117] A. Aviram and M. A. Ratner, "Molecular rectifiers," *Chemical Physics Letters*, vol. 29, no. 2, pp. 277–283, Nov. 1974. [Online]. Available: http://www.sciencedirect.com/science/article/pii/0009261474850311

[118] D. Natelson, L. H. Yu, J. W. Ciszek, Z. K. Keane, and J. M. Tour, "Single-molecule transistors: Electron transfer in the solid state," *Chemical Physics*, vol. 324, no. 1, pp. 267–275, May 2006. [Online]. Available: http://www.sciencedirect.com/science/article/pii/S0301010405006245

[119] M. F. Crommie, C. P. Lutz, and D. M. Eigler, "Imaging standing waves in a two-dimensional electron gas," *Nature*, vol. 363, no. 6429, pp. 524–527, Jun. 1993. [Online]. Available: https://www.nature.com/articles/363524a0

[120] B. Xu and N. J. Tao, "Measurement of Single-Molecule Resistance by Repeated Formation of Molecular Junctions," *Science*, vol. 301, no. 5637, pp. 1221–1223, Aug. 2003. [Online]. Available: https://science.sciencemag.org/content/301/5637/1221

[121] Xu, Zhang, Li, and Tao, "Direct Conductance Measurement of Single DNA Molecules in Aqueous Solution," *Nano Letters*, vol. 4, no. 6, pp. 1105–1108, Jun. 2004. [Online]. Available: https://doi.org/10.1021/nl0494295

[122] L. Grüter, M. T. González, R. Huber, M. Calame, and C. Schönenberger, "Electrical Conductance of Atomic Contacts in Liquid Environments," *Small*, vol. 1, no. 11, pp. 1067–1070, 2005. [Online]. Available: https://onlinelibrary.wiley.com/doi/abs/10.1002/smll.200500145

[123] J. Repp, G. Meyer, S. M. Stojković, A. Gourdon, and C. Joachim, “Molecules on Insulating Films: Scanning-Tunneling Microscopy Imaging of Individual Molecular Orbitals,” *Physical Review Letters*, vol. 94, no. 2, p. 026803, Jan. 2005. [Online]. Available: https://link.aps.org/doi/10.1103/PhysRevLett.94.026803

[124] S.-Y. Jang, P. Reddy, A. Majumdar, and R. A. Segalman, “Interpretation of Stochastic Events in Single Molecule Conductance Measurements,” *Nano Letters*, vol. 6, no. 10, pp. 2362–2367, Oct. 2006. [Online]. Available: https://doi.org/10.1021/nl0609495

[125] M. Tsutsui, K. Shoji, M. Taniguchi, and T. Kawai, “Formation and Self-Breaking Mechanism of Stable Atom-Sized Junctions,” *Nano Letters*, vol. 8, no. 1, pp. 345–349, Jan. 2008. [Online]. Available: https://doi.org/10.1021/nl073003j

[126] M. Kamenetska, M. Koentopp, A. C. Whalley, Y. S. Park, M. L. Steigerwald, C. Nuckolls, M. S. Hybertsen, and L. Venkataraman, “Formation and Evolution of Single-Molecule Junctions,” *Physical Review Letters*, vol. 102, no. 12, p. 126803, Mar. 2009. [Online]. Available: https://link.aps.org/doi/10.1103/PhysRevLett.102.126803

[127] W. Hu and L. J. Webb, “Direct Measurement of the Membrane Dipole Field in Bicelles Using Vibrational Stark Effect Spectroscopy,” *The Journal of Physical Chemistry Letters*, vol. 2, no. 15, pp. 1925–1930, Aug. 2011. [Online]. Available: https://doi.org/10.1021/jz200729a

[128] S. Kano, T. Tada, and Y. Majima, “Nanoparticle characterization based on STM and STS,” *Chemical Society Reviews*, vol. 44, no. 4, pp. 970–987, 2015. [Online]. Available: https://pubs.rsc.org/en/content/articlelanding/2015/cs/c4cs00204k

[129] A. R. Champagne, A. N. Pasupathy, and D. C. Ralph, “Mechanically Adjustable and Electrically Gated Single-Molecule Transistors,” *Nano Letters*, vol. 5, no. 2, pp. 305–308, Feb. 2005. [Online]. Available: https://doi.org/10.1021/nl0480619

[130] M. A. Reed, C. Zhou, C. J. Muller, T. P. Burgin, and J. M. Tour, “Conductance of a Molecular Junction,” *Science*, vol. 278, no. 5336, pp. 252–254, Oct. 1997. [Online]. Available: https://science.sciencemag.org/content/278/5336/252

[131] J. Reichert, R. Ochs, D. Beckmann, H. B. Weber, M. Mayor, and H. v. Löhneysen, “Driving Current through Single Organic Molecules,” *Physical Review Letters*, vol. 88, no. 17, p. 176804, Apr. 2002. [Online]. Available: https://link.aps.org/doi/10.1103/PhysRevLett.88.176804

[132] R. Huber, M. T. González, S. Wu, M. Langer, S. Grunder, V. Horhoiu, M. Mayor, M. R. Bryce, C. Wang, R. Jitchati, C. Schönenberger, and M. Calame, "Electrical Conductance of Conjugated Oligomers at the Single Molecule Level," *Journal of the American Chemical Society*, vol. 130, no. 3, pp. 1080–1084, Jan. 2008. [Online]. Available: https://doi.org/10.1021/ja0767940

[133] M. T. González, S. Wu, R. Huber, S. J. van der Molen, C. Schönenberger, and M. Calame, "Electrical Conductance of Molecular Junctions by a Robust Statistical Analysis," *Nano Letters*, vol. 6, no. 10, pp. 2238–2242, Oct. 2006. [Online]. Available: https://doi.org/10.1021/nl061581e

[134] C. Kergueris, J.-P. Bourgoin, S. Palacin, D. Esteve, C. Urbina, M. Magoga, and C. Joachim, "Electron transport through a metal-molecule-metal junction," *Physical Review B*, vol. 59, no. 19, pp. 12 505–12 513, May 1999. [Online]. Available: https://link.aps.org/doi/10.1103/PhysRevB.59.12505

[135] S. Wu, M. T. González, R. Huber, S. Grunder, M. Mayor, C. Schönenberger, and M. Calame, "Molecular junctions based on aromatic coupling," *Nature Nanotechnology*, vol. 3, no. 9, pp. 569–574, Sep. 2008. [Online]. Available: https://www.nature.com/articles/nnano.2008.237

[136] D. Dulić, S. J. van der Molen, T. Kudernac, H. T. Jonkman, J. J. D. de Jong, T. N. Bowden, J. van Esch, B. L. Feringa, and B. J. van Wees, "One-Way Optoelectronic Switching of Photochromic Molecules on Gold," *Physical Review Letters*, vol. 91, no. 20, p. 207402, Nov. 2003. [Online]. Available: https://link.aps.org/doi/10.1103/PhysRevLett.91.207402

[137] D. Djukic and J. M. van Ruitenbeek, "Shot Noise Measurements on a Single Molecule," *Nano Letters*, vol. 6, no. 4, pp. 789–793, Apr. 2006. [Online]. Available: https://doi.org/10.1021/nl060116e

[138] E. Lörtscher, H. B. Weber, and H. Riel, "Statistical Approach to Investigating Transport through Single Molecules," *Physical Review Letters*, vol. 98, no. 17, p. 176807, Apr. 2007. [Online]. Available: https://link.aps.org/doi/10.1103/PhysRevLett.98.176807

[139] J.-H. Tian, B. Liu, Li, Z.-L. Yang, B. Ren, S.-T. Wu, Tao, and Z.-Q. Tian, "Study of Molecular Junctions with a Combined Surface-Enhanced Raman and Mechanically Controllable Break Junction Method," *Journal of the American Chemical Society*, vol. 128, no. 46, pp. 14 748–14 749, Nov. 2006. [Online]. Available: https://doi.org/10.1021/ja0648615

[140] J. Fock, J. K. Sørensen, E. Lörtscher, T. Vosch, C. A. Martin, H. Riel, K. Kilså, T. Bjørnholm, and H. v. d. Zant, "A statistical approach to inelastic electron tunneling spectroscopy on fullerene-terminated molecules," *Physical*

Chemistry Chemical Physics, vol. 13, no. 32, pp. 14 325–14 332, Aug. 2011. [Online]. Available: https://pubs.rsc.org/en/content/articlelanding/2011/cp/c1cp20861f

[141] T. Konishi, M. Kiguchi, M. Takase, F. Nagasawa, H. Nabika, K. Ikeda, K. Uosaki, K. Ueno, H. Misawa, and K. Murakoshi, "Single Molecule Dynamics at a Mechanically Controllable Break Junction in Solution at Room Temperature," *Journal of the American Chemical Society*, vol. 135, no. 3, pp. 1009–1014, Jan. 2013. [Online]. Available: https://doi.org/10.1021/ja307821u

[142] H. Park, A. K. L. Lim, A. P. Alivisatos, J. Park, and P. L. McEuen, "Fabrication of metallic electrodes with nanometer separation by electromigration," *Applied Physics Letters*, vol. 75, no. 2, pp. 301–303, Jul. 1999. [Online]. Available: https://aip.scitation.org/doi/abs/10.1063/1.124354

[143] H. Park, J. Park, A. K. L. Lim, E. H. Anderson, A. P. Alivisatos, and P. L. McEuen, "Nanomechanical oscillations in a single-C 60 transistor," *Nature*, vol. 407, no. 6800, pp. 57–60, Sep. 2000. [Online]. Available: https://www.nature.com/articles/35024031

[144] H. S. J. v. d. Zant, E. A. Osorio, M. Poot, and K. O'Neill, "Electromigrated molecular junctions," *physica status solidi (b)*, vol. 243, no. 13, pp. 3408–3412, 2006. [Online]. Available: https://onlinelibrary.wiley.com/doi/abs/10.1002/pssb.200669185

[145] D. R. Ward, N. K. Grady, C. S. Levin, N. J. Halas, Y. Wu, P. Nordlander, and D. Natelson, "Electromigrated Nanoscale Gaps for Surface-Enhanced Raman Spectroscopy," *Nano Letters*, vol. 7, no. 5, pp. 1396–1400, May 2007. [Online]. Available: https://doi.org/10.1021/nl070625w

[146] D. R. Ward, G. D. Scott, Z. K. Keane, N. J. Halas, and D. Natelson, "Electronic and optical properties of electromigrated molecular junctions," *Journal of Physics: Condensed Matter*, vol. 20, no. 37, p. 374118, Aug. 2008. [Online]. Available: https://doi.org/10.1088%2F0953-8984%2F20%2F37%2F374118

[147] L. H. Yu and D. Natelson, "The Kondo Effect in C60 Single-Molecule Transistors," *Nano Letters*, vol. 4, no. 1, pp. 79–83, Jan. 2004. [Online]. Available: https://doi.org/10.1021/nl034893f

[148] J. Park, A. N. Pasupathy, J. I. Goldsmith, C. Chang, Y. Yaish, J. R. Petta, M. Rinkoski, J. P. Sethna, H. D. Abruña, P. L. McEuen, and D. C. Ralph, "Coulomb blockade and the Kondo effect in single-atom transistors," *Nature*, vol. 417, no. 6890, pp. 722–725, Jun. 2002. [Online]. Available: https://www.nature.com/articles/nature00791

[149] W. Liang, M. P. Shores, M. Bockrath, J. R. Long, and H. Park, “Kondo resonance in a single-molecule transistor,” *Nature*, vol. 417, no. 6890, pp. 725–729, Jun. 2002. [Online]. Available: https://www.nature.com/articles/nature00790

[150] Y. Li, P. Zolotavin, P. Doak, L. Kronik, J. B. Neaton, and D. Natelson, “Interplay of Bias-Driven Charging and the Vibrational Stark Effect in Molecular Junctions,” *Nano Letters*, vol. 16, no. 2, pp. 1104–1109, Feb. 2016. [Online]. Available: https://doi.org/10.1021/acs.nanolett.5b04340

[151] Y. Li, P. Doak, L. Kronik, J. B. Neaton, and D. Natelson, “Voltage tuning of vibrational mode energies in single-molecule junctions,” *Proceedings of the National Academy of Sciences*, vol. 111, no. 4, pp. 1282–1287, Jan. 2014. [Online]. Available: https://www.pnas.org/content/111/4/1282

[152] A. N. Pasupathy, R. C. Bialczak, J. Martinek, J. E. Grose, L. A. K. Donev, P. L. McEuen, and D. C. Ralph, “The Kondo Effect in the Presence of Ferromagnetism,” *Science*, vol. 306, no. 5693, pp. 86–89, Oct. 2004. [Online]. Available: https://science.sciencemag.org/content/306/5693/86

[153] L. H. Yu, Z. K. Keane, J. W. Ciszek, L. Cheng, M. P. Stewart, J. M. Tour, and D. Natelson, “Inelastic Electron Tunneling via Molecular Vibrations in Single-Molecule Transistors,” *Physical Review Letters*, vol. 93, no. 26, p. 266802, Dec. 2004. [Online]. Available: https://link.aps.org/doi/10.1103/PhysRevLett.93.266802

[154] A. N. Pasupathy, J. Park, C. Chang, A. V. Soldatov, S. Lebedkin, R. C. Bialczak, J. E. Grose, L. A. K. Donev, J. P. Sethna, D. C. Ralph, and P. L. McEuen, “Vibration-Assisted Electron Tunneling in C140 Transistors,” *Nano Letters*, vol. 5, no. 2, pp. 203–207, Feb. 2005. [Online]. Available: https://doi.org/10.1021/nl048619c

[155] L. H. Yu, Z. K. Keane, J. W. Ciszek, L. Cheng, J. M. Tour, T. Baruah, M. R. Pederson, and D. Natelson, “Kondo Resonances and Anomalous Gate Dependence in the Electrical Conductivity of Single-Molecule Transistors,” *Physical Review Letters*, vol. 95, no. 25, p. 256803, Dec. 2005. [Online]. Available: https://link.aps.org/doi/10.1103/PhysRevLett.95.256803

[156] H. B. Heersche, Z. de Groot, J. A. Folk, H. S. J. van der Zant, C. Romeike, M. R. Wegewijs, L. Zobbi, D. Barreca, E. Tondello, and A. Cornia, “Electron Transport through Single ${\mathrm{Mn}}_{12}$ Molecular Magnets,” *Physical Review Letters*, vol. 96, no. 20, p. 206801, May 2006. [Online]. Available: https://link.aps.org/doi/10.1103/PhysRevLett.96.206801

[157] D.-H. Chae, J. F. Berry, S. Jung, F. A. Cotton, C. A. Murillo, and Z. Yao, “Vibrational Excitations in Single Trimetal-Molecule Transistors,” *Nano Letters*, vol. 6, no. 2, pp. 165–168, Feb. 2006. [Online]. Available: https://doi.org/10.1021/nl0519027

[158] H. Song, Y. Kim, Y. H. Jang, H. Jeong, M. A. Reed, and T. Lee, “Observation of molecular orbital gating,” *Nature*, vol. 462, no. 7276, pp. 1039–1043, Dec. 2009. [Online]. Available: https://www.nature.com/articles/nature08639

[159] M. Galperin, M. A. Ratner, A. Nitzan, and A. Troisi, “Nuclear Coupling and Polarization in Molecular Transport Junctions: Beyond Tunneling to Function,” *Science*, vol. 319, no. 5866, pp. 1056–1060, Feb. 2008. [Online]. Available: https://science.sciencemag.org/content/319/5866/1056

[160] N. J. Tao, “Electron transport in molecular junctions,” *Nature Nanotechnology*, vol. 1, no. 3, pp. 173–181, Dec. 2006. [Online]. Available: https://www.nature.com/articles/nnano.2006.130

[161] X. Lu, M. Grobis, K. H. Khoo, S. G. Louie, and M. F. Crommie, “Charge transfer and screening in individual ${\mathrm{C}}_{60}$ molecules on metal substrates: A scanning tunneling spectroscopy and theoretical study,” *Physical Review B*, vol. 70, no. 11, p. 115418, Sep. 2004. [Online]. Available: https://link.aps.org/doi/10.1103/PhysRevB.70.115418

[162] M. A. Ratner, “Bridge-assisted electron transfer: effective electronic coupling,” *The Journal of Physical Chemistry*, vol. 94, no. 12, pp. 4877–4883, Jun. 1990. [Online]. Available: https://doi.org/10.1021/j100375a024

[163] M. Büttiker, Y. Imry, R. Landauer, and S. Pinhas, “Generalized many-channel conductance formula with application to small rings,” *Physical Review B*, vol. 31, no. 10, pp. 6207–6215, May 1985. [Online]. Available: https://link.aps.org/doi/10.1103/PhysRevB.31.6207

[164] B. Capozzi, Q. Chen, P. Darancet, M. Kotiuga, M. Buzzeo, J. B. Neaton, C. Nuckolls, and L. Venkataraman, “Tunable Charge Transport in Single-Molecule Junctions via Electrolytic Gating,” *Nano Letters*, vol. 14, no. 3, pp. 1400–1404, Mar. 2014. [Online]. Available: https://doi.org/10.1021/nl404459q

[165] J. Zhang, A. M. Kuznetsov, I. G. Medvedev, Q. Chi, T. Albrecht, P. S. Jensen, and J. Ulstrup, “Single-Molecule Electron Transfer in Electrochemical Environments,” *Chemical Reviews*, vol. 108, no. 7, pp. 2737–2791, Jul. 2008. [Online]. Available: https://doi.org/10.1021/cr068073+

[166] J. Chen, W. Wang, M. A. Reed, A. M. Rawlett, D. W. Price, and J. M. Tour, “Room-temperature negative differential resistance in nanoscale molecular

junctions," *Applied Physics Letters*, vol. 77, no. 8, pp. 1224–1226, Aug. 2000. [Online]. Available: https://aip.scitation.org/doi/abs/10.1063/1.1289650

[167] K. Ismail, B. S. Meyerson, and P. J. Wang, "Electron resonant tunneling in Si/SiGe double barrier diodes," *Applied Physics Letters*, vol. 59, no. 8, pp. 973–975, Aug. 1991. [Online]. Available: https://aip.scitation.org/doi/abs/10.1063/1.106319

[168] D. Natelson, Y. Li, and J. B. Herzog, "Nanogap structures: combining enhanced Raman spectroscopy and electronic transport," *Physical Chemistry Chemical Physics*, vol. 15, no. 15, pp. 5262–5275, 2013. [Online]. Available: https://pubs.rsc.org/en/content/articlelanding/2013/cp/c3cp44142c

[169] M. Galperin, M. A. Ratner, and A. Nitzan, "Molecular transport junctions: vibrational effects," *Journal of Physics: Condensed Matter*, vol. 19, no. 10, p. 103201, Feb. 2007. [Online]. Available: https://doi.org/10.1088%2F0953-8984%2F19%2F10%2F103201

[170] H. Song, M. A. Reed, and T. Lee, "Single Molecule Electronic Devices," *Advanced Materials*, vol. 23, no. 14, pp. 1583–1608, 2011. [Online]. Available: https://onlinelibrary.wiley.com/doi/abs/10.1002/adma.201004291

[171] S. Gregory, "Inelastic tunneling spectroscopy and single-electron tunneling in an adjustable microscopic tunnel junction," *Physical Review Letters*, vol. 64, no. 6, pp. 689–692, Feb. 1990. [Online]. Available: https://link.aps.org/doi/10.1103/PhysRevLett.64.689

[172] M. Taniguchi, M. Tsutsui, K. Yokota, and T. Kawai, "Inelastic electron tunneling spectroscopy of single-molecule junctions using a mechanically controllable break junction," *Nanotechnology*, vol. 20, no. 43, p. 434008, Oct. 2009. [Online]. Available: https://doi.org/10.1088%2F0957-4484%2F20%2F43%2F434008

[173] B. C. Stipe, M. A. Rezaei, and W. Ho, "Single-Molecule Vibrational Spectroscopy and Microscopy," *Science*, vol. 280, no. 5370, pp. 1732–1735, Jun. 1998. [Online]. Available: https://science.sciencemag.org/content/280/5370/1732

[174] T. Shamai and Y. Selzer, "Spectroscopy of molecular junctions," *Chemical Society Reviews*, vol. 40, no. 5, pp. 2293–2305, 2011. [Online]. Available: https://pubs.rsc.org/en/content/articlelanding/2011/cs/c0cs00155d

[175] A. Nitzan and M. A. Ratner, "Electron Transport in Molecular Wire Junctions," *Science*, vol. 300, no. 5624, pp. 1384–1389, May 2003. [Online]. Available: https://science.sciencemag.org/content/300/5624/1384

[176] X. H. Qiu, G. V. Nazin, and W. Ho, "Vibronic States in Single Molecule Electron Transport," *Physical Review Letters*, vol. 92, no. 20, p. 206102, May 2004. [Online]. Available: https://link.aps.org/doi/10.1103/PhysRevLett.92.206102

[177] J. G. Kushmerick, J. Lazorcik, C. H. Patterson, R. Shashidhar, D. S. Seferos, and G. C. Bazan, "Vibronic Contributions to Charge Transport Across Molecular Junctions," *Nano Letters*, vol. 4, no. 4, pp. 639–642, Apr. 2004. [Online]. Available: https://doi.org/10.1021/nl049871n

[178] M. Galperin, M. A. Ratner, and A. Nitzan, "Inelastic electron tunneling spectroscopy in molecular junctions: Peaks and dips," *The Journal of Chemical Physics*, vol. 121, no. 23, pp. 11 965–11 979, Nov. 2004. [Online]. Available: https://aip.scitation.org/doi/abs/10.1063/1.1814076

[179] N. Agraït, C. Untiedt, G. Rubio-Bollinger, and S. Vieira, "Onset of Energy Dissipation in Ballistic Atomic Wires," *Physical Review Letters*, vol. 88, no. 21, p. 216803, May 2002. [Online]. Available: https://link.aps.org/doi/10.1103/PhysRevLett.88.216803

[180] R. C. Jaklevic and J. Lambe, "Molecular Vibration Spectra by Electron Tunneling," *Physical Review Letters*, vol. 17, no. 22, pp. 1139–1140, Nov. 1966. [Online]. Available: https://link.aps.org/doi/10.1103/PhysRevLett.17.1139

[181] W. Wang, T. Lee, I. Kretzschmar, and M. A. Reed, "Inelastic Electron Tunneling Spectroscopy of an Alkanedithiol Self-Assembled Monolayer," *Nano Lett.*, vol. 4, no. 4, p. 4, 2004.

[182] H. Song, Y. Kim, J. Ku, Y. H. Jang, H. Jeong, and T. Lee, "Vibrational spectra of metal-molecule-metal junctions in electromigrated nanogap electrodes by inelastic electron tunneling," *Applied Physics Letters*, vol. 94, no. 10, p. 103110, Mar. 2009. [Online]. Available: https://aip.scitation.org/doi/full/10.1063/1.3097217

[183] J. Lambe and R. C. Jaklevic, "Molecular Vibration Spectra by Inelastic Electron Tunneling," *Physical Review*, vol. 165, no. 3, pp. 821–832, Jan. 1968. [Online]. Available: https://link.aps.org/doi/10.1103/PhysRev.165.821

[184] J. M. Beebe, H. J. Moore, T. R. Lee, and J. G. Kushmerick, "Vibronic Coupling in Semifluorinated Alkanethiol Junctions: Implications for Selection Rules in Inelastic Electron Tunneling Spectroscopy," *Nano Letters*, vol. 7, no. 5, pp. 1364–1368, May 2007. [Online]. Available: https://doi.org/10.1021/nl070460r

[185] A. Sleigh, C. Adkins, and W. Phillips, "Study of adsorbed molecular species by inelastic electron tunnelling spectroscopy," *Vacuum*, vol. 38, no. 4,

pp. 301–304, Jan. 1988. [Online]. Available: http://www.sciencedirect.com/science/article/pii/0042207X88900656

[186] A. Troisi, J. M. Beebe, L. B. Picraux, R. D. v. Zee, D. R. Stewart, M. A. Ratner, and J. G. Kushmerick, "Tracing electronic pathways in molecules by using inelastic tunneling spectroscopy," *Proceedings of the National Academy of Sciences*, vol. 104, no. 36, pp. 14 255–14 259, Sep. 2007. [Online]. Available: https://www.pnas.org/content/104/36/14255

[187] M. A. Reed, "Inelastic electron tunneling spectroscopy," *Materials Today*, vol. 11, no. 11, pp. 46–50, Nov. 2008. [Online]. Available: http://www.sciencedirect.com/science/article/pii/S1369702108702384

[188] L. J. Lauhon and W. Ho, "Effects of temperature and other experimental variables on single molecule vibrational spectroscopy with the scanning tunneling microscope," *Review of Scientific Instruments*, vol. 72, no. 1, pp. 216–223, Jan. 2001. [Online]. Available: https://aip.scitation.org/doi/abs/10.1063/1.1327311

[189] J. Klein, A. Léger, M. Belin, D. Défourneau, and M. J. L. Sangster, "Inelastic-Electron-Tunneling Spectroscopy of Metal-Insulator-Metal Junctions," *Physical Review B*, vol. 7, no. 6, pp. 2336–2348, Mar. 1973. [Online]. Available: https://link.aps.org/doi/10.1103/PhysRevB.7.2336

[190] P. K. Hansma, "Inelastic electron tunneling," *Physics Reports*, vol. 30, no. 2, pp. 145–206, Apr. 1977. [Online]. Available: http://www.sciencedirect.com/science/article/pii/0370157377900540

[191] L. Novotny and B. Hecht, *Principles of Nano-Optics.* Cambridge University Press, Sep. 2012, google-Books-ID: RHC_AwAAQBAJ.

[192] J. M. Pitarke, V. M. Silkin, E. V. Chulkov, and P. M. Echenique, "Theory of surface plasmons and surface-plasmon polaritons," *Reports on Progress in Physics*, vol. 70, no. 1, pp. 1–87, Dec. 2006. [Online]. Available: https://doi.org/10.1088%2F0034-4885%2F70%2F1%2Fr01

[193] N. K. Grady, N. J. Halas, and P. Nordlander, "Influence of dielectric function properties on the optical response of plasmon resonant metallic nanoparticles," *Chemical Physics Letters*, vol. 399, no. 1, pp. 167–171, Nov. 2004. [Online]. Available: http://www.sciencedirect.com/science/article/pii/S000926140401557X

[194] P. B. Johnson and R. W. Christy, "Optical Constants of the Noble Metals," *Physical Review B*, vol. 6, no. 12, pp. 4370–4379, Dec. 1972. [Online]. Available: https://link.aps.org/doi/10.1103/PhysRevB.6.4370

[195] C. Clavero, "Plasmon-induced hot-electron generation at nanoparticle/metal-oxide interfaces for photovoltaic and photocatalytic devices," *Nature Photonics*, vol. 8, no. 2, pp. 95–103, Feb. 2014. [Online]. Available: http://www.nature.com/articles/nphoton.2013.238

[196] J. Lehmann, M. Merschdorf, W. Pfeiffer, A. Thon, S. Voll, and G. Gerber, "Surface Plasmon Dynamics in Silver Nanoparticles Studied by Femtosecond Time-Resolved Photoemission," *Physical Review Letters*, vol. 85, no. 14, pp. 2921–2924, Oct. 2000. [Online]. Available: https://link.aps.org/doi/10.1103/PhysRevLett.85.2921

[197] C. Lee, Y. Park, and J. Y. Park, "Hot electrons generated by intraband and interband transition detected using a plasmonic Cu/TiO2 nanodiode," *RSC Advances*, vol. 9, no. 32, pp. 18 371–18 376, Jun. 2019. [Online]. Available: https://pubs.rsc.org/en/content/articlelanding/2019/ra/c9ra02601k

[198] M. Moskovits, "Surface-enhanced Raman spectroscopy: a brief retrospective," *Journal of Raman Spectroscopy*, vol. 36, no. 6-7, pp. 485–496, 2005. [Online]. Available: https://onlinelibrary.wiley.com/doi/abs/10.1002/jrs.1362

[199] G. L. Eesley, "Generation of nonequilibrium electron and lattice temperatures in copper by picosecond laser pulses," *Physical Review B*, vol. 33, no. 4, pp. 2144–2151, Feb. 1986. [Online]. Available: https://link.aps.org/doi/10.1103/PhysRevB.33.2144

[200] P. Pyykko and J. P. Desclaux, "Relativity and the periodic system of elements," *Accounts of Chemical Research*, vol. 12, no. 8, pp. 276–281, Aug. 1979. [Online]. Available: https://doi.org/10.1021/ar50140a002

[201] A. Derkachova, K. Kolwas, and I. Demchenko, "Dielectric Function for Gold in Plasmonics Applications: Size Dependence of Plasmon Resonance Frequencies and Damping Rates for Nanospheres," *Plasmonics (Norwell, Mass.)*, vol. 11, pp. 941–951, 2016. [Online]. Available: https://www.ncbi.nlm.nih.gov/pmc/articles/PMC4875142/

[202] M. R. Beversluis, A. Bouhelier, and L. Novotny, "Continuum generation from single gold nanostructures through near-field mediated intraband transitions," *Physical Review B*, vol. 68, no. 11, p. 115433, Sep. 2003. [Online]. Available: https://link.aps.org/doi/10.1103/PhysRevB.68.115433

[203] H. Ehrenreich and H. R. Philipp, "Optical Properties of Ag and Cu," *Physical Review*, vol. 128, no. 4, pp. 1622–1629, Nov. 1962. [Online]. Available: https://link.aps.org/doi/10.1103/PhysRev.128.1622

[204] H. Yu, Y. Peng, Y. Yang, and Z.-Y. Li, "Plasmon-enhanced light–matter interactions and applications," *npj Computational Materials*, vol. 5, no. 1, pp. 1–14, Apr. 2019. [Online]. Available: https://www.nature.com/articles/s41524-019-0184-1

[205] V. Amendola, R. Pilot, M. Frasconi, O. M. Maragò, and M. A. Iatì, "Surface plasmon resonance in gold nanoparticles: a review," *Journal of Physics: Condensed Matter*, vol. 29, no. 20, p. 203002, Apr. 2017. [Online]. Available: https://doi.org/10.1088%2F1361-648x%2Faa60f3

[206] K. Kolwas, A. Derkachova, and M. Shopa, "Size characteristics of surface plasmons and their manifestation in scattering properties of metal particles," *Journal of Quantitative Spectroscopy and Radiative Transfer*, vol. 110, no. 14, pp. 1490–1501, Sep. 2009. [Online]. Available: http://www.sciencedirect.com/science/article/pii/S0022407309001186

[207] D. K. Gramotnev and S. I. Bozhevolnyi, "Nanofocusing of electromagnetic radiation," *Nature Photonics*, vol. 8, no. 1, pp. 13–22, Jan. 2014. [Online]. Available: https://www.nature.com/articles/nphoton.2013.232

[208] H. J. Lezec, A. Degiron, E. Devaux, R. A. Linke, L. Martin-Moreno, F. J. Garcia-Vidal, and T. W. Ebbesen, "Beaming Light from a Subwavelength Aperture," *Science*, vol. 297, no. 5582, pp. 820–822, Aug. 2002. [Online]. Available: https://science.sciencemag.org/content/297/5582/820

[209] G. Ghafoori, J. Boneberg, P. Leiderer, and E. Scheer, "Tuning the transmission of surface plasmon polaritons across nano and micro gaps in gold stripes," *Optics Express*, vol. 24, no. 15, pp. 17 313–17 320, Jul. 2016. [Online]. Available: https://www.osapublishing.org/oe/abstract.cfm?uri=oe-24-15-17313

[210] A. Ganser, D. Benner, R. Waitz, J. Boneberg, E. Scheer, and P. Leiderer, "Time-resolved optical measurement of thermal transport by surface plasmon polaritons in thin metal stripes," *Applied Physics Letters*, vol. 105, no. 19, p. 191119, Nov. 2014. [Online]. Available: https://aip.scitation.org/doi/full/10.1063/1.4901956

[211] S. Berweger, J. M. Atkin, R. L. Olmon, and M. B. Raschke, "Adiabatic Tip-Plasmon Focusing for Nano-Raman Spectroscopy," *The Journal of Physical Chemistry Letters*, vol. 1, no. 24, pp. 3427–3432, Dec. 2010. [Online]. Available: https://doi.org/10.1021/jz101289z

[212] C. Huck, J. Vogt, M. Sendner, D. Hengstler, F. Neubrech, and A. Pucci, "Plasmonic Enhancement of Infrared Vibrational Signals: Nanoslits versus Nanorods," *ACS Photonics*, vol. 2, no. 10, pp. 1489–1497, Oct. 2015. [Online]. Available: https://doi.org/10.1021/acsphotonics.5b00390

[213] J. T. van Wijngaarden, E. Verhagen, A. Polman, C. E. Ross, H. J. Lezec, and H. A. Atwater, "Direct imaging of propagation and damping of near-resonance surface plasmon polaritons using cathodoluminescence spectroscopy," *Applied Physics Letters*, vol. 88, no. 22, p. 221111, May 2006. [Online]. Available: https://aip.scitation.org/doi/full/10.1063/1.2208556

[214] N. Ittah and Y. Selzer, "Electrical Detection of Surface Plasmon Polaritons by 1g0 Gold Quantum Point Contacts," *Nano Letters*, vol. 11, no. 2, pp. 529–534, Feb. 2011. [Online]. Available: https://doi.org/10.1021/nl103398z

[215] T. B. Möller, A. Ganser, M. Kratt, S. Dickreuter, R. Waitz, E. Scheer, J. Boneberg, and P. Leiderer, "Fast quantitative optical detection of heat dissipation by surface plasmon polaritons," *Nanoscale*, vol. 10, no. 25, pp. 11 894–11 900, 2018. [Online]. Available: https://pubs.rsc.org/en/content/articlelanding/2018/nr/c8nr02489h

[216] C. Ropers, C. C. Neacsu, T. Elsaesser, M. Albrecht, M. B. Raschke, and C. Lienau, "Grating-Coupling of Surface Plasmons onto Metallic Tips: A Nanoconfined Light Source," *Nano Letters*, vol. 7, no. 9, pp. 2784–2788, Sep. 2007. [Online]. Available: https://doi.org/10.1021/nl071340m

[217] M. V. Bashevoy, F. Jonsson, K. F. MacDonald, Y. Chen, and N. I. Zheludev, "Hyperspectral imaging of plasmonic nanostructures with nanoscale resolution," *Optics Express*, vol. 15, no. 18, pp. 11 313–11 320, Sep. 2007. [Online]. Available: https://www.osapublishing.org/oe/abstract.cfm?uri=oe-15-18-11313

[218] B. Steinberger, A. Hohenau, H. Ditlbacher, A. L. Stepanov, A. Drezet, F. R. Aussenegg, A. Leitner, and J. R. Krenn, "Dielectric stripes on gold as surface plasmon waveguides," *Applied Physics Letters*, vol. 88, no. 9, p. 094104, Feb. 2006. [Online]. Available: https://aip.scitation.org/doi/full/10.1063/1.2180448

[219] M. Kuttge, E. J. R. Vesseur, J. Verhoeven, H. J. Lezec, H. A. Atwater, and A. Polman, "Loss mechanisms of surface plasmon polaritons on gold probed by cathodoluminescence imaging spectroscopy." *Applied Physics Letters*, vol. 93, no. 11, p. 113110, Sep. 2008. [Online]. Available: https://aip.scitation.org/doi/full/10.1063/1.2987458

[220] M. Müller, V. Kravtsov, A. Paarmann, M. B. Raschke, and R. Ernstorfer, "Nanofocused Plasmon-Driven Sub-10 fs Electron Point Source," *ACS Photonics*, vol. 3, no. 4, pp. 611–619, Apr. 2016. [Online]. Available: https://doi.org/10.1021/acsphotonics.5b00710

[221] N. Hiramatsu, F. Kusa, K. Imasaka, I. Morichika, A. Takegami, and S. Ashihara, "Propagation length of mid-infrared surface plasmon polaritons

on gold: Impact of morphology change by thermal annealing," *Journal of Applied Physics*, vol. 120, no. 17, p. 173103, Nov. 2016. [Online]. Available: https://aip.scitation.org/doi/full/10.1063/1.4966934

[222] K. E. Cilwa, K. R. Rodriguez, J. M. Heer, M. A. Malone, L. D. Corwin, and J. V. Coe, "Propagation lengths of surface plasmon polaritons on metal films with arrays of subwavelength holes by infrared imaging spectroscopy," *The Journal of Chemical Physics*, vol. 131, no. 6, p. 061101, Aug. 2009. [Online]. Available: https://aip.scitation.org/doi/full/10.1063/1.3204693

[223] A. Otto, "Investigation of electrode surfaces by surface plasmon polariton spectroscopy," *Surface Science*, vol. 101, no. 1, pp. 99–108, Dec. 1980. [Online]. Available: http://www.sciencedirect.com/science/article/pii/0039602880906019

[224] ——, "Excitation of nonradiative surface plasma waves in silver by the method of frustrated total reflection," *Zeitschrift für Physik A Hadrons and nuclei*, vol. 216, no. 4, pp. 398–410, Aug. 1968. [Online]. Available: https://doi.org/10.1007/BF01391532

[225] E. Kretschmann, "Die Bestimmung optischer Konstanten von Metallen durch Anregung von Oberflächenplasmaschwingungen," *Zeitschrift für Physik A Hadrons and nuclei*, vol. 241, no. 4, pp. 313–324, Aug. 1971. [Online]. Available: https://doi.org/10.1007/BF01395428

[226] A. V. Zayats and I. I. Smolyaninov, "Near-field photonics: surface plasmon polaritons and localized surface plasmons," *Journal of Optics A: Pure and Applied Optics*, vol. 5, no. 4, pp. S16–S50, Jun. 2003. [Online]. Available: https://doi.org/10.1088%2F1464-4258%2F5%2F4%2F353

[227] B. Lamprecht, J. R. Krenn, G. Schider, H. Ditlbacher, M. Salerno, N. Felidj, A. Leitner, F. R. Aussenegg, and J. C. Weeber, "Surface plasmon propagation in microscale metal stripes," *Applied Physics Letters*, vol. 79, no. 1, pp. 51–53, Jun. 2001. [Online]. Available: https://aip.scitation.org/doi/abs/10.1063/1.1380236

[228] P. Dawson, F. de Fornel, and J.-P. Goudonnet, "Imaging of surface plasmon propagation and edge interaction using a photon scanning tunneling microscope," *Physical Review Letters*, vol. 72, no. 18, pp. 2927–2930, May 1994. [Online]. Available: https://link.aps.org/doi/10.1103/PhysRevLett.72.2927

[229] D. Benner, J. Boneberg, P. Nürnberger, G. Ghafoori, P. Leiderer, and E. Scheer, "Transmission of surface plasmon polaritons through atomic-size constrictions," *New Journal of Physics*, vol. 15, no. 11, p. 113014, Nov. 2013. [Online]. Available: https://doi.org/10.1088%2F1367-2630%2F15%2F11%2F113014

[230] O. Marti, H. Bielefeldt, B. Hecht, S. Herminghaus, P. Leiderer, and J. Mlynek, "Near-field optical measurement of the surface plasmon field," *Optics Communications*, vol. 96, no. 4, pp. 225–228, Feb. 1993. [Online]. Available: http://www.sciencedirect.com/science/article/pii/0030401893902657

[231] K. F. MacDonald, Z. L. Sámson, M. I. Stockman, and N. I. Zheludev, "Ultrafast active plasmonics," *Nature Photonics*, vol. 3, no. 1, pp. 55–58, Jan. 2009. [Online]. Available: https://www.nature.com/articles/nphoton.2008.249

[232] V. A. Zenin, A. Andryieuski, R. Malureanu, I. P. Radko, V. S. Volkov, D. K. Gramotnev, A. V. Lavrinenko, and S. I. Bozhevolnyi, "Boosting Local Field Enhancement by on-Chip Nanofocusing and Impedance-Matched Plasmonic Antennas," *Nano Letters*, vol. 15, no. 12, pp. 8148–8154, Dec. 2015. [Online]. Available: https://doi.org/10.1021/acs.nanolett.5b03593

[233] J. F. Donohue and E. Y. Wang, "Observation of radiative surface plasmons in metal-oxide-metal tunnel junctions," *Journal of Applied Physics*, vol. 59, no. 9, pp. 3137–3143, May 1986. [Online]. Available: https://aip.scitation.org/doi/abs/10.1063/1.336892

[234] R. A. Ferrell, "Predicted Radiation of Plasma Oscillations in Metal Films," *Physical Review*, vol. 111, no. 5, pp. 1214–1222, Sep. 1958. [Online]. Available: https://link.aps.org/doi/10.1103/PhysRev.111.1214

[235] K. A. Willets and R. P. Van Duyne, "Localized Surface Plasmon Resonance Spectroscopy and Sensing," *Annual Review of Physical Chemistry*, vol. 58, no. 1, pp. 267–297, 2007. [Online]. Available: https://doi.org/10.1146/annurev.physchem.58.032806.104607

[236] H. Xu, J. Aizpurua, M. Käll, and P. Apell, "Electromagnetic contributions to single-molecule sensitivity in surface-enhanced Raman scattering," *Physical Review E*, vol. 62, no. 3, pp. 4318–4324, Sep. 2000. [Online]. Available: https://link.aps.org/doi/10.1103/PhysRevE.62.4318

[237] H. Xu and M. Käll, "Polarization-Dependent Surface-Enhanced Raman Spectroscopy of Isolated Silver Nanoaggregates," *ChemPhysChem*, vol. 4, no. 9, pp. 1001–1005, 2003. [Online]. Available: https://onlinelibrary.wiley.com/doi/abs/10.1002/cphc.200200544

[238] A. Otto, "What is observed in single molecule SERS, and why?" *Journal of Raman Spectroscopy*, vol. 33, no. 8, pp. 593–598, 2002. [Online]. Available: https://onlinelibrary.wiley.com/doi/abs/10.1002/jrs.879

[239] K. L. Kelly, E. Coronado, L. L. Zhao, and G. C. Schatz, "The Optical Properties of Metal Nanoparticles: The Influence of Size, Shape, and Dielectric

Environment," *The Journal of Physical Chemistry B*, vol. 107, no. 3, pp. 668–677, Jan. 2003. [Online]. Available: https://doi.org/10.1021/jp026731y

[240] S. Link and M. A. El-Sayed, "Size and Temperature Dependence of the Plasmon Absorption of Colloidal Gold Nanoparticles," *The Journal of Physical Chemistry B*, vol. 103, no. 21, pp. 4212–4217, May 1999. [Online]. Available: https://doi.org/10.1021/jp984796o

[241] B. Tandon, A. Yadav, D. Khurana, P. Reddy, P. K. Santra, and A. Nag, "Size-Induced Enhancement of Carrier Density, LSPR Quality Factor, and Carrier Mobility in Cr–Sn Doped In2o3 Nanocrystals," *Chemistry of Materials*, vol. 29, no. 21, pp. 9360–9368, Nov. 2017. [Online]. Available: https://doi.org/10.1021/acs.chemmater.7b03351

[242] B. Tandon, S. Ghosh, and D. J. Milliron, "Dopant Selection Strategy for High-Quality Factor Localized Surface Plasmon Resonance from Doped Metal Oxide Nanocrystals," *Chemistry of Materials*, vol. 31, no. 18, pp. 7752–7760, Sep. 2019. [Online]. Available: https://pubs.acs.org/doi/10.1021/acs.chemmater.9b02917

[243] J. B. Herzog, M. W. Knight, Y. Li, K. M. Evans, N. J. Halas, and D. Natelson, "Dark Plasmons in Hot Spot Generation and Polarization in Interelectrode Nanoscale Junctions," *Nano Letters*, vol. 13, no. 3, pp. 1359–1364, Mar. 2013. [Online]. Available: https://doi.org/10.1021/nl400363d

[244] G. Baffou and R. Quidant, "Thermo-plasmonics: using metallic nanostructures as nano-sources of heat," *Laser & Photonics Reviews*, vol. 7, no. 2, pp. 171–187, 2013. [Online]. Available: https://onlinelibrary.wiley.com/doi/abs/10.1002/lpor.201200003

[245] G. Baffou, C. Girard, and R. Quidant, "Mapping Heat Origin in Plasmonic Structures," *Physical Review Letters*, vol. 104, no. 13, p. 136805, Apr. 2010. [Online]. Available: https://link.aps.org/doi/10.1103/PhysRevLett.104.136805

[246] Z. J. Coppens, W. Li, D. G. Walker, and J. G. Valentine, "Probing and Controlling Photothermal Heat Generation in Plasmonic Nanostructures," *Nano Letters*, vol. 13, no. 3, pp. 1023–1028, Mar. 2013. [Online]. Available: https://doi.org/10.1021/nl304208s

[247] R. H. M. Groeneveld, R. Sprik, and A. Lagendijk, "Ultrafast relaxation of electrons probed by surface plasmons at a thin silver film," *Physical Review Letters*, vol. 64, no. 7, pp. 784–787, Feb. 1990. [Online]. Available: https://link.aps.org/doi/10.1103/PhysRevLett.64.784

[248] M. B. Lundeberg, Y. Gao, A. Woessner, C. Tan, P. Alonso-González, K. Watanabe, T. Taniguchi, J. Hone, R. Hillenbrand, and F. H. L. Koppens, “Thermoelectric detection and imaging of propagating graphene plasmons,” *Nature Materials*, vol. 16, no. 2, pp. 204–207, Feb. 2017. [Online]. Available: https://www.nature.com/articles/nmat4755

[249] S. Kallatt, G. Umesh, N. Bhat, and K. Majumdar, “Photoresponse of atomically thin MoS 2 layers and their planar heterojunctions,” *Nanoscale*, vol. 8, no. 33, pp. 15 213–15 222, 2016. [Online]. Available: https://pubs.rsc.org/en/content/articlelanding/2016/nr/c6nr02828d

[250] J. F. Sierra, I. Neumann, M. V. Costache, and S. O. Valenzuela, “Hot-Carrier Seebeck Effect: Diffusion and Remote Detection of Hot Carriers in Graphene,” *Nano Letters*, vol. 15, no. 6, pp. 4000–4005, Jun. 2015. [Online]. Available: https://doi.org/10.1021/acs.nanolett.5b00922

[251] T. Inagaki, K. Kagami, and E. T. Arakawa, “Photoacoustic observation of nonradiative decay of surface plasmons in silver,” *Physical Review B*, vol. 24, no. 6, pp. 3644–3646, Sep. 1981. [Online]. Available: https://link.aps.org/doi/10.1103/PhysRevB.24.3644

[252] P. Dombi, A. Hörl, P. Rácz, I. Márton, A. Trügler, J. R. Krenn, and U. Hohenester, “Ultrafast Strong-Field Photoemission from Plasmonic Nanoparticles,” *Nano Letters*, vol. 13, no. 2, pp. 674–678, Feb. 2013. [Online]. Available: https://doi.org/10.1021/nl304365e

[253] T. Rybka, M. Ludwig, M. F. Schmalz, V. Knittel, D. Brida, and A. Leitenstorfer, “Sub-cycle optical phase control of nanotunnelling in the single-electron regime,” *Nature Photonics*, vol. 10, no. 10, pp. 667–670, Oct. 2016. [Online]. Available: https://www.nature.com/articles/nphoton.2016.174/

[254] J. Vogelsang, J. Robin, B. J. Nagy, P. Dombi, D. Rosenkranz, M. Schiek, P. Groß, and C. Lienau, “Ultrafast Electron Emission from a Sharp Metal Nanotaper Driven by Adiabatic Nanofocusing of Surface Plasmons,” *Nano Letters*, vol. 15, no. 7, pp. 4685–4691, Jul. 2015. [Online]. Available: https://doi.org/10.1021/acs.nanolett.5b01513

[255] S. Wu and M. T. Sheldon, “Optical Power Conversion via Tunneling of Plasmonic Hot Carriers,” *ACS Photonics*, vol. 5, no. 6, pp. 2516–2523, Jun. 2018. [Online]. Available: https://doi.org/10.1021/acsphotonics.8b00347

[256] W. Li and J. G. Valentine, “Harvesting the loss: surface plasmon-based hot electron photodetection,” *Nanophotonics*, vol. 6, no. 1, pp. 177–191, Jan. 2017. [Online]. Available: http://www.degruyter.com/view/j/nanoph.2017.6.issue-1/nanoph-2015-0154/nanoph-2015-0154.xml

[257] M. Vadai, N. Nachman, M. Ben-Zion, M. Bürkle, F. Pauly, J. C. Cuevas, and Y. Selzer, “Plasmon-Induced Conductance Enhancement in Single-Molecule Junctions,” *The Journal of Physical Chemistry Letters*, vol. 4, no. 17, pp. 2811–2816, Sep. 2013. [Online]. Available: https://doi.org/10.1021/jz4014008

[258] M. Vadai and Y. Selzer, “Plasmon-Induced Hot Carriers Transport in Metallic Ballistic Junctions,” *The Journal of Physical Chemistry C*, vol. 120, no. 37, pp. 21 063–21 068, Sep. 2016. [Online]. Available: https://doi.org/10.1021/acs.jpcc.6b03554

[259] D. C. Guhr, D. Rettinger, J. Boneberg, A. Erbe, P. Leiderer, and E. Scheer, “Influence of Laser Light on Electronic Transport through Atomic-Size Contacts,” *Physical Review Letters*, vol. 99, no. 8, p. 086801, Aug. 2007. [Online]. Available: https://link.aps.org/doi/10.1103/PhysRevLett.99.086801

[260] B. Kopp, Z. Yi, D. Benner, F.-Q. Xie, C. Obermair, T. Schimmel, J. Boneberg, P. Leiderer, and E. Scheer, “Revealing thermal effects in the electronic transport through irradiated atomic metal point contacts,” *Beilstein Journal of Nanotechnology*, vol. 3, no. 1, pp. 703–711, Oct. 2012. [Online]. Available: https://www.beilstein-journals.org/bjnano/articles/3/80

[261] E.-D. Fung, O. Adak, G. Lovat, D. Scarabelli, and L. Venkataraman, “Too Hot for Photon-Assisted Transport: Hot-Electrons Dominate Conductance Enhancement in Illuminated Single-Molecule Junctions,” *Nano Letters*, vol. 17, no. 2, pp. 1255–1261, Feb. 2017. [Online]. Available: https://doi.org/10.1021/acs.nanolett.6b05091

[262] P. P. Pal, N. Jiang, M. D. Sonntag, N. Chiang, E. T. Foley, M. C. Hersam, R. P. Van Duyne, and T. Seideman, “Plasmon-Mediated Electron Transport in Tip-Enhanced Raman Spectroscopic Junctions,” *The Journal of Physical Chemistry Letters*, vol. 6, no. 21, pp. 4210–4218, Nov. 2015. [Online]. Available: https://doi.org/10.1021/acs.jpclett.5b01902

[263] X. N. He, J. Allen, P. N. Black, T. Baldacchini, X. Huang, H. Huang, L. Jiang, and Y. F. Lu, “Coherent anti-Stokes Raman scattering and spontaneous Raman spectroscopy and microscopy of microalgae with nitrogen depletion,” *Biomedical Optics Express*, vol. 3, no. 11, pp. 2896–2906, Nov. 2012. [Online]. Available: https://www.osapublishing.org/boe/abstract.cfm?uri=boe-3-11-2896

[264] A. Zumbusch, G. R. Holtom, and X. S. Xie, “Three-Dimensional Vibrational Imaging by Coherent Anti-Stokes Raman Scattering,” *Physical Review Letters*, vol. 82, no. 20, pp. 4142–4145, May 1999. [Online]. Available: https://link.aps.org/doi/10.1103/PhysRevLett.82.4142

[265] S. L. Kleinman, E. Ringe, N. Valley, K. L. Wustholz, E. Phillips, K. A. Scheidt, G. C. Schatz, and R. P. Van Duyne, “Single-Molecule Surface-Enhanced Raman Spectroscopy of Crystal Violet Isotopologues: Theory and Experiment,” *Journal of the American Chemical Society*, vol. 133, no. 11, pp. 4115–4122, Mar. 2011. [Online]. Available: https://doi.org/10.1021/ja110964d

[266] D. Natelson, D. R. Ward, F. Hüser, F. Pauly, J. C. Cuevas, D. A. Corley, and J. M. Tour, “Plasmons in nanoscale metal junctions: optical rectification and thermometry,” *arXiv:1107.1147 [cond-mat]*, p. 80961O, Sep. 2011, arXiv: 1107.1147. [Online]. Available: http://arxiv.org/abs/1107.1147

[267] C. M. Galloway, E. C. L. Ru, and P. G. Etchegoin, “Single-molecule vibrational pumping in SERS,” *Physical Chemistry Chemical Physics*, vol. 11, no. 34, pp. 7372–7380, 2009. [Online]. Available: https://pubs.rsc.org/en/content/articlelanding/2009/cp/b904638k

[268] D. R. Ward, D. A. Corley, J. M. Tour, and D. Natelson, “Vibrational and electronic heating in nanoscale junctions,” *Nature Nanotechnology*, vol. 6, no. 1, pp. 33–38, Jan. 2011. [Online]. Available: https://www.nature.com/articles/nnano.2010.240

[269] D. P. Fromm, A. Sundaramurthy, A. Kinkhabwala, P. J. Schuck, G. S. Kino, and W. E. Moerner, “Exploring the chemical enhancement for surface-enhanced Raman scattering with Au bowtie nanoantennas,” *The Journal of Chemical Physics*, vol. 124, no. 6, p. 061101, Feb. 2006. [Online]. Available: https://aip.scitation.org/doi/full/10.1063/1.2167649

[270] P. L. Stiles, J. A. Dieringer, N. C. Shah, and R. P. Van Duyne, “Surface-Enhanced Raman Spectroscopy,” *Annual Review of Analytical Chemistry*, vol. 1, no. 1, pp. 601–626, 2008. [Online]. Available: https://doi.org/10.1146/annurev.anchem.1.031207.112814

[271] S. Nie and S. R. Emory, “Probing Single Molecules and Single Nanoparticles by Surface-Enhanced Raman Scattering,” *Science*, vol. 275, no. 5303, pp. 1102–1106, Feb. 1997. [Online]. Available: https://science.sciencemag.org/content/275/5303/1102

[272] P. G. Etchegoin and E. C. L. Ru, “A perspective on single molecule SERS : current status and future challenges,” *Physical Chemistry Chemical Physics*, vol. 10, no. 40, pp. 6079–6089, 2008. [Online]. Available: https://pubs.rsc.org/en/content/articlelanding/2008/cp/b809196j

[273] A. D. McFarland, M. A. Young, J. A. Dieringer, and R. P. Van Duyne, “Wavelength-Scanned Surface-Enhanced Raman Excitation Spectroscopy,”

The Journal of Physical Chemistry B, vol. 109, no. 22, pp. 11 279–11 285, Jun. 2005. [Online]. Available: https://doi.org/10.1021/jp050508u

[274] D. R. Ward, N. J. Halas, J. W. Ciszek, J. M. Tour, Y. Wu, P. Nordlander, and D. Natelson, “Simultaneous Measurements of Electronic Conduction and Raman Response in Molecular Junctions,” *Nano Letters*, vol. 8, no. 3, pp. 919–924, Mar. 2008. [Online]. Available: https://doi.org/10.1021/nl073346h

[275] P. C. Andersen, M. L. Jacobson, and K. L. Rowlen, “Flashy Silver Nanoparticles,” *The Journal of Physical Chemistry B*, vol. 108, no. 7, pp. 2148–2153, Feb. 2004. [Online]. Available: https://doi.org/10.1021/jp0306646

[276] A. Otto, W. Akemann, and A. Pucci, “Normal Bands in Surface-Enhanced Raman Scattering (SERS) and Their Relation to the Electron-Hole Pair Excitation Background in SERS,” *Israel Journal of Chemistry*, vol. 46, no. 3, pp. 307–315, 2006. [Online]. Available: https://onlinelibrary.wiley.com/doi/abs/10.1560/IJC_46_3_307

[277] S. Mahajan, R. M. Cole, J. D. Speed, S. H. Pelfrey, A. E. Russell, P. N. Bartlett, S. M. Barnett, and J. J. Baumberg, “Understanding the Surface-Enhanced Raman Spectroscopy “Background”,” *The Journal of Physical Chemistry C*, vol. 114, no. 16, pp. 7242–7250, Apr. 2010. [Online]. Available: https://doi.org/10.1021/jp907197b

[278] Jiang, K. Bosnick, M. Maillard, and L. Brus, “Single Molecule Raman Spectroscopy at the Junctions of Large Ag Nanocrystals,” *The Journal of Physical Chemistry B*, vol. 107, no. 37, pp. 9964–9972, Sep. 2003. [Online]. Available: https://doi.org/10.1021/jp034632u

[279] A. Zawadowski and M. Cardona, “Theory of Raman scattering on normal metals with impurities,” *Physical Review B*, vol. 42, no. 16, pp. 10 732–10 734, Dec. 1990. [Online]. Available: https://link.aps.org/doi/10.1103/PhysRevB.42.10732

[280] M. Galperin and A. Nitzan, “Raman Scattering and Electronic Heating in Molecular Conduction Junctions,” *The Journal of Physical Chemistry Letters*, vol. 2, no. 17, pp. 2110–2113, Sep. 2011. [Online]. Available: https://doi.org/10.1021/jz2008853

[281] ——, “Raman scattering from biased molecular conduction junctions: The electronic background and its temperature,” *Physical Review B*, vol. 84, no. 19, p. 195325, Nov. 2011. [Online]. Available: https://link.aps.org/doi/10.1103/PhysRevB.84.195325

[282] D. Richards, R. G. Milner, F. Huang, and F. Festy, “Tip-enhanced Raman microscopy: practicalities and limitations,” *Journal of Raman Spectroscopy*, vol. 34, no. 9, pp. 663–667, 2003. [Online]. Available: https://onlinelibrary.wiley.com/doi/abs/10.1002/jrs.1046

[283] K. F. Domke, D. Zhang, and B. Pettinger, “Toward Raman Fingerprints of Single Dye Molecules at Atomically Smooth Au(111),” *Journal of the American Chemical Society*, vol. 128, no. 45, pp. 14 721–14 727, Nov. 2006. [Online]. Available: https://doi.org/10.1021/ja065820b

[284] C. C. Neacsu, J. Dreyer, N. Behr, and M. B. Raschke, “Scanning-probe Raman spectroscopy with single-molecule sensitivity,” *Physical Review B*, vol. 73, no. 19, p. 193406, May 2006. [Online]. Available: https://link.aps.org/doi/10.1103/PhysRevB.73.193406

[285] W. Zhang, B. S. Yeo, T. Schmid, and R. Zenobi, “Single Molecule Tip-Enhanced Raman Spectroscopy with Silver Tips,” *The Journal of Physical Chemistry C*, vol. 111, no. 4, pp. 1733–1738, Feb. 2007. [Online]. Available: https://doi.org/10.1021/jp064740r

[286] J. A. Hutchison, S. P. Centeno, H. Odaka, H. Fukumura, J. Hofkens, and H. Uji-i, “Subdiffraction Limited, Remote Excitation of Surface Enhanced Raman Scattering,” *Nano Letters*, vol. 9, no. 3, pp. 995–1001, Mar. 2009. [Online]. Available: https://doi.org/10.1021/nl8030696

[287] Y. Fang, H. Wei, F. Hao, P. Nordlander, and H. Xu, “Remote-Excitation Surface-Enhanced Raman Scattering Using Propagating Ag Nanowire Plasmons,” *Nano Letters*, vol. 9, no. 5, pp. 2049–2053, May 2009. [Online]. Available: https://doi.org/10.1021/nl900321e

[288] J.-C. Weeber, J. R. Krenn, A. Dereux, B. Lamprecht, Y. Lacroute, and J. P. Goudonnet, “Near-field observation of surface plasmon polariton propagation on thin metal stripes,” *Physical Review B*, vol. 64, no. 4, p. 045411, Jul. 2001. [Online]. Available: https://link.aps.org/doi/10.1103/PhysRevB.64.045411

[289] J.-C. Weeber, Y. Lacroute, and A. Dereux, “Optical near-field distributions of surface plasmon waveguide modes,” *Physical Review B*, vol. 68, no. 11, p. 115401, Sep. 2003. [Online]. Available: https://link.aps.org/doi/10.1103/PhysRevB.68.115401

[290] J. B. Herzog, M. W. Knight, and D. Natelson, “Thermoplasmonics: Quantifying Plasmonic Heating in Single Nanowires,” *Nano Letters*, vol. 14, no. 2, pp. 499–503, Feb. 2014. [Online]. Available: https://doi.org/10.1021/nl403510u

[291] K. M. Evans, P. Zolotavin, and D. Natelson, "Plasmon-Assisted Photoresponse in Ge-Coated Bowtie Nanojunctions," *ACS Photonics*, vol. 2, no. 8, pp. 1192–1198, Aug. 2015. [Online]. Available: https://doi.org/10.1021/acsphotonics.5b00250

[292] P. Zolotavin, A. Alabastri, P. Nordlander, and D. Natelson, "Plasmonic Heating in Au Nanowires at Low Temperatures: The Role of Thermal Boundary Resistance," *ACS Nano*, vol. 10, no. 7, pp. 6972–6979, Jul. 2016. [Online]. Available: https://doi.org/10.1021/acsnano.6b02911

[293] A. Fursina, S. Lee, R. G. S. Sofin, I. V. Shvets, and D. Natelson, "Nanogaps with very large aspect ratios for electrical measurements," *Applied Physics Letters*, vol. 92, no. 11, p. 113102, Mar. 2008. [Online]. Available: https://aip.scitation.org/doi/full/10.1063/1.2895644

[294] W. Zhu, M. G. Banaee, D. Wang, Y. Chu, and K. B. Crozier, "Lithographically Fabricated Optical Antennas with Gaps Well Below 10 nm," *Small*, vol. 7, no. 13, pp. 1761–1766, 2011. [Online]. Available: https://onlinelibrary.wiley.com/doi/abs/10.1002/smll.201100371

[295] S. J. Bauman, E. C. Novak, D. T. Debu, D. Natelson, and J. B. Herzog, "Fabrication of Sub-Lithography-Limited Structures via Nanomasking Technique for Plasmonic Enhancement Applications," *IEEE Transactions on Nanotechnology*, vol. 14, no. 5, pp. 790–793, Sep. 2015.

[296] P. S. Ho and T. Kwok, "Electromigration in metals," *Reports on Progress in Physics*, vol. 52, no. 3, pp. 301–348, Mar. 1989. [Online]. Available: https://doi.org/10.1088%2F0034-4885%2F52%2F3%2F002

[297] D. Burgess, "Electromigration History and Failure Analysis," *Electronic Device Failure Analysis*, vol. 16, no. 3, pp. 14–196, 2014. [Online]. Available: https://www.asminternational.org/documents/10192/19808932/edfa1603p14.pdf/4028dce9-090c-4e21-aad6-2bbaa169b87c

[298] J. R. Black, "Physics of Electromigration," in *12th International Reliability Physics Symposium*, Apr. 1974, pp. 142–149, iSSN: 0735-0791.

[299] J. Black, "Electromigration—A brief survey and some recent results," *IEEE Transactions on Electron Devices*, vol. 16, no. 4, pp. 338–347, Apr. 1969.

[300] A. Mahapatro, S. Ghosh, and D. Janes, "Nanometer scale electrode separation (nanogap) using electromigration at room temperature," *IEEE Transactions on Nanotechnology*, vol. 5, no. 3, pp. 232–236, May 2006.

[301] M. L. Trouwborst, S. J. van der Molen, and B. J. van Wees, “The role of Joule heating in the formation of nanogaps by electromigration,” *Journal of Applied Physics*, vol. 99, no. 11, p. 114316, Jun. 2006. [Online]. Available: https://aip.scitation.org/doi/full/10.1063/1.2203410

[302] S. R. Emory, R. A. Jensen, T. Wenda, M. Han, and S. Nie, “Re-examining the origins of spectral blinking in single-molecule and single- nanoparticle SERS,” *Faraday Discussions*, vol. 132, no. 0, pp. 249–259, 2006. [Online]. Available: https://pubs.rsc.org/en/content/articlelanding/2006/fd/b509223j

[303] Z. Ioffe, T. Shamai, A. Ophir, G. Noy, I. Yutsis, K. Kfir, O. Cheshnovsky, and Y. Selzer, “Detection of heating in current-carrying molecular junctions by Raman scattering,” *Nature Nanotechnology*, vol. 3, no. 12, pp. 727–732, Dec. 2008. [Online]. Available: https://www.nature.com/articles/nnano.2008.304

[304] Z. Liu, S.-Y. Ding, Z.-B. Chen, X. Wang, J.-H. Tian, J. R. Anema, X.-S. Zhou, D.-Y. Wu, B.-W. Mao, X. Xu, B. Ren, and Z.-Q. Tian, “Revealing the molecular structure of single-molecule junctions in different conductance states by fishing-mode tip-enhanced Raman spectroscopy,” *Nature Communications*, vol. 2, no. 1, pp. 1–6, May 2011. [Online]. Available: https://www.nature.com/articles/ncomms1310

[305] R. Matsuhita, M. Horikawa, Y. Naitoh, H. Nakamura, and M. Kiguchi, “Conductance and SERS Measurement of Benzenedithiol Molecules Bridging Between Au Electrodes,” *The Journal of Physical Chemistry C*, vol. 117, no. 4, pp. 1791–1795, Jan. 2013. [Online]. Available: https://pubs.acs.org/doi/10.1021/jp3112638

[306] J. M. Klingsporn, N. Jiang, E. A. Pozzi, M. D. Sonntag, D. Chulhai, T. Seideman, L. Jensen, M. C. Hersam, and R. P. V. Duyne, “Intramolecular Insight into Adsorbate–Substrate Interactions via Low-Temperature, Ultrahigh-Vacuum Tip-Enhanced Raman Spectroscopy,” *Journal of the American Chemical Society*, vol. 136, no. 10, pp. 3881–3887, Mar. 2014. [Online]. Available: https://doi.org/10.1021/ja411899k

[307] S. W. Wu, N. Ogawa, and W. Ho, “Atomic-Scale Coupling of Photons to Single-Molecule Junctions,” *Science*, vol. 312, no. 5778, pp. 1362–1365, Jun. 2006. [Online]. Available: https://science.sciencemag.org/content/312/5778/1362

[308] J. Lee, S. M. Perdue, D. Whitmore, and V. A. Apkarian, “Laser-induced scanning tunneling microscopy: Linear excitation of the junction plasmon,” *The Journal of Chemical Physics*, vol. 133, no. 10, p. 104706, Sep. 2010. [Online]. Available: https://aip.scitation.org/doi/full/10.1063/1.3490398

[309] R. C. Maher, L. F. Cohen, J. C. Gallop, E. C. Le Ru, and P. G. Etchegoin, "Temperature-Dependent Anti-Stokes/Stokes Ratios under Surface-Enhanced Raman Scattering Conditions," *The Journal of Physical Chemistry B*, vol. 110, no. 13, pp. 6797–6803, Apr. 2006. [Online]. Available: https://doi.org/10.1021/jp056466r

[310] X. Huo, W. Sun, H. Liu, L. Peng, and S. Xu, "Response to "Comment on 'Unexpected size effect in the thermopower of thin-film stripes'" [J. Appl. Phys. 115, 236101 (2014)]," *Journal of Applied Physics*, vol. 115, no. 23, p. 236102, Jun. 2014. [Online]. Available: https://aip.scitation.org/doi/10.1063/1.4884736

[311] C. R. M. Grovenor, "Diffusion induced grain boundary migration in thin gold/copper films," *Acta Metallurgica*, vol. 33, no. 4, pp. 579–586, Apr. 1985. [Online]. Available: http://www.sciencedirect.com/science/article/pii/0001616085900227

[312] B. Feldman, S. Park, M. Haverty, S. Shankar, and S. T. Dunham, "Simulation of grain boundary effects on electronic transport in metals, and detailed causes of scattering," *physica status solidi (b)*, vol. 247, no. 7, pp. 1791–1796, 2010. [Online]. Available: https://onlinelibrary.wiley.com/doi/abs/10.1002/pssb.201046133

[313] X. Wang, C. I. Evans, and D. Natelson, "Photothermoelectric Detection of Gold Oxide Nonthermal Decomposition," *Nano Letters*, vol. 18, no. 10, pp. 6557–6562, Oct. 2018. [Online]. Available: https://doi.org/10.1021/acs.nanolett.8b03153

[314] P. Tantitarntong, P. Zalar, N. Matsuhisa, K. Nakano, S. Lee, T. Yokota, K. Tajima, and T. Someya, "High Sensitivity Tuning of Work Function of Self-Assembled Monolayers Modified Electrodes Using Vacuum Ultraviolet Treatment," *ACS Applied Materials & Interfaces*, vol. 9, no. 34, pp. 28 151–28 156, Aug. 2017. [Online]. Available: https://doi.org/10.1021/acsami.7b09756

[315] R. W. Zehner, B. F. Parsons, R. P. Hsung, and L. R. Sita, "Tuning the Work Function of Gold with Self-Assembled Monolayers Derived from X-[C6h4-CC-]nC6h4-SH (n = 0, 1, 2; X = H, F, CH3, CF3, and OCH3)," *Langmuir*, vol. 15, no. 4, pp. 1121–1127, Feb. 1999. [Online]. Available: https://doi.org/10.1021/la981114f

[316] O. Yamashita, "Effect of metal electrode on Seebeck coefficient of p- and n-type Si thermoelectrics," *Journal of Applied Physics*, vol. 95, no. 1, pp. 178–183, Dec. 2003. [Online]. Available: https://aip.scitation.org/doi/abs/10.1063/1.1630361

[317] B. H. Hamadani, D. A. Corley, J. W. Ciszek, J. M. Tour, and D. Natelson, "Controlling Charge Injection in Organic Field-Effect Transistors Using

Self-Assembled Monolayers," *Nano Letters*, vol. 6, no. 6, pp. 1303–1306, Jun. 2006. [Online]. Available: https://doi.org/10.1021/nl060731i

[318] L. T. Gan, R. Yang, R. Traylor, W. Cai, W. D. Nix, and J. A. Fan, "High-Throughput Growth of Microscale Gold Bicrystals for Single-Grain-Boundary Studies," *Advanced Materials*, vol. 31, no. 32, p. 1902189, 2019. [Online]. Available: https://onlinelibrary.wiley.com/doi/abs/10.1002/adma.201902189

[319] K. Zhang, X. B. Pitner, R. Yang, W. D. Nix, J. D. Plummer, and J. A. Fan, "Single-crystal metal growth on amorphous insulating substrates," *Proceedings of the National Academy of Sciences*, vol. 115, no. 4, pp. 685–689, Jan. 2018. [Online]. Available: https://www.pnas.org/content/115/4/685

[320] "EBSD - Electron Backscatter Diffraction - Nanoanalysis." [Online]. Available: https://nano.oxinst.com/products/ebsd/

[321] J. Alkorta, "Limits of simulation based high resolution EBSD," *Ultramicroscopy*, vol. 131, pp. 33–38, Aug. 2013. [Online]. Available: http://www.sciencedirect.com/science/article/pii/S0304399113000909

[322] C. Maurice, R. Fortunier, J. Driver, A. Day, K. Mingard, and G. Meaden, "Comments on the paper "Bragg's law diffraction simulations for electron backscatter diffraction analysis" by Josh Kacher, Colin Landon, Brent L. Adams & David Fullwood," *Ultramicroscopy*, vol. 110, no. 7, pp. 758–759, Jun. 2010. [Online]. Available: http://www.sciencedirect.com/science/article/pii/S0304399110000306

[323] T. B. Britton, C. Maurice, R. Fortunier, J. H. Driver, A. P. Day, G. Meaden, D. J. Dingley, K. Mingard, and A. J. Wilkinson, "Factors affecting the accuracy of high resolution electron backscatter diffraction when using simulated patterns," *Ultramicroscopy*, vol. 110, no. 12, pp. 1443–1453, Nov. 2010. [Online]. Available: http://www.sciencedirect.com/science/article/pii/S0304399110002214

[324] S. I. Wright, M. M. Nowell, and D. P. Field, "A Review of Strain Analysis Using Electron Backscatter Diffraction," *Microscopy and Microanalysis*, vol. 17, no. 3, pp. 316–329, Jun. 2011. [Online]. Available: https://www.cambridge.org/core/journals/microscopy-and-microanalysis/article/review-of-strain-analysis-using-electron-backscatter-diffraction/5318630F3BF9A8AB3C9ABD63C46F6698

[325] S. I. Wright, "A Review of Automated Orientation Imaging Microscopy OIM," *J Comput Assist Microsc*, vol. 5, pp. 207–221., 2003. [Online]. Available: https://www.researchgate.net/profile/Stuart_Wright/publication/269037434_A_Review_of_Automated_

Orientation_Imaging_Microscopy_OIM/links/55f199e208ae199d47c3535a/ A-Review-of-Automated-Orientation-Imaging-Microscopy-OIM.pdf

[326] K. H. Zou, K. Tuncali, and S. G. Silverman, "Correlation and Simple Linear Regression," *Radiology*, vol. 227, no. 3, pp. 617–628, Jun. 2003. [Online]. Available: https://pubs.rsna.org/doi/abs/10.1148/radiol.2273011499

[327] J. K. A. Amuzu, "The effect of tensile stress on the thermoelectric E. M. F. in copper, gold, and silver," *physica status solidi (a)*, vol. 63, no. 1, pp. K7–K10, 1981. [Online]. Available: https://onlinelibrary.wiley.com/doi/abs/10.1002/pssa.2210630151

[328] A. Kinbara and H. Haraki, "Internal Stress of Evaporated Thin Gold Films," *Japanese Journal of Applied Physics*, vol. 4, no. 4, p. 243, Apr. 1965. [Online]. Available: https://iopscience.iop.org/article/10.1143/JJAP.4.243/meta

[329] S. Jin, M. Huang, Y. Kwon, L. Zhang, B.-W. Li, S. Oh, J. Dong, D. Luo, M. Biswal, B. V. Cunning, P. V. Bakharev, I. Moon, W. J. Yoo, D. C. Camacho-Mojica, Y.-J. Kim, S. H. Lee, B. Wang, W. K. Seong, M. Saxena, F. Ding, H.-J. Shin, and R. S. Ruoff, "Colossal grain growth yields single-crystal metal foils by contact-free annealing," *Science*, vol. 362, no. 6418, pp. 1021–1025, Nov. 2018. [Online]. Available: https://science.sciencemag.org/content/362/6418/1021

[330] P. Parajuli, R. Mendoza-Cruz, U. Santiago, A. Ponce, and M. J. Yacamán, "The Evolution of Growth, Crystal Orientation, and Grain Boundaries Disorientation Distribution in Gold Thin Films," *Crystal Research and Technology*, vol. 53, no. 8, p. 1800038, 2018. [Online]. Available: https://onlinelibrary.wiley.com/doi/abs/10.1002/crat.201800038

[331] P. Hoppe, "NanoSIMS: A new tool in cosmochemistry," *Applied Surface Science*, vol. 252, no. 19, pp. 7102–7106, Jul. 2006. [Online]. Available: http://www.sciencedirect.com/science/article/pii/S0169433206004302

[332] A. J. Mortlock, A. H. Rowe, and A. D. L. Claire, "The atomic diffusion of platinum in gold," *The Philosophical Magazine: A Journal of Theoretical Experimental and Applied Physics*, vol. 5, no. 56, pp. 803–814, Aug. 1960. [Online]. Available: https://doi.org/10.1080/14786436008241219

[333] M. Hansen, K. Anderko, and H. W. Salzberg, "Constitution of Binary Alloys," *Journal of The Electrochemical Society*, vol. 105, no. 12, pp. 260C–261C, Dec. 1958. [Online]. Available: http://jes.ecsdl.org/content/105/12/260C

[334] C. I. Evans, P. Zolotavin, A. Alabastri, J. Yang, P. Nordlander, and D. Natelson, "Quantifying Remote Heating from Propagating Surface Plasmon

Polaritons," *Nano Letters*, vol. 17, no. 9, pp. 5646–5652, Sep. 2017. [Online]. Available: https://doi.org/10.1021/acs.nanolett.7b02524

[335] V. I. Belotelov, A. N. Kalish, A. K. Zvezdin, A. V. Gopal, and A. S. Vengurlekar, "Fabry–Perot plasmonic structures for nanophotonics," *JOSA B*, vol. 29, no. 3, pp. 294–299, Mar. 2012. [Online]. Available: https://www.osapublishing.org/josab/abstract.cfm?uri=josab-29-3-294

[336] N. Ittah, G. Noy, I. Yutsis, and Y. Selzer, "Measurement of Electronic Transport through 1g0 Gold Contacts under Laser Irradiation," *Nano Letters*, vol. 9, no. 4, pp. 1615–1620, Apr. 2009. [Online]. Available: https://doi.org/10.1021/nl803888q

[337] A. Kolloch, D. Benner, M. Bädicker, R. Waitz, T. Geldhauser, J. Boneberg, P. Leiderer, and E. Scheer, "Characterization and applications of plasmon fields in metal nanostructures," in *Smart Nano-Micro Materials and Devices*, vol. 8204. International Society for Optics and Photonics, Dec. 2011, p. 820404. [Online]. Available: https://www.spiedigitallibrary.org/conference-proceedings-of-spie/8204/820404/Characterization-and-applications-of-plasmon-fields-in-metal-nanostructures/10.1117/12.911835.short

[338] R. Arielly, A. Ofarim, G. Noy, and Y. Selzer, "Accurate Determination of Plasmonic Fields in Molecular Junctions by Current Rectification at Optical Frequencies," *Nano Letters*, vol. 11, no. 7, pp. 2968–2972, Jul. 2011. [Online]. Available: https://doi.org/10.1021/nl201517k

[339] C. I. Evans and D. Natelson, "Remote Excitation of Hot Electrons via Propagating Surface Plasmons," *The Journal of Physical Chemistry C*, vol. 123, no. 15, pp. 10 057–10 064, Apr. 2019. [Online]. Available: https://doi.org/10.1021/acs.jpcc.9b01174

[340] D. Natelson, C. I. Evans, and P. Zolotavin, "Photovoltages and hot electrons in plasmonic nanogaps," in *Quantum Sensing and Nano Electronics and Photonics XV*, vol. 10540. International Society for Optics and Photonics, Jan. 2018, p. 105400S. [Online]. Available: https://www.spiedigitallibrary.org/conference-proceedings-of-spie/10540/105400S/Photovoltages-and-hot-electrons-in-plasmonic-nanogaps/10.1117/12.2289114.short

[341] J. Marschall and A. Majumdar, "Charge and energy transport by tunneling thermoelectric effect," *Journal of Applied Physics*, vol. 74, no. 6, pp. 4000–4005, Sep. 1993. [Online]. Available: https://aip.scitation.org/doi/abs/10.1063/1.354443

[342] C. R. Leavens and G. C. Aers, "Vacuum tunnelling thermopower: Normal metal electrodes," *Solid State Communications*, vol. 61, no. 5, pp. 289–295, Feb. 1987. [Online]. Available: http://www.sciencedirect.com/science/article/pii/0038109887902997

[343] A. D. Smith, M. Tinkham, and W. J. Skocpol, "New thermoelectric effect in tunnel junctions," *Physical Review B*, vol. 22, no. 9, pp. 4346–4354, Nov. 1980. [Online]. Available: https://link.aps.org/doi/10.1103/PhysRevB.22.4346

[344] P. Reddy, S.-Y. Jang, R. A. Segalman, and A. Majumdar, "Thermoelectricity in Molecular Junctions," *Science*, vol. 315, no. 5818, pp. 1568–1571, Mar. 2007. [Online]. Available: https://science.sciencemag.org/content/315/5818/1568

[345] Y.-S. Liu and Y.-C. Chen, "Seebeck coefficient of thermoelectric molecular junctions: First-principles calculations," *Physical Review B*, vol. 79, no. 19, p. 193101, May 2009. [Online]. Available: https://link.aps.org/doi/10.1103/PhysRevB.79.193101

[346] B. Ludoph and J. M. v. Ruitenbeek, "Thermopower of atomic-size metallic contacts," *Physical Review B*, vol. 59, no. 19, pp. 12 290–12 293, May 1999. [Online]. Available: https://link.aps.org/doi/10.1103/PhysRevB.59.12290

[347] B. Meyerson and F. W. Smith, "Thermopower of doped semiconducting hydrogenated amorphous carbon films," *Solid State Communications*, vol. 41, no. 1, pp. 23–27, Jan. 1982. [Online]. Available: http://www.sciencedirect.com/science/article/pii/0038109882902423

[348] K. Takai, M. Oga, H. Sato, T. Enoki, Y. Ohki, A. Taomoto, K. Suenaga, and S. Iijima, "Structure and electronic properties of a nongraphitic disordered carbon system and its heat-treatment effects," *Physical Review B*, vol. 67, no. 21, p. 214202, Jun. 2003. [Online]. Available: https://link.aps.org/doi/10.1103/PhysRevB.67.214202

[349] I. Tsuyumoto, T. Hosono, and M. Murata, "Thermoelectric Power in Nonstoichiometric Orthorhombic Titanium Oxides," *Journal of the American Ceramic Society*, vol. 89, no. 7, pp. 2301–2303, 2006. [Online]. Available: https://ceramics.onlinelibrary.wiley.com/doi/abs/10.1111/j.1551-2916.2006.00979.x

[350] J. Tang, W. Wang, G.-L. Zhao, and Q. Li, "Colossal positive Seebeck coefficient and low thermal conductivity in reduced TiO2," *Journal of Physics: Condensed Matter*, vol. 21, no. 20, p. 205703, Apr. 2009. [Online]. Available: https://doi.org/10.1088%2F0953-8984%2F21%2F20%2F205703

[351] P. K. Tien and J. P. Gordon, "Multiphoton Process Observed in the Interaction of Microwave Fields with the Tunneling between Superconductor

Films," *Physical Review*, vol. 129, no. 2, pp. 647–651, Jan. 1963. [Online]. Available: https://link.aps.org/doi/10.1103/PhysRev.129.647

[352] D. C. Guhr, D. Rettinger, J. Boneberg, A. Erbe, P. Leiderer, and E. Scheer, "Influence of chopped laser light onto the electronic transport through atomic-sized contacts," *Journal of Microscopy*, vol. 229, no. 3, pp. 407–414, 2008. [Online]. Available: https://onlinelibrary.wiley.com/doi/abs/10.1111/j.1365-2818.2008.01920.x

[353] M. Kornbluth, A. Nitzan, and T. Seideman, "Light-induced electronic non-equilibrium in plasmonic particles," *The Journal of Chemical Physics*, vol. 138, no. 17, p. 174707, May 2013. [Online]. Available: https://aip.scitation.org/doi/full/10.1063/1.4802000

[354] C. S. Kumarasinghe, M. Premaratne, Q. Bao, and G. P. Agrawal, "Theoretical analysis of hot electron dynamics in nanorods," *Scientific Reports*, vol. 5, p. 12140, Jul. 2015. [Online]. Available: https://www.nature.com/articles/srep12140

[355] J. B. Khurgin, "Hot carriers generated by plasmons: where are they generated and where do they go from there?" *Faraday Discussions*, vol. 214, no. 0, pp. 35–58, May 2019. [Online]. Available: https://pubs.rsc.org/en/content/articlelanding/2019/fd/c8fd00200b

[356] H. Zheng, H. J. Liu, X. J. Tan, H. Y. Lv, L. Pan, J. Shi, and X. F. Tang, "Enhanced thermoelectric performance of graphene nanoribbons," *Applied Physics Letters*, vol. 100, no. 9, p. 093104, Feb. 2012. [Online]. Available: https://aip.scitation.org/doi/full/10.1063/1.3689780

[357] F. Mazzamuto, V. Hung Nguyen, Y. Apertet, C. Caër, C. Chassat, J. Saint-Martin, and P. Dollfus, "Enhanced thermoelectric properties in graphene nanoribbons by resonant tunneling of electrons," *Physical Review B*, vol. 83, no. 23, p. 235426, Jun. 2011. [Online]. Available: https://link.aps.org/doi/10.1103/PhysRevB.83.235426

[358] M. Topsakal, V. M. K. Bagci, and S. Ciraci, "Current-voltage $(I\text{\ensuremath{-}}V)$ characteristics of armchair graphene nanoribbons under uniaxial strain," *Physical Review B*, vol. 81, no. 20, p. 205437, May 2010. [Online]. Available: https://link.aps.org/doi/10.1103/PhysRevB.81.205437

[359] Y. Li, X. Jiang, Z. Liu, and Z. Liu, "Strain effects in graphene and graphene nanoribbons: The underlying mechanism," *Nano Research*, vol. 3, no. 8, pp. 545–556, Aug. 2010. [Online]. Available: https://doi.org/10.1007/s12274-010-0015-7

[360] M. Tsutsui, T. Kawai, and M. Taniguchi, “Unsymmetrical hot electron heating in quasi-ballistic nanocontacts,” *Scientific Reports*, vol. 2, p. 217, Jan. 2012. [Online]. Available: https://www.nature.com/articles/srep00217

[361] “What is confocal Raman microscopy? - HORIBA.” [Online]. Available: https://www.horiba.com/us/en/scientific/products/raman-spectroscopy/raman-academy/raman-faqs/what-is-confocal-raman-microscopy/

[362] natelsonoptics, “natelsonoptics/opticsexperiment: Optics experiment code,” Jan. 2020. [Online]. Available: https://zenodo.org/record/3599781#.XhPRw0dKibg

[363] ——, “natelsonoptics/Ruoyu_optics: Optics experiment code for Ruoyu’s computer,” Jan. 2020. [Online]. Available: https://zenodo.org/record/3599783#.XhPRvUdKibg

[364] “Welcome to PyDAQmx’s documentation! — PyDAQmx 1.0.0 documentation.” [Online]. Available: https://pythonhosted.org/PyDAQmx/

[365] “PyVISA: Control your instruments with Python — PyVISA 1.11.0.dev0 documentation.” [Online]. Available: https://pyvisa.readthedocs.io/en/latest/

[366] P. CladÃ©, “ThorlabsPM100: Interface to the PM100a/D power meter from Thorlabs.” [Online]. Available: http://pythonhosted.org/ThorlabsPM100

[367] “PyUSB.” [Online]. Available: http://pyusb.github.io/pyusb/

[368] “pyusb/pyusb,” Jan. 2020, original-date: 2011-09-02T18:36:18Z. [Online]. Available: https://github.com/pyusb/pyusb

[369] T. P. f. N. developers, “pythonnet: .Net and Mono integration for Python.” [Online]. Available: https://pythonnet.github.io/

[370] “contextlib — Utilities for with-statement contexts — Python 3.8.1 documentation.” [Online]. Available: https://docs.python.org/3/library/contextlib.html